A blade design methodology for overspeed power regulation in horizontal axis tidal turbines

Katie Gracie-Orr, BEng (Hons)

A thesis submitted for the
Degree of Doctor of Philosophy

Energy Systems Research Unit
Department of Mechanical & Aerospace Engineering
University of Strathclyde

February 2017

Declaration of authenticity and author's rights

This thesis is the result of the author's original research. It has been composed by the author and has not been previously submitted for examination which has led to the award of a degree.

The copyright of this thesis belongs to the author under the terms of the United Kingdom Copyright Acts as qualified by University of Strathclyde Regulation 3.50. Due acknowledgement must always be made of the use of any material contained in, or derived from, this thesis.

Signed: _____

Date: _____

The path

Many feet make one path
I like to walk on a foot path
I walk over the grass
and turn to see if I have made a path
Two feet once only
is not enough
I return to the foot path
to feel one of the bunch
I add my feet
I look back
What a path we made

Ivor Cutler

I dedicate this thesis to those alongside
to my husband and my family.

Contents

List of figures

List of tables

Acknowledgements

Firstly, to my supervisor Cameron Johnstone, for an excellent research idea, for guidance and encouragement, for applying for all those funding grants, and for pushing me out of my comfort zone – thank you.

To Darrel Doman and Mike Pegg, my Canadian supervisors, for looking after me across the pond and welcoming me to the Dal family, for helping me explain my research clearly and working with me on the nitty-gritty.

To SuperGen Phase3 UKCMER for support, encouragement, engaging research and brilliant DTP weeks.

To Robynne Murray, my collaborative partner, for enthusiasm, for making me dig deeper, for always knowing exactly what I'm talking about and for all the good times.

To Thomas Nevalainen for use of your blade element momentum theory code, for being a constant and intelligent pal with whom to discuss everything from the forces on aerofoils to the quirks of coding in MATLAB. To Stephanie Sanchez-Ordonez, thank you for your happiness and for your hard work in our second set of tank tests. To Andy Grant, Tom McCombes, Song Fu, Jose Manuel Rivera Camacho and Kate Porter, thank you for your innumerable slices of advice, input and cheer.

Special thanks to Michael Togneiri and Ian Masters of Swansea University for allowing us to use the aerofoil data you captured – this had a significant impact on the progress of my research. Likewise, a special thank you to Charles Keay, Ed Nixon, Grant Dunning, Sandy Day, both Bills, Steven Martin and Ian Milne at the Kelvin Hydrodynamics Laboratory and the Department of Naval Architecture. Your help, experience and your turbine rig were much appreciated, thank you for everything. And in the same vein, thank you very much to Cardiff Marine Energy Research Group, for lending us your turbine rig and letting us drive it in a van all the way up to Glasgow. Particular and warm thanks must go to Matthew Allmark for not only designing the machine but for speaking with us on the phone, at length, during the set-up.

To Peter Davies and Rebecca Sykes for your support, for the opportunity to work with you at Lloyd's Register, and for your openness and positive attitude.

The λ-based style of the cavitation analyses undertaken in this research was inspired by a conversation with Ralf Starzmann, to whom I owe great thanks for his enthusiasm – both for discussing my work with me and for tidal energy engineering in general.

To the ESRU research group for your support. In particular, for PhD-companionship

and true friendship: to nearly-Dr Allison for an incredible knowledge of MATLAB, of mathematics, of LaTeX, for your willingness to teach, and for making this excellent thesis template for Strathclyders; to Eric Baster for your kindness and even keel, and for laughing at me; and to Jacob Dibble for being sophisticated and chilled out and then completely loosing your cool on the hill.

Many thanks all of the PhD office crew for some excellent chats, for your interesting research and your valuable friendship.

To to Andrea Felling, for MATLAB genius, great willingness to help and delicious home-made pasta. To Nick Osbourne for enthusiasm to match my own. To Imke Meyer for inspiring professionalism and a supreme taste in wine. To Alice Goward Brown for our determined catch-ups and shared love of wood fires and cold water. To Tom Lake for grape-vine skills, Hannah Buckland for yoga in the paddock, to INORE for a mad week in Halifax, and to all of the SuperGen Phase3 UKCMER contingent (and friends) – thank you for years of friendship, sea-swims, dog-adoption, dinners, one lock-in, and much wine.

To the tidal and offshore renewable energy community at large, I owe many warm thanks. Without the conversations we have had around conference lunches, drinks, at posters and after presentations, by email, on buses and up hills, in Europe and in Canada, this would have been, by far, a less entertaining and enriching experience.

To my colleagues at SgurrEnergy, a brilliant group of people and a team I'm delighted to be part of, thank you for your support over the last 9 months.

To all of my friends – guys, it's done!! I really cannot thank you enough for always being there, for cheering me up, for understanding and for encouraging me to do this.

To my family – words are not enough, but I know you know what I mean. You've always been there, you have propelled me and encouraged me, you've fed me, you've heard all of the ups and downs, and been at least as excited as me in the successes.

To my husband Niall, my constant companion in all excellent and mad things, and my greatest support. You have a limitless capacity for kindness and care. You've helped me up every time it's been hard and you've made the best bits of doing this PhD even better. Let me thank you for everything you have done over these last, difficult periods of write-up. For cooking dinner and cleaning-up afterwards, for getting me up to write in the morning and shutting my computer again late at night, for taking me out to play frisbee for a break and for making, oh, at least a thousand cups of perfect tea. And for never, even once, complaining.

This work has been funded by the Engineering and Physical Sciences Research Council, through SuperGen Phase3, UKCMER. Without this funding, no PhD would have been undertaken and so I am eternally grateful. Further funding from UK Science and Innovation, Offshore Energy Research Association (Nova Scotia) and Scottish Development International has allowed the on-going collaboration between our two research groups through the Strathclyde-Dalhousie Collaboration.

Abstract

Employed in tidal turbines, overspeed power regulation (OSPR) can improve the structural robustness and decrease the complexity associated with active pitch methods, while removing the difficulties of operating in stalled flow. This may be a method by which the cost of tidal energy can be brought down. The aim of this research was to investigate the OSPR method, increase understanding of associated benefits and constraints, and develop a methodology for the design of suitable blades. It is identified that: the challenges to OSPR are higher rotational velocities, leading to increased voltage levels, an increased chance of cavitation on the rotor, and potentially detrimental thrust forces; these challenges may be best overcome with blade design alterations limiting the maximum rotational velocity.

The blade design methodology uses a design platform to set boundary conditions, an existing blade design as the base case, and a blade element momentum theory (BEMT) tool as the modelling method. Blade root pitch setting, twist and chord length distribution are the variable parameters investigated. A set of OSPR performance metrics and a design space sensitivity analysis, with whole-blade cavitation analyses and diagnostic plots of torque and angle of attack, are used to ascertain how function-based and then precise blade design alterations affect rotor performance.

Tow tank tests defined base case rotor performance and verified the BEMT tool. Tests on the new blades allowed comparison to the base case test performance and to the BEMT prediction. Simulations showed that the new blade design regulated power without cavitation inception, without an increase in the thrust forces and with only a 3.6% drop in efficiency – as per the set boundary conditions and design requirements.

The blade design methodology can be used to overcome challenges associated with overspeed and produce blades which give significant performance improvements for use in OSPR.

Chapter 1

Introduction

1.1 A sustainable way of living

Energy – how we obtain it, harness it, transport it, use it and, even, dispose of it – is fundamental to our way of life as human beings and as societies. We see vast differences through time and across the world in our relationship with energy, from timber fuelling cooking fires in the ancient past and at the hearth of today's poorest, through lucrative vats of fossil fuels bringing real progress and prosperity to the West, to the development of machines that capture the energy that is all around us. Today we live in challenging times in which unrest and economic and political uncertainty mingle with depletion in our fossil fuel resource; the base of scientific evidence which tells us we are changing the amount of heat in our planet is growing; our global use of energy is still increasing...

We have an opportunity to use what we have learned in our decades of industrial energy capture, distribution and use to empower and accelerate a transition to a future in which our energy use is sustainable. In this scenario, what we use today does not limit what future generations can use. Our relationship with energy can define us as a society that worked hard, did the maths, made the mistakes, did the learning, built the machines, structured the networks and succeeded in creating a prosperous and just way of life.

We are well on our way to meeting this goal; renewable energy sources are being exploited at an increasing rate, particularly hydro, wind and solar, with a nacent tidal energy industry following suit.

1.2 Tidal energy

1.2.1 Tidal stream power

The tidal motion of the seas provides the opportunity of a stream of flowing fluid from which kinetic energy can be harnessed, transferred to a mechanical motion and thereby to an electromagnetic system and utilised in the production of electricity. This stream power is relatively low in density in open ocean conditions, but is concentrated where

the tide is forced to turn a corner round a headland or is constricted in channels [1]. Areas of highly concentrated tidal power occur along many coastlines, notably along the coasts of: north-western Europe, particularly the North and West coast of Scotland, Wales, England [2], the east coast of Ireland and the north of France; in Nova Scotia in the Bay of Funday where the world's highest tidal ranges lead to some of the fastest tides; the eastern coast of North and South America; and the western seaboard of the Pacific Ocean [3].

1.2.2 Fundamentals of the tides

The phrase "tidal energy" pertains to the energy available in a body of water which flows in accordance with the sum of a set of harmonic forces known as the tidal constituents. Of these constituents, the greatest influence comes from the harmonic of the gravitational pull between the Moon and the waters of the Earth as the Moon orbits the Earth. The secondary forcing harmonic - having just 46% of the influence of the Moon - comes from the gravitational pull between the Sun and the waters as the Earth, Moon and Sun change their relative positions. As Hardisty explains in The analysis of tidal stream power [4, ch. 1-2], Newton's equilibrium theory of the tides provides a mathematical model explaining how these gravitational forces exert influence on the Earth's waters. Considering only the gravitational relationships between the Earth, the Moon and the Earth's waters in a simplified model - ignoring land masses, bathymetry and other celestial bodies - helps a conceptual understanding of the theory. On the side of Earth facing the Moon, the sum of the gravitational forces pulling the water onto the Earth and towards the Moon redistributes the water, creating a Moon-wards bulge. The Moon and Earth are also gravitationally attracted to one another and are therefore set at a certain distance. On the far side of Earth proximity to the Moon is least and therefore the force between the waters and the Moon is smaller than at the mid and moon-side waters; this results in a second, smaller equilibrium bulge facing the opposite direction to the first. As the Earth's surface and the Moon move in relation to one another under the harmonics of Moon orbit and Earth spin, the bulge is moved round the globe as a tidal wave. A point on the surface of Earth will thereby experience changing water depth. The water depth will be greatest when the point on the Earth's surface is in-line with the Moon, giving the basis of high tide (HW). The water depth will be lowest when the point is at right angles to the Moon, giving the basis of low tide (LW). When in-line with a point on the Earth's surface and the Moon, the force exerted by the Sun in this model augments the Moon's influence and the equilibrium bulges are at their largest; this results in Spring tides. When the Sun, the point on the Earth and the Moon made a right angle, the Sun's gravitational effect minimises the net force, and the distribution of water is most even; this results in Neap tides. This is known as the Spring-Neap cycle of the tides, in which the difference between the depth of high water (HW) andlow water (LW) – known as tidal range – varies through two Springs and two Neaps in a

lunar month.

This simplified model does not, however, fully explain the tides as experienced on Earth. As Hardisty [4] discusses, The non-uniform orbital distances between Moon, Earth and Sun affect tidal ranges, giving, for example, higher Spring tides at equinox and smaller ranges when Neap tides coincide with solstice. The influence of other celestial bodies is lesser than those of the Moon and Sun, but is still important in the creation of the tidal system. Factors of influence other than gravitational forces include the Coriolis effect: the Earth's axis lies at 66.5° to its plane of orbit round the Sun and the spinning of the Earth around this axis exerts a further force - the Coriolis force - on the Earth's waters, having the effect of rotating the tidal wave in an anti-clockwise sense in the Northern Hemisphere, and in a clockwise sense in the Southern Hemisphere. Atmospheric pressure, wind velocities and thermal ocean currents can also affect the tides. The presence of bathymetry and land masses greatly adds to the dynamic complexity to the localised motion of the tides, directing water around coastlines, accelerating tides through constrictions, augmenting tidal periods in bays, causing HW to propagate along the sides of islands at different rates, and generally giving rise to localised accelerations and phase differences in HW timing, HW heights and HW-LW cycle times.

Although the system response is complex, the problem has been worked on for centuries. Astronomers and mathematicians such as Nicolaus Copernicus and Tycho Brahe, Galileo Galilei, Johannes Kepler - who conceived the Keplerian system, which, with amendments, is the model used today – and, ultimately, Isaac Newton, provided the measurements and mathematics which gave us the models of planetary motion and gravitational attraction which drive the tides. The cumulative work of thinkers, observers, astronomers, mathematicians and engineers has resulted in a thorough understanding of how the tides are governed, how the tides will flow and, therefore, when and how much energy will be available. This has significant implications for the usefulness of tidal energy in the electricity mix. For example, in the North Atlantic the semi-diurnal (twice daily) wave of tidal flow propagates towards the Celtic Sea and flushes around the British Isles roughly every five hours. The phase difference between HW at different locations as the waves move through and round means that tidal energy could contribute to the reliability of a renewables-based electricity network [4, ch. 2]. Predictive models, based on the harmonic constituents, bathymetry and shore-line data, can predict the washing of the tide - in with the flood, and out with the ebb - and the velocities that will be induced at given 'tidal diamond' locations.

The tides - and therefore the energy available in the tides - are not only guaranteed, but also predictable.

1.2.3 Tidal energy capture devices

The areas of concentrated tidal power are the focus points for deployment of devices designed to capture tidal energy. The primary job – and therefore the first goal of the nascent industry – of a tidal energy capture device is to harness the power available in the tides. The second requirement of a device created for energy capture is to do so in the most cost-effective manner.

Focussing first on the primary aspect, there are several forms of tidal energy capture devices, summarised in, for example, reference books such as [The analysis of tidal stream power] [4] and review papers such as [State of the art in tidal current energy extracting technologies] [5]. These define three main concept categories of tidal stream energy device: horizontal axis tidal stream turbines (HATSTs), vertical axis tidal stream turbines (VATSTs) and novel devices which do not fall into either of these categories, such as those based on planar oscillations.

This work focusses on HATSTs, within which category, as demonstrated by Zhang et al. [5], the majority of deployed devices have been, and upon which most development has taken place. There are many HATST concepts in the industry, some of which have seen the greatest success to date in the capture of tidal stream energy, for example, Nautricity Ltd's CoRMaT, Schottel Hydro's SCHOTTEL Instream Turbine, Andritz Hydro Hammerfest's HS series, Atlantis Resources Corporation Ltd's AR1000 Turbine, Nova Innovation's Nova devices, and the slightly alternative designs of turbines such as Open-Hydro's Open Centre Turbine.

The physical mechanisms of energy capture will be discussed further in this thesis.

Though with additional aspects, the system and function of HATSTs is similar to that of the prolific "Danish concept" wind turbines, in comprising a rotor of blades numbering two or more, a drive train, a power take-off system and a support structure, and acting to extract energy from an axially-flowing fluid in which it is immersed. It is therefore possible to draw many analogues between the two technologies, and for the tidal energy community – research and industry-based – to learn from the foregoing experience of the wind energy community; each of which in turn has and can benefit from the vast knowledge base of the shipping industry, particularly as relating to propeller design. Throughout this thesis and as is the case for much of the research in tidal energy, therefore, wind turbine technology and experience will be referenced and made use of.

In addition to the functions and aspects of survivability for which wind turbines must be designed, tidal turbines are required to cope with a conductive, corrosive fluid, existing at pressures – depending on deployment depth – of multiples of standard atmosphere. This fluid, sea water, is more viscous and dense than air and therefore transmits greater forces to a turbine. Because tidal energy is at its greatest density in bathymetrical or coastal constrictions, the resource is almost always of a turbulent nature, much more so than, for example, a clean coastal wind. Freestream turbulence, as will be discussed, is a challenging aspect of the tidal energy resource. The tendency

for marine life to attach itself to underwater structures is a further challenge which the industry must face and which is not the case for onshore wind turbines (though the sub-sea components of offshore wind turbines undoubtedly must consider the potential impact). Tidal turbines must also be either water-tight at, often, significant depths or be, at least partially, designed to cope with flooding. In either case, the electrical aspects must be insulated or removed from the water which, given the chance, will seep the captured energy away.

Looking to the second aspect of the job of a tidal energy capture device, a common metric of cost-effectiveness used broadly across the energy industry is the levelised cost of electricity (LCOE), measured in terms of GBP (or, more commonly outside of a UK context, USD) per MW h [6]. This metric is the ratio of the total invested and operational cost in an electricity production plant to the total energy the plant will produce over its lifetime [7]. In order to become economically viable in the long term, the LCOE of tidal energy devices must come into line with that of other renewable energy sources. This means that tidal technology and practices must produce energy at a similar cost to other renewable sources while managing the technical challenges shared with those other industries as well as additional challenges. These including those associated with access to variable deployment sites subject to increasingly capricious weather, and survival in the turbulent, wet, salty marine environment.

1.2.4 Increasing robustness and simplicity

Cost reduction, then, in order to become economically competitive with other sources of renewable energy, is essential for the development of the tidal energy industry. The industry is still in the process of identifying techniques and technologies which are most reliable in the marine environment, and most cost-effective, whether in development, manufacture, deployment, operation or maintenance. However, developments which limit the complexity and increase the robustness, and thereby increase the reliability, of turbine systems will lead to reduced failures. This may – depending on any drawbacks associated with the developments – provide the industry with a means to reduce the LCOE.

Compared to the wind energy industry, failures leading to maintenance requirements in the tidal industry have the significant additional problem of difficult access. The weather and tidal-state requirements associated with performing maintenance on tidal turbines give fewer and shorter windows of opportunity even than in the offshore-wind industry, while the vessels often required are exceedingly expensive to hire. These factors combine to produce processes of greater cost to the developer than in a wind turbine deployment. Wind turbine availability - the percentage of time for which a turbine is technically available, able to produce energy - generally exceeds 95 % for onshore machines and, for offshore deployments, generally starts at 90% in the first year and increases to $95 - 98\%$ in subsequent years [8]. Due to the afore-mentioned access

challenges, tidal turbines will need to compete with or improve upon these availability levels in order to obtain acceptable levels of cost of energy. It is therefore desirable to remove as many of the vulnerabilities, complexities and systems which add cost to tidal turbine technologies.

In the wind industry, the increased energy capture possible with variable pitch turbine blades operated in variable speed outweighed the disadvantages associated with the increased complexity, and became the technology of choice for modern wind turbines. However, it cannot be denied that there were disadvantages. As reported in an evaluation of an extensive 10 year study of 350 MW worth of wind turbines [9], failures in the pitching mechanisms - considering pitch drives, bolted joints and bearings but not the blades themselves - were the driving factor for the 85% higher rotor failure rate of pitch regulated turbines than passive stall regulated ones. This demonstrates that driving down failure rates for tidal turbines by increasing the robustness of the rotor design may be an important way of increasing the cost-effectiveness of this renewable technology.

1.3 Aims of the research

The method of power regulation is one area of the turbine design with which complexity and vulnerabilities are associated; use of the overspeed method may contribute to the required reduction in complexity and improve the robustness of tidal turbines. The rotor design is fundamentally important in how power is regulated. The aim of this research, therefore, was to investigate the overspeed power regulation method, increase understanding of the associated benefits and constraints, and develop a methodology for the design of blades suitable for use in overspeed power regulation.

To achieve this aim, the research goals were to identify:

- potential issues with, and therefore design requirements for, the proposed operating method
- whether these requirements could be met with changes to the rotor design
- how the impact of any rotor design changes could measured in terms of these requirements
- what information could be gathered about the changes and impacts made by these blade design changes
- whether this information could be used to develop a blade which meets the requirements
- how this works in practice.

1.4 Overview

1.4.1 Overview of the thesis

This thesis describes the development and application of a blade design methodology for HATSTs controlled with OSPR. Chapter 2 gives the background context to turbine performance and operation, the fluid dynamics and flow phenomena involved. An overview of power regulation is given and a discussion of generator topologies with regards to the requirement of variable speed imposed by an overspeed-regulated device follows. A deeper discussion of power regulation is then given, which considers the different methods and rotor configurations. A discussion of previous research into and application of overspeed regulation methods is presented. Finally, a discussion of other blade design methodologies is given.

In Chapter 3, the empirical performance of two turbines is presented, in an investigation of turbine operation – with particular emphasis on performance in overspeed. The results of wind tunnel tests provide a starting point from which, along with consideration of the literature, the potential challenges associated with OSPR are identified. The chapter goes on to present tow tank tests performed on a currently available blade design, which allowed a base case blade design and base case performance to be defined. The empirical data gathered in the tow tank also provided a final set of data with which to verify the performance prediction tool used in this research. The chapter concludes by defining the challenges of designing for OSPR, and identifying the specific performance characteristics of most importance in improving turbine design for use with OSPR.

In Chapter 4, the blade design methodology is developed. The mathematical and theoretical bases of Blade Element Momentum Theory (BEMT), the tool used to model rotor performance in this research, are presented. The basis, theory, and application method of the component aspects of the blade design methodology are presented in turn. OSPR metrics are developed to measure positive and detrimental effects had by blade design alterations on the appropriateness of a blade for use in OSPR. The concepts of the design platform, the design space analysis, and the diagnostic and cavitation plots are introduced.

In Chapter 5, the blade design methodology is applied to a specific set of design requirements and boundary conditions, defined in a design platform. Each stage of the application is specifically discussed, and the results and analyses from each set of blade design alterations are considered. The usefulness of each of the components of the blade design methodology are demonstrated. The methods employed are shown to be successful, both in generating information regarding the impact of blade design alterations on rotor performance for OSPR, and in identifying how a blade design which increasingly meets the design requirements may be developed. In the second half of the chapter, a second set of tow tank tests are presented, designed to verify the success of both the blade design and the methodology used to develop it.

In Chapter 6, the performance of a new blade design, specifically developed for

OSPR within the defined design platform, is presented and discussed. The blade was developed for a full-scale rotor and the performance of this blade is compared to the performance of the base case blade, both modelled at full-scale using BEMT. The favourable performance of the new blade for use in OSPR is demonstrated. The results of the tow tank tests on the new blade are discussed. The performance is compared to that of the prototype-scale BEMT prediction, as well as to the empirical performance of the base case blade, captured in the first set of tow tank tests.

Finally, in Chapter 7, the work undertaken and the results of each section of the research are summarised. Conclusions are drawn with regards to the contributions made. A future work section discusses the next steps which would give further development to the blade design methodology. Suggestions are made with regards to further verification. And, finally, the usefulness of research to produce further aerofoil data obtained in a range of flow conditions appropriate to modelling the performance of small turbines is discussed.

1.4.2 Approach taken in the blade design methodology

In general, it is possible to consider any blade design, any design alteration, and/or to couple these with any other design alterations. There are two extremes of possible blade design methodologies - incremental and algorithmic. The blade design methodology here presented was developed with the aim to: remove much of the time and expertise required in the incremental-alterations option; break down and open-up for viewing the "black-box" of the optimisation algorithm option; and produce information which provides some of the experiential knowledge gained by – and often limited to – the engineer and computer, respectively, in the alternative options. Alterations made by eye, randomly or incrementally would be exceedingly time-consuming, and a successful blade design may be long in the coming, unless the engineer has expertise or experience. On the other hand, it is possible to write optimisation algorithms which consider a wide range of blade shapes and optimise based on a set of objectives and constraints. An advantage of this option is that, once the algorithm and implementation programme have been developed, the time required to produce a blade design can be significantly reduced.

In the former case, the engineer uses experience to by-pass many of the options an algorithm would trial, based on an understanding of constraints and the relationships between inputs and outputs; however by the same necessary process of selection, the engineer may not consider possible options which could inform or improve the blade design, particularly were local maxima or minima to be encountered. Furthermore, while either of these options should result in successful blades, it may not be standard for either process to output information on the impact of alterations to the blade design parameters. This, importantly, is experiential knowledge which would be useful in general for engineers working on turbines, and in particular for the development or

fine-tuning of both the blade in design, and those of future turbine installations.

The methodology, then, will have some of the advantages of each of the two extreme alternative approaches, and some of the disadvantages. It can be seen, therefore, as a balance between the two, with the further advantage of outputting useful information which can be stored and shared. The methodology has been specifically developed for the design of blades for use in overspeed power regulation (OSPR) tidal turbines, yet with alternative metrics could be easily applied in the design of fixed pitch (FP) blades for use with a different power regulation method.

Most of the work previously undertaken in this field has been focused on optimising a blade design for a given turbine configuration. This work therefore aims to develop a methodology which explicitly considers the impact of a wide range of geometrical blade design parameters to develop and facilitate an understanding of the effect of blade design changes on cavitation inception, turbine efficiency and structural loads, and is not specifically limited to one turbine configuration.

1.4.3 Scope of the methodology

The methodology is focused primarily on the hydrodynamic aspects of rotor design; in the main design methodology, analysis of the structural properties of blade designs is limited to consideration of the C_T-λ curve.

The tidal sites which provide the design platform are considered in so far as the depth, the deployment depth, and operation of the turbine within the range of inflow velocities from cut-in to cut-out. It is assumed that the turbine will be parked and/or yawed above these flow speeds and, as requiring assumptions to be made with regards to the drive-train and generator design, no assumptions are made as to the methods of start-up or shut-down. The effect of turbulence and the velocity and depth-altering effects of waves are not incorporated into the methodology at this stage. Some suggestions as to how this may be undertaken, and to what ends, are given in the Chapter 7. No control system is implemented at this blade design stage, and therefore perfect transition from region I to III (Fig. 2.10) is assumed.

A structural feasibility study was developed to verify that the design produced are practicable. This is presented in Appendix B and was included to provide assurance of the design's feasibility rather than to aid the structural design, which is outside the scope of this research.

1.5 Contributions made

The major contributions to the field of tidal energy made in this thesis are:

- an increase in the knowledge held on the operation of HATSTs in overspeed, as pertaining to the use of overspeed for power regulation
- an increase in the knowledge of the impact of blade design alterations

- a blade design methodology for overspeed power regulation of horizontal axis tidal turbines
- a blade design which has been shown to be able – in a steady flow – to regulate power by overspeed without increasing the thrust force, without the occurrence of cavitation inception on the blades, and with only a 3 % decrease in optimum power capture.

The blade design methodology developed sets the geometrical parameters of blade root pitch setting, twist distribution and chord length distribution as variables. In the first stages of alterations made, the changes are defined by function-based alterations, and in the later stages by hand-picked fine-tuning changes, informed by the foregoing findings. A design platform is used to give a scenario in which the blade design changes can be assessed for performance in maximum power point tracking and overspeed power regulation as the flow increases from cut-in to cut-out. The methodology uses a set of metrics – developed to ascertain how the blade design changes affected the suitability of blade designs for use in overspeed power – and a design space sensitivity analysis approach, alongside a whole-blade cavitation analysis and diagnostic plots of the torque distribution and angle of attack. The combination of these methods and tools gives an efficient yet open-box procedure, which allows information to be gathered and used in an iterative spiral in which blade permutations are made increasingly suitable for overspeed power regulated tidal turbines.

The concept of using OSPR performance metrics in a design space analysis has been developed in the research, the purpose of which is to enable the rotor design to be moulded to a set of explicitly defined performance requirements, set for a specific deployment site.

The expedited application of blade design alterations via the use of function-based alterations has, to the knowledge of the author – not been previously presented as a method within an "open-box" design procedure. In combination with batch-run BEMT-predictions and the design space sensitivity analysis, this allows many blade design alterations to be analysed efficiently while retaining a pattern in the alterations made. The advantage of this is that the effects of making a *type* of change can be investigated and – with the visual-numerical approach herein presented – appreciated, both in terms of each individual change made and in terms of the *range* over the change was made.

It has been shown that the blade design methodology can be used to overcome challenges associated with overspeed and produce blades which give a significant performance improvement in terms of applicability in overspeed power regulation.

1.6 Relevant publications

1.6.1 Journal papers

- Lead author; relates to Chapter 4:

Katie Gracie-Orr, Thomas M. Nevalainen, Cameron M. Johnstone, Robynne E. Murray, Darrel A. Doman, Michael J. Pegg, *Development and initial application of a blade design methodology for overspeed power-regulated tidal turbines*, International Journal of Marine Energy, Volume 15, (2016), 140–155.

- Joint-lead author; relates to the second half of Chapter 3:

  Darrel A. Doman, Robynne E. Murray, Michael J. Pegg, Katie Gracie, Cameron M. Johnstone, Thomas Nevalainen, *Tow-tank testing of a 1/20th scale horizontal axis tidal turbine with uncertainty analysis*, International Journal of Marine Energy, Volume 11 (2015), 105–119.

1.6.2 Conference papers

- Lead author; Relate to Chapter 4 and first half of Chapter 3, respectively.
  - K. Gracie, T.M. Nevalainen, C.M. Johnstone, R.E. Murray, D.A. Doman, M.J. Pegg, *Development of a blade design methodology for overspeed power-regulated tidal turbines*, European Wave and Tidal Energy Conference, Nantes, 2015.
  - K. Gracie, R.E. Murray, C.M. Johnstone, D.A. Doman and M.J. Pegg, *Fixed-Pitch Blades for Passive-Feather Power Regulation of Second-Tier Site Tidal Turbine*, European Wave and Tidal Energy Conference, Aalborg, 2013.
- Joint-lead author; relates to first half of Chapter 3:

  D.A. Doman, Robynne E. Murray, M.J. Pegg, Katie Gracie, C.M. Johnstone, and Thomas Nevalainen, *Dynamic testing of a 1/20th scale tidal turbine*, Asian Wave and Tidal Energy Conference, Tokyo, 2014.

1.6.3 Poster presentations

Lead author on all below:

- Katie Gracie, Cameron Johnstone, *A blade design methodology for overspeed power regulated tidal turbines* SuperGen UKCMER Annual Assembly 2015
- K. Gracie, T.M. Nevalainen, C.M. Johnstone, R.E. Murray, D.A. Doman, M.J. Pegg, *Impact analysis of blade shape on performance of tidal turbine for passive feather power regulation, Poster presentation*, International Conference on Ocean Energy, Halifax, 2014. Relates to initial investigations undertaken, which became the basis of the design methodology.
- Katie Gracie, Cameron Johnstone, *Development of a blade design methodology for over-speed power regulated tidal turbines* SuperGen UKCMER Annual Assembly 2014. *First prize for best poster*

- Katie Gracie, Cameron Johnstone, *Fixed-Pitch Blades for Passive-Feather Power Regulation of Tidal Turbines* SuperGen UKCMER Annual Assembly 2013

- Katie Gracie, Cameron Johnstone, *Investigating the passive regulation of power output for a tidal turbine over the range of the tidal cycle* SuperGen UKCMER Annual Assembly 2012

1.6.4 Conference presentations, no paper

- Sole presenter; Related to overall background, aims and methods of research. Katie Gracie, *A blade design methodology for overspeed power regulated horizontal axis tidal turbines*, Invited to session titled "Design, R&D, vessel update and something very different ", AllEnergy, Glasgow, May 2015.

- Joint presentation; Related to overall background, aims and methods of research. Robynne Murray and Katie Gracie, *Development of high performance tidal turbine rotors*, Ocean Energy Research Association Research and Development Conference, Halifax, May 2014.

1.7 Tools used

It is appropriate, at this point, to give due reference to the tools which were used in this research and methodology, which were not developed as part of this research, nor by the author. Acknowledgement and thanks go to the developers of these excellent and invaluable tools, for use and support.

1.7.1 BEMT

The BEMT tool used throughout this research was developed in the course of separate PhD research undertaken in parallel at the Energy Systems Research Unit, the University Strathclyde [10]. The development of this BEMT tool was not work undertaken in this project, and is accordingly not detailed here. However, as the tool itself was used extensively in this project, and the experimental work obtained in this project was used in the verification of the code, the basis of the method is outlined in Section 4.2 and it will be referred to throughout this thesis.

1.7.2 NREL tools

Several of the tools used in this research were developed and made available by the National Renewable Energy Laboratory (NREL). These included AirfoilTools, AirfoilPrep and XFOIL. Reference is given to these where used. These tools were used to provide modelled aerfoil data in cases where empirical data was not available or appropriate.

1.7.3 Aerofoil data

Though not strictly a tool, due acknowledgement must be made of the low Reynolds number aerofoil data provided by the Marine Energy Research Group at the University of Swansea.

1.7.4 Turbine rigs

The turbine rig and instrumentation used in the first set of tow tank tests were developed by the Department of Naval Architecture at the University of Strathclyde.

The turbine rig and instrumentation used in the second set of tank tests were developed by Cardiff Marine Energy Research Group at the School of Engineering, Cardiff University.

Chapter 2

Background of tidal energy - fluid dynamics and turbines

2.1 Theory of HATSTs in tidal flow

As discussed in, for example, [11, ch. 3] and [4, ch. 3], the fundamental concept of a HATST is to exploit the lift-creating properties of blades with aerofoil-shaped cross-sections to develop power from a rotational velocity, Ω, and a mechanical torque, Q_{mech}, at the rotor. This then turns a shaft, which produces relative rotational motion between the armature and stator of a generator, developing electromagnetic torque, Q_{em}, and producing electrical power, P_{E}. The mechanical power produced at the rotor, P_{mech} is dependent on the power available in the tidal stream, P_{T}, and the mechanical efficiency of the rotor, generally expressed as the coefficient of power, C_{P}. It is important to note that, as Burton et al. point out, the definition of C_{P} does not take the Betz limit into account; that is to say, this expression of rotor efficiency does not account for the maximum possible energy extraction from a free stream of fluid, and any C_{P} value should therefore be considered according to this "Betz limit" maximum 59.3 %, rather than an impossible 100 %. The Betz limit will be defined later, in Eq. (4.13), Section 4.2.

Considering the following definitions,

$$P_{\text{T}} = \frac{1}{2}\rho A U_{\infty}^{3} \ , \tag{2.1}$$

and

$$P_{\text{mech}} = Q_{\text{mech}}\Omega \ , \tag{2.2}$$

C_{P} can be defined as

$$C_{\text{P}} = \frac{P_{\text{mech}}}{P_{\text{T}}} = \frac{Q_{\text{mech}}\Omega}{\frac{1}{2}\rho A U_{\infty}^{3}} \ . \tag{2.3}$$

As Eq. (2.1) shows, the power available in a tidal stream is related to the cube of the free-stream velocity, U_{∞}. The function of HATSTs is to exploit this velocity in the most effective manner.

The efficiency of power capture at the rotor face, C_{P}, is a primary performance characteristic and is a function of the rotor design - particularly of the blade design. In a similar manner, the coefficient of thrust, C_{T}, is the ratio of experienced thrust force, F_{T}, to the dynamic force of the fluid [13]. This parameter is defined as

$$C_{\mathrm{T}} = \frac{F_{\mathrm{T}}}{\frac{1}{2}\rho A U_{\infty}^{2}} \ , \tag{2.4}$$

and allows the structural implications - an important aspect of effectiveness - of a rotor design to be assessed [11].

The ratio of the free-stream tidal velocity and the tangential velocity at the tip of the rotor blades is defined as the tip speed ratio, λ:

$$\lambda = \frac{\Omega R}{U_{\infty}}. \tag{2.5}$$

This value is of great use in quantifying the performance of a rotor design in a nondimensional manner. Plots of C_{P} and C_{T} against λ are frequently used to this end. The value of λ pertains to the resulting angle between the fluid and the blade, which is influential on the performance of the blade.

A related value, the local speed ratio, λr is defined as the ratio between the blade and the flow at radial position r on the blade:

$$\lambda_{r} = \frac{\Omega r}{U_{\infty}}. \tag{2.6}$$

A HATST operates in a range of flow velocities defined by a cut-in velocity, U_{C} - beneath which losses and inertia prohibit operation - and a maximum velocity, U_{max}. In-between these, as will be discussed in greater detail in Sections 2.3.1 and 2.4, is the rated flow velocity, U_{R}.

2.1.1 Performance curves

The operation of a HATST is informed by performance curves. Turbine performance curves allow the performance of the rotor to be characterised in dimensionless form which, by default, allows the expected power and thrust at the face to be defined for any given tidal stream velocity, according to Eqs. (2.3) and (2.4). Example curves are presented in Fig. 2.1. One caveat to this, as explained in [14, ch. 5] and investigated in [15], is that the performance is only characterised non-dimensionally for operation in which the W values are either above the Reynolds Number (Re) independence for the blades' aerofoil(s), or result in Re values not significantly different from those associated with the empirically or model-derived performance curve. (It should be noted that this applies also to the Mach number; however, the velocities and compressibility of fluids relevant to the discussion of tidal energy are such that the Mach number is not relevant to this discussion.)

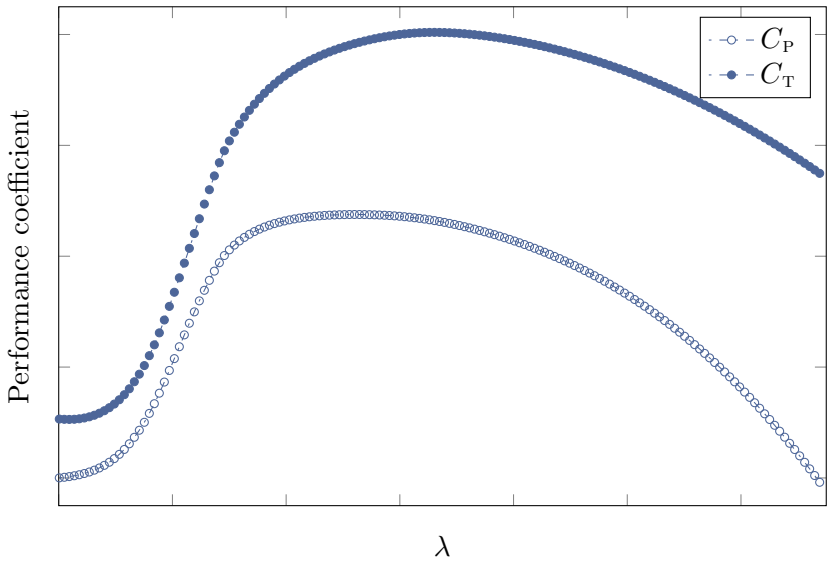

Figure 2.1: Characteristic performance curves of a typical HATST

A fully populated performance curve describes rotor performance over the range of flow conditions between the fully-stalled condition on the far LHS, where $\lambda \to 0$, to the fully feathered condition, also termed the runaway point, on the far RHS, where $C_P = 0$ and $\lambda = \lambda_{rw}$.

At the design stage, these curves can be used to rapidly assess design iterations, tune the rotor design to site conditions and link-in the generator design and performance. In the operation stage, prior knowledge of the performance curves allow algorithms to be developed which assess the flow scenario and apply the appropriate control action to alter or maintain the structural or power performance of the turbine system.

2.1.2 Momentum and blade element theories

The terms C_P and C_T are functions of the rotor design, primarily of the blade design, and allow the effectiveness of a given device to be analysed. In order to assess the power available in the flow, an conceptual and mathematical model of from where the extracted power originates must be developed. The initial work from which the basis of tidal stream power analysis comes was undertaken for the performance analysis and design of propellers. Combined, the theories of momentum and blade elements have provided this capability – with increasing accuracy – to engineers working on propellers and turbines since the late 19th century. As discussed in 'Marine propellers and propulsion'[16, ch. 8], Rankine proposed the theory of axial momentum in 1865, which was developed to take account of rotational momentum by R.E. Froude in 1887. The originally contrasting blade element theory was developed in 1878 by W. Froude. These two theories of rotor disks and blade elements can be combined in the now well-known BEMT. BEMT has had significant use as a design tool in the shipping, wind and tidal energy industries, as indicated by the development and extensive use of tools such as NREL's FAST, and

GH Garrad Hassan' Bladed and Tidal Bladed tools

The theory and back ground of BEMT is covered thoroughly in [12, ch. 3], [13, ch. 3], [11, ch. 4-6], amongst other texts. The background and theories are briefly described here and, as BEMT was the rotor performance prediction tool used in this research, the topic is covered more thoroughly in Section 4.2.

According to the Rankine-Froude Momentum Theory, all the energy extracted by a turbine in a free-stream flow comes from the total change in momentum of the fluid. The rotor disk is treated as an actuator disk in this theory. Consideration of the conservation of mass and the pressure change across the actuator disk allow calculation of these momentum changes and the forces which are their cause. The changes in axial and tangential flow induced by the presence of the rotor are taken into account with velocity induction factors, a and a' respectively, upon which expressions for rotor power and thrust are found to depend.

Slightly modified from its original formulation, to include the inductions factors, the BLADE ELEMENT THEORY says that a blade can be divided into elements of non-differential length, each of which can be considered as an isolated aerofoil section operating in a 2D flow field, with no radial flow between the blade sections. The theory states further that the power and force over the whole rotor can be obtained by summing the contributions from each of these blade elements, and then from each blade [12, 16, 11, 13].

Blade element momentum theory

The BEMT - as its title suggests, is the combination of the momentum and the blade element theories. The basis of BEMT is that by setting the annuli used in momentum theory analysis to be of the same radial position and length as the blade elements used in blade element theory, BEMT can be used to determine the torques and forces on the rotor. From each theory are derived terms for the elemental axial force and elemental torque; these equations are equated and, normally by an iterative process, a final value for each blade element is converged upon. These are then summed to give the whole rotor torque and thrust. This process is repeated for an investigated range of flow conditions to produce the performance curves of the rotor design. A thorough discussion of the development of BEMT can be found in [16, ch. 8] and a more succinct discussion of particular relevance to wind energy (and therefore to tidal energy) can be found in [12, ch. 3], [13, ch. 3], [11, ch. 1-6]. This brief overview of the historical development of BEMT for rotor performance analysis is largely based on the discussions in Marine propellers and propulsion [16].

The development of an accepted version of BEMT included some corrections to the initial theories. Based on the work on vortex theory he undertook with Lanchester, Prandtl suggested the correction known as the Prandtl tip loss factor, which considers the effect of the formation of trailing vortices and the associated induced velocities

present on propellers. This vortex theory was confirmed in 1919 with empirical data, and its inclusion allowed the BEMT method to make use of the wealth of 2D aerofoil data produced in wind tunnels. Betz worked on the effects of induced drag by considering the vortex systems, deriving the limits of power extraction from a free steam. Prandtl and, later, Goldstein investigated the difference made by considering a finite number of blades on the effect these vortices have on the induced flow. The trailing vortices of a rotor of infinite blades would be close together and that this would not be the case for a rotor with a small number of blades. For the real rotor, then, there must therefore be a difference between the mean induced velocity of an annulus and that locally at a blade's lifting line at the same radius. Goldstein developed the Goldstein correction factor, K, which is a ratio between this mean circulation around an annulus and the circulation at a corresponding position on a helicoidal surface. Tachmindji and Milam furthered this work by considering propellers of non-zero hub radius.

As discussed in [12] further developments and empirical corrections have been offered to correct for an under-prediction of thrust in the higher λ range. The momentum theory would predict flow reversal in the wake when the axial induction factor increases beyond around 0.4. This is not physically the case, instead the wake expands as the radially-moving air separates at the edge of the rotor and causes a large pressure drop behind the rotor. The energy required by the wake to achieve the required far wake pressure is obtained by increased turbulent mixing which entrains flow from the surrounding free-stream. This turbulent state cannot be predicted by the blade element or momentum theories, and empirical corrections are therefore required. Glauert produced experimental data showing rotor performance in the turbulent wake state, and proposed an empirical correction factor to increase the values of C_{T} towards those derived experimentally. In [17], Shen et al. discussed what is known as the Spera correction. In [18], Buhl proposed a corrective equation which solved a numerical discontinuity issue in the previous corrections for high induction, while fitting the data as well as many previous attempts.

Prediction of rotor performance in the region of low λ also proved problematic. A notable solution was proposed by Viterna and Corrigan; in [19] they found that the aerodynamic behaviour of stalled aerofoils was approximately that of a flat plate of the same aspect ratio, and proposed the manner in which this correction could be integrated into BEMT.

Section 2.2 gives further discussion of the flow over aerofoils and blades, and the influential flow phenomena.

The BEMT tool used

The BEMT code used in this research was developed by in a parallel PhD undertaken within the Energy Systems Research Unit at the University of Strathclyde. In his PhD thesis [10], Nevalainen gives detailed description of the correction factors included in

his composition of steady BEMT. In Section 4.2, further detail of the induction factor correction method implemented for this research, and the reason for its selection, along with the final sets of equations and the solution method are discussed.

2.2 Fluid flow phenomena on turbine rotors

This section gives a general discussion of aerofoil behaviour, a definition of key terms, and a background to the flow phenomena that will be discussed in this thesis.

Aerofoils are the basic cross-sectional shape of most rotor blades. In general, the performance of the aerofoil cross-section(s) form the basis of any understanding or prediction of rotor blade performance. Aerofoil performance tends to be obtained as behaviour in two-dimensional (2D) flow, under a specific flow condition or set of conditions. In order for this behaviour to be applicable to a rotor, the influence of certain flow phenomena need to be considered and, where possible, accounted for in either (or in each) the production of the aerofoil data, in the performance model predicting rotor behaviour, or in the empirical test conditions in which rotor behaviour is measured. If there is not appropriate representation of the flow conditions in any of these three related areas, it will be difficult to match predicted and actual rotor performance. It is therefore of importance to understand what effects may be governing or influencing aerofoil and rotor performance.

The influence of Reynolds number, free-stream turbulence [20], 3D effects [21, 22] and cavitation are amongst the flow conditions which can affect the performance of aerofoils and thus of blades and rotors. Therefore, the suitability and usefulness of empirically derived aerofoil data – whether at low Reynolds numbers or otherwise – in predicting the performance of 3D wings and blades [23, 24] is also affected by these factors.

2.2.1 2D aerofoils in planar flow

The theoretical basis of the generation of lift, and the attending subject of drag, will not be covered in this thesis; knowledge of these subjects is assumed or can be obtained in the literature. The function of aerofoils as lifting surfaces is key to the operation of turbine blades, and is described conceptually in texts such as Aircraft flight [25, ch. 1], with some more of the mathematical background in Wind energy explained [13, ch. 3] and with thorough mathematical background in Fundamentals of aerodynamics [26] and Theory of wing sections [14], for example.

Fig. 2.2 shows an aerofoil section in planar, two-dimensional (2D) flow – that is to say, flow which is uni-directional, directly in the axis of the aerofoil and non-rotating. The resulting forces on the aerofoil are shown in the two coordinate systems used regularly in the literature - the first aligned with the flow and the second resolved to the chord line. The forces produced on an aerofoil are what drives round the rotor of a

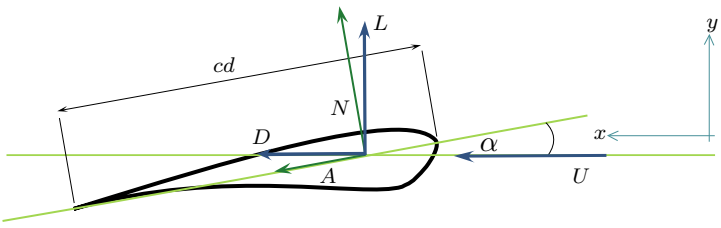

Figure 2.2: Planar aerofoil in 2D flow showing definition of the normal, tangential lift and drag forces, the angle of attack and the chord length.

turbine, and are functions of the angle of attack, α, between the blade chord line, c, and the flow incoming to the aerofoil. c is defined as the linear distance from the leading edge (sometimes known as the nose of the aerofoil) to the trailing edge, as illustrated in Fig. 2.2). The definition of α is also shown in Fig. 2.2. As described in [26], the force of lift, L, acts perpendicular to the incoming fluid vector, U; the force of drag, D, parallel with U, acts to counter the relative velocity between the aerofoil and the fluid through which it is moving. The normal, N, and axial, A, forces are the components of the sum force on the aerofoil, resolved into the coordinates of the aerofoil rather than the flow field. The aerofoil coordinates are referenced to the chord line.

For any aerofoil design the dimensionless response of the aerofoil to α is quantified in terms of the dimensionless 2D coefficients of lift, C_l, and drag, C_d. As discussed in [14, ch. 1], the forces on a wing, L_wing and D_wing, are defined:

$$L_\mathrm{wing} = \frac{1}{2}\rho U^2 S C_\mathrm{l} \tag{2.7}$$

and

$$D_\mathrm{wing} = \frac{1}{2}\rho U^2 S C_\mathrm{d} \tag{2.8}$$

where S is the planar area of a wing. The force on an aerofoil section, then, can be defined by taking the differential form of Eqs. (2.7) and (2.8) [11, ch. 6]:

$$dL = \frac{1}{2}\rho U^2 c\ C_\mathrm{l} dr \tag{2.9}$$

$$dD = \frac{1}{2}\rho U^2 c\ C_\mathrm{d} dr\ . \tag{2.10}$$

Aerofoil data is generally presented in both tabular and graphical forms, such as the plots of coefficient of lift (C_l) and moment (C_m) against α and of coefficient of drag (C_d) and moment (C_m) against C_l shown in Figs. 2.3 and 2.4. These data describe the aerofoil's lift and drag response, maximum lift-drag ratio, stall characteristics and aerodynamic moment, over a range of α – generally from around $-20°$ to some point after stall and before stall recovery, usually 20° - 30° – and for a range of discrete Re values. Fig. 2.3 gives an example of the behaviour of an aeorfoil with a sharp stall characteristic; Fig. 2.4 shows an example of more benign stall behaviour. These will be discussed further in Section 2.2.3.

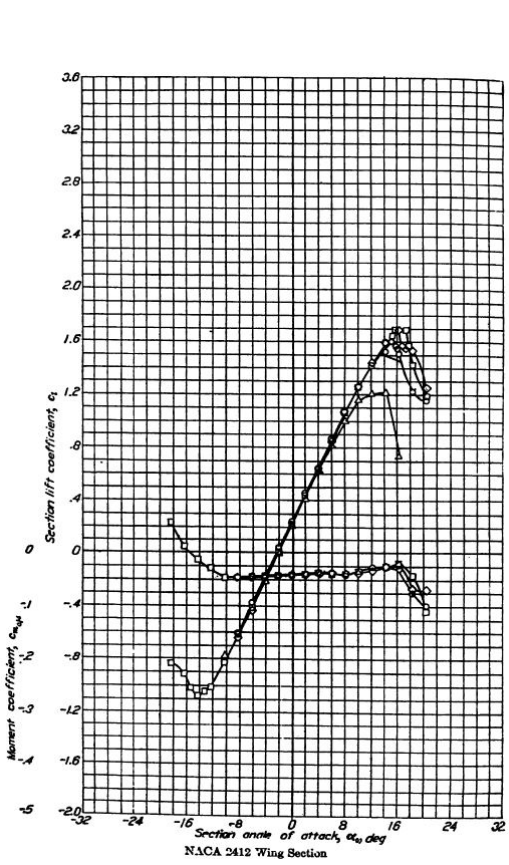

(a) Relationships between angle of attack with coefficient of lift, and angle of attack with coefficient of moment.

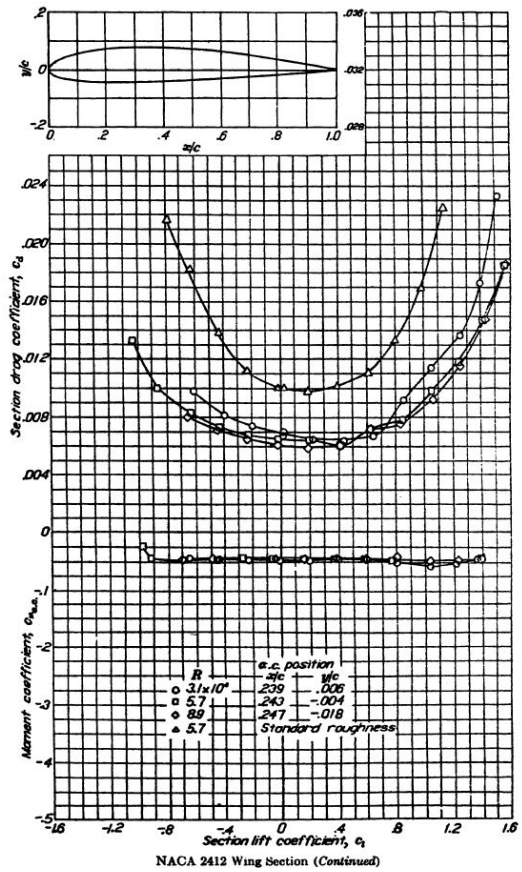

(b) Relationships between coefficient of lift with coefficient of drag, and coefficient of lift with coefficient of moment.

Figure 2.3: Example of a steep stall aerofoil behaviour and *Re* influence, NACA 2412. Figures taken from Theory of wing sections [14, App. IV]

Empirical data in graphical and tabulated form is widely available, for many aerofoils, in texts such as Abbot and von Doenhoff's Theory of wing sections [14] - from which Figs. 2.3 and 2.4 are taken - and online in such databases as the National Wind Technology Centre (NWTC) Information Portal [27], at NREL. Predicted aerofoil data is also available, as are tools with which to generate predictions of the response of existing and new aerofoils under input flow scenarios, such as Drela's XFoil [28].

2.2.2 3D effects

In most practical applications, aerofoils do not operate in a 2D but in a 3D flow environment. This has an impact on how the aerofoil behaves, bringing new phenomena both to the performance of the aerofoil and to the effects on the flow. A brief discussion of 3D effects is given here in order to give context to the following sections and to highlight some of the issues pertinent to the modelling of tidal turbine performance and to operation of tidal turbines in the sea.

At the free ends of even an aerofoil operating in planar flow in a true free stream,

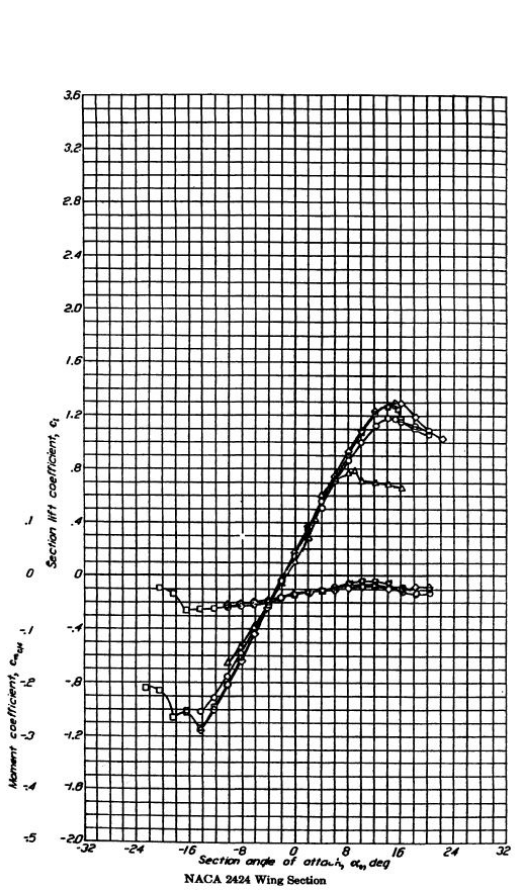

(a) Relationships between angle of attack with coefficient of lift, and angle of attack with coefficient of moment.

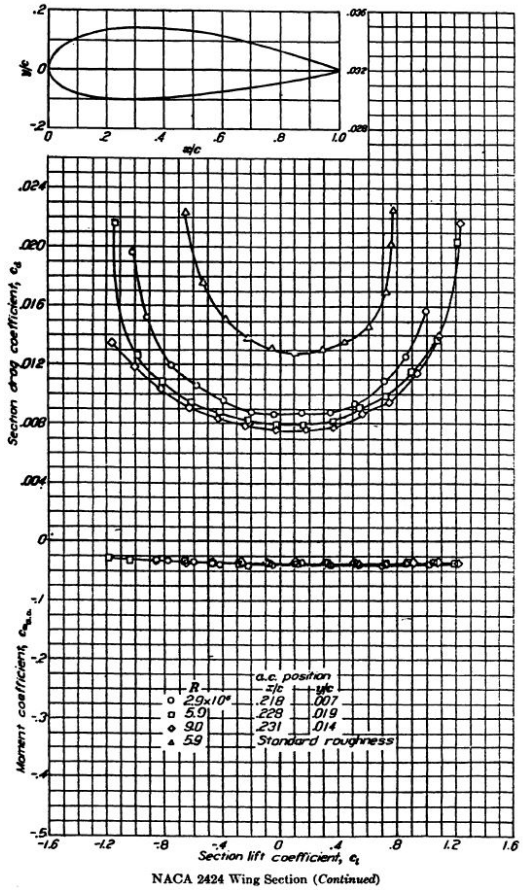

(b) Relationships between coefficient of lift with coefficient of drag, and coefficient of lift with coefficient of moment.

Figure 2.4: Example of a more benign stall aerofoil behaviour, with *Re* influence, NACA 2422. Figures taken from Theory of wing sections [14, App. IV]

vortices will be shed during the interaction of fluid and foil. The shedding of these vortices induces an alteration to the pressure which in turn influences the velocity of the fluid. This results in a spanwise tendency in the flow and can have a significant impact on the performance of the aerofoil, as discussed in [14, ch. 1]. Such effects are augmented by the rotational movement of the blades of a turbine, which movement exerts further spanwise forces on the flow. Entrained fluid mass (discussed in [16, ch. 11]) is of greater importance to tidal turbines than to wind turbines due to the increased density of the fluid; such added mass will undergo the forces of rotational motion, augmenting the 3D effects and increasing the difficulty in modelling tidal turbine behaviour. As will be discussed, design codes such as BEMT include some empirical corrections to account for these effects. Research continues in this field in terms of predicting tidal turbine behaviour; the dynamic, dense, viscous and turbulent nature of tidal flows increase the challenge of using 2D aerofoil data obtained in wind tunnels, as has been given consideration in such work as presented in [29], [30] and [31].

Dynamic 3D flow has a significant effect on the stall behaviour of turbines. This will

be discussed in Section 2.2.5.

2.2.3 Boundary layer effects

The condition of the boundary layer – the closest layers of flow to the surface of the aerofoil – is a crucial factor in the performance of aerofoils.

As implied, and as can be directly seen in Figs. 2.3 and 2.4, the magnitude of lift and drag force on a 2D aerofoil section are functions of the angle of attack. In low angles of attack, the boundary layer is generally fully attached to the aerofoil as it propagates down the surface. The effect of viscosity in these conditions produces an adverse pressure gradient from the nose to trailing edge, which can be overcome by the energy in the flow, $\frac{1}{2}\rho W^2$. As α increases, the adverse pressure gradient increases until, at some point, the pressure reduces the velocity of the layers nearest the aerofoil surface to zero. Further increases in pressure encountered by the flow leads to flow reversal and separation from the aerofoil surface: the beginnings of stall.

As discussed in [14, ch. 5] stall, the separation of the boundary layer to a degree that loss of lift occurs, can begin at the trailing edge or nearer the aerofoil nose. Leading edge stall occurs suddenly, due to the inability of the flow to overcome the fist incidence of minimum pressure gradient, and results in a sharp peak in the lift coefficient and sudden loss of lift. This kind of stall behaviour can be seen in the performance of a NACA 2412 aerofoil in Fig. 2.3a, taken from [14]. Trailing edge stall is characterised by a more gradual loss of lift, induced by separation of the turbulent boundary layer from the tailing edge under the adverse pressure gradient. As the gradient increases and the energy is increasingly unable to overcome the adverse pressure, the point of turbulent separation moves towards the tip until the lift coefficient ceases to increase and begins to decrease. An example of this more gradual loss of lift can be seen in the performance of a NACA 2424 aerofoil in Fig. 2.4a, taken from [14]. However stall occurs, the increase in drag under the circumstances of separated flow is great. At this stage, the aerofoil is experienced by the flow as a barrier rather than a surface over which to run; the profile drag resulting from the pressure of this is accordingly great.

Reynolds number

The aerofoil performance described above is non-dimensionalised with the coefficient of lift and drag, as discussed. However, as revealed by dimensional analysis techniques (see [26, ch. 1]), there are a set of dimensionless parameters which, if varying between the scenarios, influence the performance of aerofoils and therefore of blades and rotors. One of the most influential of these parameters is the Reynolds number (Re), defined as the ratio of the inertia forces to the viscous forces [26]. In the case of an aerofoil, this definition can be expressed as

$$Re = \frac{\rho W c}{\mu} \ , \tag{2.11}$$

where ρ and μ are the density and dynamic viscosity of the working fluid, c is the chord length and W (or U in the case of the planar flow shown in Fig. 2.2) is the relative flow between the aerofoil and the working fluid.

The dependence of C_l is established in [26, ch. 1]. Turbulent boundary layers, due to increased mixing, are more able to entrain energy and overcome pressure gradients. As Figs. 2.3a and 2.4a demonstrate, once the critical Re has been exceeded and the boundary layer flow can be characterised as turbulent, an increase in Re generally increases the maximum coefficient of lift. The Re range for the data shown in Fig. 2.3a is 2.9×10^6 to 9×10^6, within which range the maximum value of C_l (C_lmax) increases from 1.5 to 1.7. Some level of convergence can be seen in C_lmax of this and most aerofoils in this Re range, so that full scale tidal rotor may not experience a huge variation in aerofoil performance over the normal operating range of velocities, and thus the rotor design could be said to be non-dimensionalised, within operational boundaries at least. However, this will depend on the rotor and turbine design and the flow environment. In a smaller rotor system operating in a range of flow velocities, this Reynolds number effect means that more power will be obtainable (disregarding any power regulation methods) when the Re increases. As Eq. (2.11) indicates, this means that changes in W during operation, caused by alterations to the rotor velocity, Ω, or flow velocity, U_∞, can significantly affect P_mech and F_T. Furthermore, the c term in Eq. (2.11) and the α term in Fig. 2.2 indicate that design alterations to the blade shape can have a significant impact of blade performance.

In low velocities, the flow moving over a smooth surface will generally be laminar, having a low Reynolds number. Laminar flows are characterised by small values of vertical velocity, resulting in low mixing with the free stream – energy is not readily transferred to the boundary layer. As Eq. (2.11) indicates, as W increases so does the Reynolds number. Around a critical Reynolds number, the flow transitions to a turbulent state. The value of critical Re varies based on the exact body and flow conditions but is frequently defined to be 5×10^5 , as a general rule [26, ch. 15]. Turbulent flows are characterised by the presence of many small eddies in the flow. Much more mixing then exists between the layers of flow in a turbulent boundary layer, as well as between the boundary layer and the free stream, increasing the average energy and velocity of the boundary layer flow. Laminar boundary layers on aerofoil sections tend to quickly transition to the turbulent state, encouraged by high Re. [14]

The subject area and literature covering aerofoil performance in low Reynolds numbers is complicated, huge and intruding [32], as evidenced, for example, by the five-volume book Summary of low-speed airfoil data [33]. It becomes very difficult to calculate the performance of aerofoils at low Re, and so numerical tools such as XFOIL cannot be used and empirical data must be employed.

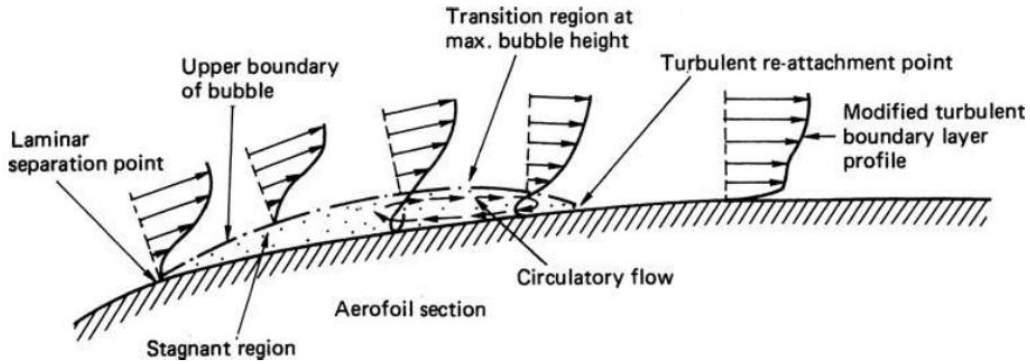

Figure 2.5: Diagrammatic description of laminar separation and reattachment of the boundary layer. Figure taken from Marine propellers and propulsion [16, Ch. 7]

Laminar separation and reattachment

In the situation where an extensive laminar boundary layer exists – e.g. in very low Reynolds number flows – a phenomenon known as laminar separation and reattachment can occur. In this situation, on encountering the peak of minimum pressure, the laminar flow separates from the aerofoil surface. Consequent mixing with the free stream increases the energy of the boundary layer flow, within which velocity fluctuation instabilities increase, leading to transition and associated thickening of the boundary layer, to the point of the reattachment of the flow as a turbulent boundary layer [16, 32, 14, 34]. This behaviour is represented in Fig. 2.5.

In very low Re flows, at Re values around 7×10^4, the situation where the separated boundary layer cannot gain sufficient energy to reattach to the surface can occur. This results in sudden, leading edge stall.

Lissaman discussed that the effect of long laminar bubbles such as this is to decrease the aerofoil efficiency [32]. In his PhD thesis [35], Milne presented research on the presence and effects of long laminar bubbles on an aerofoil (the NREL S814). He found that these bubbles were present at Re in the tested region of $1 \times 10^5 - 3 \times 10^5$, and caused a significant increase in drag. Fig. 2.6, taken from [32], illustrates the wide range of effects which can be produced by hysteresis caused by laminar separation and reattachment.

2.2.4 Free stream turbulence

Perhaps more pertinent to full-scale turbines than the foregoing sections, though just as important at the small scale, the turbulence in the free stream has a significant effect on the performance of aerofoils and rotors. In Effects of turbulence on tidal turbines: Implications to performance, blade loads, and condition monitoring [36] Blackmore et al. define turbulence as a description of "the chaotic motions within a fluid flow". In Turbulence in marine environments (TiME): A framework for understanding turbulence and its effects on tidal devices, [37], in which Clark disseminates the purpose,

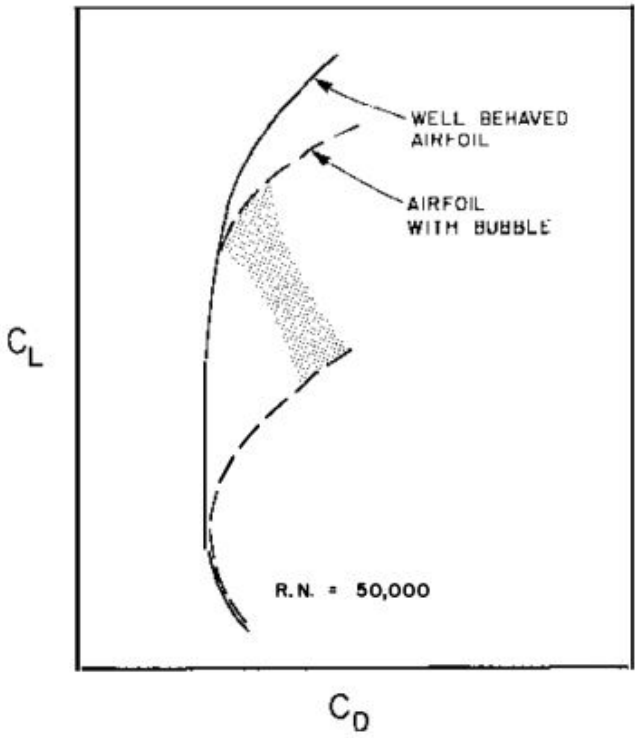

Figure 2.6: Comparison of aerofoil behaviour in $Re = 5 \times 10^4$ with and without the presence of laminar bubbles, showing wide range of effects caused by the hysteresis of separation and reattachment. Figure taken from Low-Reynolds-number airfoils [32]

methodologies and findings of the Turbulence in Marine Environments (TIME) project [38], turbulent flow is given the definition: "A turbulent flow is both chaotic (highly unstable, sensitive to changes in initial conditions) and dissipative (governed ultimately by viscous effects)". Turbulent flow is characterised by the presence of chaotic flow disturbances (or eddies) within the free stream. Disturbances are induced in the free stream by differences in velocity between layers of flow, which cause shearing. These velocity differentials can be created by the boundary shear effect of a fluid moving over a solid, by protrusions (from micro to macro scale) of the solid boundaries containing the flow, or from other external sources causing a change in velocity, such as an object or another fluid moving through the fluid or on its surface.

The variations in flow angle and velocity associated with turbulence have a direct impact on the performance of turbines, both in terms of power and of structural loading. As discussed in [36], the fluctuations in the forces acting on the rotor due to turbulence can cause fatigue and can be detrimental to the structural longevity of the turbine system. If not either constrained to the rotor-side of the shaft or conditioned out by power electronics, turbulent events on the turbine my also reduced power quality.

In both [37] and in the TIME project documents themselves, turbulence - as pertaining to the marine environment and the tidal energy industry - is classified in three categories:

- Small scale turbulence; turbulent events at this scale are of the size of the chord length of the turbine blades.
- Medium scale turbulence; the length scale of medium eddies are larger than the blade chord length, and no larger than the diameter of the turbine.
- Large scale turbulence; turbulent disturbances at this scale are larger than the turbine diameter, causing a machine-scale gust effect, and are "on the scale of turbine separations in an array".

Clark presents a tabulated analysis of the effects the different scales of turbulence can have on the various aspects of turbine performance, operation and installation. Regarding effects had by turbulence on the blades, it is noted that each of the turbulent scales can have an impact. At the small scale, velocity changes can be made to the boundary layer, which can result in altered drag values and point of transition, and can exacerbate or suppress cavitation and dynamic stall behaviour. These effects can be periodic in nature or can alter the mean force values. Medium scale turbulence is of concern with regards to sudden changes in loading as velocities and angles of attack change over a single blade or part of a blade. Cavitation and dynamic stall can also be thereby induced or suppressed, over a greater portion of the blade(s) than by eddies of a smaller length scale.

The result of the induced excursions in load - whether increasing the mean loading or increasing the fatigue stress - can lead to significant effects at the rotor and in the drive train, as discussed in [31]. In line with this discussion Blackmore et al. found, in experiments on a small scale turbine in which the turbulence intensity was varied, that increased turbulence of a small scale relative to the turbine resulted in reduced power and reduced thrust force; increased turbulence at a larger scale relative to the turbine had the opposite effect, increasing the load and power [36].

2.2.5 Stall behaviour in rotational flow

Some of the specific effects on stall occurring in the operation of turbines in real freestream environments are outlined here. Dynamic stall effects, as discussed by McCroskey [39], Butterfield et al. [40], Leishman [24], Larsen et al. [41], Reddy and Kaza [42], Hu et al. [43], Du and Selig [44], and many others, have been a challenging field in wind energy for decades, as evidenced by the continued publication of papers on the subject. Dynamic stall can occur on aerofoils operating in unsteady conditions. Empirical evidence shows that once the static stall α has been exceeded, the formation of a leading edge vortex (LEV) occurs which then propagates along the aerofoil, creating increased suction on the upper surface and thus increasing the lift. Once the LEV reaches the trailing edge, these values peak and then abruptly drop to significantly lower values. The formation of subsequent LEVs can occur, which have similar but reduced effects on aerofoil performance.

On the reduction of α, hysteresis in reattachment can occur wherein reattachment is delayed and occurs at an α lower than the static stall angle [39]. A further effect, known as stall-flutter can occur in a situation of dynamic stall in which the net damping (related to the work done over a full oscillation in and out of stall) is negative and the aerofoil extracts energy from the fluid. This negative damping effect can incur fatigue damage not predicted by design models which did not or were not able to predict dynamic stall. [42] The hysteresis of reattachment can result in over-prediction of power capture and an under-prediction of fatigue loading. It is such a common feature of turbine operation that the IEC standards for the power performance testing of wind turbines [45] outlines how two power curves may be produced in the testing process – one as the turbine transitions into stall and past the cut-out wind speed, and a second as the turbine cuts-in again.

Dynamic, 3D flow on a blade can result in a delay in stall as the loss of lift is suppressed past the expected angle of stall by the spanwise component of velocity [12, 44]. Occurring particularly at the blade root and tip sections where spanwise flow is greater, this effect can produce higher loads – both electrical and structural – than expected and can therefore cause significant damage to the machine if stall delay was not considered in the design stage.

However, understanding of the behaviour of dynamic and stalled flow is increasing, as evidenced by the increased accuracy of wind turbine performance prediction achieved in models which include dynamic stall, as in, for example, [41].

Research into these effects increases the applicability of models in designing the performance of turbine rotors.

2.2.6 Cavitation

Submersion in a liquid gives tidal turbines the additional challenge of possible cavitation inception on the blades. Cavitation, as discussed in [16, ch. 9], is the occurrence of bubbles of vaporised liquid in the working fluid, due to sustained pressure drops to or beyond the (gauge) vaporisation pressure of the fluid. That is to say, the suction pressure on a aerofoil operated underwater can become so great that it overcomes the hydrostatic pressure and the bonding forces holding the molecules together in their liquid state, causing the liquid to vaporise. Cavitation is most likely to occur in a fluid in which minute nuclei - groups of molecules of gas or vapour - exist. Nuclei, either within crevices in the body or entrained in the flow, which encounter a reduction in pressure of the surrounding fluid can grow to become fully-formed cavities.

Cavitation, as discussed in [16, 46, 47] can manifest on a blade surface as bubbles or as a sheet, and can occur on the aerofoil nose and on the back and face surfaces. Fig. 2.7, taken from Marine propellers and propulsion [16], shows an example of sheet (a) and bubble (b) cavitation occurring on the blades of a tested propeller.

Where on the aerofoil cavitation inception occurs is dependent on where the minimum

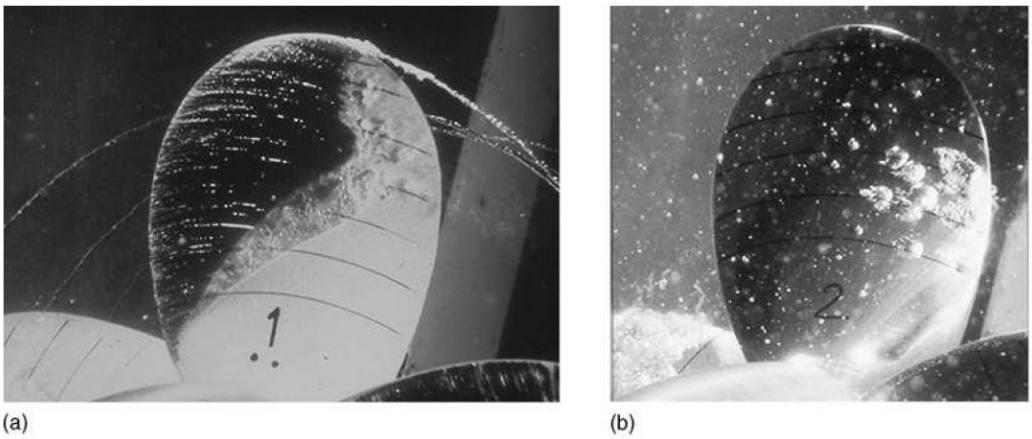

Figure 2.7: Photographs showing sheet (a) and bubble (b) cavitation on the blades of a tested propeller. Figure taken from Marine propellers and propulsion [16, Ch. 9].

coefficient of pressure occurs, which changes with the angle of attack. This has been discussed in various texts and papers, such as [16], [46], [47]. Fig. 2.8a illustrates a generic cavitation envelope, showing the relationship between angle of attack and cavitation number which determines whether and where cavitation occurs.

As discussed in these and other references, cavitation on the surface of blades is a cause for concern and should be either prevented at the design and/or operation stage or prevented from causing damage in some other manner. The presence of cavities on turbines blades can lead to significant performance alterations. The bubbles effectively alter the camber of the aerofoil, increasing the maximum lift; a phenomenon which has been seen to cause increases in power past the predicted levels [16]. The form drag can also be augmented. Periodically induced cavitation can, with these changes in force, induce fatigue on the blades in a manner not predicted by a steady-state model which does not account for cavitation inception. Possibly the most important aspect of cavitation inception on turbine blades, however, is the destructive potential of cavity implosion. As a cavity is flushed over the aerofoil it encounters an increase in pressure which can force the vapour back into liquid form. It is understood that when cavities implode at the surface of a solid, the proximity of the wall forces an asymmetry upon the implosion, which then tends to channel its massive amounts of energy into the surface of the solid near or upon which the collapse occurs. Fig. 2.8b shows a Plesset and Chapman model of cavity collapse, illustrating the formation of a microjet, the mechanism of cavitation erosion damage. This microjet acts like a drill, boring into the solid surface. As well as the structural damage this has on the blade, cavity-induced surface roughness encourages further cavitation.

Cavitation inception is not a favourable flow behaviour, in general, for tidal turbines.

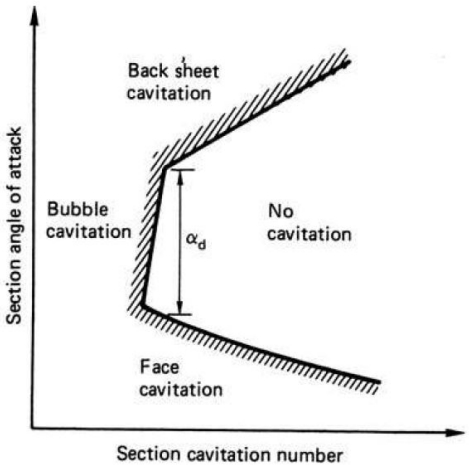

(a) Diagram of a generic cavitation envelope showing the influence of angle of attack on cavitation occurrence and location of cavitation inception point.

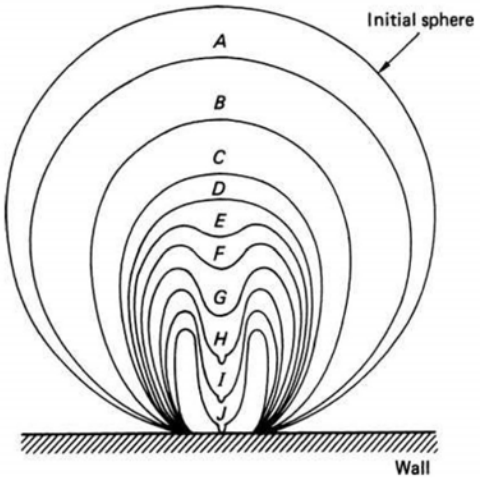

(b) Diagram of the collapse (computed) of a cavitation bubble in proximity to the solid surface, showing the high-pressure microjet predicted by the spherical bubble model developed by Plesset and Chapman, 1971.

Figure 2.8: Figures taken from Marine propellers and propulsion [16, Ch. 9].

2.3 Operation and system components

As a topic, the system of a tidal turbine and its operation in tidal flow is large, broad and complex and is covered thoroughly in reference texts such as The analysis of tidal stream power [4] or – as the system of a tidal turbine is very much like that of a wind turbine – Wind energy explained [13] and Wind energy handbook [12]. For the purpose and within the scope of this thesis, the system component of particular interest is the rotor design, especially the hydrodynamic aspects. The operation methodology, including power regulation technique, is a vital aspect of a holistic approach to turbine design and analysis, impacts and is impacted by the system components, and is of key importance to the focus of this thesis. The methodology of operation is generally undertaken electrically via the generator and thus the generator topology is of importance. Though neither generator, power electronics nor controller design are the focus, a background understanding of these systems, as pertaining to the requirements arising from the rotor design and proposed operation method, is useful. An overview is therefore given here.

The modes of operation, the associated technologies and concepts such as fixed speed (FS) and variable speed (VS) operation, FP and variable pitch (VP) blades, power conversion and generator systems, are inter-related topics of high importance to the understanding of renewable energy turbines operating in a free stream. This section develops an understanding of the principles involved, based on books such as [12, 11, 13] and papers as cited in the text; deeper context will been gained from texts with a more specific focus, such as [48, 49]. A more in-depth discussion of power regulation will then be given in Section 2.4

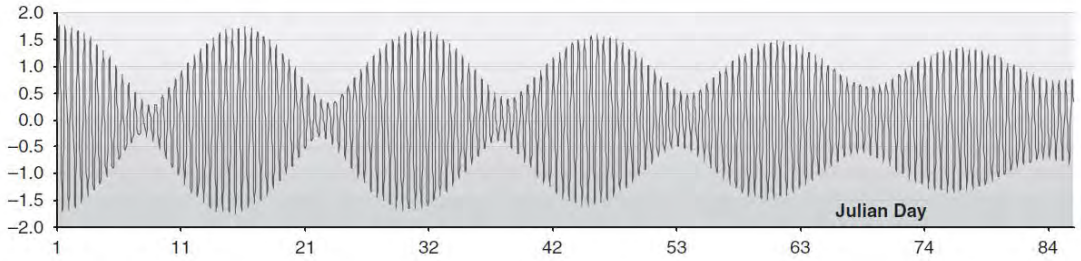

Figure 2.9: Diagram of three months (5.5 spring-neap cycles) of tidal velocities recomposed from harmonic constituents. Figure taken from The analysis of tidal stream power [4, Ch. 5].

2.3.1 Power variability and regulation

The periodic variability of tidal flow velocities gives rise to an according periodic variability in the power available in the flow.

For the greater part of the tidal cycle, flow velocities are less than the maximum, and the maximum for each day and each spring tide varies according to the influences discussed in Section 1.2.2, as Fig. 2.9 (taken from The analysis of tidal stream power [4, Ch. 5]) shows. During most tidal states, turbines are generally operated in such a way as to maintain the rotor efficiency, C_{P}, at the optimum value, C_{Po}. As the velocity of the tide increases, the available power increases. The variability of tidal flow velocity means that high values of power are frequently available, but for only a small percentage of the time. Fig. 2.9 illustrates this point, showing the variability of the tidal velocity over roughly 84 days and 5 spring-neap cycles.

Due to the small amount of time over any month in which the tide is particularly fast-flowing, it is most economically efficient to optimise the turbine system to capture rated power, P_{R}, at a value less than the maximum flow velocity, $U_{\infty\mathrm{max}}$, and to spill or *regulate* the excess power when the available power exceeds the rated value. The first flow velocity at which P_{R} can be obtained is called the rated flow velocity, $U_{\infty\mathrm{R}}$. Taking $\pm$ 1.25 $\mathrm{m\,s^{-1}}$ as an example $U_{\infty\mathrm{R}}$ and comparing this to Fig. 2.9, it can be seen that small but regularly occurring portions of velocity exceed this $U_{\infty\mathrm{R}}$. By designing the turbine to capture its P_{R} at a power lower than the maximum value, the turbine system is operated at its most efficient for a greater proportion of time. This means a smaller and less expensive generator, drive train components and rotor. By spilling excess power, the entire system can be protected from electrical and structural over-loading when the tide exceeds $U_{\infty\mathrm{R}}$. This power regulation is achieved by reduction of the efficiency of the rotor in capturing power, and is shown - both with the ideal case and with a case in which power is regulated poorly - in region III of Fig. 2.10.

Tidal turbines therefore require to be operated in various manners. As illustrated in Fig. 2.10, the operational states of tidal turbines can generally be split into 4 main regions:

- When there is insufficient energy available in the tide to overcome the inertia of the rotor and drive-train, the turbine is generally parked (or, in some way, taken

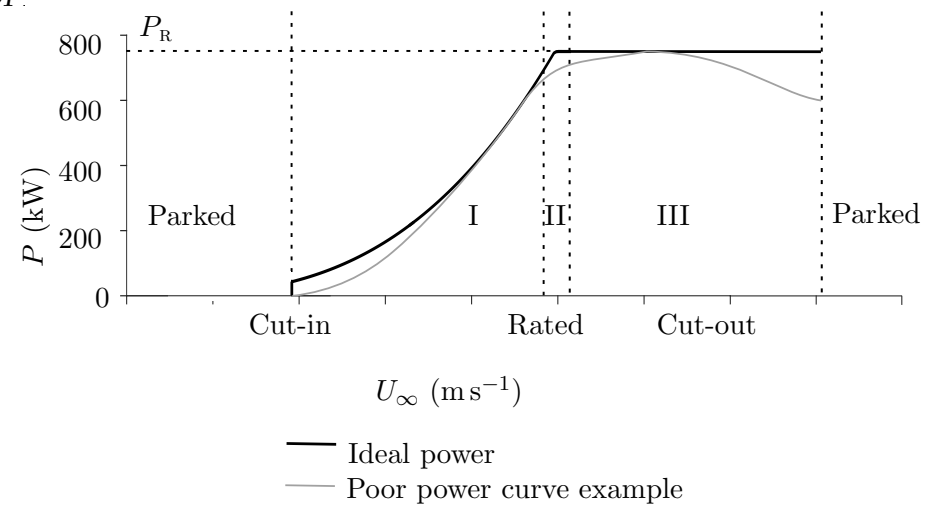

Figure 2.10: Operational regions for HATSTs in terms of inflow velocity and power. Ideal and an example power curve shown; example power curve is for a passive stall (FPFS) regulated turbine, extracted from [49, ch. 4]

out of operation).

- As the flow speed increases to exceed the cut-in flow velocity, $U_{\infty\text{cut-in}}$, the first power-extraction region begins, within which the efficiency of the turbine is maximised to extract as much power from the flow as possible; this operational mode is known as maximum power point tracking (MPPT), shown as Region I in Fig. 2.10.

- When the extractable power reaches the rated power of the turbine, P_R, the tidal flow velocity is termed the rated velocity, $U_{\infty R}$; after this point the mode of operation transitions to power regulation, shown as Region III in Fig. 2.10, the purpose of which is to cap the power extracted by the turbine at the rated power value, preventing any damage to the system.

- Finally, when the flow speed increases to such an extent that either or both the power regulation method or the structural integrity of the system cannot manage the power in the tide, the turbine is parked, yawed, furled or otherwise removed from normal interaction with the flow.

There are additional regions in-between these, transition regions which require special control. Region II in Fig. 2.10 marks the transition between operation in MPPT and in power regulation. In this region, at a flow velocity slightly lower than $U_{\infty R}$, the power captured nears P_R and the system transitions from operation in MPPT to power regulation operation. The efficiency with which this is managed has an effect on the energy captured over a period of time; though Fig. 2.10 shows a perfect transition between Regions I and III, this is not always achieved in practice and is dependent on the rotor design, power regulation method, controller design and electrical sub-system [13, 49].

Power regulation and MPPT are achieved through manipulation of the vector relationship between the velocity of the tide and the tangential velocity of the blades to control the size and angle of the relative flow vector. This relationship is defined:

$$W = \sqrt{U_\infty^2 + \Omega^2 R^2} \ . \tag{2.12}$$

Control of W can be achieved by means of operation in VS to control the rotor velocity, Ω, by active alterations to the blade root pitch setting, β (see Fig. 2.12), using VP blades, or with the use of passively-adaptive blades which respond to the flow in such a way as to alter the blade twist along the blade span, θ_r. The latter two options directly control the angle of attack, α, between the relative flow vector and the blade or blade sections. The manner in which these operation methods can be achieved are discussed in Sections 2.3.2 and 2.3.5. Power regulation methods are discussed in greater detail in Section 2.4.

2.3.2 Fixed and variable speed operation

Operation in FS, while allowing a simple design, limits the turbine to operate most efficiently at one flow speed [12, 11, 48]. Due to this limitation, two-speed turbines were introduced, which allowed some flexibility with regards to maximising rotor efficiency over variying wind speeds [12]. As discussed in [48, ch. 5], two-speed operation was achieved by the incorporation of two generators in the design - one high-speed and one low-speed machine. The increases in mass and complexity of these systems, however, limited the deployment of such machines.

The operation and control of turbines in VS is discussed in [13, ch. 8] and [48, ch. 2, 7 and 9], for example, and provides the system with the advantage of increased aerodynamic efficiency - and thus increased energy yield - by facilitating MPPT over a broad range of flow velocities. Figure 7.12 of [11] gives a particularly clear illustration of this concept. In this operation mode, the optimum λ is maintained as U_∞ varies between $U_{\infty\text{cut-in}}$ and $U_{\infty\text{R}}$, whether with varying tidal state or with wave or large-scale turbulence-induced disturbance. The vector relationship described in Eq. (2.12) illustrates that the value of Ω may be used to control W as variations occur in U_∞. As will be discussed in Section 2.3.3, both the wind and tidal industries currently successfully employ several techniques to control λ so as to track the optimum C_P for maximum power capture.

As mentioned in the foregoing section, and discussed in more depth in Section 2.4, VS capability also allows regulation of power and/or thrust, depending on the objectives, by facilitating transition of the blades into a stalled or feathered flow condition. Furthermore, structural stresses and the effect on the condition of the power output of disturbances in the flow can be mitigated with the use of a VS system.

Though increased cost of manufacture and losses in the system are drawbacks, these are generally of less impact than the advantages gained.

2.3.3 Generator topologies and power conditioning

Though the focus of this thesis is rotor design for a specific type of operation in VS, the rotor design will have a reciprocal design-influence relationship with the generator topology. This section therefore discusses the different kinds of generator and power conditioning topologies, with emphasis on the robustness and applicability to operation in VS applications.

The function of a generator is to convert mechanical power to electrical power. As previously mentioned, in their basic function, HATSTs are very much like wind turbines: a prime mover interacts with a flowing fluid (though whether tidal stream flow can be defined as a free-stream is debated due to the the possible effects of the free surface) which creates alternating current (AC) electricity in a generator, which is connected, in some manner, to either a battery, a direct current (DC) load or a grid. If connected to a DC load or a battery, a certain voltage is likely to be required; if connected to a grid, the AC output will be required to be of a certain frequency and voltage. It is not always possible for these conditions to be guaranteed by renewable energy turbines, due to variations in the fluid velocity; some form of power conditioning is therefore required in the system. This generally involves a rectifier converting AC at the generator rotor to DC and, unless for DC load or battery connection, an inverter converting this back to a conditioned AC again. There are several different kinds and combinations of converters, some are mentioned in the discussion below. In Wind energy explained [13], Manwell et al. provide an accessible and technically relevant description of the electrical aspects of wind turbines. In Power conversion and control of wind energy systems, Wu et al. give a thorough technical discussion of the topic, and Table 5-1 in this text gives a succinct summary of generator-power converter configurations used in modern, large wind energy turbines, alongside the attending system characteristics.

In the particular case of tidal energy systems, the expense and difficulty associated with maintenance operations requires the systems, including the generator, to be robust, reliable and without the need for regular maintenance. The present high capital and deployment costs also mean that low cost and mass solutions are desirable. Depending on the blade design and operation methods, the variation in stream velocity may lead to the requirement for variable speed operation. When a generator design is selected or made, the advantages of different generator topologies must be balanced against the design requirements, the capital costs, and the operation and maintenance costs - within which the accessibility of the system must be considered.

Discussed in [13, ch. 5], generator topologies fall into two main categories: induction machines and synchronous machines. Each of which nominally operate at or near the synchronous speed - the frequency of the grid to which they are connected. When used in conjunction with power converter technology, either topology can be used in variable speed operation to a greater or lesser degree. There are present examples of wind turbines [48, ch. 1] and tidal turbine design which operate in VS with both induction

and synchronous, geared and gearless topologies. A brief summary of the requirements of each generator type for VS operation are given in [13, Sect. 5.6].

Induction generators

Induction machines produce a current to the outlet terminals due to a slight difference in the rotational velocity of the magnetic fields. Being connected directly to the grid, the stator field rotates precisely at the synchronous speed while the rotor field rotates (in generating mode) at a slightly faster velocity causing a higher voltage at the terminals. The ratio of the difference between the synchronous speed and the rotor speed is termed 'slip' and will generally have a value of roughly 2 % [13]. Standard or squirrel cage induction generators (SQIGs) are robust with low capital costs and have full VS range, if they are coupled with power electronic systems [13, 48]. However, SQIGs require a source of reactive power; the converters which can provide this are expensive and the losses they incur can be as high as the efficiencies gained aerodynamically by operating in VS [13]. Wound rotor induction generators have lower losses and require less expensive and smaller converters than SQIGs; however, the need for brushes and slip rings mean that these systems are less robust and more costly overall [13]. In high slip and slip power recovery wound rotor generators, the slip can be increased by varying the resistance of the generator's rotor, giving the generator a speed variability of roughly 10 % above the synchronous speed [48, ch. 5]. The losses increase with resistance in the rotor, again causing reductions in overall system efficiency.

In the wind industry, the most commonly-used generator for large and grid-connected machines are doubly-fed induction generators (DFIGs) [13, 48, 50], which have a wound rotor configuration with two converters correcting the output of the rotor, and a direct line from stator to grid. The converters are normally reduced capacity, voltage source converters, through which flows only a percentage of the total power flow, reducing system costs [48, ch. 5]. The deviation from synchronous speed achievable with this DFIG configuration is significant - from ±30%, suggested by Wu et al. [48], up to ±50 %, suggested by Manwell et al. [13] - and is sufficient for VS control of wind turbines.

A feature common to all induction generators is the system dampening effect of the variability possible in the slip. With modern power electronics, this is advantageous; the response of the generator acts to cushion any rapid changes in aerodynamic torque, providing some protection to the connected grid, network or load [12, 11, 13], even in FS operation.

Induction machines were originally very popular as they provided a robust, cheap power take-off and could be linked directly to the grid. However, as the grid capacity grew and the contribution of wind power grew, in FS machines the damping action of the induction generator - so useful these days in VS operation - resulted in energy losses and the problem of dissipating the associated heat [12]. The capability of the grid to cope with unstable voltage levels and facilitate power regulation was historically

not what it is today and therefore the difficulties with FS induction machines were one of the drivers of innovation in power electronics to decouple the fixed-frequency grid from the variable speed wind. The development of this capability has enabled the use of induction generators in VS (and VSVP) applications to the extent that, as noted, the DFIG arrangement has dominated the wind turbine market. Today, however, there are a number of competitors which use the alternative synchronous generator topology in the largest scale turbines.

Synchronous generators

The basic principle of synchronous generators, as described in [13, ch. 5], is the generation of current due to the a phase difference between the grid-induced rotating AC field in the stator and a rotating magnetic field on the rotor. In the standard format, the rotor field is produced by DC excitement from an external generator, which interacts with the stator field, producing a resultant field. In a synchronous generator, the rotor turns at synchronous speed with the stator field, but with a phase difference, causing an electromechanical torque which acts to bring the fields back in phase. A constantly applied torque on the rotor will ensure this does not happen, maintaining the phase angle and therefore current generation. The angle between the rotor and resultant field - the power angle - will be positive when the machine is generating electricity, and acts as a spring in relation to the input rotor torque. This spring-type connection between the rotor and stator fields does not provide dampening to the system as with slip in an induction machine. Standard format synchronous generators, with their simple, robust design, are used in large power stations wherein the rotor speed does not need to respond to changing fluid velocities. For application in a renewable energy system, however, in which aerodynamic disturbances, such as turbulence, are communicated to the generator and through the spring-type connection to the line side, the generator is generally decoupled from the grid via a power conversion system. VS operation can thereby also be achieved, allowing optimisation of the aerodynamic efficiency.

Synchronous generators in variable speed application

Synchronous generators are commonly operated in VS applications for small-scale wind systems, up to around 10 kW. The design, operation and control of this kind of generator is discussed in [48] and [13, ch. 5], for example. There are many configurations with which synchronous generators can be operated in VS; all of these require power converters on both the grid and the generator side. The rotor field of synchronous generators can be produced with a wound rotor and external exciter, or with permanent magnets. AC excitement on a wound rotor synchronous generator (WRSG) reduces the robustness of the rotor configuration and requires regular maintenance, but is a simple solution; DC excitement can be produced with a reliable system with low maintenance requirements, but higher capital cost and complexity. The permanent magnets in a permanent magnet

synchronous generator (PMSG) system have a high capital costs and a limited lifetime due to demagnetisation; however, the power density can be higher than in a WRSG, there are no winding losses nor associated heat dissipation, and there is no requirement for brushes or slip rings, making for a simple, robust system.

The basic operating principles are the same as for FS synchronous generators, but the inclusion of a full-capacity power converter system decouples the generator from the grid and allows the turbine to be run as a fully VS device. Both rectifier and inverter are required, as well as a harmonic filter, voltage control and, for grid-connection, a transformer to step up the voltage. As opposed to around 30 % as in a DFIG system, 100 % of the power goes through the converters. While this increases the cost, it allows separate control of the generator and line-sides of the converter system, increasing the operational speed range and allowing some control over system characteristics such as generator torque-current relationship [48].

The option of incorporating a large numbers of pole pairs in synchronous generators introduces the possibility of direct-drive systems, which are simpler and have lower maintenance costs than systems with gear boxes [13, 48]. Gear box failure has been a significant cause of down-time in the wind industry; while the electrical system is reported to be the cause of the most numerous failures, downtime due to gearbox failures has been (variously) reported to be the highest or one of the highest causes of down time alongside generator, electrical system failures and pitching mechanism failures [51, 52, 53]. The option of using gearless drive systems in tidal applications, where access for maintenance is more difficult and costly, is therefore highly appealing. The capital and maintenance cost and mass savings made on the gearbox must, however, be balanced against the larger generator diameter and extra electromagnetic material in the rotor, whether permanent or wound.

There are very many options with regards to the specific power conditioning configuration of synchronous generators; these are thoroughly discussed in [48, ch. 5, section 5]. Synchronous generators introduce the possibility of using diode-type rectifiers, which reduces generator-side converter costs. Diode rectifiers can be used in conjunction with DC boost converters to bring the voltage up to sufficient levels for the inverter, which is especially useful for low flow speeds. Alternatively, the possibility of torque ripple and generator losses attending diode rectifiers can be mitigated with the use of more costly pulse width modulation (PWM) converters, or other topologies and control schemes such as proposed in [54]. Low or medium-rated voltage source, current source, silicon-controlled (thyristor) or PWM converters can be used back-to-back, or on the line side only. Multi-stage converters, multi-phase configuration and multi-generator systems are amongst the further options.

2.3.4 Generators in tidal energy applications

There are examples of both induction and synchronous generators in tidal energy applications. An induction machine was used for Marine Current Turbine Ltd's VS-controlled SeaFlow device, which was controlled within the required speed range of ±25 % nominal speed with a frequency converter [55]. A DFIG, with a power converter which was specifically developed for VS operation by taking into account the rotor's apparent power and power angle, was proposed for a prototype turbine for the the Uldolmok strait [56, 57]. The SCHOTTEL Instream Turbine (SCHOTTEL IT) series employ induction generators for use in their VS turbines, which require significant speed ranges due to the power regulation method [58].

Though not all developers openly share their technology choices, the literature reflects that a higher number of tidal turbine systems use PMSGs. Such systems include Marine Current Turbine Ltd's later SeaGen turbine, deployed in Strangford Lough [59], the OpenHydro and VoithHydro turbines [60], Natricity's CoRMaT [61] and the generator design conceived for the GESMEY project [62].

In [50], Benelghali et al. present a comparison between a DFIG and a PMSG operated in VS for the tracking of optimum power point. Their analysis concludes that of the two compared topologies the PMSG allowed a higher energy yield which, they propose, in combination with the reduced maintenance costs compensates for the increased capital cost of the full-capacity power electronics. Much research and development has been put into the optimisation of PMSGs for tidal energy. Drouen et al. published a study [63] of a direct-driven PMSG positioned around the rim of the rotor blades. The power converter configuration included a PWM voltage source converter to control the rotor speed, and a DC bus with converter and current control to reduce harmonic disturbance. Using a multi-physics model, they concluded that this configuration produced a turbine system with cheaper active parts than a comparison-case conventional generator. C-GEN, a light-weight, air (or water)-cooled, modular PMSG was designed at Edinburgh University's School of Engineering for use in renewable devices [59]. The novel generator design can be optimised for a given renewable energy capture system using a multi-physics tool developed to consider the electromagnetic, structural and thermal designs, and the operating methods and specific configuration of the renewable energy device. Applied to the Scottrenewables turbine, a direct drive power train with axially stacked C-GEN generators was found to be most appropriate [64]; a similarly configured 600 kW generator concept was found to be most suitable for deployment in MCT's SeaGen device, with which design the gearbox was removed while the drive-train mass was not significantly altered [59]. Moury and Iqbal presented a PMSG with a printed circuit board stator design, designed to have no cogging torque nor iron losses, for use in small, low-speed tidal energy devices [65]. The generator of the aforementioned CoRMaT device was specifically developed to allow direct drive with low mass, simple mooring and low maintenance requirements; the contra-rotating rotor and 'stator' gives twice the

relative speed between a rotor and a stationary stator, without the need for a gearbox, while removing the requirement of a station-keeping system which neutralises reactive torque [61].

Though power conditioning systems are always required , the PMSG topography is versatile. It has the advantages of requiring no commutator, brushes or slip rings, resulting in a more robust machine with lower maintenance requirements and higher speed range than a DFIG [50], lower losses than a squirrel cage system, no soft-starter requirement [13, 48], less complexity than a wound rotor synchronous generator [48], and allows the introduction of low maintenance, robust gear-less turbine systems. On the other hand, a 2008 study of wind turbine reliability reported that induction generators have a failure rate half that of synchronous machines [9], the magnetism of magnetic materials decays with time and are heavy, and the option of some level of grid control possible with induction machines may be of importance in a renewables-heavy electricity mix.

There are advantages and disadvantages to each technology, and the particular deployment site, turbine configuration, electrical distribution-system requirements and exact operation methodology must be considered in the decision of the most appropriate generator topology and rotor design combination for the given VS application. It may be that either the generator, the operation techniques or the rotor design will come first – in which case the later design decisions will be constrained by the foregoing – or that all three design decisions may be optimised together. Some examples of design decisions and constraints for overspeed regulated tidal turbines will be discussed in Section 2.5.2.

2.3.5 Turbine rotor

The design of the rotor - specifically the hydrodynamic design of the blades - is the focus of the work presented in this thesis.

The rotor, as previously discussed, is the hydrodynamic aspect of a turbine's power-capture function - this is the component which interacts with the tidal stream to generate electricity. A rotor can be hydrodynamically defined by the variables defined below and in Figs. 2.11 and 2.12 and listed below:

- the number of blades, B
- the turbine radius, R
- the hub radius, R_{H}
- the blade geometry
- the blade pitch setting, β
- whether the blades are FP or VP
- the blades' structural design - rigid or flexible - and, if flexible, in what manner

The hub radius, R_{hub}, defines the distance between the blade roots and the axis of rotation. Together, R_{hub} and the blade length, l_{B}, make up the turbine radius, R:

$$R = R_{\text{hub}} + l_{\text{B}} \ . \tag{2.13}$$

As the global coordinate system in Fig. 2.11 shows, the rotor blades rotate around the shaft axis, labelled x_{scrscg}, and the plane of rotation is the y_{scrscg}-z_{scrscg} plane, centred at the centre of the blade root aerofoil sections where they meet the hub.

The blade geometry comprises:

- a blade length, L_{B},
- at least one aerofoil section
- a twist distribution, θ_r
- and a chord distribution, c_r.

The chord line of a blade section passes through the leading and trailing edges of the blade as shown in Fig. 2.12. As noted, and as illustrated in Figs. 2.11 and 2.12, the blades of a HATST are of aerofoil shape in cross section, which may vary along the radius. The last two of these geometrical parameters can be expressed as functions of the radius or blade length, or as discrete values at nodes positioned radially along the blade length. The twist distribution is used to control the local incident angle of attack, α_r, at each cross-section as r, and therefore the tangential velocity, Ωr, varies [12]; the sections are normally set at sequentially larger angles to the root cross section. The blades are generally set at a non-zero angle, β, defined by the angle between the root section and the rotor plane. The definitions of these angles and the coordinate system in which they are defined are shown in Fig. 2.12.

Fixed and variable pitch

A rotor may have blades which are fixed in their pitch angle - FP blades - or the blades may be connected to the hub via a VP system which allows the angle of the blade pitch to be altered during operation. The pitching capability is generally achieved via an electronic controller with a hydraulic system, and sometimes with an electronic motor system [66]. VP blades allow rapid, blade-specific and, often, very sensitive adaptations to the flow conditions and thus facilitate increased energy capture, smoother power flow and reduced structural loading compared to FP blade systems. VP blades can also develop high starting torques which can increase the annual energy capture, and can bring the rotor to a slower speed before application of the parking break [12]. However, active pitch mechanisms add mechanical, structural and control-based complexity to the system, decreasing the robustness and increasing the turbine's vulnerability [49]. VP blade connections to the hub must include bearings which are required to withstand

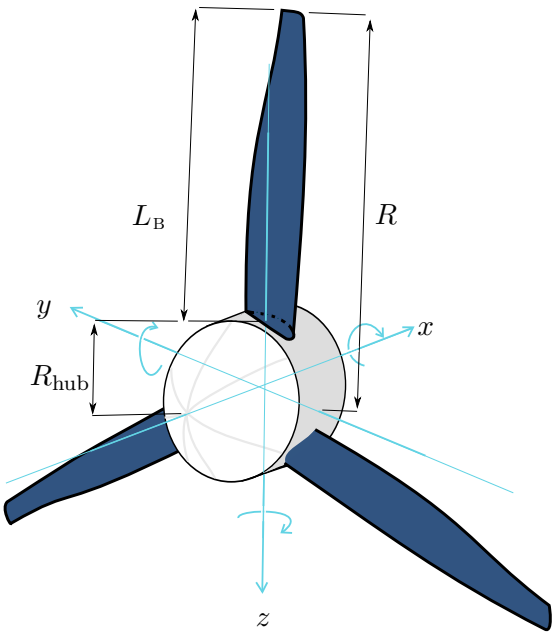

Figure 2.11: Definition of rotor parameters rotor radius, R, rotor hub radius, R_{hub}, blade length, L_{B}, and global coordinate system centred at shaft axis and in middle of rotor plane.

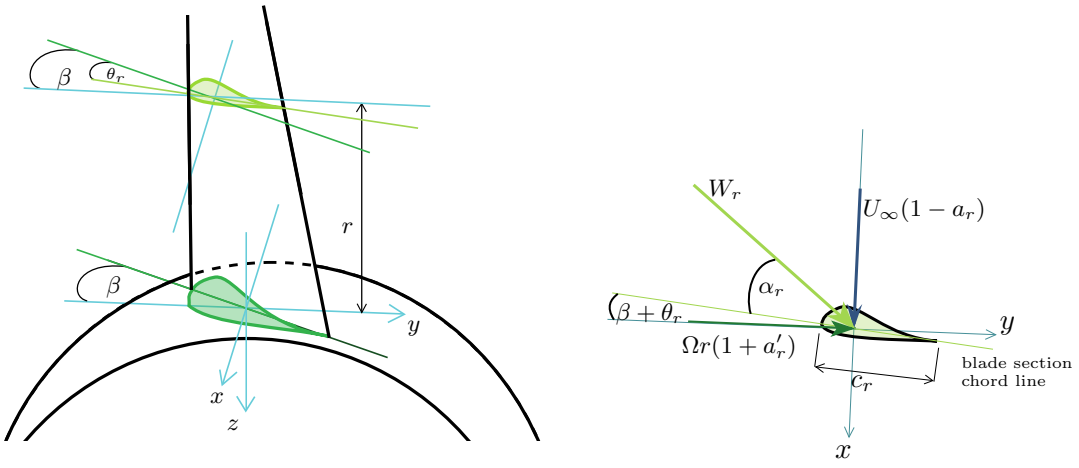

Figure 2.12: *Left*: Orthogonal view diagram of rotor, blade at top dead centre position, coordinate system and angle definitions. β is measured from rotor plane and has a positive value here; θ_r is measured from the blade root chord line and is negative here. *Right*: Plan view diagram of 2D flow vectors for a blade section, also showing definition of chord..

the entire blade root bending moments and forces resulting from the blade's interaction with the flow, while maintaining the pitching ability of the connection [13]. In FP blade systems, on the other hand, the bolt or stud-type connections between the blade root and hub are required simply to hold the blades in place, giving a more structurally robust system. However, FP blades cannot adapt to individually-experienced flow conditions and, even in VS operation, rotors with FP blades generally have a reduced energy yield and increased structural and fatigue loading characteristic than a rotor with VP blades [66]. Turbine systems always require safety breaking systems; a hydraulic system is often used on the tip of FP blades to provide an aerodynamic break, and this is also a source of failure.

Though there are disadvantages to consider, wind turbines with FP blades have lower failure rates than those with VP blades. In the wind industry, as reported in an evaluation of an extensive 10 year study of 350 MW worth of wind turbines [9], failures in the pitching mechanisms - considering pitch drives, bolted joints and bearings but not the blades themselves - were the driving factor for the 85% higher rotor failure rate of pitch regulated turbines than passive stall regulated ones.

The specific functions, advantages and challenges associated with systems employing VP and FP blades are discussed in Section 2.4.

2.4 Power regulation

As discussed in Section 2.3.1, the variables which may be manipulated for the regulation of power are the pitch angle, β, the local twist angle, θr and the rotational velocity of the blades, Ω. Sections 2.3.2 and 2.3.5 discussed the mechanisms and basics aspects of VS operation, FP and VP blade designs. Drawing from these introductions, the following section will discuss the different methods of power regulation. While the capture of tidal energy introduces additional aspects to consider, the development of power regulation techniques in the wind industry is of interest in that it has informed and continues to inform the development of power regulation techniques in the tidal energy industry. The discussion will therefore follow the trends in the development of the wind industry which has grown in the last century, particularly since the 1970s [66]. Finally, some recent research in the field, specific to tidal energy, will be discussed. As the focus of this thesis, the overspeed method of power regulation is given a separate section, see Section 2.5.

2.4.1 Methods of power regulation

The basic aim of power regulation is to reduce the efficiency, C_P, of the rotor when the tide exceeds the rated flow velocity, thereby capping the power running through the generator below or (ideally) at the rated power value, according to Eq. (2.3). As discussed in, e.g., [49, ch. 4], there are four main techniques with which this is achieved

in the wind industry:

- passive stall with FP blades and FS operation
- passive stall with FP blades and VS operation
- active pitch control - either to stall or to feather - with VP blades and FS operation
- active pitch control - either to stall or to feather - with VP blades and VS operation.

Yaw regulation - wherein the flow vectors are controlled rotating the turbine rotor out of the flow - has also been used, though less frequently [11].

The first wind turbines generating electrical rather than mechanical energy, created in 1891 in Denmark by Poul LaCour and improved upon during the World Wars, were FP, FS stall regulated machines [66]. Until the late 1990s, this was the most frequently used method of power regulation [12]. As reported in "Comprehensive renewable energy. Volume 2: Wind energy" [67], the number of installed wind turbines using FP, FS passive stall control was first exceeded by the number using active pitch control in 1998. By 2006, the ratio of VP to passive stall turbines was 3.8. Enabled by the development of power converter electronics, interest in VS operation increased, and power regulation by active pitch with a VS capability began to dominate the market. In parallel, but to a lesser degree, speed-assisted stall power regulation with FP blades and VS operation has been developed since the late 1980s [68, 69]. As noted in [70] in 1998, there are turbines in operation in which the power is regulated in this manner. However, most large-scale wind turbines developed today are regulated by active pitch control, with VP blades, and are designed for VS operation, as discussed in [48, ch. 1] and [67], for example.

Passive stall power regulation

Passive stall power regulation is achieved with FP blades which are aerodynamically designed such that, as the flow speed increases past the rated value, the boundary layer flow over the blades separates from the upper surface of the aerofoil sections, reducing the aerodynamic efficiency. The blades are aerodynamically shaped to facilitate, in general, a gradual stall along the blade to reach and/or not exceed the rated power capture.

With each passive stall power regulation method, the transition from MPPT operation to power regulation and the extent to which the rotor efficiency is dropped are dictated by the blade pitch angle and aerodynamic design, the flow velocity range [11], the generator and, if present, the power electronics topology [48] and control scheme [49, 70].

Passive stall with FP blades in FS operation

In a FS machine the angle of attack across the blade increases passively to the point of stall simply due to the increase in U_∞ (Fig. 2.12 illustrates the causal vector relationship). In this kind of system, the rotor is operated with an induction generator and coupled

directly to the grid; the turbine speed is therefore very close to grid frequency, within the slip region of the machine [11, 48, 49].

Passive stall with FP blades in VS operation

Stall regulation with FP blades and a VS drive train is also known as "speed-assisted" stall regulation. The VS capability allows control over Ω and, thereby, for the efficiency of power capture below rated wind speed to be varied for MPPT, and facilitates greater control over the rotor in transition into, during and out of stall.

Advantages and disadvantages of passive stall power regulation

The main advantages of passive stall regulation are the simplicity in the design and operation, and the structural integrity of the FP blade root connections [49]. As previously noted, one study of 10 years worth of wind turbine data reported, in 2008, that turbines with FP blades had significantly lower instances of rotor failure [9].

The obvious disadvantage of FP, FS power regulated systems is reduced energy capture in Region I, below rated flow speed, an over-smoothed transition region which does not maximise energy capture [49], and reduced power capture in the higher wind speeds. As discussed in [12, ch. 4], perfect stall regulation is not possible to perform in reality, which leads the losses discussed. The power curve displaying poor performance shown in Fig. 2.10 is extracted from [49, ch. 4] and is typical of the non-ideal performance of passive stall regulation.

These problems can be mitigated with VS capacity which allows control of the magnitude and angle of the relative velocity vector. This facilitates MPPT by allowing the rotor to accelerate to the maximum efficiency for each flow velocity, and then allows the system to track a reduced C_P locus in the power regulation region as required by the wind velocity, as discussed in [49, ch. 4] and [69]. In [49], the operating points required by variable speed machines to achieve the ideal (or close to the ideal) power curve are given, the difficulties and solutions are discussed. Thiringer and Linders [69] note the difficulty associated with high rotor inertias in maintaining the exact speed to obtain the power required as the aerodynamic forces change under fluctuating wind speeds. It has been reported that these transient power fluctuations are comparatively soft compared to those resulting from a FS, active pitch regulated rotor in similar wind conditions [66], [11, Ch. 7]. As the literature demonstrates ([49, 48, 68, 69, 71, 72, 73], for example), the successfulness of VS operation for power regulation depends on a well-designed controller; simulation and experimentation reported in these papers have demonstrated that this can be achieved, whether with a constant-torque or constant-power demand.

Difficulties associated with the aerodynamics of post-stalled flow means that power and loads are not necessarily easy to predict once stall has occurred [24, 42]. This subject was covered in Section 2.2.5. The structural disadvantages of passive stall power regulation are discussed in [12]: the structural advantage of vibration damping provided

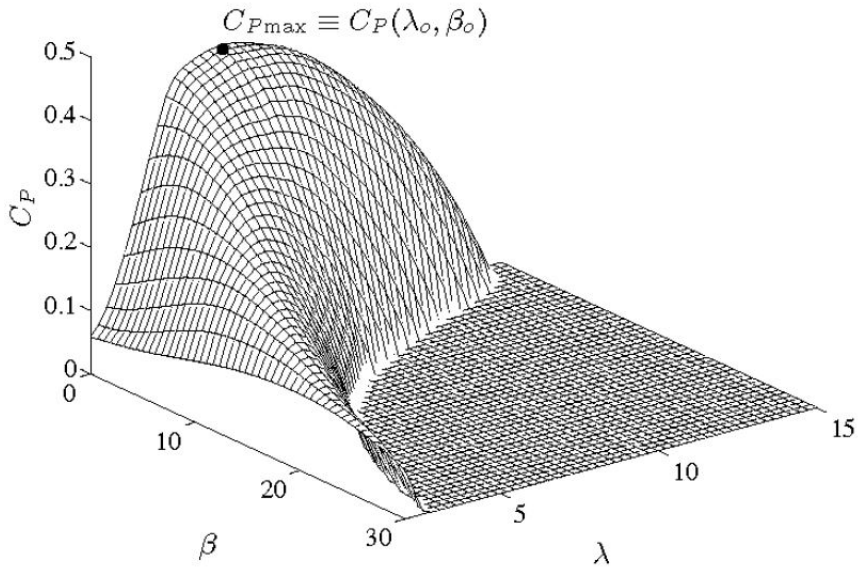

Figure 2.13: 3D plot showing the effect of blade pitch alterations on the C_P-λ curve. Figure taken from [49, ch. 2].

by attached flow is lost in the post-stall condition; furthermore, when the rotor is parked in high winds beyond the cut-out velocity, the high forces cannot be regulated. The fatigue life is therefore lower than a blade with continually attached flow, and the structure needs to be large and strong enough to withstand high forces. A further disadvantage of passive-stall regulation in a VS systems is the overcapacity required within the generator to produce the electromechanical torque that regulates rotor speed, noted in [72]. This is an unavoidable aspect of passive-stall regulated machines.

Active pitch control power regulation

Active pitch control was first developed for use within FS turbines, and allows direct control of the angle of attack via the blade pitch setting angle, β [49]. The effect on C_P of altering the blade pitch setting, for a typical wind turbine, is discussed in, e.g., [49, chs. 2 & 4], and [12, ch. 4]. As shown in Fig. 2.13, taken from [49, ch. 2], each pitch setting results in a unique, known C_P-λ curve; by making alterations to the pitch setting in response to the flow conditions it is therefore possible to alter the power (and thrust) performance of the rotor as required.

Active pitch – VP blades in FS operation

Pitch regulation in FS turbines allows greater flexibility in control of the relative flow vector than the FP FS case, and can therefore result in greater energy capture. When deployed, this technique was generally used to regulate power in Region III.

Active pitch – VP blades in VS operation

The final option is the combination of VS and VP, in which type of turbine the VS capability is commonly used to maximise energy capture in Region I below rated flow speed by means of MPPT, and the VP capability is employed as the power regulation technique in Region III [49, ch. 4].

Advantages and disadvantages of variable pitch power regulation

As discussed in [12], the basis of pitching to stall is the same as for passive stall. The pitch angle alterations required for power regulation by this method are very small, meaning response time is low. The alternative is pitching to feather, which requires larger alterations to the pitch angle [49]. A difficulty with active pitch control in a FS turbine is that the reaction of the pitching system to fluctuations in the wind speed have to be quick; this has lead to an unfavourable comparison with passive stall power regulation in that the resulting fluctuations in power are higher for the active pitch case than than passive stall case [66, sect. 5.3.2]. On the other hand, the power output in the regulated region is generally reported to be nearer the rated power value for active pitch regulated turbines than for passive stall regulated systems [66, 48]. The possibility of transient load regulation with VP blades is an advantage of these systems, and for VS VP systems, the combination of both regulation techniques in higher wind velocities can be beneficial in terms of dynamic performance [49].

All of the afore-mentioned challenges of operating in stalled flow hold for VP implementation in pitch-to-stall. Though the time-lag in pitch-to-feather is longer, the advantages of attached flow have meant that this has been the most common power regulation method in which VP blades are used [12].

The greatest disadvantage of VP power regulations methods is the reduced robustness of the blade-hub connection, discussed in Section 2.3.5, with effects on the failure rates of wind turbines such as those previously discussed in Section 1.2.4. As noted in An up-to-date review of large marine tidal current turbine technologies [60], more than half of the tidal turbine technologies curently in the later stages of development and deployment use FP blades.

2.4.2 Passive bend-twist power regulation

The use of composite blades for power and load regulation by passive adaptation to the flow conditions has been put forth by Nicholls-Lee et al., Murray et al., Barber and Motley, and are currently employed by SCHOTTEL HYDRO in their SCHOTTEL ITs.

The basis of this novel concept is that the structural composition of the turbine blades can be designed such that the twist distribution – and thus the local angle of attack and performance – changes under axial loading, allowing predictable but passive alteration of axial and tangential loads.

2.4.3 Analysis of power regulation techniques for tidal turbines

In [77], Whitby and Ugalde-Loo compared the performance of a VS VP (pitch to feather) and a VS FP turbine and control system, modelled in GH Tidal Bladed. They found that the VS VP pitch to feather system was more stable in power regulation and had lower loads across the entire operation, particularly than at flow conditions requiring the alternative design to operate in deep stall. The VS VP also had a higher energy capture, due to the reduction in flow states for which a FP rotor can maximise efficiency compared to a VP alternative.

In [78], Arnold et al. discussed the merits of a VS regulation technique with FP blades, in which the rotor is encouraged to stall through use of the VS capability. A tidal turbine's smaller rotational inertia than that of a wind turbine was noted in this paper as an advantage to the controller and the drive-train in terms of the smaller torques required for speed control. The authors discuss the proposed "underspeed" method in terms of its advantages over active pitch and overspeed power regulation (see Section 2.5), and while the discussion does not consider alternative rotor designs which may mitigate the negative aspects of the overspeed method, the presented underspeed regulation method, including the performance of the proposed controller, was shown to be successful. Compared to the pitch and overspeed regulated turbines simulated, the simulation results indicated lower loads and smaller excursions in load to the peak values for the underspeed-controlled turbine. The power quality, however, due to the unstable nature of stalled flow, was found to be lower for the underspeed case; the required torque was also higher for the underspeed case than for either of the others, both at the optimum and maximum operating points, which would have consequences for the generator design.

2.5 Overspeed power regulation

2.5.1 The Overspeed Method

The advantages of avoiding stall and having robust FP blades can be combined by regulating power with a VS FP turbine which goes into overspeed, rather than slowing down to go into stall, when $U_{\infty \mathrm{R}}$ is exceeded. In such an overspeed power regulation (OSPR) turbine system, Q_{em} is reduced during power regulation, allowing Ω to increase, effecting an increase in the magnitude of W, and a decrease in α. Essentially, rather than passive-stall, active pitch-to-stall or active pitch-to-feather, this method results in a passive-feather effect on the blades. This technique, therefore, can be used to reduce C_{P} in a predictable way and – with proper implementation – regulate power as effectively as any of the other methods.

2.5.2 Existing work in overspeed regulation

Research in the field of overspeed control has been undertaken, and there exist some tidal turbine designs which employ overspeed as the control method. The following section details four separate research/industry projects looking at overspeed regulation. The review of the first four projects considers the aspects of these projects focussed on rotor design; the fifth briefly discusses the aspects considered in work looking at the requirements for generators and control topologies used in overspeed regulation.

Overspeed regulation with passively-adaptive blades

The SCHOTTEL IT developed by SCHOTTEL HYDRO is one such device. As detailed in [79] this turbine system employs three FP blades connected to an induction generator through a planetary gearbox. The rotor is held at optimum efficiency in Region I (Fig. 2.10) flow velocities in MPPT with VS operation. In Region III, the turbine is allowed to increase its rotational velocity in what the authors term a "controlled overspeed", which reduces the efficiency of power capture. The SCHOTTEL IT has the further technology of passively-adaptive blades. These composite blades couple bending under axial force with twisting and are designed to limit the thrust force as the flow and rotor speeds increase. Experimental data – obtained in tow-tests in which a 50 kW turbine was attached to a tug boat and driven through the water of Rotterdam harbour – presented in [80] illustrated the success of this combination of regulation methods. Plots of measured power and thrust, captured as the rotor velocity was varied under four bands of increasing flow speeds, showed how the shape of the power and thrust performance curves changed with the tow speed. It was shown that the required drop in C_T as the flow velocity increased was achieved. Figures were presented illustrating that the power regulation was successful, and showing the reduction in the increase of thrust force after $U_{\infty \text{cut-in}}$ was exceeded. It was stated that this resulted in a reduction of the thrust force by 50% at 5 $\mathrm{m\,s^{-1}}$, the maximum flow speed in which the turbine was tested. The authors further noted that the twisting of the blades resulted in a reduction in runaway point (the maximum value of λ in turbine mode, at which $C_P = 0$) as the inflow increased. Cavitation was mentioned in the paper as having been considered in the design stage of the blades; the authors state that "cavitation inception can be delayed in overspeed conditions". In A stepwise approach towards the development and full-scale testing of a marine hydrokinetic turbine [58], the methods of investigation undertaken into cavitation inception were detailed as "3-RANS [Reynolds averaged Navier-Stokes equations] CFD [computational fluid dynamics] simulations" and model-scale tests conducted in both a tow tank and a cavitation tunnel, the aim of which were to converge upon a finalised rotor design which "minimised cavitation behaviour" while meeting the performance requirements.

The SCHOTTEL IT turbines are the turbine technology which will be used in the Black Rock Tidal deployment planned for the Bay of Funday in Nova Scotia, Canada

[81].

Overspeed regulation in a gravity-secured turbine

Another tidal turbine device in which overspeed is the power regulation method is the DeltaStream concept developed by Tidal Energy Limited (TEL). A single TEL turbine unit, on its $\frac{1}{3}$ of frame, was deployed in a full-scale test/demonstration site in Ramsey Sound in December 2015 [82]. Though the company recently went into administration [83], the technology, research and work done remain - it is not unlikely, and should be hoped, that the learning done by TEL will be retained in the industry, as has been the case after previous company collapses in the marine energy industry [84, 85].

As detailed in Design of a gravity stabilised fixed pitch tidal turbine of 400kW [86], this turbine system comprises three HATSTs deployed together on a gravity-stabilised triangular frame. The identical turbine unit rotors are each of FP design and can yaw to face the tidal flow (or to be parked out of the highest velocities when required). The turbine units discussed in [86] had a power rating of 400 kW. The design constraints influencing the rotor design were the maximum allowable thrust of 40.5 t for each turbine (based on an assumed system mass, and therefore friction force, and a safety factor of 1.35), a minimised close-down time, the afore-mentioned power rating, and the requirement of cavitation-free operation.

The influence on the C_P and C_T-λ curves of three blade designs with 2°, 6° and 10° "tip stagger" (which, it is assumed, relates to the twist distribution, though exact definition of how/from where the measurement is taken was not given, nor were any twist or chord distribution plots presented, possibly for reasons of intellectual property protection) is presented. These illustrate that higher degrees of "stagger" resulted in lower maximum C_P and C_T values, occurring at lower λ values and resulting in runaway points at lower values of λ.

The station-keeping maximum thrust force requirement was most heavily discussed in this paper, in which the optimum operational λ was found to be in the low regions due to the reduced drag-power ratio – achieved, as noted, with the higher values of "tip stagger" for which the results were presented. These low λ operating regions were also identified as beneficial in terms of cavitation inception; it was noted that "Cavitation is also improved at low TSR since larger chords and low relative velocities increase the minimum static pressure".

The results of an investigation into the optimum λ-chord length combination were presented, in which indication was given of the combination which gave maximum rotor efficiency and that which gave the maximum power to thrust ratio. The aerofoil design was also discussed in this paper; a symmetrical rather than cambered foil was chosen in order to minimise drag in low lift conditions and thus minimise thrust force in overspeed. The paper gave details of the analysis of unsteady blade loading due to free-stream disturbance in the tide, concluding that unsteadiness in the tide reduces the maximum

safe steady flow speed in which power can be captured, that the effects of unsteadiness require to be statistically established, and could best be reduced by lowering the inertia of the turbine system, and employing "soft" electronics.

Overspeed regulation within an existing turbine system

At the European Wave and Tidal Energy Conference (EWTEC) 2013, Biskup et al. presented a paper [87] describing research undertaken to ascertain whether modifications to the blade tips of the Voith Hydro Ocean Current Technologies HyTide turbine could facilitate alteration of the power regulation technique to overspeed, within the constraints pre-set by the generator and drive-train design. The turbine system upon which the effect of modifications were investigated was a bi-directional HATST, rated at 110 kW at 2.9 $\mathrm{m\,s^{-1}}$, and incorporated the capability of surviving the structural loads occurring in the fault position of runaway. The research aim was to achieve an increased gradient on the overspeed side of the C_P-λ curve, while maintaining the position of the optimum operating point (in terms of λ) and the plateaued region around the maximum efficiency, which reduces the control problem in MPPT. Two targets were set to achieve this aim: C_P at the optimum operating point was not to change; the reduction in rotor efficiency was to be maximised by a set target runaway λ. These targets were to be met which a bi-directional tip modification. This tip modification was required to perform in such a way that the radial force imparted by the tip modification increased steeply between the optimum and runaway points, as the local angle of attack became smaller with increasing rotor velocity.

The paper noted that there could be several tip modifications which would meet the requirements, and focussed on a bi-directional "double-wing" addition to the tip. The two symmetrical winglets were stacked in the axial direction, facing in opposing directions, at the blade tip. The variable design parameters were the chord length, the thickness and the axial distance between the centre of the aerofoils. The Reynolds-averaged Navier-Stokes (RANS)-based computational fluid dynamics (CFD) code ANSYS CFX was used to undertake the investigations of performance alteration caused by each permutation of the tip modification. BEMT predictions were also used, including for cross-code comparison of the results with generally good agreement.

Plots of the axial and circumferential forces over the blade length at the optimum and targeted runaway operating point showed that the tip modifications gave only slight alterations to the un-modified blade force distributions for most of the blade length, but added areas of highly opposing force in the region of the added tip modification. CFD modelling illustrated suppression of the tip vortices, the local and wake flow fields.

Plots comparing the initial and modified performance curves showed that the applied tip modification achieved the required increase in gradient on the overspeed side of the C_P-λ curve while maintaining the previous value of rotor efficiency at the previous optimum λ. However, the actual peak of the C_P-λ curve was shifted leftwards to a lower

λ, and the maximum efficiency was increased; the plateau region of high C_P was therefore lost. The paper concluded that though these changes were effected, the performance alterations were not compatible with the requirements of the existing turbine design. Further, the conclusion discussed that even the indicated increase possible in maximum power did not necessitate the investigated modifications at this stage in the development of the technology because this could more easily be achieved with longer blades.

The design methodology focussed on achieving the aims with blade tip modifications, based on a set of design requirements, two target operating conditions and consideration of the required tangential force response to changes in the local angle of attack at the tip modification. The research mentioned that parameter studies were used to ascertain the ideal configuration of the tip modification, but does not discuss the manner in which these studies were undertaken. No mention of cavitation inception analysis was given in the paper.

A holistic design methodology for overspeed regulation

Unlike the foregoing example of research, which was focussed on enabling overspeed operation in an existing turbine system, and unlike the previous two examples which aimed to – and were successful in – incorporating overspeed operation in the system from the beginning of the design process, the work presented by Winter was not technology-specific. In a series of conference papers, Winter developed the case for a different approach to blade design for tidal turbines than previously employed for wind turbines, presented a novel design methodology, and applied it to the design of blades for used in an overspeed regulated turbine.

The design methodology presented in [89] focussed, rather than on maximising the rotor efficiency, on optimising the impact of rotor performance – emphasis was given to the thrust characteristics – on the whole turbine system, throughout operation, without sacrificing the power performance. Equations familiar from BEMT theory (see Sections 4.2 and 4.2.3) were rearranged to set the chord and twist distribution as functions of the remaining variables. The value of λ at the optimum operating point (therein referred to as the "design tip speed ratio") and the "design axial induction factor" were set as the only two variable design parameters; the remaining parameters – blade number, hub radius, design lift coefficient and design angle of attack – were set. This gave a 2D design region within which combinations of design λ and axial induction factor existed, resulting in a series of blades of varying twist and chord distribution. By setting design constraints such as limits on the allowable rotor radius, torque and thrust, the feasible region in the 2D design space was reduced. Winter and Tryfonas suggested that a cost function, based on the lifetime cost of the turbine according to the rotor design, could be used to ascertain which option within the constrained design space would produce the cheapest turbine. While no further work on this was presented, this would seem to be an excellent final-stage selection method.

In [88], Winter goes on to present simulations, undertaken in the BEMT code "Tidal Bladed" developed by GL Garrad Hassan, of the performance of a blade designed with the overspeed method for overspeed power regulation. A control method was proposed which uses the torque-speed relationship of the generator and rotor to stabilise the rotor at the desired rotational velocity. Unsteady flow was included in the simulations with turbulent flow disturbances of varying intensity, and a JOHNSWAP wave spectrum. The required rotor velocities, rotor forces and electrical output were obtained from the programme for varying flow states; these results showed that the power was successfully regulated at flow speeds above 3 $\mathrm{m\,s^{-1}}$.

Tank tests were undertaken and the results were presented in [89]. The results gave a fair match to the predicted thrust data, though much scatter was present in the data. This was possibly due to the difficulties of working at small scale, including, as Winter and Tryfonas mentioned, accurately setting the pitch. Low confidence was reported in the results for the power performance, which did not show a good match to the prediction and had greater scatter than the thrust measurements.

The design methodology presented in this research was based on allowing two performance characteristics – the optimum λ and the optimum axial induction factor – to be free variables, while setting other variables in the equations defining the twist and chord distribution to known values. The space was then bounded, resulting in a set number of blade geometries defined by the allowable value combinations of the free variables. The method did not include cavitation inception in the bounding design constraints, but did include maximum torque, thrust, blade chord, rotor radius and blade root bending moment.

Generator and controls for overspeed regulation

Zhou et al. presented research [90] into the generator side of OSPR. One aspect of this paper is the note that "over-nominal speed operation" (speeds which exceed the speed at which the generator is design to be most efficient, at which the system should be designed to operate at rated flow) results in increased voltage levels, which may cause saturation in the system. The paper discussed the operation requirements of a control strategy applied to a PMSG topology operated in overspeed, and suggested a flux weakening control method in which injection of demagnetising current into the generator effects the required increase in rotor velocity. Two control methods were compared, and both tidal current and wave-induced changes in flow velocity were considered. It was explicitly discuses that the C_{P}-λ relationship affects the performance requirements of the control scheme, and that this relationship is influenced by rotor design.

2.5.3 Challenges and constraints in overspeed regulation

The operation technique of a tidal turbine has effects on, and is therefore constrained by, the rest of the turbine. This introduces challenges to the task of rotor design. As

mentioned in [58] and [86], the increase in the range of rotational velocities introduces cavitation as a consideration. As hinted by the inclusion of a maximum torque design boundary in [89], the torque characteristics are another consideration, as is the thrust performance. The basic requirement of generators and controllers for overspeed regulated turbines, as discussed, is VS capability up to the range required by the site flow and rotor design combination. However, system response times, stability, complexity, cost and robustness must also influence the choice of generator, power electronics and control topology.

How and when these design variables are considered in the rotor design depends – as illustrated by the various examples above – on the stage of design at which overspeed becomes a considered operation technique. Furthermore, the design constraints will have a reciprocally influential relationship with such variables as the intended or prospective deployment sites, the specific design focus, the required energy yield, cost of energy, proximity to shore, available capital – and so on.

2.6 Blade design methodologies

There are many approaches to blade design, and these – as discussed – are dependent on many factors. Some examples of design approaches are given below.

2.6.1 The ideal wind turbine blade

The design of an ideal wind turbine blade is covered in texts such as Wind energy handbook [12, ch. 3], Aerodynamics of wind turbines [11, ch. 8] and Wind energy explained [13, ch. 3]. As Eqs. (4.26) and (4.27) and Fig. 2.12 show, the local pitch angle, β_r, required for the blade can be expressed in terms of α_r and the local flow angle, ϕ. With the requirement of maximum aerofoil efficiency, a value of $\alpha_r = \alpha_o$ can be set. For optimum aerodynamic efficiency, the ideal performance criterion can be set: $a = \frac{1}{3}$. The following design choices can be made: a design value of λ, a blade number, turbine radius and aerofoil section(s). If the simplifying assumptions, that $C_d = 0$ and there is no tip loss (the infinite blade number condition), are made, the values of ϕ and cd can be found for each value of r, giving the blade geometry. As derived in, e.g. [13],

$$\phi_r = \frac{2}{3} tan^{-1}(\frac{1}{\lambda_r}) \tag{2.14}$$

and

$$cd_r = \frac{8\pi r}{BC_l}(1 - cos(\phi_r) \tag{2.15}$$

where λ_r is the local speed ratio, the ratio between the speed of the blade section at radial position r and the freestream fluid; $\lambda_r = \lambda\frac{r}{R}$. Though assumptions are made this does take the rotation of the wake into consideration.

As discussed in [12, 11, 13], a blade designed in this way would be idealised for

maximum aerodynamic efficiency at one selected operating point. Although the twist is dependent on λ_o - which is dependent on the inflow velocity - and so the blades take some account of the flow field into which they would be deployed, the off-design performance is not optimised. This blade design may also be difficult, and therefore expensive, to manufacture. As discussed in [13, ch. 3], this is not the current approach to blade design. In the 1990s development took place which focused blade design methodology on maximising energy captured; this focus later shifted to maximising the economic value of wind energy, minimising the cost per MW h. According to the general blade design methodology in [13], this approach requires a design process within which the "ideal" blade is iteratively altered and its performance is analysed considering the overall cost of energy.

2.6.2 HarpOpt

In 2001, NREL presented a blade design methodology for HATSTs. The fundamental hydrodynamic design of this complete-blade-system methodology is undertaken with "HarpOpt". Presented in [91], Lawson et al. discuss that this is a tool designed to produce an optimised blade outer - that is the twist and chord distribution - and is the combination of their BEMT code "WTPerf" and a genetic algorithm. The optimisation input or fixed parameters, in the case discussed in [91], were the hub and rotor radii, the aerofoil design, the rated power, maximum rotational velocity, operating flow range, site and deployment depth and a VS-VP control scheme. The optimisation objectives were the maximisation of energy produced over the input range of flow velocities, while regulating power at the 550kW rated value and avoiding blade geometries or operating conditions with which cavitation inception may occur. In 2011, the developers presented [92] a figure outlining the overall "hydro-structural" blade design methodology. The blade design output by HarpOpt is input, along with the extreme operating conditions (influenced by weather and turbulent free-stream disturbances), into a CFD RANS code which assesses the extreme loading. These results are combined with the material and mechanical properties and fabrication constraints of composites to obtain a structural blade design. The output of this is an optimised composite layup for the blade design. A structural analysis is then undertaken on this blade design for the conditions specified, returning the structural properties over the length of the blade.

2.6.3 Design of passively-adaptive blades

A current area of research in terms of HATST blade technology is the concept of passively-adaptive composite bend-twist coupled blades. The basis of the concept is that the blades (or some structural component of the blades) are composed of layers of composites with varying ply directions. The ply, or fibre lay-up, directions are optimised in order to provide both structural integrity and a twisting under axial force in such a way as to maximise and/or shed power and reduce thrust loads [75].

In her papers and PhD thesis [93, 94], Nichols-Lee developed a blade design methodology for passively adaptive blades based on a combination of BEMT, Finite Element Method (FEM) and CFD tools. In this modular design tool, FEM and CFD codes were loosely coupled and interfaced through an iterative Matrix Laboratory (MATLAB)-based programme which passed each CFD solution to the FEM module, which calculated the deformation and passed the solution back to the CFD module which calculated the flow-induced loading, and so on until convergence was found. These performance results for the final blade shape were then checked with a BEMT tool. This tool modelled the performance of the turbine as the hydrodynamic performance of the blade under the twist induced by the fluid forces on a box spar. The induced twist was determined according to an analytical solution for twist as a function of a design reference twist (input maximum twist at blade tip occurring at U_D) and radial position.

In her papers [95, 75] and thesis [96], Murray presented further research into the concept of bend-twist coupled passively adaptive blades. A design methodology was developed which models the performance and structural response of bend-twist blades under the fluid forces of a range of flow conditions.

This tool was based on an experimentally verified FEM model, coupled to a BEMT model developed in a separate PhD program [31]. The coupling considered the fluid forces output from the BEMT model of the flow and un-deformed blade shape, and passed these to the FEM model. The FEM model outputs were read by the BEMT code as a new blade shape and the forces were again calculated, and so on until convergence. Bend-twist coupled composite blades were then tested, alongside rigid blades of the un-deformed shape, in a tow tank. It was shown that the bend-twist blades reduced the thrust loads by up to 10 % under the same flow conditions.

A modelled case study of a turbine with a blade length of 4 m showed a 10 % increase in power capture in Region I of the power curve, and a 10 % and 5 % reduction the power and thrust loads, respectively, in Region III of the power curve.

2.6.4 Broader blade design consideration

As reported in their paper investigating the effect of blade structural stiffness [97], Morris et al. used two-way coupled fluid-structure interface (FSI) modelling to determine blade deflection and the effect had on the energy extraction capabilities of HATST rotors. The investigation was undertaken by varying the material modulus – the structural stiffness – of the blades of 2, 3 and 4-bladed HATSTs and comparing the hydrodynamic performance of the rotor. Both the fluid and structural aspects of the model used ANSYS modules – Fluent and Mechanical, respectively – and a frame of reference rotating around the rotor axis was included within the main channel of Fluent model. The stiffness of the modelled blades was varied from that of glass composites, 10 GPa, to that of steel, 200 GPa and the torque, power and thrust variation were found for each rotor type (2, 3 and 4-bladed).

The paper found that the amount of deflection varied inversely with number of blades, due to the amount of thrust per blade. The power output of a 3-bladed HATST was found to decrease with deflection. The response of the 2 and 4-bladed rotors was more complex with an initial increase in power and a subsequent decrease for the 4-bladed rotor; due to the response pattern, it was assumed that the power output of the 2-bladed rotor would also eventually decrease with deflection.

A conclusion of this work was that blades could be designed such that the flexural response optimises performance at the design conditions.

In a slight departure from design of the actual blades, Batten et al. presented a design methodology to match turbine design to deployment site conditions, within which BEMT was used to predict turbine performance based on XFoil aerofoil data and an existing blade design [98]. The basis of the design methodology was to set assigned values to some of the design parameters, such as turbine radius and drive-train efficiency, to determine flow speeds based on a tidal site – the Portland Bill site was used in the paper – and to vary the design λ and design U_∞ in order to ascertain which combination gave the optimum combination of annual energy yield and maximum thrust.

In [74], Nicholls-Lee, Turnock, and Boyd presented a deatiled analysis of performance prediction tools for use in tidal turbine rotor design. The paper discussed the mertis of BEMT, CFD and FEM tools, as well as different optimisation methods. Genetic algorithms were seen to make intelligent selections of useful design alterations, which were then combined and taken forward to subsequent performance analyses in a convergence loop, which avoids local maxima and minima, working towards multiple objectives. It was concluded that genetic algorithms were the best suited of the considered optimisation methods for the production of optimised tidal turbine blades.

2.7 Conclusion

The foregoing chapter summarised the performance of horizontal axis tidal stream turbines, noted some of the influential flow phenomena and discussed the components, methods and operation techniques pertinent to a background for this thesis. Variable-speed operation, and fixed-pitch and variable-pitch blades have been discussed in terms of the requirements each puts on the rest of the turbine system, the possibilities and constraints each give to the operation techniques, including the power regulation method, and the energy-yield and structural advantages and disadvantages of each have been discussed. Several approaches to blade design have been discussed, with particular emphasis on existing approaches to design for overspeed regulation.

The advantages of FP blades are clear, and while it is not suggested that overspeed regulation out-performs all other methods, there is sufficient support for this as the power regulation method that an in-depth investigation was considered worthwhile. The following chapters of this thesis, therefore, will detail the outcome of three and a half year's research into overspeed power regulation for application in tidal turbines.

The proposed methodology of blade design for overspeed power regulation considers some of the same aspects included in the aforementioned design work on overspeed regulation, and takes an alternative approach to any. As noted in Section 1.4, this research has not given explicit consideration to torque limitations imposed by generator design. This was partly due to project time and scope limits, and has the advantage of keeping this design parameter as a free variable, allowing either the adaptation of a current generator design to suit the case, or the application of novel generator designs such as the C-GEN [59] design discussed in Section 2.3.4. Though the research presented in this thesis has not yet considered the impact of alternative aerofoil designs, cavitation inception is a key driver of aerofoil selection and this has been explicitly considered and presented, which was not the case for the (presented aspects) of the research projects discussed in this chapter.

Chapter 3

Empirical investigation of turbine performance

3.1 Wind turbine tests - performance in overspeed

3.1.1 Introduction

To begin to investigation of the possible characteristics and challenges of turbine operation in overspeed, performance data in the overspeed region was required. Operation of turbines in the overspeed region is not a common technique; this data is therefore not easy to come by in the literature. Though non-dimensionalised performance curves and rated power curves have been published for the small and the large scale (for example, [99] and [87]), with the exception of some results showing thrust and power with flow velocity [80], researched and reported power and thrust performance into the overspeed range of turbines in engineering terms – Watts, Amps, Volts and Newtons – does not appear to be widely available. A first stage of this project was therefore an empirical investigation of the effects of overspeeding a device. The aim of the experiments was to establish an indication of potential engineering challenges associated with overspeed, and, by quantifying these challenges for the particular device tested, to give a numerical indication of the effects of overspeeding.

Based on the mathematical theories of BEMT, electrical machines and aerofoil theory, the challenges hypothesised for allowing HATSTs to overspeed were higher structural loads, higher voltages and possible cavitation.

The premise of the experiments was that by placing a turbine in a flowing fluid and incrementally altering the electrical load on the generator from open-circuit to short-circuit conditions, the turbine performance could be measured in terms of the output terminal voltage, V_{T}, and current, I_{T}, the rotor's rotational velocity, Ω, and the axial force, F_{T}, resulting from a set (and measured) fluid flow velocity, U_{∞}, and resistive load, R_{load}, across the terminals. These measured quantities could then be used to inform the power output and structural reactions of the turbine over a range of

conditions, including the changes in performance in the overspeed region.

The experiment undertaken was performed on an existing, commercially available small wind turbine, an Ampair® 100, in a wind tunnel. Operating in air at this early stage had the great advantage of removing any need for waterproofing and provided a time-efficient method of gaining insight and understanding of turbine performance in overspeed, with reduced complexity compared to tow tank or flume testing. By using a wind tunnel at this stage, it was possible to construct the experiment quickly and access the turbine and its electrical system very easily during the testing.

3.1.2 Instrumentation and Data Capture

Turbine

The Ampair® 100 is classed as a small turbine, with a diameter of 0.928 m and a rated power of 100 W, at the rated wind speed of 10 $\mathrm{m\,s^{-1}}$. The tested device was factory set for 25 V output at rated conditions. The power is rectified to DC within the hub, giving an output which can be used, for example, to directly power DC devices on-board ships, or to charge a battery. Due to the requirement of operating in the overspeed region, all tests were run at inflow velocities below the rated to avoid transition into the generator's power-regulated mode; from discussions with the developers, it was known that the turbine did not have an rpm-limiter installed [100]. Thus, effects in the results from any existing turbine system limits were avoided.

Tunnel and flow velocity measurement

The test were preformed in the University of Strathclyde's wind tunnel, with the turbine mounted towards the rear of the 1.52meter diameter open working section. A pitot tube and manometer arrangement was mounted at deployed hub height, at the edge of the working section. The axis of the pitot tube was aligned to the flow direction and the pitot tube measurement was calibrated for the actual flow velocity at the turbine position with a hot wire anemometer.

The manometer used was an Airflow Type 4 Test Set. This instrument has an accuracy of ± 1%. Following the instructions provided for this manometer [101], the velocity of the air in the tunnel was calculated. The difference between p_{B}, the ambient barometric pressure, and p_{vel}, the velocity pressure, was read from the scale on the appropriate arm. The scale on the long arm is marked 0 to 50 cm, corresponding to 0 to 5000 pa. Taking the scale reading and multiplying this by 100, then by the appropriate manometer coefficient (0.1 for these tests) gave the velocity pressure, p_{vel}. An empirical formula was then used to calculate U_∞:

$$U_\infty = 1.291\sqrt{\frac{p_{\mathrm{atm}}}{p_{\mathrm{B}}}\frac{T_{\mathrm{a}}}{T_{\mathrm{c}}}p_{\mathrm{vel}}}\ , \tag{3.1}$$

where p_{atm} is standard atmospheric pressure, 1.01325 Pa, and T_c is calibration temperature, 293 K. The barometric pressure, p_B, was obtained from the METAR website for North England, Scotland and Ireland [102], which is updated every few hours and was therefore a reliable source of information. The data for Glasgow Airport was used. The temperature of the air, T_a, was measured by a CHY 500 Type K digital thermometer, which has an accuracy of $\pm$ 0.05% of the reading + $0.3°C$ within the range $-50°C$ to $1372°C$. The sensitivity of the velocity measurements to the accuracy of the temperature probe was shown to be in the order of 1×10^{-3}, thus the device was deemed suitably accurate [103].

Resistive load bank

The power terminals of the turbine were accessible directly from the power output cable by stripping the outer protection, separating and exposing the negative and positive power lines. It was then possible to connect these into a circuit through a load bank of various resistance values. A main-line switch was installed on the positive power line to break the circuit and allow safe alteration of the connected resistive load. The resistive load bank and the measurement instrumentation were installed at the side of the tunnel. Figs. 3.1 and 3.2 show the turbine mounted in the wind tunnel, and the data capture and load bank arrangement at the side of the tunnel.

Sixteen different resistive loads were connected across the turbine terminals, with a higher density of tests points around the optimum to high resistance values to give a clear picture of the performance from peak efficiency to the far right-hand side of the C_P-λ curve, in the overspeed region. The resistive values required to obtain these data points were identified through trial and error. Table 3.1 gives the resistive loads used; each resistor had a power rating of at least 100 W.

Table 3.1: Load resistance values (Ω)

open circuit
50500
1506
686
472
333
202
100.6
80.8
50.9
30.6
22.5
10.6
5.4
0.7

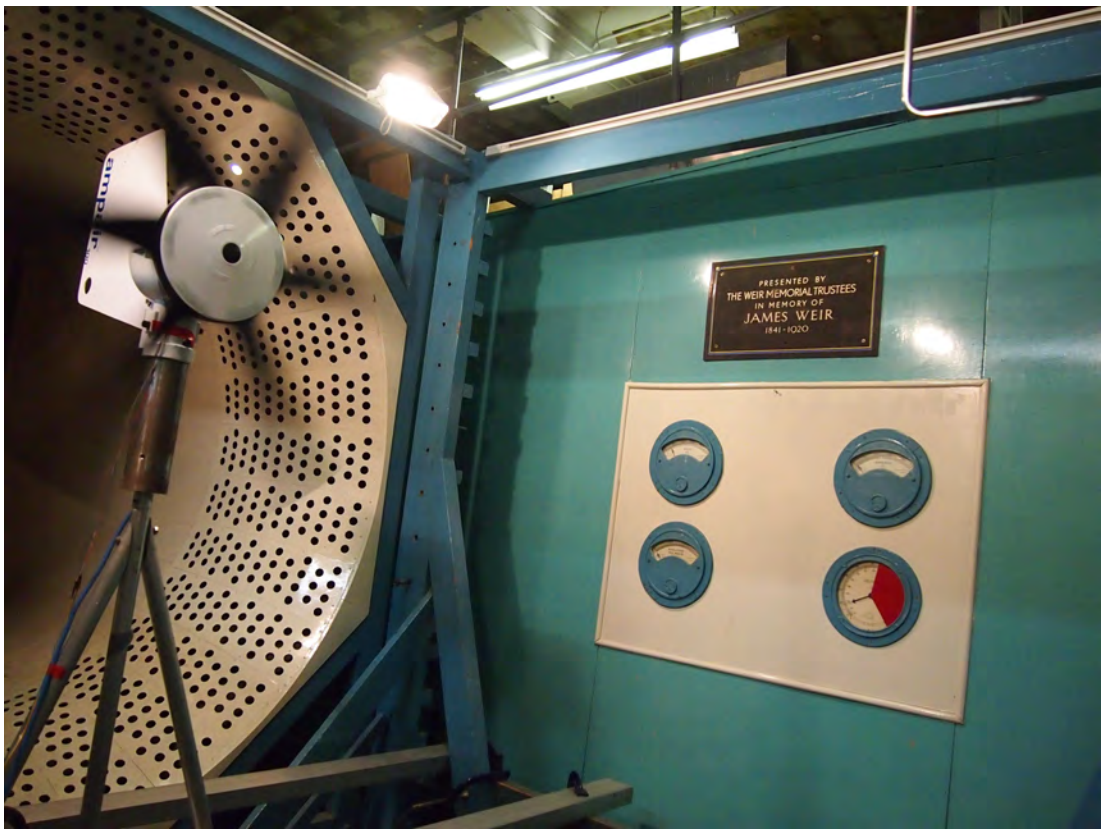

Figure 3.1: Photograph of Ampair® 100 installed in wind tunnel, with pitot tube at top right corner facing directly into the flow.

Rotor velocity

To capture the rotational velocity of the rotor, the turbine was instrumented with a reflective object sensor, an OPB704-W, from Optek Technologies Inc. One half of the forward-facing edge of an OPB704-W emits light from an LED, the other half detects light with a transistor [104]. A voltage of 3 V was supplied; detected reflection of the emitted light transmitted a low-voltage return signal while no detection of reflection returned the supply voltage. The OPB704-W was mounted on a purpose-made bracket attached to the turbine, facing the downstream side of the rotor. The rotor circumference in view of the OPB704-W was covered in tape to provide two surfaces - one half with a matt black tape, the other with highly reflective metal tape. The return signal thereby gave a high-low voltage data stream pulsing in time, from which it was possible to calculate the rotor velocity.

Axial thrust load

To capture the thrust load on the turbine, a full-bride strain gauge assembly was attached to the stand on which the turbine was mounted. The stand was clamped in a horizontal position and the gauges were calibrated using several known masses suspended from a point a measured distance from the gauges. The strain values, σ, were

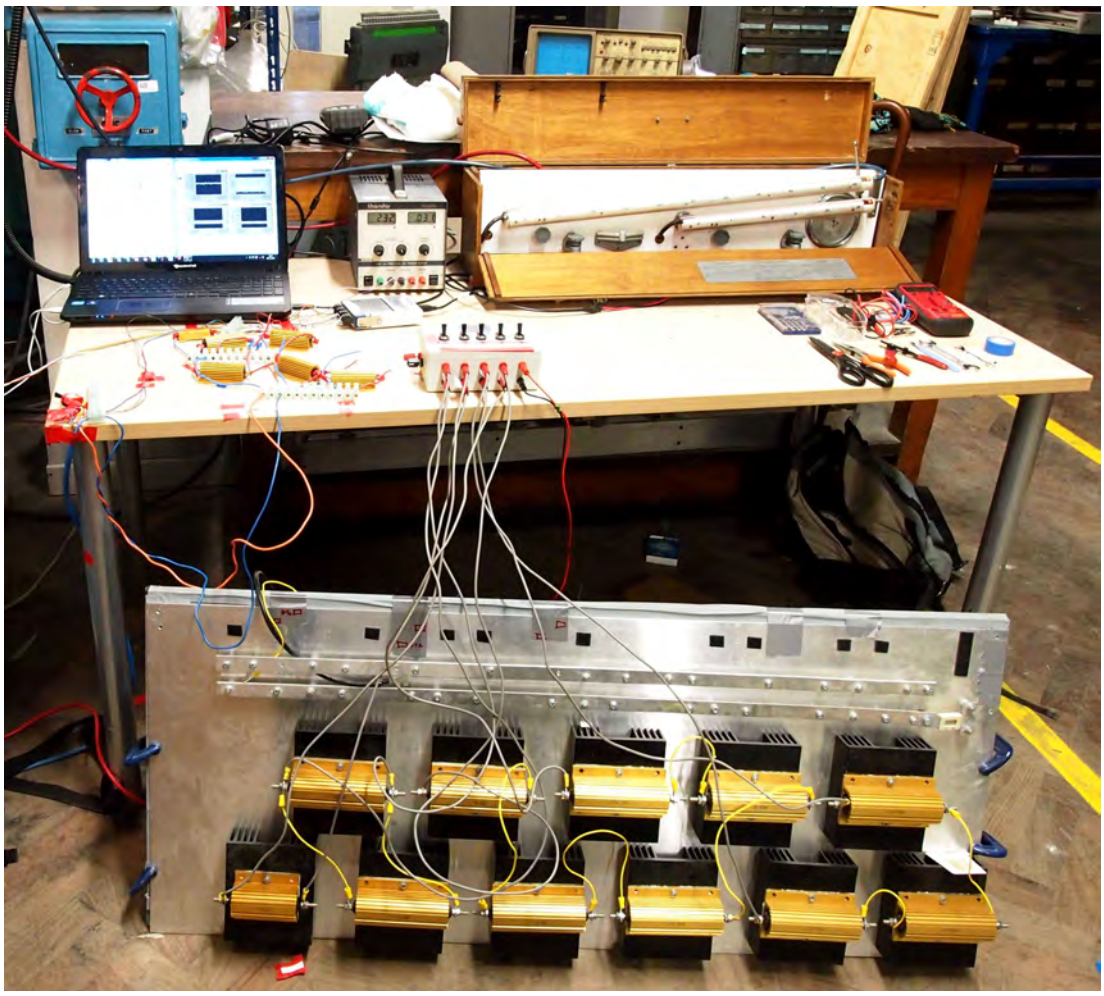

Figure 3.2: Experimental data capture and resistive load circuit

plotted on an x-y scatter plot against the corresponding force produced by the mass; a linear trend line was fitted with a coefficient of determination, r^2, value of 0.999. The equation of this line was combined with the ratio of the distance from the suspension point to the gauges, L_C, and the centre of the hub to the gauges, L_H, giving Eq. (3.2). Once the stand was returned to the upright position and the turbine mounted, there was a residual strain present, giving a 'zero' thrust value which was removed from all subsequent signals in the post-processing stage. The stand was mounted in the tunnel such that the strain gauges were aligned to the flow direction, giving a true axial force reading.

$$F_T = \frac{L_C}{L_H}(21527\sigma + 0.449) \tag{3.2}$$

Current and voltage

The current flowing from the generator was measured from Ohm's Law, with a shunt resistor of very low and highly accurate resistance 0.005 Ω ±0.1%. This resistor was

Table 3.2: Comparison of NI9219-acquired mean and DMV-obtained terminal voltage

U_∞ $(\mathrm{m\,s^{-1}})$	5.1			5.4			5.7		
R_{load} (Ω)	333	1500	680	680	1500	333	100	333	43
$\overline{V}$ from NI9219 (V)	39.4	44.2	42.5	46.7	48.6	43.8	35.7	45.8	25.9
DVM voltage (V)	39.4	44	42.5	46.6	48.6	43.7	35.6	45.7	25.9
% Difference	0.1	0.5	0.1	0.3	0.1	0.1	0.3	0.2	0.1

fitted in series with the turbine's positive power cable; for safe capacity its power rating was therefore 100 W. The voltage drop across this was read by the data acquisition system (DAQ) system and used to reliably calculate the current. The voltage drop across the load bank was read directly. This was used in conjunction with the calculated current to give the power output of the turbine.

The main data acquisition DAQ instrumentation, an NI 9219, was able to read a maximum of 60 V which proved to become insufficient as the turbine sped up with higher resistive values connected across the terminals. To ensure accurate data capture, a digital volt meter (DVM) was therefore used to measure the mean voltage reading of the higher voltage tests. The accuracy of this technique was ascertained by comparing the mean voltage reading from the NI 9219 to the DVM mean reading in 9 separate test conditions wherein the voltage did not exceed 60 V. Table 3.2 gives details of these test scenarios: the flow velocity; the two mean voltage readings, from the NI 9219 and the DVM; and the percentage difference. Over the 9 test runs, it was seen that the mean percentage difference was 0.2 %, with a maximum of 0.5 % - sufficiently accurate for the purposes of this early stage investigation.

Data capture

The load bank resistance and inflow velocities were recorded manually for each test. The remaining data were collected electronically, post-processed and recorded as mean values under the appropriate inflow velocity/load bank resistance combination. The electronically measured quantities were recorded with a National Instruments 9219 data acquisition box, mounted in an NI USB 9162 carrier. The highest available frequency of 50 samples per second per channel was used [105].

A virtual instrument was created in LabVIEW which recorded the three outputs: strain, OPB704-W voltage and shunt resistance voltage. These results, along with a time stamp, were captured in text files named according to the inflow velocity and the load resistance of the test scenario.

3.1.3 Test Procedure

The wind velocity of the tunnel was set, the p_{vel} value was read from the manometer and the velocity was calculated and recorded. For each velocity, the open circuit test was run first, followed by tests generally in order of decreasing load resistance. In cases

where a resistor was to be used in more than one load circuit, use of the second circuit was postponed to allow the resistor to cool back to room temperature before that test scenario was run. Between each test run, the circuit was broken by the power line switch while the load circuits were altered - this allowed the turbine to increase its rotational velocity and removed the potential of lower resistance values influencing subsequent tests. Furthermore, each new test scenario was allowed to settle for a couple of minutes to ensure both the air flow and turbine conditions were in reaction only to the current test scenario. Data was then captured for around 60-90 s, giving at least 3500 sample points.

3.1.4 Post Processing

The captured data was fed as arrays into a MATLAB script written to analyse this test data. The strain measurement was converted to the mean thrust load using Equation 3.2 and taking the mean of this array. Similarly, the mean voltage across the shunt resistor was obtained, converted to a current reading according to Ohm's Law and used with the mean V_{T} reading from the DVM to calculate the power:

$$P_{\mathrm{out}} = \frac{V_{\mathrm{shunt}}}{R_{\mathrm{shunt}}} V_{\mathrm{load}} \ . \tag{3.3}$$

Entering the load resistance values and constants such as diameter and flow density finalised the preparation of the data. To allow use of the open circuit tests, the open circuit resistance (of actual value $\infty\ \Omega$) was approximated as a million million Ω.

The voltage signal from the OPB704-W required some processing before being used to calculate the rotor's rotational velocity. A script was produced which returned a value of 1 for each data point of value greater or equal to 3.2, and a value of 0 for data points of smaller value than 3.2. This gave a binary signal representative of the raw data. This cleaned-up data was then used to identify the positions in the matching time array at which the binary OPB704-W signal changed from 0 to 1, i.e., the times at which the rotor had undergone a complete revolution. The difference between subsequent times was found, creating a new array. The mean and standard deviation of this array was found, giving the mean and standard deviation of the period, T, of the rotor. It was found that the relative standard deviation was small (7%), indicating that the data capture process was not skipping over any signal points. The period of the rotor was converted to the angular velocity according to Eq. (3.4).

$$\Omega = \frac{2\pi}{T} \ . \tag{3.4}$$

Eq. (2.3) and Eq. (2.4) give the calculation of the coefficients of power and thrust. The λ values were calculated from Eq. (2.5).

The values of λ and recorded V_{T}, as well as C_{P} and C_{T}, for the sixteen test runs were grouped in a set of arrays for each U_{∞}, to allow the creation of graphs for visualisation

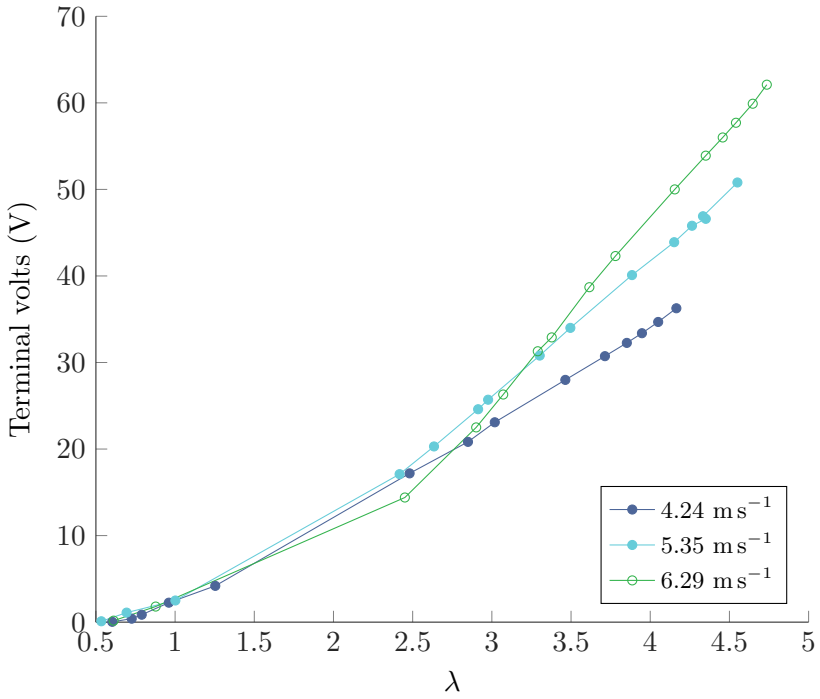

Figure 3.3: Voltage results for tested wind turbine; change in mean terminal voltage with λ from test results according to inflow velocity

of the manner in which these characteristics varied.

Similar tests, producing C_P and C_T-λ curves have previously been run on an Ampair® by Comyn et al., based at the University of Alberta [106]. The performance curves produced therein were digitised to stand as a comparison to the results produced at lower U_∞ here.

3.1.5 Results and Discussion

Figs. 3.3 to 3.5 show the curves of V_T, C_P and C_T, as they vary with λ. Excepting the C_T-λ results for U_∞ 4.24 which are too scattered to benefit from this, the results are presented with point-to-point lines included to enable easy identification of the different U_∞ test scenarios and the trends associated with the data. Data from the testing performed previously, at higher inflow velocities, are also shown for comparison and are marked "UAlberta".

Voltage increase in overspeed

Figure 3.3 shows the manner in which the mean V_T varied with λ for each inflow velocity. The first obvious conclusion which can be drawn is that the voltage increased with the rotor speed. This general trend was expected as the voltage created in an electrical generator is proportional to the rotational velocity [107]. The new piece of information found is the extent to which the voltage can be expected to increase with λ in the overspeed region. Table 3.3 gives the actual and percentage increase in λ and voltage

Table 3.3: $\Delta\lambda$ and Voltage in the Overspin Region

U_∞ $(\mathrm{m\,s^{-1}})$	4.24	5.35	6.29
λ_O	2.48	2.91	3.07
Voltage at λ_O (V)	17.2	24.6	26.3
λ_R	4.13	4.53	4.74
Voltage at λ_R (V)	39.7	55.7	69.3
Actual $\Delta\lambda$	1.65	1.61	1.66
Actual Increase in Voltage (V)	22.5	31.1	43.0
% $\Delta\lambda$	66.4	55.4	54.2
% Increase in Voltage	131.0	126.4	163.5

occurring between the point of maximum C_P and maximum λ for each inflow velocity. The significant outcome is that the V_T was increased in the overspeed region at all flow speeds, by over 100 %.

The results showed that the percentage increase in voltage was smaller at 5.35 $\mathrm{m\,s^{-1}}$ than at 4.24 $\mathrm{m\,s^{-1}}$, but much greater between 4.24 $\mathrm{m\,s^{-1}}$ and 6.29 $\mathrm{m\,s^{-1}}$. The position of the runaway point for the curve is dependent on the rotor and generator efficiencies, as noted; this will influence the percentage increase in voltage between the optimum and runaway point. However, the general trend here suggests that the increase in voltage between optimum and maximum λ increases as U_∞ moves towards the rated velocity.

Power performance

The peak of the C_P-λ curves, Fig. 3.4, tended to move upwards and to the right as the U_∞ value of the scenario increased. This trend was thought to be the result of a combination of Reynolds number effects increasing the efficiency of the rotor as the involved velocities increased, and increasing generator efficiency as U_∞ increased towards the rated value. The latter hypothesis was confirmed in communications with the developers of the turbine. The maximum C_P value, obtained in the test with U_∞ equal to 6.29ms^{-1}, was 0.23.

Thrust performance

Figure 3.5 showed that the force of thrust on the turbine varied significantly more at the slowest U_∞ value of 4.24 ms^{-1} compared to the thrust occurring with the slightly higher inflow velocities. This was most likely due to vibrations induced by the blades passing the stand, as has previously been experimentally observed [61]. The C_T-λ curves showed general decrease in C_T as the inflow velocity increased, most likely as a result of increased aerodynamic efficiency as the Reynolds number increased. Once more, the general trend in the results of this project suggested that a fairly good match existed between the C_T-λ data produced in these lower U_∞ test scenarios and those produced at higher inflow velocities [106]. The difference between the results, however, seems to

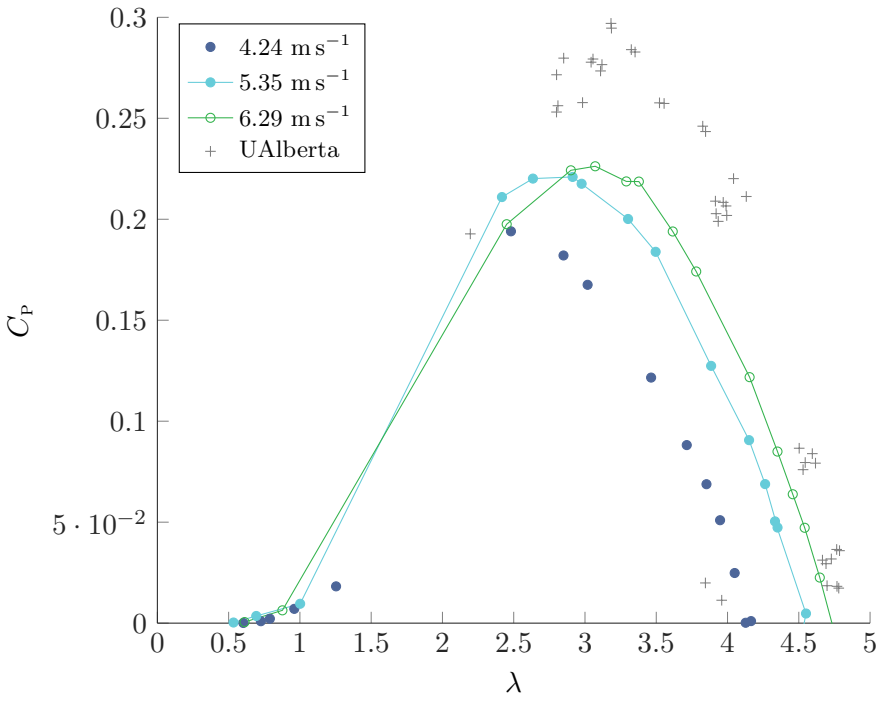

Figure 3.4: Tested wind turbine C_P-λ curves from test results, according to inflow velocity, plotted alongside previously published data [106] for the same wind turbine at a faster inflow velocity

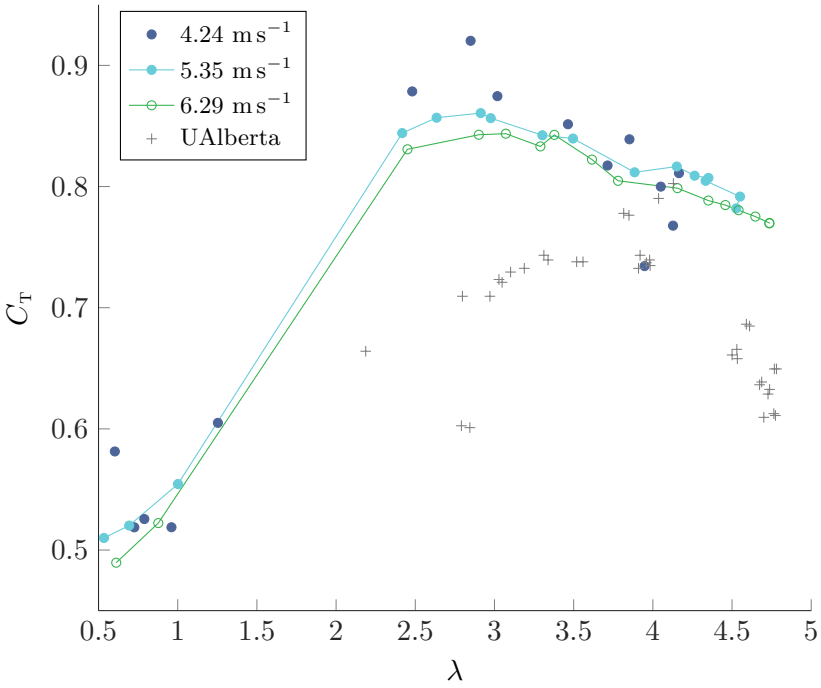

Figure 3.5: Tested wind turbine C_T-λ curves from test results according to inflow velocity, plotted alongside previously published data [106] for the same wind turbine at a faster inflow velocity.

be slightly greater than in the case of the C_P-λ curves; this may be due to a resonance vibration being reached for the length of the stand the turbine is mounted on.

3.1.6 Discussion of the results

The generally favourable comparison with the previously published test results - particularly in the trends of C_P and λ - gave good confidence in the testing and post-processing methodologies.

The tests confirmed that, by decreasing the load on the generator, it is possible to increase λ and thus decrease C_P. As the inflow velocity increased, the maximum value of λ also increased (as shown in Fig. 3.3 and Table 3.3).

The limitation on the testable U_∞ for overspeed performance, resulting from the turbine's power regulation system, meant that the region of Re-independence for this turbine could not be identified or worked in, giving a progression of the performance curves - especially that of power performance - as the inflow increased. This meant that the extent of increase in voltage in the overspeed region, and the general performance coefficients, were found in terms of the tested inflow velocity, rather than in truly dimensionless terms. However, the conclusion can be drawn that V_T can be expected to increase by a large percentage between the peak of the power curve and the runaway point. This has significant implications for the design of turbines to be used in an OSPR method.

A turbine of standard design using overspeed to regulate power capture would require a generator design which would allow for high voltages. High voltages can lead to arcing between insufficiently insulated cables, creating a short circuit. To avoid this, thicker insulation would be required which would lead to heavier, larger and thus less economically efficient machines.

The tests showed that, for this turbine, as λ was increased beyond the optimum value, the coefficient of thrust tended to decrease. However, the decrease was slight and the proposed method of power regulation would require a turbine to operate in the higher reaches of λ than other methods. If blades of a standard design were used in a turbine to be operated in overspeed, the thrust forces would become very large. This indicates that the structural design of the blades, both in terms of the hydrodynamic force on the blades, and in terms of the structural integrity of the turbine system, will also be an important design factor.

Cavitation cannot be discussed with reference to these wind turbine tests; however, it was noted that the significant increase in Ω required to reduce the C_P to zero would, according to the discussion presented in Section 2.2.6, increase the possibility of cavitation on submerged turbine blades.

Conclusions

The increased voltages, thrust loads and cavitation potential expected from operation in overspeed of a turbine with standard blade design suggests that either the cost of these effects must be borne, or that a design change which limits these effects will be required. These effects may be limited with a design change which reduces the increase in λ between the peak of the C_P-λ curve and the runaway point: a design which limits the maximum rotational velocity of the rotor. It is the blades which are the aspect of a turbine that interact with the flow and determine the shape of the C_P-λ curve. This required change will therefore be a blade design alteration.

3.2 Base case blade performance

3.2.1 Objectives of tow tank experiments

The argument developed in the foregoing section highlighted challenges relating to voltage levels, cavitation inception and structural forces for turbine operation in overspeed. It was established that new blade designs would be required to make the operation of tidal turbines in OSPR safe and economically viable. The next stage was to experimentally determine a tidal turbine base case performance from which to measure the effect of blade design alterations.

As discussed in Section 2.1.2, BEMT tools can be used to predict the performance of tidal turbine rotor designs. Due to the rapid prototyping enabled with BEMT, this was the tool selected for use in this project, with which to make predictions of blade performance as the design parameters were altered. The joint purpose of these experiments, therefore, was to provide empirical data for the calibration and verification of a BEMT tool. Used alongside other experimental data found in the literature, this data would verify the BEMT code for use as a design tool in this project.

The required output of this set of experiments were a set of performance characteristics, obtained from the mean values of measured, repeatable data taken over a time long enough and at a frequency high enough to result in statistically viable tests in which no aliasing affected the captured data.

3.2.2 Test outline

The experiments were undertaken on a $\frac{1}{20}$ scale HATST rotor, in the University of Strathclyde's Kelvin Hydrodynamics Laboratory tow tank. The tow tank has a cross-sectional area of 4.6 m by 2.5 m, is 76 m in length and is shown in Fig. 3.6.

The experiments were performed at four carriage speeds, and the rotational velocity of the rotor was altered between tests to capture the performance over the full range of λ, from the left of stall to the runaway point. An existing test turbine rig, designed and built by the Department of Naval Architecture, was used for these experiments and is shown in Figs. 3.8 to 3.10.

Figure 3.6: Photograph along the length of the Kelvin Hydrodynamics Laboratory's tow tank, taken from the tow carriage during testing in 2013

Test turbine systems require to emulate the operation of their full-scale counterparts in such a way that measurements can be taken in controlled, understood test scenarios. In this system, the test operation used a motor to drive the rotor at a constant rotational speed while the turbine system was towed through the tank and the shaft torque was measured (on the rotor side). This measured torque value, Q, gave the difference between two torques created by the test operation. These torques can be described as: Q_{H}, the torque produced by the hydrodynamic interaction between the rotor as it is turned at a certain speed, and the water through which the rotor is travelling; and Q_{M}, the torque required from the motor to turn the rotor through the water under the force of the towing action. In turning the rotor under these conditions, the motor essentially acts as a variable torque break on the shaft, having the same braking effect as a generator putting a varying electromagnetic torque on the shaft as it converts mechanical to electrical energy.

The set (and then also measured) variables in each test scenario were the carriage velocity, U_∞, and the rotational velocity, Ω. The measured variables were: shaft torque, Q, axial thrust on the shaft, F_{T}, axial blade root bending moment, M_{y}, and in-plane blade root bending moment, M_{x}. The coordinate system of these measurements was as shown in Figs. 2.11 and 3.10.

3.2.3 Test set-up and instrumentation

Captured data

To facilitate direct comparison of different turbine systems, regardless of size or design, it is a recommendation from EquiMar [108] that nondimensionalised turbine performance

Table 3.4: Measured quantities and instrumentation

Final variable	Measurement	Instrumentation
C_{P}	Primary shaft torque, Q (N m) Shaft rotational velocity, Ω (rad s^{-1})	Torque and thrust transducer Proximity switch
λ	Carriage speed, U_∞ (m s^{-1}) Shaft rotational velocity, Ω (N m)	Carriage speed Proximity switch
C_{T}	Rotor thrust load, F_{T} (N)	Torque and thrust transducer
$C_{\mathrm{M}y}$	Axial blade root bending moment, M_{y} (N m)	Strain gauge, blades 1 and 2
$C_{\mathrm{M}x}$	Radial blade root bending moment, M_{x} (N m)	Strain gauge, blade 3

characteristics should be used in discussion or presentation of the performance of a turbine rotor. The relevant performance characteristics for the tests presented here are detailed, along with the required measured quantities and instrumentation for each, in Table 3.4

Base case rotor

The base case blade geometry is detailed in Table 3.5. The blade length and chord geometries are expressed as a fraction of the total blade length, L_b, giving a non-dimensionalised, scalable blade design. θ_r is measured in different ways, from tip to root or root to tip. In this work, as Fig. 2.12 showed, it is measured from root to tip, starting with a negative value measured anti-clockwise from the chord line of the blade root section. The blade case blade design is pictured in Fig. 3.7.

As detailed in Table 3.6, the blades were of length, $L_{\mathrm{b}} = 0.292$ m, and were bolted on to the test turbine hub with a coupling flange, giving a total hub radius, R_{h} of 0.089 m. The coupling flange was a brass piece of circular cross section, and was used in conjunction with a pin designed to enable an accurate blade root pitch setting. This resulted in a 0.762 m diameter rotor. Fig. 3.8 shows the rotor with the nose cone removed exposing the blade-hub coupling and blade root-hub connection, and the blades of NREL S814 aerofoil shape. To firmly connect the blade and hub in all degrees of freedom, bolts were secured through the flanges and the pin was slotted into a hole drilled on the bottom side of the blades, at a point on the chord line. The pin's position on the chord line of the blade coincided with the midpoint of the hub depth.

Considerable effort was given to ensuring each blade was set at the same root pitch setting, and that the value and uncertainty of the root pitch were quantified. To achieve this, a depth gauge fixed in the horizontal plane and used to measure the distance, d_1, between the edge of the rotor hub and the trailing edge of the blade at the root. The

Table 3.5: Geometry of base case blade design

$r/L_b(-)$	$c_r/L_b(-)$	$\theta_r(\ ^\circ)$
0	0.22	0
0.1	0.21	-4.9
0.2	0.21	-10.6
0.3	0.19	-14.2
0.4	0.18	-16.7
0.5	0.17	-18.3
0.6	0.16	-19.2
0.7	0.14	-19.9
0.8	0.13	-20.4
0.9	0.12	-20.8
1	0.09	-21.1
	$\beta\ ^\circ$	28.9 $\pm 0.88\ ^\circ$

Table 3.6: Details of base case rotor

R(m)	R_h(m)	L_b(m)
0.381 ± 0.0005	0.089 ± 0.0005	0.292 ± 0.0005

blades were rotated about the pins until d_1 was the same for each. A CAD model of the rotor was then used to determine the angle between the blade chord-line and the rotor plane. In the CAD, the blades were constrained to have one degree of freedom in rotation about the pin position on the hub. The blade root trailing edge was rotated to the distance d_1 from the hub edge, and the resulting angle was read out from the CAD programme. The angle of the blade root pitch setting is given in Table 3.5, along with the uncertainty in this measurement.

The blades were numbered 1-3, for reference to the instrumentation attached to each. Blades 1 and 2 were strain gauged at the root for measuring out-of-plane (axial) blade root bending moment; the strain gauge at the root of blade 3 was to measure in-plane (radial) blade root bending moment.

Turbine test rig

As the diagrams in Fig. 3.9, and the photograph in Fig. 3.10 show, this rotor arrangement was attached to a horizontal axis test rig, and suspended from the tow carriage on a custom-made arrangement which ensured a zero yaw angle on the high-speed shaft. The rig was positioned such that tip of a blade at top-dead-centre position was located 0.70 m below the free surface of the water.

Figure 3.7: Photograph of the base case blade tested in the tow tank

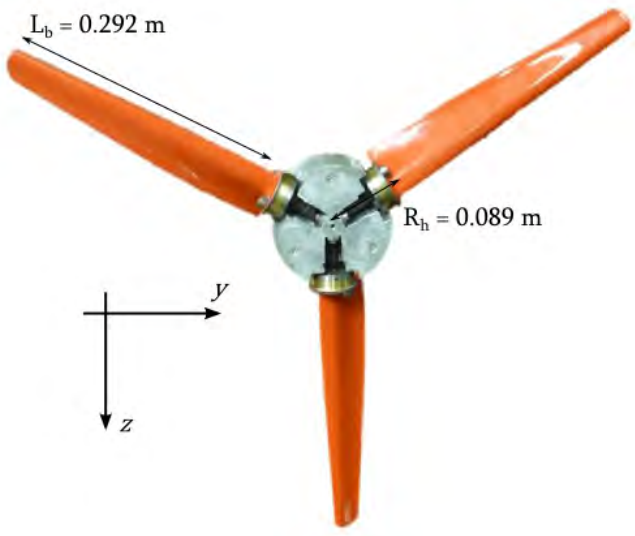

Figure 3.8: Image of tested rotor, showing hub, blade root connections and blades, with dimensions and coordinate system.

Instrumentation

Fig. 3.9 gives a diagram of the test set-up, including the carriage, test rig, instrumentation and DAQ system.

The motor was positioned at the rear of the test rig. A 10:1 gear box was used to step down the rotational speed of the motor to give that of the rotor, and a thrust bearing ensured the axial forces were not transferred from the rotor to the motor. The shaft transmitted the torques between motor and rotor, and was split and joined at the thrust bearing. It was not possible, despite best efforts, to align the joint on the shaft perfectly; a sinusoidal variation in thrust was therefore present in the captured data. This was considered in the post processing, as will be discussed in Section 3.2.7.

The rotor was positioned just over one full diameter upstream of the support to minimise fluid interactions with the support. Strain gauges attached to the blade roots were used to measure the axial (on blade 1 and 2) and radial (on blade 3) blade root bending moments. The strain gauges were positioned on cylindrical steel transducers which were isolated from the water with waterproofing material, as shown in Fig. 3.8.

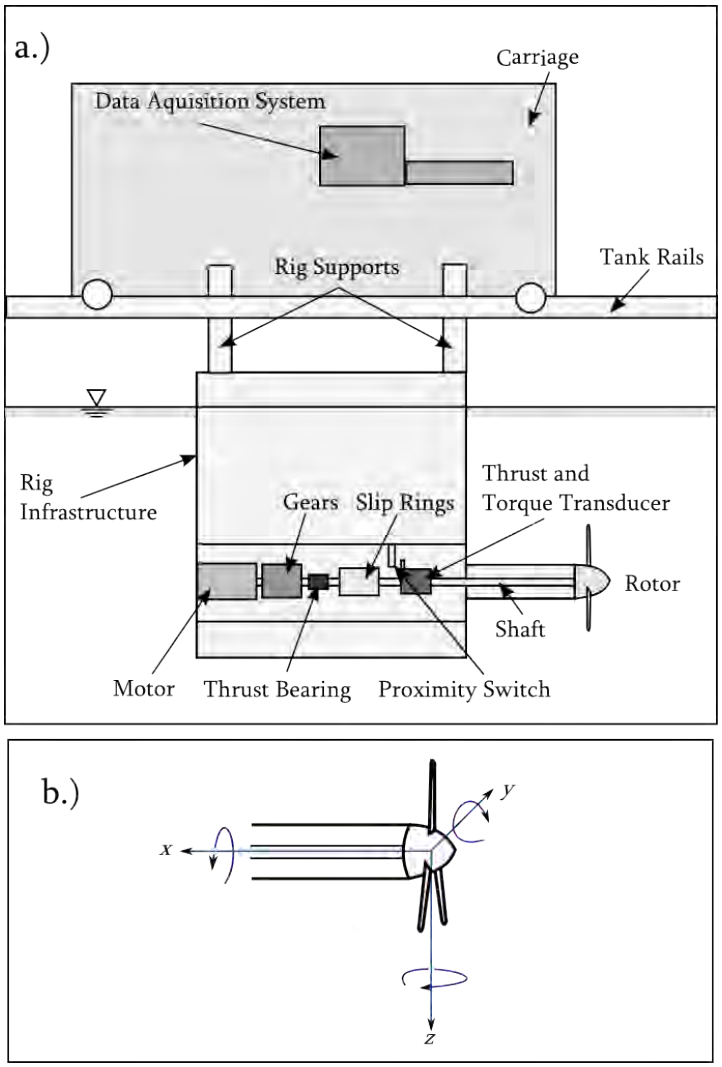

Figure 3.9: Diagram of a.) Tow tank carriage and turbine test setup b.) rotor section with coordinate system

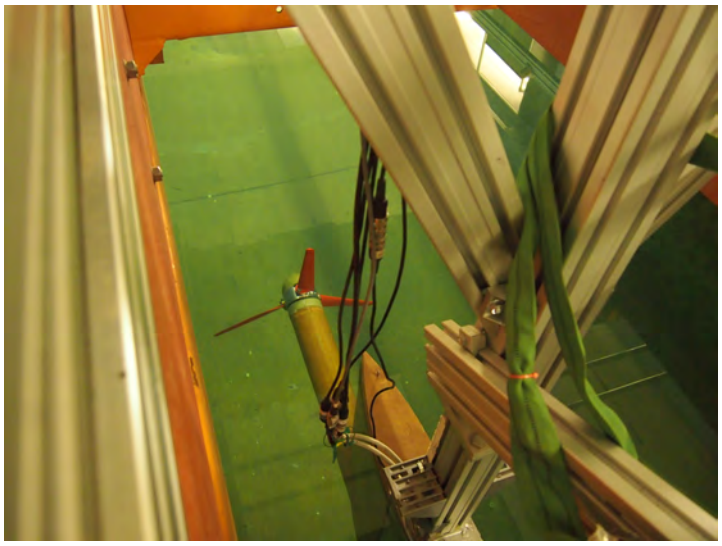

Figure 3.10: Photograph of base case rotor design on tested rig, taken from carriage during testing in 2013

The upper section of each steel transducer was bolted firmly to the coupling flange.

The hollow shaft carried the instrument wires from the rotor to the slip rings. A seal ensured there was no water ingress into the test rig.

A Futek FSH00747 torque and thrust biaxial sensor was used to measure the thrust and the torque on the rotor system.

A proximity sensor was used as a pulse counter to count the number of shaft revolutions in a given time period. The pulse switch was lined up in such a way that each pulse in the output signal corresponded to passage through top-dead-centre position of the blade named blade 1; it was therefore also possible to use the proximity switch signal to ascertain the shaft's angular displacement at any point in time. This was the primary source of measurement for rotational speed; however, the higher frequency motor encoder was also used as a check for the proximity sensor.

An IS 1163 SW 110/20 CAT slip ring was used to feed the electrical signal from the rotating dynamometer and strain gauges to the DAQ.

Data was logged using a Cambridge Electronic Design Power 1401 DAQ and the DAQ programme, Spike, and exported as text files for post processing in MATLAB. The DAQ was on-board the carriage, allowing for real-time viewing and pre-processing of the captured data, which informed the test procedure with regards to the collection of appropriate data points.

3.2.4 Calibration

The test measurand (thrust, torque, and bending moment) sensors were calibrated by applying a weight of known mass to a point of application on a lever arm, as shown in Fig. 3.11, and measuring the output voltage from the instrumentation. The force, torque or moment and output voltage pairs were then plotted against one-another. The equation for a generic applied measurand, G, obtained with a least squares linear regression method, was:

$$V = b\,G + a\ . \tag{3.5}$$

To convert a measured voltage to the required test measurand, calibration equations were obtained from the inverse of Eq. (3.5), having the general form:

$$G = \frac{V}{b} - \frac{a}{b}\ . \tag{3.6}$$

The output voltage was passed through amplifiers; therefore the first step in the calibration process was to zero the amplifiers and set their gains such that the voltage output captured the full range of the weights applied, based on a maximum voltage of 10 V. It was ensured that the applied weights (and thus the calibration process) covered the range of values anticipated for each measurement during the testing.

Several sets of calibrations were undertaken, with the initial calibrations being done to ensure components were fully functional, and the final calibrations being undertaken

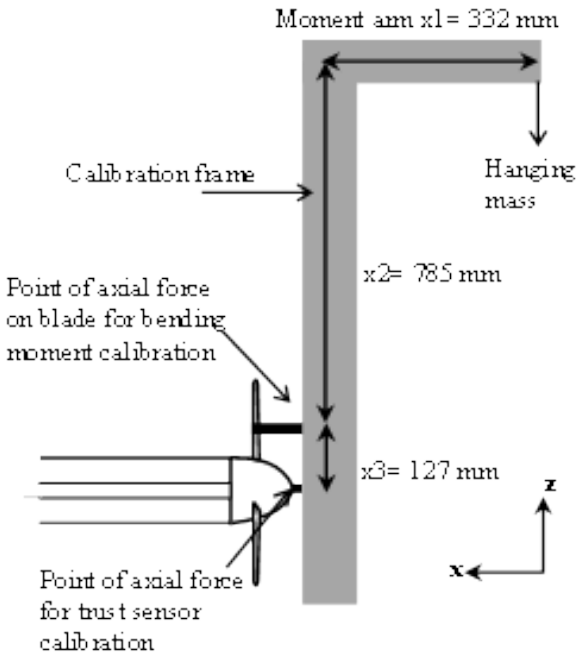

Figure 3.11: Calibration set-up showing load points for axial blade root bending moment calibration and thrust calibration.

immediately prior to testing once the set-up was fully commissioned.

The uncertainty analysis undertaken on the calibration processes is detailed in Section 3.2.8.

Thrust calibration

The thrust sensor was calibrated both statically and dynamically (with the rotor rotating). In the static process, there was significant static friction in the system which resulted in inaccurate readings, and hence these results were not used. Dynamic calibrations were undertaken by rotating the rotor at a range of different rotational speeds while applying various weights to a moment arm. A point applicator was used to transfer the load from the moment arm to the centre of the rotor hub, at a position shown in Fig. 3.11. The maximum load expected (estimated based on a value of C_T from [109], and the known swept area of the turbine) was set equal to an 8 V output on the amplifier, so that the voltage would be below the 10 V cut-off, including any noise in the signal. A series of masses were loaded and unloaded to the moment arm, and the results were captured by the DAQ programme, Spike. Both large weights (up to 10 kg), and small weights (starting at 0.1 kg and increasing by increments of 0.1 kg), were used to assess the sensitivity of the measurements. It was found that the thrust loads as a function of voltage were almost identical for a wide range of rotational velocities, as shown in Fig. 3.12, with low sensitivity to the increment of force applied.

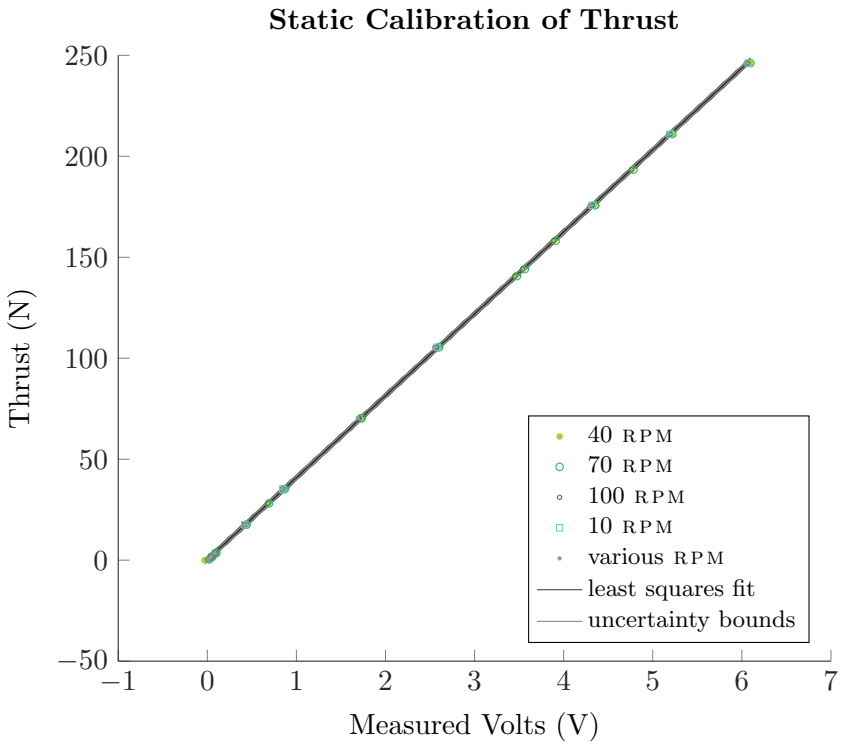

Figure 3.12: Dynamic calibration of thrust: thrust calibration results at various rotational velocities, including least squares regression fit and uncertainty bounds.

Torque calibration

The torque sensor was calibrated statically. Although dynamic calibration is required for oscillatory (unsteady) testing, static calibration was appropriate for the steady conditions speeds used in these tests. To calibrate the load cell statically, two lever arms were attached to the front of the hub that, when loaded, resulted in a radial torque on the shaft. A pulley with hanging weights was attached to one lever arm to achieve an upward force on one side of the shaft, while hanging weights were applied to the other arm to apply a downward force on the opposite side, as shown in Fig. 3.13. Hanging weights were loaded and unloaded on both lever arms, applying a known torque. The results of the torque calibration are shown in Fig. 3.14. The calibration trends for the torque sensor were highly linear.

Blade root bending moment calibration

Each blade root strain gauge transducer required separate calibration. It was known, from previous tests, that one of the gauges measuring axial bending moment was broken. As discussed in Section 3.2.8, this calibration processes, and the uncertainty analysis undertaken on the data, identified which was the broken and which was the functioning gauge.

As shown in Figs. 3.11 and 3.15, the transducers were calibrated by applying a known load at a fixed point approximately one third of the distance from the rotor-hub

Figure 3.13: Calibration of torque transducer using mass weights and a pulley system, equal force was applied to each side of the hub for accurate torque calibration.

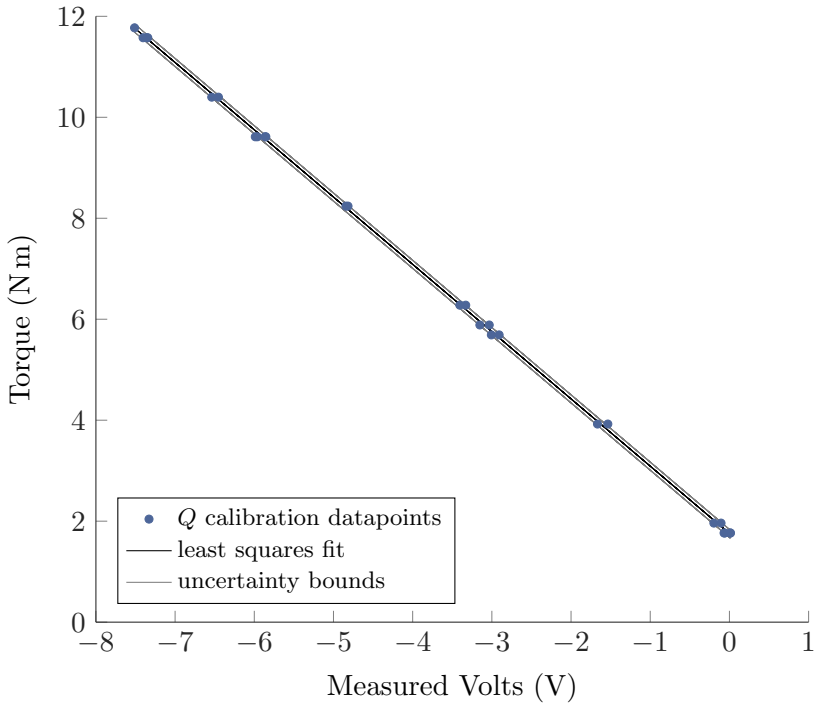

Figure 3.14: Calibration of torque: torque calibration results including least squares regression fit and uncertainty bounds.

connection to the blade tip, creating a known bending moment. It was assumed that, on average, each blade would take one third of the total thrust force, so the maximum applied bending moment was set to one third of the maximum load used in the thrust calibrations. Masses were applied to transducers 1 and 2 corresponding to a maximum expected bending moment at the root of the blade of 16.22 N m. A range of masses, from 0 kg to 30 kg were applied to the lever arm in 18 increments, and then systematically removed in the same increments as they were loaded. Smaller load increments were applied at the lower and upper ends of the range to assess the sensitivity of the readings.

The calibration curves, with the least squares fit and uncertainty bounds, derived for the calibration of axial blade root bending moment are shown in Fig. 3.21.

The method of uncertainty analysis is discussed in Section 3.2.8.

3.2.5 Design of experiment

Scope of tests

The four carriage speeds in this set of test were: 0.5 $\mathrm{m\,s^{-1}}$, 0.8 $\mathrm{m\,s^{-1}}$, 0.9 $\mathrm{m\,s^{-1}}$ and 1 $\mathrm{m\,s^{-1}}$. For each carriage speed, the motor was run at a range of rotational velocities, shown in Table 3.7, to sufficiently populate the rotor performance curves and clearly characterise the performance and load trends of the turbine. This table also details the chord Reynolds number range in the tests for each inflow velocity, calculated for the chord at 70 % of the blade length.

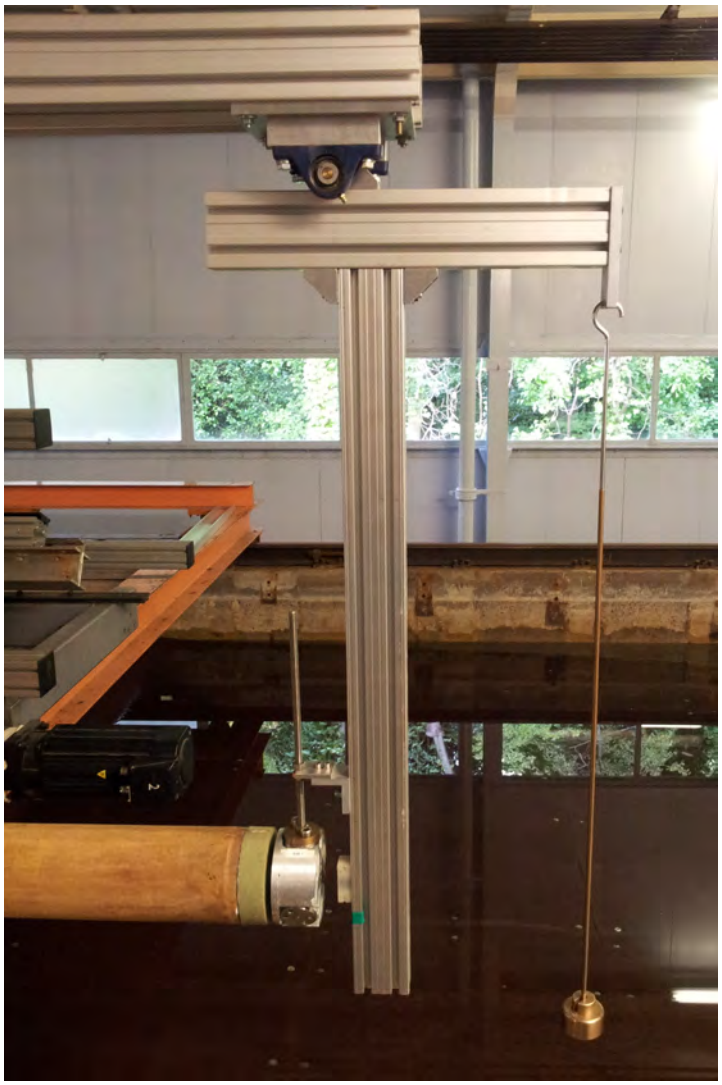

Figure 3.15: Calibration of axial blade root bending moment: the lever system of the calibration station allowed application of axial force to a bar bolted in place of the blade, at a known distance from the hub.

Table 3.7: Test velocity and Reynolds number ranges

$U_\infty(\mathrm{m\,s^{-1}})$	Ω RANGE (RPM)	RE RANGE (-)
0.5	37-88	43,000-95,000
0.8	57-121	66,000-140,000
0.9	69-140	91,000-150,000
1	67-161	99,000-170,000

Best practice

During testing, the voltage readings were converted to measurements in engineering terms using the appropriate form of Eq. (3.6) directly in the DAQ programme. This meant that the live data output was in engineering units, allowing quick identification of trends and any obvious errors during the test runs. A reading of, e.g., thrust force in Newtons is easier to identify and gauge for accuracy than a reading for thrust force in volts.

The test programme was designed observing the requirements outlined in EquiMar Deliverable D3.4, "Best practice for tank testing of small marine energy devices" [108]. Tests were run in a non-sequential order, and were scheduled (blocked) to avoid random errors such as time of day (affecting steadiness of tank), carriage operators (affecting data collection) and tank temperature (varying over the day). By choosing the tow and rotor velocities of the tests at random, it was also ensured that any sources of uncertainty described as "nuisance factors" in the EquiMar document [108] could be eliminated.

Repeatability

To ascertain the repeatability of the tests, a number of repeat runs were performed. In particular one set of conditions, with an inflow velocity of 1 $\mathrm{m\,s^{-1}}$ and rotor velocity of 110.7 RPM, was repeated 5 times.

Additionally, an investigation into the effects of settling time was performed. The advice of the tank technicians was to let the tank settle until "steady to the eye". This length of time was left between two identical tests; an hour's break over lunch was left next; and no break at all was left between the last two runs in this exercise. Analysis of the data for these tests showed that there was no noticeable difference in the mean of the measurements between the hour's break and the "steady to the eye" cases, but that a significant difference was found when no break at all was left between test runs. The test were, accordingly, undertaken with a break until the tank was "steady to the eye" between runs.

3.2.6 Test procedure

The individual steps taken for each test run were as follows:

1. MATLAB was used to produce a motor control curve (voltage waveform text file) corresponding to the desired rotational speed, based on motor calibration between input voltage and output rotational speed. This waveform file was used to ramp up the rotor rotational speed gradually and keep it constant over the test run.

2. Motor control curve was loaded into the DAQ programme, Spike.

3. Data collection was started in Spike and a steady zero reading was obtained for all sensors, obtaining an up-to-date measure of the offsets, while the rotor spun at very low speed.

4. Motor control curve was activated, and the rotor was ramped up to the desired rotational speed.

5. The carriage was ramped up to the desired inflow speed once the rotor rotational speed was steady.

6. The carriage was towed down the length of the tank, and gradually slowed near the end.

7. The rotor was ramped down once the carriage stopped.

8. Spike data collection was stopped, and the carriage was brought back to the starting position.

9. The measured data (torque, thrust, bending moments, rotational and inflow velocity inputs, etc.) were exported as a text file from Spike for post processing.

Motor control and quality checking

During the testing, particularly at higher inflow velocities, some challenges were encountered wherein the motor controller was not able to maintain enough torque to counter the hydrodynamic torque and control the rotor velocity, resulting in a varying torque signal. These issues were resolved and tests in which this occurred were marked in the data collection system, as discussed in the next section on post-processing. Tests were run at inflow speeds of 1.2 and 1.3 $\mathrm{m\,s^{-1}}$ as well as the velocities indicated in Table 4; however, the motor controller instability occurred in most of the tests and the torque output fluctuated, bringing the accuracy of these data sets into question. Time constraints prevented a re-tuning of the motor controller, thus these tests were not repeated and are not reported here.

3.2.7 Post-processing

Data region selection

In data post-processeing, a MATLAB script was written which read the data for the test case and displayed a plot of the torque, the rotor velocity and the carriage velocity against time, from the beginning of the zero region to the end of data capture. This plot allowed the beginning and the end of the zero and steady test regions to be identified and manually defined for each individual test, preventing erroneous automatic selection of test regions. Amongst the data output to text files from Spike, were: a time stamp, voltage data from the proximity switch (at a rate of 1 pulse-per-revolution) and voltage data from the motor encoder feedback (at a rate of 10 pulses-per-revolution). As for the

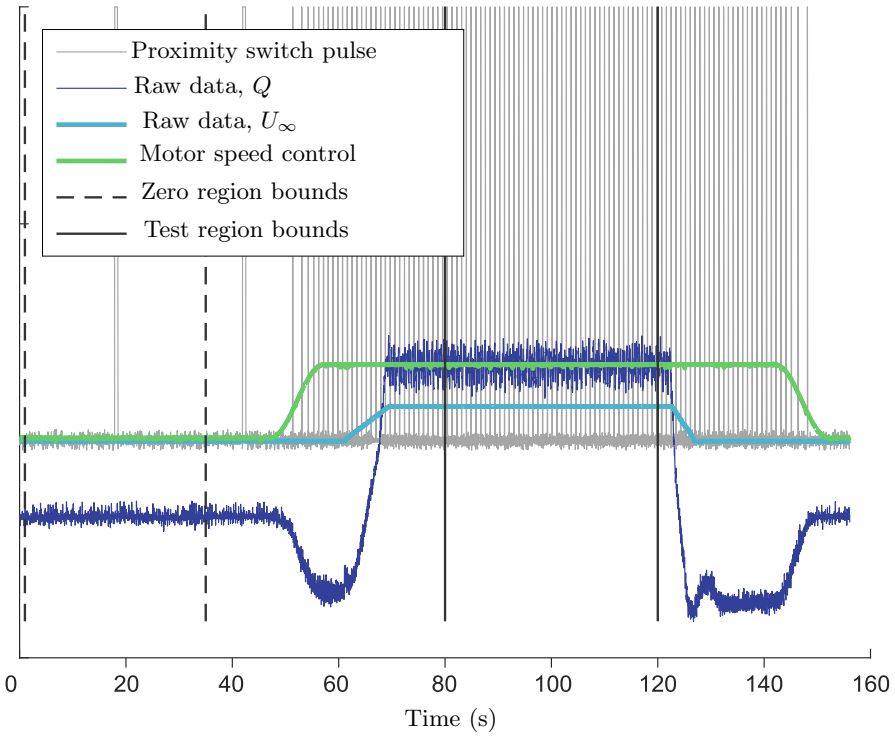

Figure 3.16: Test region selection method: example of (unfiltered) test data showing manually-selected zero and steady test regions. Data signals shown represent the required information to make an informed choice of cut-in and cut-out points.

tests in the wind tunnel, it was possible with this data to define when a new revolution of the rotor began, by converting the 1-pulse-per-revolution data stream to a binary pulse form. With this information, the user-defied beginning and end times of the zero and steady test regions were then corrected by the code to occur at the beginning of the closest subsequent rotor rotation. This allowed the recorded values to be averaged with confidence, avoiding any miscalculation of the mean values due to either the slight misalignment of the shaft or to the changing buoyancy forces on the blades. Fig. 3.16 gives an example of data captured during the tests, illustrating the method of region selection. The binary proximity switch pulse data particularly guided the selection of the zero region such that a full rotation would be captured after the script's automatic re-positioning of the cut-in and cut-out points according to pulse location.

Zero values

The zero region, taken at the beginning of each test - during which the carriage was completely still and the motor turned at 3 RPM - was used to calculate the offest or zero values. The motor was turned very slowly in this period to allow misalignments and buoyancy forces to be recorded in order that

- the changes could be negated over a full revolution by taking the mean value; and

- the sinusoidal effects of each could be characterized (and, if required, removed) for any use of the data which required time or frequency-domain information.

With the exception of the rotor velocity, it was assumed that the mean values of the recorded data were zero at this very low rotational speed and that, due to the care taken to ensure appropriate calibration and amplification factors, all noise in the data was Gaussian and could therefore be assumed to be zero over the mean.

The zero values of the measurements taken were offset values; the removal of these corrected for any drift or alterations in the base values.

Moving average rotor velocity

The binary pulse signals and the time stamp were used to provide a moving average recording of the rotor velocity. The time between each revolution, dt_{rev}, was found, and the moving average rotational velocity, Ω_{avg}, was calculated from:

$$\Omega_{\text{avg}} = \frac{60}{dt_{\text{rev}}} \ . \tag{3.7}$$

Plotting the Ω_{avg} array against time values taken at the start of each rotor revolution allowed a visual check on the steadiness of the rotor, which was important due to the challenges experienced with the motor controller during the testing.

The standard deviation of Ω_{avg} was calculated and recorded using both the proximity switch data and the 10 pulses-per-revolution data. The higher frequency pulse data was at a higher resolution, and therefore gave a good indication of whether there had been substantial instability in the motor controls. However, the proximity switch-derived rotational speed was used to record the rotor velocity and its standard deviation. The standard variability of this reading was used to express the uncertainty in the measurement of rotor velocity:

$$\mu_{\Omega} = \text{std}(\Omega) \ . \tag{3.8}$$

High values of μ_{Ω} indicated that there might have been motor controller issues during the test run in question. This method of data processing identified each of the test runs in which highly varying torque signals were observed. All other tests with high values of μ_{Ω} were identified and looked at in detail; tests which also showed variations in torque were discarded. This meant that the final processed data set only contained data which had not been affected by the issues experienced with the motor controller.

Data reduction

The data streams, corrected for offsets, were put into the appropriate data reduction equations, as detailed in Eqs. (2.2) and (2.5). For each test, the means of these data were taken, giving the required performance characteristics.

3.2.8 Uncertainty analysis

The uncertainty associated with the calculated parameters, caused by the bias and precision uncertainties in the instruments, was calculated.

Uncertainty analysis of calibration process

As for all calculations, there was uncertainty associated with the recorded values. To reduce this uncertainty as much as possible, and to quantify the final uncertainty in the performance characteristics, the precision and bias uncertainties associated with the calibration and data reduction processes were calculated. The calibration of torque, Q, is used as an example for the uncertainty analyses method employed.

During the calibration process, the calibration the equation - of which the general form was Eq. (3.6) - was obtained. This gave a highly linear calibration curve, well-fitted to the data. The uncertainty in the linear regression analysis of the scatter data was obtained following The International Towing Tank Conference (ITTC) and The National Institute of Standards and Technology (NIST) recommendations, as noted in the following discussion.

In the ITTC recommended Procedures and Guidelines document, "Uncertainty Analysis Instrument Calibration" [110] the ITTC defines the summed square of residuals (SSR) as:

$$x_{\mathrm{SSR}} = \sum_{i=1}^{n} (y_i - a - bx_i t)^2 \ , \tag{3.9}$$

where x is the known value, y is the measured value, there are n sample points, i is the sample number, and a is the constant and b the gradient of the line. The document states that the standard error of estimate, SEE, is "a measure of the standard deviation for the linear regression analysis", which is defined as:

$$x_{\mathrm{SEE}} = \sqrt{\frac{x_{\mathrm{SSR}}}{n-2}} \ . \tag{3.10}$$

Applying the ITTC method to the calibration, the precision uncertainty associated with the linear regression method of calibration of torque, $\mu_{\mathrm{Pcal,Q}}$, was determined from:

$$\mu_{\mathrm{Pcal,Q}} = Q_{\mathrm{SEE}} \ . \tag{3.11}$$

The bias uncertainty in torque, resulting from sources such as the uncertainty in the mass of the weights used, was calculated by the law of propagation of uncertainty, as detailed in the Engineering Statistics Handbook from NIST [111], and outlined in EquiMar Deliverable D 3.4 [108]. This method allows uncertainties in the variables influencing a measured value to be carried through to that final value, according to the influence that each uncertainty has on the measurement. For example, for a function, f, of multiple variables, $x_i, x_{ii} ... x_n$, which can be assumed to have no covariance, the

uncertainty in the calculated value of f is found from:

$$\mu_f = \sqrt{\left(\frac{\partial f}{\partial x_i}\right)^2 \Delta x_i^2 + \left(\frac{\partial f}{\partial x_{ii}}\right)^2 \Delta x_{ii}^2 + ... + \left(\frac{\partial f}{\partial x_n}\right)^2 \Delta x_n^2} \ , \tag{3.12}$$

where the finite differences, Δ, describe the uncertainty in the variable. Dividing this by the original expression, f, gives the fractional uncertainty in the measured value.

When applied to the calculation of uncertainty in torque, the function equation was the data reduction equation for the calibration of torque:

$$Q_{\text{app}} = mgl \ . \tag{3.13}$$

In this application, the finite differences were the bias uncertainties, μ_{B}, for each variable. The values of these are detailed in Table 3.8. The expression giving uncertainty in Q was, therefore:

$$\mu_{\text{BQ}} = \sqrt{\left(\frac{\partial Q}{\partial m}\right)^2 \mu_{\text{Bm}}^2 + \left(\frac{\partial Q}{\partial g}\right)^2 \mu_{\text{Bg}}^2 + ... + \left(\frac{\partial Q}{\partial l}\right)^2 \mu_{\text{Bl}}^2} \ . \tag{3.14}$$

Calculation of the partial derivatives yielded:

$$\mu_{\text{BQ}} = \sqrt{(gl)^2 \mu_{\text{Bm}}^2 + (ml)^2 \mu_{\text{Bg}}^2 + (mg)^2 \mu_{\text{Bl}}^2} \ . \tag{3.15}$$

Dividing Eq. (3.15) by the original expression for torque, Eq. (3.13), gives a simplified expression of the uncertainty as a fraction of the torque:

$$\frac{\mu_{\text{BQ}}}{Q_{\text{app}}} = \sqrt{\frac{\mu_{\text{Bm}}^2}{m^2} + \frac{\mu_{\text{Bg}}^2}{g^2} + \frac{\mu_{\text{Bl}}^2}{l^2}} \ . \tag{3.16}$$

The bias uncertainty in the calibration of torque, μ_{BQcal}, was then calculated (in N m) by multiplying Eq. (3.16) by the mean torque applied in the calibration process, $\bar{Q}_{\text{cal}}$. Thus,

$$\mu_{\text{BQcal}} = \bar{Q}_{\text{cal}} \sqrt{\frac{\mu_{\text{Bm}}^2}{m^2} + \frac{\mu_{\text{Bg}}^2}{g^2} + \frac{\mu_{\text{Bl}}^2}{l^2}} \ . \tag{3.17}$$

Combining the precision and bias uncertainties according to the method outlined in EquiMar Deliverable D3.4 [108], the total uncertainty, in N m, associated with the calibration of torque was defined by:

$$\mu_{\text{Qcal}} = \sqrt{\mu_{\text{PQcal}}^2 + \mu_{\text{BQcal}}^2} \tag{3.18}$$

Table 3.8: Bias values in calibration of torque

Measurement	Source of bias	Bias value
Mass, m (kg)	Mean bias of mass weights used	0.015
Gravitational constant, g ($\mathrm{m\,s^{-2}}$)	Measurement uncertainty	0.001
Moment arm, l (m)	Smallest division on measurement instrument	0.0005

Table 3.9: Calculated uncertainty in calibration of instrumentation

Variable	Mean value	Uncertainty values		
		Precision	Bias	Combined
Q(N m)	6.799	0.067	0.043	0.080
F_{T}(N)	83.98	0.680	0.029	0.681
M_y(N m)	3.599	0.025	0.016	0.030
M_x(N m)	1.987	0.025	0.020	0.032

Calculated uncertainty values

The uncertainty in each of the measurements for which a calibration process was undertaken was found in this manner. The uncertainty values for each measured variable are given in Table 3.9. The data in Table 3.9 showed that the combined uncertainty in the calibration of each instrument was two orders of magnitude smaller than the associated mean value of that measurement, giving good confidence in the calibration process.

Uncertainty analysis for performance characteristics

For each test run the uncertainty in the final results, caused by the bias and precision uncertainties in the instruments, was calculated. The method of propagation of uncertainty, as previously described, was used. Taking the uncertainty analysis for C_{P} as an example, the uncertainty, $\mu_{C_{\mathrm{P}}}$, was given by the squared total derivative of the expression of uncertainty in C_{P}, divided through by the original expression for C_{P} (Eq. (2.3)):

$$\mu_{C_{\mathrm{P}}} = \sqrt{\left(\frac{\mu_{\mathrm{Qcal}}}{\bar{Q}_{\mathrm{cal}}}\right)^2 + \left(\frac{\mu_{\Omega}}{\bar{\Omega}}\right)^2 - \left(\frac{\mu_{\rho\mathrm{B}}}{\rho}\right)^2 - \left(\frac{\mu_{\mathrm{A}}}{A}\right)^2 - \left(\frac{3\ \mu_{U_\infty \mathrm{B}}}{\bar{U_\infty}}\right)^2}\ \bar{C}_{\mathrm{P}}\ , \tag{3.19}$$

where the mean values were the average values of those measurements made during the steady region of that particular test run. This gave the uncertainty in the calculated value for C_{P} in the appropriately nondimensionalised units.

The same process was undertaken for each of the required results detailed in Table 3.4.

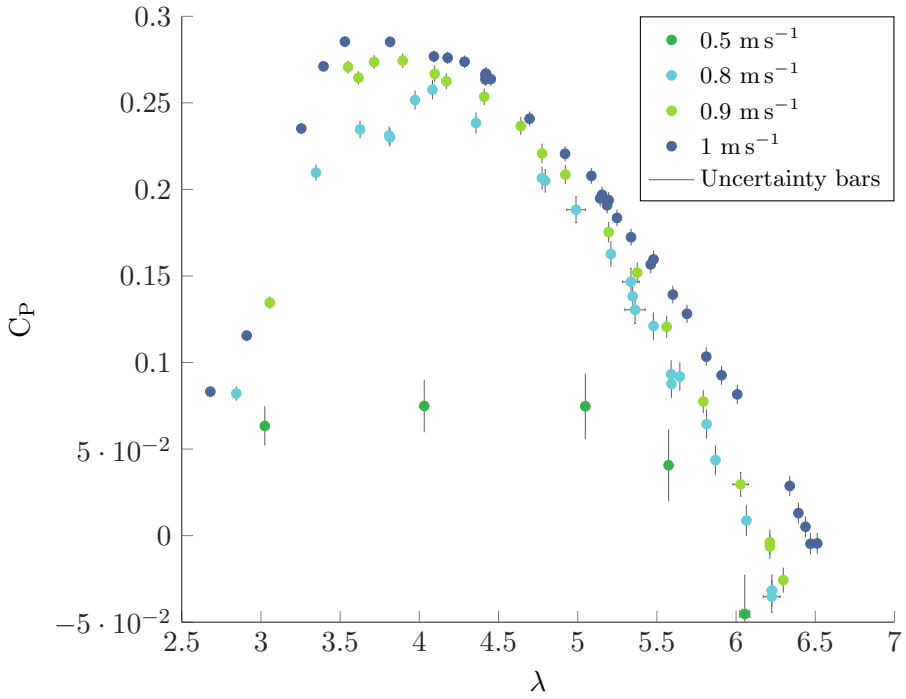

Figure 3.17: C_P-λ plot of tow tank results, showing uncertainty bars in each axis.

3.2.9 Results

The results are fully presented in tabular form in **??**.

Mean value results

Fig. 3.17 shows the series of C_P-λ curves obtained at the three carriage speeds. The uncertainty bars are also plotted, each for C_P and for λ. Fig. 3.18 shows the series of C_T-λ curves obtained at the three carriage speeds. Again, for each data point the combined uncertainty in both C_T and λ are shown with error bars.

Fig. 3.17 shows a general trend for each of the four tow velocities presented, with some mild scatter in the data. In the higher tow velocity tests, 0.8 m s^{-1} to 1 m s^{-1}, the efficiency of the rotor increased with increasing λ, peaked and then began decreasing. The peak efficiency occurred at an optimum λ of 4.08 for the 0.8 m s^{-1} tests, with a C_P of 0.263; at a λ of 3.90 for the 0.9 m s^{-1} tests, with a C_P of 0.274; and at a λ of 3.53 for the 1 m s^{-1} tests, with a C_P of 0.285. A noticeable factor in the results is significantly degraded performance at 0.5 m s^{-1}. Due to this, many fewer tests were run at this speed. The possible reasons behind this will be discussed in Section 3.2.10. The efficiency of the rotor presented here is well below Betz limit of 0.59, which is due to the non-optimal pitch setting of the blades as discussed further in the following section.

Fig. 3.18 showed that the C_T for the rotor increased steeply before levelling off and peaking at a λ of approximately 4.5, after which C_T decreased to about 0.40. Comparison between the plots of C_P and C_T showed that, for each flow speed, the peak

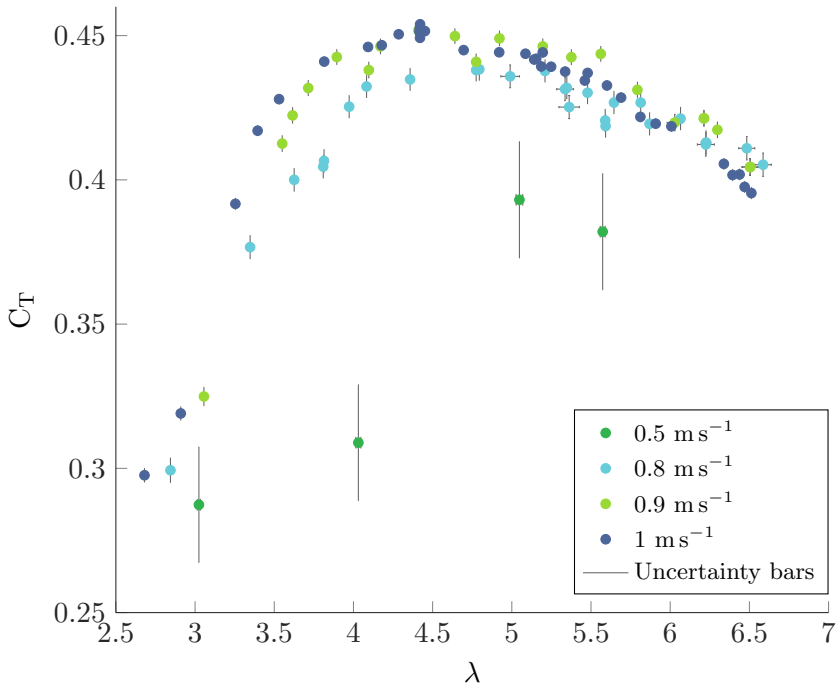

Figure 3.18: C_T-λ plot of tow tank results, showing uncertainty bars in each axis.

power capture efficiency of the rotor roughly coincided with the transition from steep to more shallow increase in C_T.

Figs. 3.19 and 3.20 show the axial and radial root bending moment coefficients with uncertainty bars. As shown in Fig. 3.19 the coefficient of axial bending moment increased steeply from 0.042 at the lowest λ, to 0.081 at a λ of 3.5, a 93% increase. For λ between 3.5 and 6.4, there was a relatively small increase in bending moment coefficient (1.34 % increase). Fig. 3.20 illustrates that the coefficient of bending moment decreased initially until λ of about 3.5, then increased continuously, reaching a maximum of 0.014 at a λ of 6.5.

The data for the 0.5 m s^{-1} tests are thought to be outlying to such a degree due to Reynolds number effects and potentially other phenomena in the flow, which are discussed further in Section 3.2.10

Uncertainty value results

With the exception of the uncertainties for the 0.5 m s^{-1} tests, the uncertainty bars shown in Figs. 3.17 to 3.20 are quite small and therefore difficult to see, illustrating the high certainty achieved in the data. The uncertainty values are included in the tabulated result given in Table A.1, in Appendix A. There was a greater percentage uncertainty in all tests at the lower mean values; this is particularly clear in the results for C_P and C_T. This was to be expected due to the uncertainty analysis method; smaller mean measured values will tend to give larger percentage uncertainty due to the decrease in the ratio of mean value to the uncertainty values which are often dominated by

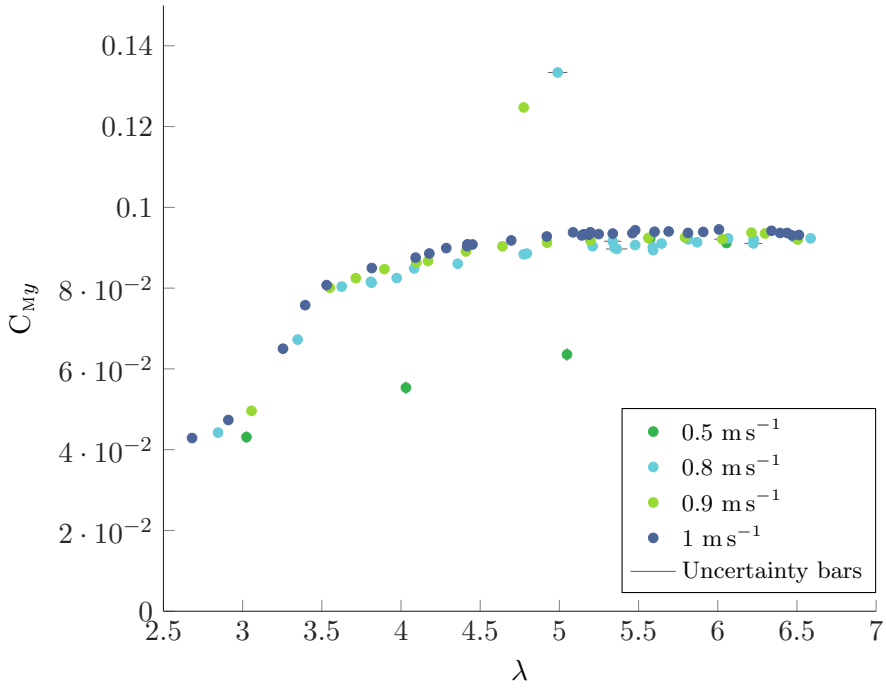

Figure 3.19: C_{My}-λ plot of tow tank results, showing uncertainty bars in each axis.

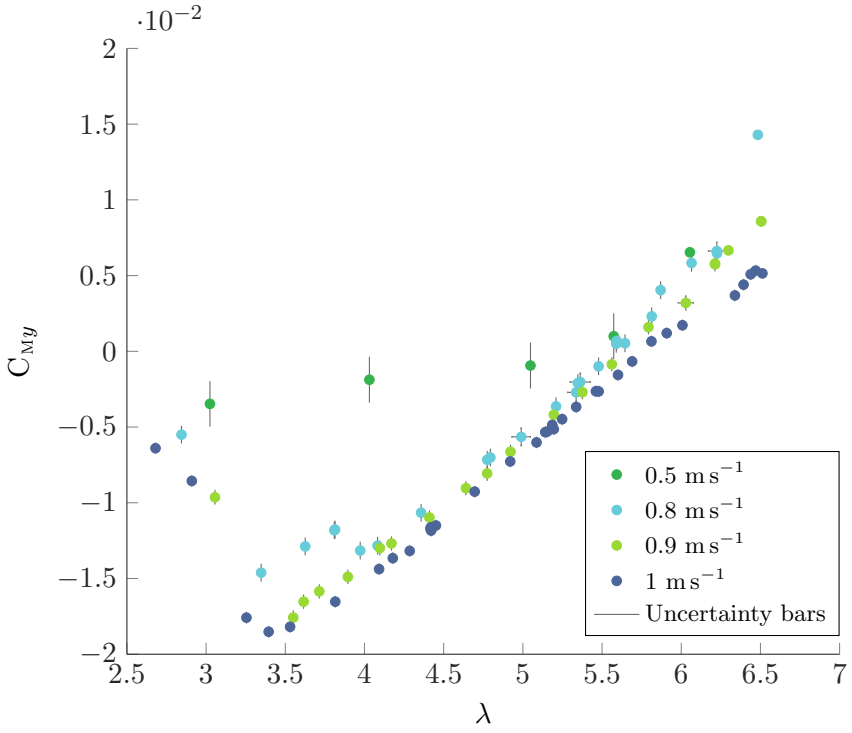

Figure 3.20: C_{Mx}-λ plot of tow tank results, showing uncertainty bars in each axis.

calibration uncertainty. This is the explanation for the high uncertainty in the 0.5 $\mathrm{m\,s^{-1}}$ tests.

However, U_{C_P} was less than 5 % for tests below a λ of 5.3 in the 0.8 $\mathrm{m\,s^{-1}}$ tests, below 5.5 for the 0.9 $\mathrm{m\,s^{-1}}$ tests and below 5.8 for the 1 $\mathrm{m\,s^{-1}}$ tests. This gave an overall uncertainty in the C_P values of less than 5% for 87% of the tests; the uncertainty of the test run with maximum uncertainty in C_P, expressed as a percentage of the optimum C_P value, was 3 %. For the 0.5 $\mathrm{m\,s^{-1}}$ tests, the Cp values were all very low and the uncertainty was therefore a larger percentage of those Cp values, driven by the unchanging uncertainty calibration values, particularly the calibration uncertainty in Q.

The uncertainty in C_T and λ was consistently under 1.7%, illustrating the high quality of the data.

Figs. 3.19 and 3.20 shows that the uncertainty in these measurements was very low in general. The uncertainty bars are barely visible for many of the tests. The uncertainty in C_{M_y} was consistently less than 1.4% for over 93% of the tests. C_{M_x} had the largest percent uncertainty; over 15% for 37% of the tests. As Table 3.10 shows, the combined uncertainty in the calibration of the radial blade root bending moment, C_{M_x}, was of the same order of magnitude as that of the axial blade root bending moment, C_{M_y}; however, the measured radial bending moments were small, making the percentage uncertainty much higher than for the other measurements.

3.2.10 Discussion

Uncertainty in blade pitch setting

The uncertainty in the blade pitch angle was calculated based on the translation between measurements made with the physical test set-up, including the blades, and the CAD model. A machining tolerance of 0.005 m existed for each dimension of the blades. When taken into consideration in the method used to set and quantify the pitch angle, along with the tolerances on the machined hub, this gave an uncertainty in the measurements used to define the angle of ±1 mm in each the axial and radial direction. The combination of the foregoing analysis and the BEMT prediction of the test data allowed the uncertainty in the blade root pitch setting to be reduced. As Fig. 4.4 shows, the BEMT slightly under-predicted the data, indicating that only the upper half of the uncertainty band was relevant in quantifying the uncertainty in the pitch setting; logic therefore allowed uncertainty value of ±1.76 ° to be reduced by half. This uncertainty was therefore reduced to a band the size of the upper window, giving the blade pitch setting with uncertainty as $\beta = 28.9\ \pm 0.88$ °, as reported in Table 3.5.

Data quality

Some of the known limitations of small-scale testing which can influence the quality of data include blockage ratio, noise in the data, carriage shake, speed tolerances and uniformity and the length of testing time at constant speed.

The blockage ratio is the ratio of the device rotor area to the channel cross-sectional area, and has importance in quantification and application of the coefficients of thrust and power, whether at full-scale or in scale-model HATSTs. Methods exist to correct for significant blockage. Gaurier et al. reported blockage ratios of 7.95 % [112], and Milne et al. reported blockage ratios 4.7 % [109], both of which were considered low and no correction to the experimental data was deemed necessary. For this system, the rotor-tank blockage ratio was 4.47 %; evidence from the literature suggested that it was not necessary to apply any correction.

A small amount of noise was captured in the data; however, because of the nature of the noise and because care was taken in the post processing to ensure the data sets were cut in and out at the same point in the angular displacement of the rotor, the noise was of equal amplitude above and below the data mean. Therefore it was possible to take the mean values of the data captured without applying a filter.

Carriage vibrations, speed tolerances, and uniformity can all affect the quality of captured data by influencing accuracy of speed control and the length of time with constant speed. However, the uncertainty in λ, which has previously been discussed to have been consistently below 1.7%, shows that the quality of the carriage velocity and rotor speed did not have a negative influence on the test results. Fig. 3.16 shows the output data from one of the 0.8 $\mathrm{m\,s^{-1}}$ tests, run with a rotor velocity of 67 revolutions per minute (RPM). As Fig. 3.16 indicates, the zero and steady bounds were manually defined as 2 s and 35 s, 80 s and 120 s respectively. With the automatic shift to the end of the subsequent rotation implemented by the processing script, this gave a total zeros time of 24 s and a total test time at steady carriage and rotational velocities of 40 s. Due to the high frequency of data capture, and the length of time at steady state in the tow tank facility, it was thus possible to obtain large sample numbers. This ensured that the effect of any fluctuations would be negated over the test period. From this figure it can be seen that both the carriage speed and the motor rotational speed input were maintained at steady values over the steady region. As discussed, during the data processing, it was ensured that the final data sets contained only those tests for which the measured rotor velocity was of a low standard deviation. These measures were undertaken to maximise the reliability of the presented data sets.

As mentioned in Section 3.2.4, there were two strain gauges designed to measure M_y, and one of these was thought to be malfunctioning. Fig. 3.21 shows the plots of calibration curve with uncertainty for both these gauges. Though the calibration curves were somewhat similar, there was an obviously greater scatter of data from the calibration of the gauge on Bar 2, and the uncertainty bounds were wider. Numerically, the analysis showed that the combined uncertainty in calibration of Bar 1 was 0.0301 N m, whereas for Bar 2 it was an order or magnitude bigger, at 0.2055 N m. This allowed the data from Bar 2 to be discounted in the post processing, and all axial blade root bending moments data were taken from the Bar 1 data stream.

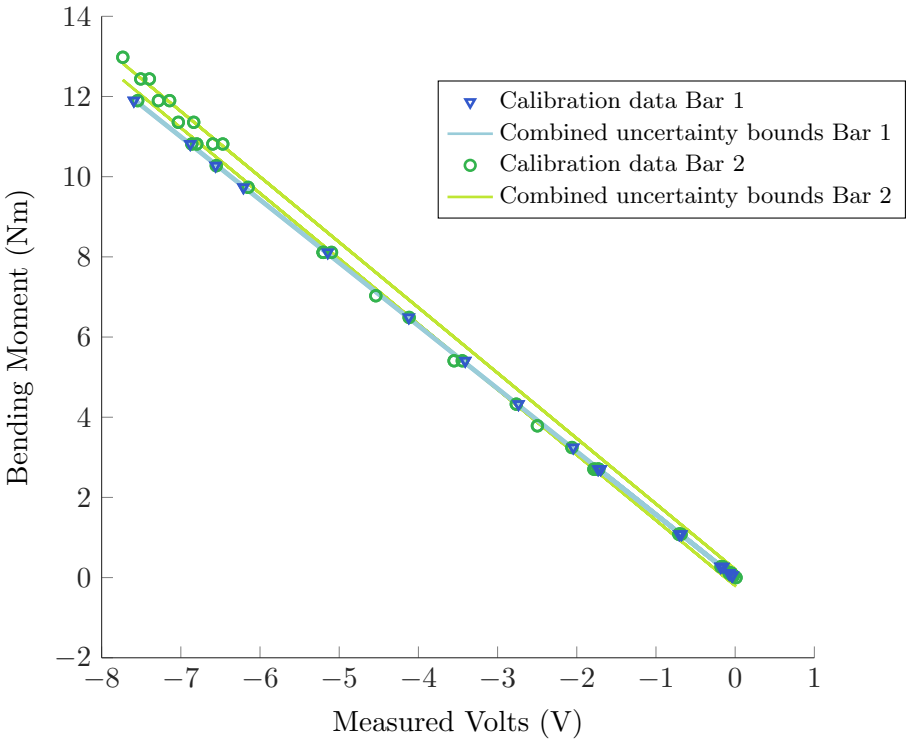

Figure 3.21: Calibration plots for axial blade root bending moment strain gauges; showing similar calibration curve and differing scatter and uncertainty bounds.

Repeatability

An analysis of the repeatability of the tests was undertaken, in which the standard deviations of C_{P}, C_{T}, C_{M_x}, C_{M_y} and λ for the 5 repeated tests were compared with the minimum uncertainty in the test sets, for each variable. Table 3.10 shows the minimum calculated uncertainty and the standard deviation for each parameter over the 5 tests.

The repeatability analysis showed that, for each of the performance characteristics, the standard deviation of the values in the set of repeated tests fell within the bounds of the known uncertainty associated with that value. Comparing the standard deviation to the minimum uncertainty facilitated the most conservative analysis of the repeatability, and thus it was found that the tests were highly repeatable.

Impact of Reynolds number and fluid dynamics effects

The effects of Reynolds number on the turbine's performance were most obvious between the results of the 0.5 $\mathrm{m\,s^{-1}}$ tests and those obtained at higher carriage speeds. The C_{P}-λ curve shown in Fig. 3.17 showed the effects most clearly, wherein the maximum efficiency and runaway position each increased with increasing carriage velocity. The peaks of the C_{P} and C_{T}-λ curves converged somewhat, as the inflow speed increased. As detailed in Table 3.7, the Reynolds number varied from 4.3×10^4 to 1.7×10^5 over the range of tests. As discussed in Section 2.2.3, while the precise effects of Reynolds number on an aerofoil are difficult to predict, it is well understood that, in general,

Table 3.10: Results of the repeatability analysis: comparison between calculated uncertainty and experimental scatter, expressed as standard deviation in values for a test repeated 5 times.

Performance characteristic	Minimum uncertainty	Standard deviation
C_{P}	0.0044	0.0013
C_{T}	0.0039	0.0017
λ	0.0077	0.0014
C_{M_y}	0.00038	0.000075
C_{M_x}	0.00063	0.00017

Table 3.11: Base case blade: test values for increase in λ and Ω from optimum operating point to runaway.

Carriage speed ($\mathrm{m\,s^{-1}}$)	λ_{O}	λ_{R}	$\Delta\lambda_{\mathrm{OR}}$	Ω_{O} (rpm)	Ω_{R} (rpm)	$\Delta\Omega_{\mathrm{OR}}$ (rpm)
0.5	4.5	5.8	1.3	56.4	72.7	16.3
0.8	4.1	6.1	2	81.9	122.3	40.4
0.9	3.9	6.2	2.3	87.9	139.7	51.8
1	3.5	6.5	2.9	88.5	161.8	73.3

as the Reynolds number increases the effect produced on aerofoil performance is an increase in maximum efficiency. Higher Reynolds numbers are defined by the dominance of inertia forces; in such flow regimes, the boundary layer has and/or entrains enough energy from the free stream that it can remain attached to the body for longer as α, and thus the lift force, increase.

As Table 3.11 shows, the Reynolds number and inflow velocity had a clear influence on the position of the runaway point on the λ axis. As the inflow velocity increased, the required increase in rotor velocity to reach zero C_{P} from the optimum operating point increased. The percentage increase was 29 % at 0.5 $\mathrm{m\,s^{-1}}$ (taking the estimated 4.5 as the optimum λ), 48 % at 0.8 $\mathrm{m\,s^{-1}}$, 59 % at 0.9 $\mathrm{m\,s^{-1}}$, and 86 % at 1 $\mathrm{m\,s^{-1}}$. This indicates that, for a turbine operating outwith any *Re*-independence, the larger the range in inflow velocities the turbine undergoes, the larger the increase in rotational velocity between the optimum and runaway points - and thus, the larger the increase in voltage and the likelihood of cavitation inception.

As discussed in Section 2.2.3, Lissaman discussed that the effect of laminar separation and reattachment is to decrease the aerofoil efficiency [32]. In empirical investigations on the performance of the NREL S814 aerofoil at similar Reynolds numbers as those in this set of tests, Milne found that a laminar separation bubble formed, often on both surfaces, affecting and degrading the performance [35]. It is possible that this phenomenon may have had an effect on the performance of the rotor in these tests, both in terms of the clear decrease in efficiency with decreasing carriage speed, and in terms

of the difficulty in using some of the available aerofoil data to predict the performance in BEMT. This latter issue will be discussed in Section 4.2.5.

Limitations of test setup

The main limitation was the ability to adjust the pitch setting of the blades, as they were fixed to the hub rigidly by two bolts, as shown in Fig. 3.8, and a pin locator. This limited the tests to being performed at a single pitch angle, which was not the optimum pitch setting for the rotor and test conditions. Therefore, this set of tests have limited applicability in the assessment of the tested NREL S814 blades as far as optimised tidal turbine performance goes. However, this was not the aim of these tests.

A further limitation of the set-up was that the bolts and weld of the blade root connection affected the flow in this region. This resulted in a 0.013 m section of the blade root for which the performance of the aerofoil was questionable. For this reason, the blades were assumed to be of functional length from the upper edge of the bolts, as shown in Fig. 3.8, giving the quoted blade length of 0.292 m.

3.2.11 Implications for operation in overspeed

The increase in Ω and λ between the optimum and runaway points were calculated. Linearly interpolating between the two points closest to the C_P axis, λ at the runaway point, λ_R was inferred for each flow speed. The values of ΩR were then obtained from Eq. (2.5). The actual values and increases from optimum to runaway are detailed in Table 3.11. Note that Ω is here expressed in RPM.

The values of $\Delta\lambda_{OR}$ for this tested turbine, around 2, were slightly larger than the values for the turbine tested in the wind tunnel, around 1.6, as reference to Table 3.3 will show. The voltage increases measured in the wind tunnel test were all over 125 %; this indicates that similar, if not slightly larger, increases in voltage would be expected for the tested turbine in the tested flow conditions.

3.2.12 Conclusions

At full scale, within a region of Re-independence, the proportionally larger increase in Ω required to regulate power capture by producing an increase in λ with increasing U_∞ would result in higher and higher voltages as the required operating U_∞ increased.

A repeatable, empirical dataset with quantified uncertainty was produced. Uncertainty analyses were undertaken to give confidence in the methods and the bounds of the data. The uncertainty in the measurements was found to be less than 5 % for over 85 % of the tests. This data achieved the aims which were set out, and allowed a base case blade and performance to be established, as well as a BEMT script to be verified for use in this project as a blade design tool.

The effects of the Reynolds number were clearly seen between the presented test sets. While this effect is significant for scale testing or small-scale devices, it should be

noted that at full-scale, the Reynolds numbers are sufficiently high that the effect ceases to have a significant impact on turbine performance.

The effects of operating this turbine in the overspeed region were increases in the rotational velocity characterised by increases in 2 to 3 λs, between the optimum operation point and runaway. The expected consequence of this would be higher voltages (as demonstrated in the wind tunnel experiments), high thrust forces, and an increased likelihood of cavitation. Having established a base case performance, the next step was to undertake an investigation of how these challenges to OSPR might be overcome. As previously discussed, the driving factor for the increase in voltage and cavitation risk is the increase in rotational velocity. It is, therefore, this factor which should be curtailed.

Chapter 4

Development of methodology

4.1 Introduction

The previous chapter concluded that the main challenges to OSPR for tidal turbines are likely to be increases in voltage, higher thrust loads and increased likelihood of cavitation on the rotor. While the levels of voltage experienced in a turbine are a function of the rotor speed, the design choices made with regards to gearbox, generator and power electronics are also heavily influential on the condition of the electrical variables (voltage, phase and frequency etc.). As this research makes no assumptions on these design choices, further quantitative analysis of voltage levels was beyond the scope. De-coupling the rotor design from the generator design in this way had the advantage of removing constraints from the rotor design process, but the disadvantage of requiring further design stages for a proposed turbine topology. The objective of this research, however, was not to design a whole turbine topology, but to increase the understanding of how the challenges of OSPR may be overcome through rotor design.

For these reasons, the issue of voltage, while unavoidably influenced by the rotor speeds resulting from rotor design, and thus mitigated or exacerbated accordingly, was not considered in the numerical analysis of turbine performance which forms the basis of the design methodology. The goals of this methodology are to facilitate the design of blades which maintain high values of optimum C_P, while resolving the discussed challenges by reducing the maximum rotor velocity. To achieve this, the methodology considers the criteria of importance in blade design noted in [113] – hydrodynamic, geometrical, structural and deployment site parameters – and also takes into account the proposed operating methodology. Considering the operating or control method within a blade design methodology has been previously done in such fore-going work as that undertaken by NREL, reported in [91], as well as in the projects discussed in 2.5.2. However, the unique aspect of the work presented in this thesis is that, due to the afore-mentioned consequences of overspeeding a rotor, this methodology takes account of the rotational velocities expected in the system. The maximum operational rotational velocity and the blade-wide cavitation behaviour are integral aspects of the new design

process. Furthermore, the methodology is explicit in its analysis and presentation of the impact of alterations made to performance by design changes: the impact made on cavitation inception, blade efficiency, thrust coefficient and the shape of the C_P-λ curve are determined and shown for each blade design iteration.

The investigation is based on a full-scale design platform which provides design constraints and can be altered according to any existing design requirements. The investigation compares the performance of altered blade designs to a base case, and measures the impact made on suitability for OSPR. The relative flow scenarios in the range of turbine operation from just after cut-in to just before cut-out are considered.

This chapter focuses on the development of this blade design methodology.

4.1.1 Diagrammatic outline of the design methodology

A brief overview of the blade design methodology was given in the introduction to the thesis. The design flow diagram of Fig. 4.1 represents the methodology, illustrating the flow of work and information, and the manner in which how each of the component parts are related.

Fig. 4.1 shows that the inputs of the methodology are in two main categories, set and variable input parameters, giving the design constraints and the design variables. The design constraints, or boundary conditions, are split into the base case blade and aerofoil shapes, and the variables of the design platform. The base case blade information is used as a realistic starting point from which all other blade designs develop and against which they are measured. At this stage, the aerofoil data was not altered and was therefore defined as a set variable. The design platform defines the simulated flow environment and the remaining rotor variables; this constrains the design problem, allowing assessment of the impact of blade design to be investigated numerically.

The performance of each blade permutation, including of the base case blade, is determined by the BEMT tool. In the first run of the tool, a shortened route is taken while the base case blade design is analysed. This design loop is shown with grey arrows (except for on shared paths) and allows the design requirements to be determined with regards to how a current rotor design performs in OSPR. From these design requirements and the base case rotor performance, the OSPR performance metrics are defined. This shortened loop then goes straight to the process of making blade design alterations; these should be function-based alterations at this stage - and the next few stages - to minimise processing/design time and maximise blade permutations attempted by minimising human bias. The altered blade designs are then fed back into the BEMT code as new blade design iterations. The impact made by each alteration is found in the design analysis, based on the OSPR metrics and the design platform. The design analysis results are then output into the design space and the visual-numerical tools of the cavitation and diagnostic plots. This information is an output of its own, experientially-obtained knowledge which can be stored and passed on to others. It is also used in the subsequent

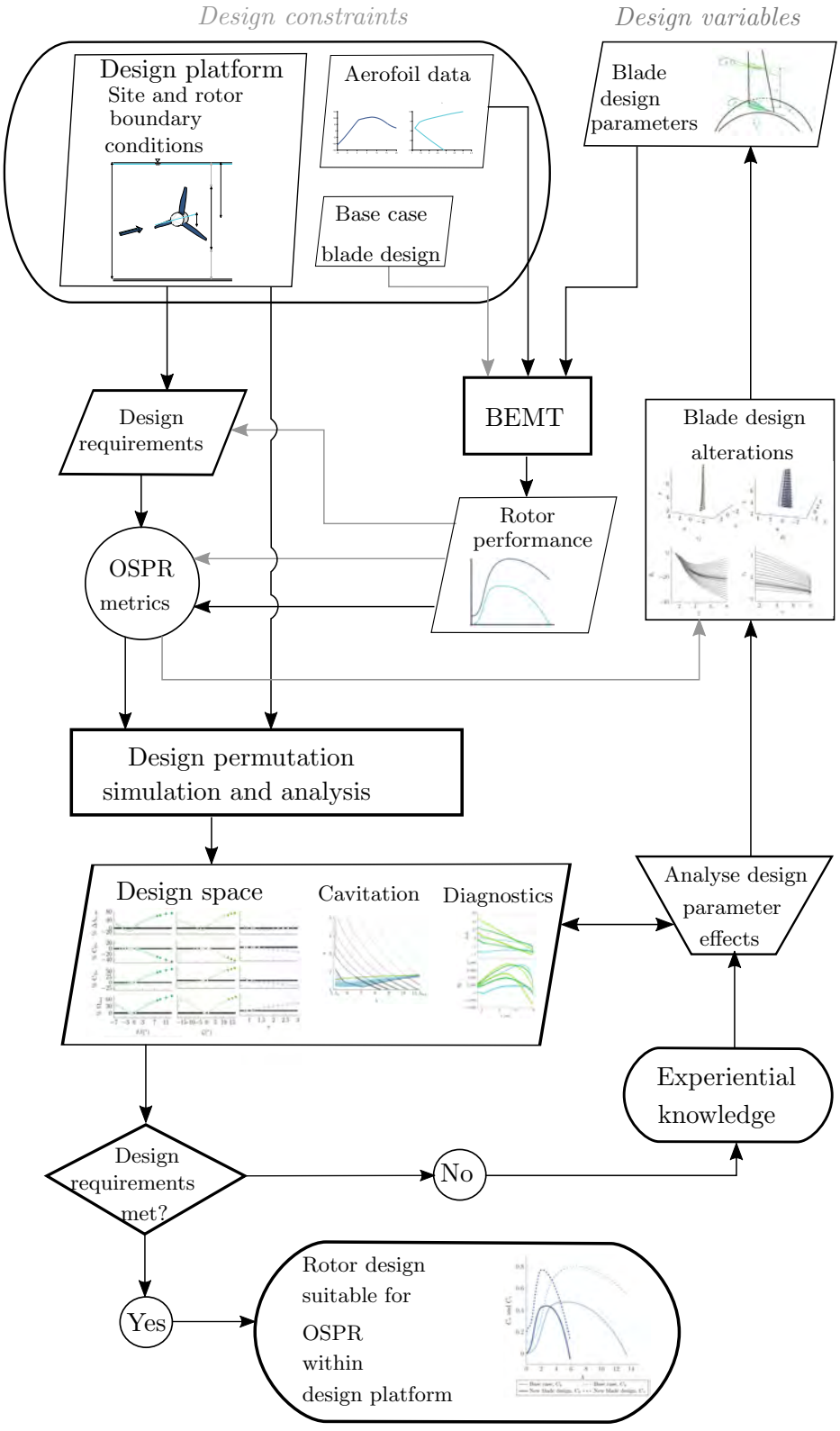

Figure 4.1: Design flow diagram: describes the design methodology in a flow-chart, illustrating the flow of information, input and output data, processes and decision points. The base case information and work flow is depicted with the grey path; this path is run once only for any given design process.

design loops. As Fig. 4.1 shows, once a decision has been made as to whether the design requirements have been met with any of the blade design parameter iterations, a *yes/no* answer is obtained. A *no* answer feeds into a manual process in which the effects of blade design parameter alterations are determined. The design space, cavitation and diagnostic visual tools are here employed once again in a two-way process which informs the assessment of blade design parameter effects. Subsequent design alterations are thereby based on the effects of the last. The new design alterations are then input as blade design parameters into the BEMT tool. As the design flow continues and blade designs become increasingly close to meeting the design requirements, new blade design alterations will probably progress to informed hand-alterations. The process continues until a *yes* answer can be returned and a rotor design is achieved which, operated within the design platform, meets the design requirements.

The details of each component section of the methodology will be focused on in turn in this chapter, in Section 4.2 to Section 4.7.

4.2 Blade element momentum theory

All predictions of blade performance in this research were made using a BEMT code. A brief history of the development of BEMT as generally used today was given in Section 2.1.2. The particular code used was developed in a parallel doctoral research programme undertaken at the University of Strathclyde **??**, and was implemented in MATLAB.

In the following sections of this chapter, Sections 4.2.1 to 4.2.3 detail the theoretical bases of BEMT, and help to give insight into the interaction between a free-stream flow and a turbine rotor. In Section 4.2.4, the empirical corrections and solution method implemented in the formulation of the code used in this research are presented. Finally, in Section 4.2.5, the prediction of the base case tow tank data discussed in the preceding chapter is presented. A brief discussion of the match between the BEMT prediction and the experimental data is included.

4.2.1 Momentum theory

Axial momentum

According to the momentum theory, all the energy extracted by a turbine in a free-stream flow comes from the total change in momentum of the fluid [12, 16, 11, 13]. This theory is based on the analysis of the interaction between an actuator disk of area A, and the flow field to which it sits normal, and allows the extracted power to be calculated. The following explanation is mainly based on that presented in Wind energy handbook [12]; where other sources have been used, these will be reference in the text.

The rotor disk of a turbine can be thought of as a disk across which a change in momentum occurs - in other words, an actuator disk. Considering the conservation of

mass, and taking the steam-tube of the tidal flow as the boundary of the control volume, it is possible to say that the mass flow rate far upstream of the disk must be the same as that at the disk and far downstream in the wake. In other words,

$$\rho A_\infty U_\infty = \rho A_\mathrm{D} U_\mathrm{D} = \rho A_\mathrm{W} U_\mathrm{W}. \tag{4.1}$$

The force applied to the actuator disk comes entirely from the overall change in momentum of the flow; this can be expressed as

$$(p_\mathrm{D}^+ - p_\mathrm{D}^-) A_\mathrm{D} = (U_\infty - U_\mathrm{W}) \rho A_\mathrm{D} U_\mathrm{D}. \tag{4.2}$$

Noting the directionality of the induced flow, the component of axial flow induced by the disk is given by the inflow velocity multiplied by an axial induction factor: $-aU_\infty$. The flow at the disk can therefore be expressed as

$$U_\mathrm{D} = U_\infty (1 - a); \tag{4.3}$$

which allows Eq. (4.2) to be re-written thus

$$(p_\mathrm{D}^+ - p_\mathrm{D}^-) A_\mathrm{D} = (U_\infty - U_\mathrm{W}) \rho A_\mathrm{D} U_\infty (1 - a). \tag{4.4}$$

The application of Bernoulli's equation to the flow at either end of the actuator disk, and the assumptions of incompressible and horizontal flow, yields the following expression for the pressure difference across the actuator disk

$$(p_\mathrm{D}^+ - p_\mathrm{D}^-) = \frac{1}{2} \rho (U_\infty^2 - U_\mathrm{W}^2). \tag{4.5}$$

Substituting this into Eq. (4.4) gives two expressions of the force on the actuator disk, which can be equalised. One expression is derived considering the pressure difference across the actuator disk, and the second is derived considering the overall change in momentum of a fluid stream tube which, far upstream, was of the same diameter as the actuator disk:

$$\frac{1}{2} \rho (U_\infty^2 - U_\mathrm{W}^2) A_\mathrm{D} = (U_\infty - U_\mathrm{W}) \rho A_\mathrm{D} U_\infty (1 - a). \tag{4.6}$$

Considering that Eq. (4.3) can be written as

$$U_\mathrm{D} = U_\infty - a U_\infty \ , \tag{4.7}$$

Eq. (4.6) can be rearranged for U_W to give

$$U_\mathrm{W} = (1 - 2a) U_\infty \ . \tag{4.8}$$

Therefore the force on the air, applied by the actuator disk, is given by

$$F_{\mathrm{T}} = 2\rho A_{\mathrm{D}} U_{\infty}^2 a(1-a) \ . \tag{4.9}$$

Power is simply the rate of work done; and work done is force times distance. The power extracted across the actuator disk from the flowing fluid can therefore be expressed as force multiplied by the rate of change of distance - given by the following

$$P_{\mathrm{mech}} = F_{\mathrm{T}} \frac{dx}{dt} = F_{\mathrm{T}} U_{\mathrm{D}} = 2\rho A_{\mathrm{D}} U_{\infty}^3 a(1-a)^2 \ . \tag{4.10}$$

Eq. (2.3) gave the ratio of what the actuator disk can extract to what would be available were the actuator disk not there; replacing the numerator in Eq. (2.3) with the right-hand expression in Eq. (4.10), an expression for the efficiency of an actuator disk can be obtained:

$$C_{\mathrm{P}} = 4a(1-a)^2 \ . \tag{4.11}$$

Differentiating Eq. (4.11) with respect to a, and equating the derivative to zero allows the maximum value of C_{P} in a free stream to be defined, and thus the value of the axial induction factor which would give maximum C_{P}.

$$\frac{\mathrm{d}C_{\mathrm{P}}}{\mathrm{d}a} = 4(1-a)(1-3a) = 0 \ . \tag{4.12}$$

This yields a value of $\frac{1}{3}$ for a, which, substituted into Eq. (4.11), gives the theoretical maximum efficiency of power capture in a free-stream flow field. Defined first by Albert Betz, this is known as the Betz limit [114]:

$$C_{\mathrm{P\ Betz}} = 0.593. \tag{4.13}$$

Similarly, the structural interaction between an actuator disk and the flow derives from the drop in pressure across the disk thickness, $p_{\mathrm{D}}^{+} - p_{\mathrm{D}}^{-}$. By setting Eq. (4.9) as the numerator in Eq. (2.4), it can be found that the definition of C_{T} based on the axial induction factor, a, is

$$C_{\mathrm{T}} = 4a(1-a). \tag{4.14}$$

Tangential momentum

The foregoing analysis considered only the change in axial momentum across a stationary actuator disk. The consideration that torque and rotational velocity are required to extract mechanical power from the flow introduces the concept of a rotor disk. As opposed to an actuator disk, as well as acting to slow the flow in the axial direction a rotor disk acts to produce mechanical torque and, according to Newton's Third Law, exerts an opposing torque on the fluid. In the far upstream, there is assumed to be zero tangential motion in the flow. As the tidal stream encounters the rotating rotor disk it

is accelerated in the tangential direction between the rotating blades. The tangential component of velocity at the rotor disk, V_{D}, is defined in terms of a tangential induction factor, a', by

$$V_{\mathrm{D}} = \Omega r a' \ . \tag{4.15}$$

Immediately downstream of the turbine, the tangential velocity will have accelerated to twice this value and will now be

$$V_r = 2\Omega r a' \ , \tag{4.16}$$

The tangential motion of the fluid is in the opposite sense to that of the rotor; from Eq. (4.15) the relative tangential flow between the rotor and the blade in the middle of the disk, $V_{\mathrm{D\ rel}}$, can therefore be expressed as

$$V_{\mathrm{D\ rel}} = (1 + a')\Omega r \ . \tag{4.17}$$

Rotor annuli

The torque produced across the rotor will vary with r, from the root to the tip. Accounting for this, a rotor disk can be thought of as comprising a series of annuli, positioned at increasing radial distance r from the axis of rotation, and each of radial length δr. There is also no reason to suppose that the axially induced flow will be same over the entire rotor. The induction factors can be accordingly given the subscript r denoting their variation between rotor annuli.

The torque produced at the rotor comes entirely from the change in angular momentum of the fluid; therefore the contribution of each differential annulus to the total torque is given, considering Eq. (4.16), from

$$\delta Q = \dot{m}_r \Delta V_r r = \rho \delta A_{\mathrm{D}} U_\infty (1 - a_r) 2\Omega a'_r r^2 \ . \tag{4.18}$$

Considering the definition of power in Eq. (2.2) δP_{mech} can be expressed as

$$\delta P_{\mathrm{mech}} = \delta Q \Omega = \rho \delta A_{\mathrm{D}} U_\infty (1 - a_r) 2\Omega^2 a'_r r^2 \ . \tag{4.19}$$

Expressing in differential form the term derived for the total power extracted from the flow by the reduction in axial momentum, Eq. (4.19) can be equated to Eq. (4.10) thus:

$$2\rho \delta A_{\mathrm{D}} U_\infty^3 a_r (1 - a_r)^2 = \rho \delta A_{\mathrm{D}} U_\infty (1 - a_r) 2\Omega^2 a'_r r^2 \ , \tag{4.20}$$

which can be reduced to

$$U_\infty^2 a_r (1 - a_r) = \Omega^2 a'_r r^2 \ . \tag{4.21}$$

Similar to the tip speed ratio, the local speed ratio is defined as

$$\lambda_r = \frac{\Omega r}{U_\infty} \,. \tag{4.22}$$

This concept allows analysis of the flow and forces around the rotor at a point on the radius. Substitution of Eq. (4.22) into Eq. (4.20) allows the annular power from momentum theory to be expressed:

$$\delta P = \left(\frac{1}{2}\rho U_\infty^3 2\pi r \delta r\right) 4a'_r(1-a_r)\lambda_r^2 \,, \tag{4.23}$$

in which expression the bracketed term is the axial mass flow through an annulus, and the rightwards term is the efficiency of the blade section.

Furthermore, this introduces an expression for C_P which explicitly considers the angular momentum, and emphasises the dependence of C_P on the tip speed ratio and the induction factors:

$$C_\text{P} = \frac{8}{\lambda^2}\int_0^\lambda a'_r(1-a_r)\lambda^3 d\lambda_r \,. \tag{4.24}$$

4.2.2 Blade element theory

Slightly modified from its original formulation to include the inductions factors, the blade element theory says that a blade can be divided into sections, elements, of non-differential length, which can each be considered as an isolated aerofoil section operating in a 2D flow field in which there is no radial flow. The theory states further that the performance of a blade can be obtained from the summed performance of each of these blade elements. [16]

Considering a blade cross section of differential length, at radial position r, and taking this assumption that the vector relationship can be thought of as two-dimensional, the flow approaching the aerofoil is defined as the vector of relative velocity between the aerofoil section and the tide, W_r, as illustrated on the right-hand side of Fig. 4.2. The axial flow comprises the axial freestream flow and the elemental axially-induced low. This is expressed with the elemental form of Eq. (4.3), $U_\infty(1-a_r)$. The tangential flow relative between the fluid and the blade element at radius r is expressed with the elemental form of Eq. (4.17), $\Omega r(1+a'_r)$. The resulting flow vector can then be defined with Pythagoras' theorem thus:

$$W_r = \sqrt{((1-a_r)U_\infty)^2 + (\Omega r(1+a'_r))^2} \,. \tag{4.25}$$

The radial position r is generally taken at a node placed in the centre of the element; the values of θ_r and c_r are defined at these nodes. As Figs. 4.2 and 4.3 illustrate, the local flow angle, ϕ, between the rotor plane and W_r is found from:

$$\phi_r = \alpha_r + \beta + \theta_r \,. \tag{4.26}$$

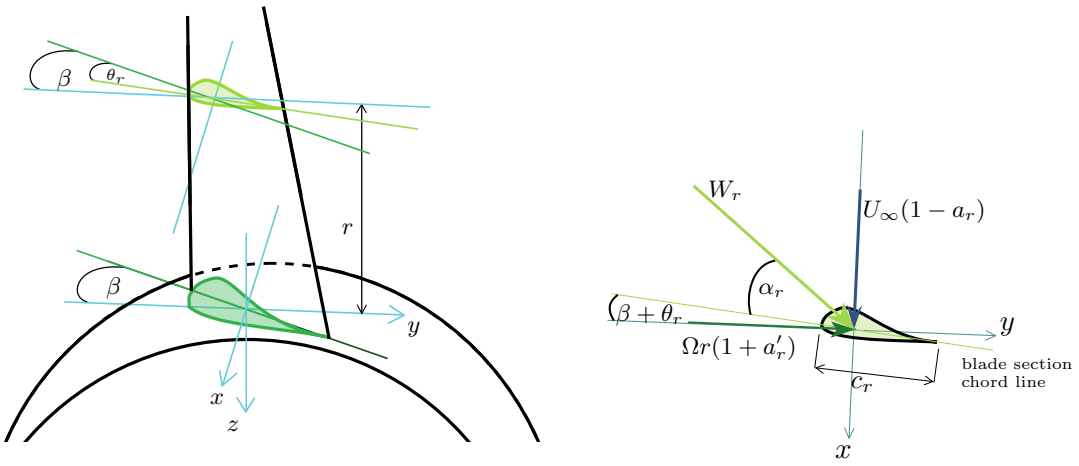

Figure 4.2: *Left*: Orthogonal view diagram of rotor, blade at top dead centre position, coordinate system and angle definitions. β is measured from rotor plane and has a positive value here; θ_r is measured from the blade root chord line and is negative here. *Right*: Plan view diagram of 2D flow vectors for a blade section, also showing definition of chord.

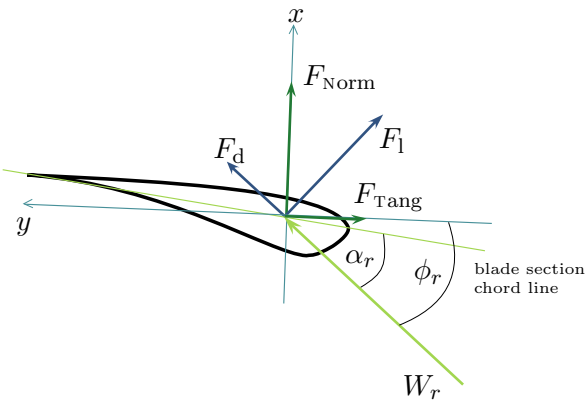

Figure 4.3: Blade section plan view showing definition of the normal, tangential lift and drag forces, the angle of attack and the chord length.

It is convenient to also define the local pitch angle:

$$\beta_r = \beta + \theta_r \tag{4.27}$$

Within the coordinate system in Fig. 4.2, θ is of negative value as it is measured from the blade root chord, has a starting value of zero and (generally) progresses up the blade in the anti-clockwise (i.e. negative) direction.

From Fig. 4.3, it can be seen that the forces in the axial and tangential direction on a blade section are defined, as in [11], with

$$dF_{\text{Norm}} = dF_{\text{l}}\ \cos\phi_r + dF_{\text{d}}\ \sin\phi_r \tag{4.28}$$

and

$$dF_{\text{Tang}} = dF_{\text{l}}\ \sin\phi_r - dF_{\text{d}}\ \cos\phi_r\ . \tag{4.29}$$

Or, expressed in coefficient terms:

$$C_{\text{Norm}} = C_{\text{l}} \cos\phi_r + C_{\text{d}} \sin\phi_r \tag{4.30}$$

and

$$C_{\text{Tang}} = C_{\text{l}} \sin\phi_r - C_{\text{d}} \cos\phi_r \ . \tag{4.31}$$

4.2.3 Blade element momentum theory

As discussed in Section 2.1.2, BEMT combines the momentum and blade element theories. The basis of BEMT is that by setting the annuli used in momentum theory analysis to be of the same radial position and length as the blade elements used in blade element theory, BEMT can be used to determine the torques and forces on the rotor. It states further that the force on an annulus can be determined as that of the sum of the forces on the blade elements of that annulus, and that this force is entirely responsible for the change in momentum of the flow which passes through the annulus.

Considering this, substituting the definition of the differential lift and drag force on aerofoil, dL and dD, given in Eqs. (2.9) and (2.10) into Eqs. (4.28) and (4.29), the blade element theory allows the annular contribution to thrust and torque of a rotor with B blades to be defined as:

$$\delta T = \frac{1}{2}\rho B W_r^2 c_r (C_{\text{l}} \cos\phi_r + C_{\text{d}} \sin\phi_r)\delta r \tag{4.32}$$

and

$$\delta Q = \frac{1}{2}\rho B W_r^2 c_r (C_{\text{l}} \sin\phi - C_{\text{d}} \cos\phi) r \delta r \ . \tag{4.33}$$

The increase in tangential velocity of the wake, given in Eq. (4.16), can be accounted for by a drop in the axial pressure in the wake. This results in an increase in the pressure difference between the upstream and far wake locations. The annular contribution to this pressure drop therefore gives an additional axial force on the annulus, which can be expressed as

$$\frac{1}{2}\rho(2\Omega r a')^2 2\pi r \delta r \ . \tag{4.34}$$

The total axial force on a rotor annulus can therefore be determined by the sum of the two components from the momentum theory Eqs. (4.9) and (4.34):

$$\delta F_{\text{T}} = 4\pi\rho \left(U_\infty^2 a(1-a) + (\Omega r a')^2\right) r \delta r \ . \tag{4.35}$$

This rate of change of axial momentum through an annulus, Eq. (4.35), can be equated to the force on the annulus, Eq. (4.32), thus:

$$4\pi\rho \left(U_\infty^2 a(1-a) + (\Omega r a')^2\right) r \delta r = \frac{1}{2}\rho B W_r^2 c_r (C_{\text{l}} \cos\phi_r + C_{\text{d}} \sin\phi_r)\delta r \ . \tag{4.36}$$

Similarly, the rate of change of angular momentum can be expressed as the mass

flow rate multiplied by the angular velocity (Eq. (4.16)$\times r$), and can be equated to the moment of the tangential force (the torque), Eq. (4.33)

$$\rho U_\infty (1-a) 2\Omega r a' r 2\pi r \delta r = \frac{1}{2}\rho B W_r^2 c_r (C_\mathrm{l} \sin\phi - C_\mathrm{d} \cos\phi) r \delta r \ . \tag{4.37}$$

The equalities stated in Eqs. (4.36) and (4.37) (variously expressed in different texts) form the basis of BEMT and allow the performance of a rotor to be predicted, at every flow state, from the summed annular performance. Of the many variables, those required to be known for the solution of the equation set are the induction factors. Expressing the chord solidity as

$$\sigma_r = \frac{B c_r}{2\pi r} \ , \tag{4.38}$$

and therefore using Eqs. (4.30) and (4.31), the solutions for a and a' are generally obtained iteratively, from rearrangements of Eqs. (4.36) and (4.37):

$$\frac{a}{1+a'} = \frac{\sigma_r}{4\ \sin\phi^2} \left(C_\mathrm{Norm} - \frac{\sigma_r}{4\ \sin^2\phi}\ C_\mathrm{Tang}^2 \right) \tag{4.39}$$

$$\frac{a}{1+a'} = \frac{\sigma_r C_\mathrm{Tang}}{4\ \sin\phi\ \cos\phi} \ . \tag{4.40}$$

From guessed starting values of a and a' – which, in this project were set based on the inflow velocity – the final values for each element and then each flow state (normally defined over a range of λ) are obtained iteratively based on convergence criteria stipulating the required difference between subsequent solutions. The rotor power at each value of λ is found from summing on side of Eq. (4.37) and considering Eq. (2.2); the rotor thrust at each value of λ is found simply from summing one side of Eq. (4.36).

It is important to note that in BEMT and in all of its applications including this work, the term C_P is frequently referred to. As is accepted in the field [12, 4, 13], C_P refers to the efficiency of the rotor and not of the whole system.

4.2.4 Formulation of the bemt code used

As mentioned in Section 2.1.2, the BEMT code employed in this research was developed by Nevalainen. As described in [75] (also in [115], with an version which was subsequently updated) and [10], in its development stages the BEMT code was taken through several verification exercises. The final verification and calibration were undertaken with the tow tank data obtained in this project as presented in Section 4.2.5. The aim was to configure the BEMT code such that the experimental base case blade data for this project – and that undertaken in a third parallel doctoral research project [96] – could be predicted well with a formulation of the code which also successfully predicted experimental data produced in separate research projects.

The following section briefly outlines the final equations, including the corrections

made to classical BEMT, which were implemented in the final formulation of Nevalainen's code used in this project. The additional aspects implemented were:

- Prandtl tip-loss correction factor
- Spera high induction correction; the "critical" value of a, a_c, after which the correction factor is implemented was set to 0.4.
- Viterna-Corrigan post stall model of aerofoil characteristics.

As detailed in [10], Nevalainen implemented the alterations to the classic solution method for BEMT put forward by Masters et al. in [116]. In this scheme, some problematic aspects of the classical solution, such as non-convergence, are worked around by the creation of an objective function, g, which considers the cumulative error of the two equalised BEMT equations for torque and for thrust. This error function is minimised with a and a' as the variable parameters. This is undertaken by MATLAB's *fmincon* function, a computationally-efficient optimisation routine or "Nonlinear programming solver" which avoids local minima [117]. The the lower and upper bounds for the variable parameters were respectively set to -1.5 and 1 for a and -1.5 and 0.5 for a'. This give a wide search space which reduced the possibility of numerical errors creating discontinuities in the performance curves and plots of α.

To produce as much detail about rotor performance as possible, and reduce error in linear interpolation between operating points, the number of blade elements was set to 140, and the number of λ points at which the calculations were made was set to 80.

Tip and hub loss

The Prandtl tip loss factor was applied, giving the value for F required in the final set of equations. It was found that inclusion of the hub loss factor did not increase the overall accuracy of prediction for the cases considered, hence F_{hub} was set to a value of 1, giving $F = F_{\text{tip}}$

$$F_{\text{tip}} = \frac{2}{\pi} \cos^{-1} \exp^{-Pr} , \tag{4.41}$$

where

$$Pr = \frac{0.5B(1 - \frac{r}{R})}{\frac{r}{R} \sin\phi} . \tag{4.42}$$

High axial induction

The Spera correction for high values of a was used to correct the value of the annular thrust force when $a \geq a_c$. Generally this modification is expressed for the annular coefficient of thrust; however to maintain consistency between the equations for ease of reading, and because the BEMT script was so written, the modification is expressed in terms of $\delta F_{\text{T}r}$. This gives a modification for Eq. (4.35) (including the Prandtl correction

factor) according to:

$$\delta F_{\mathrm{T}r} = \begin{cases} 4F\pi\rho\left(U_\infty^2 a(1-a) + (\Omega r a')^2\right) r\delta r & \text{if } a \leq a_\mathrm{c} \\ 4(a_\mathrm{c}^2 + (1-2a_\mathrm{c})a)F\pi\rho U_\infty^2 + F(a'\Omega r)^2) r\delta r & \text{if } a > a_\mathrm{c} \end{cases}$$

Therefore, when $a > a_\mathrm{C}$, the value used for a was calculated according to an empirical equation:

$$a = \frac{1}{2}\left(2 + K(1-2a_\mathrm{c}) - \sqrt{K(1-2a_\mathrm{c}) + 2^2 + 4(Ka_\mathrm{c}^2 - 1)}\right) \ , \tag{4.43}$$

where

$$K = \frac{F\ \sin^2\phi}{\sigma_r C_{\mathrm{Norm}}} \ . \tag{4.44}$$

Stalled flow

For instances of post-stalled flow, the coefficient of lift and drag were updated with the Viterna-Corrigan model. The model depends on values of the stall angle of attack, α_s, lift and drag coefficients, $C_{\mathrm{l\,s}}$ and $C_{\mathrm{d\,s}}$, which were defined in the code according to the aerofoil used and the Re for which the lift and drag data were obtained. The model equations were:

$$C_\mathrm{l} = \frac{1}{2}C_{\mathrm{d\ max}}\ \sin(2\alpha_r) + K_\mathrm{L}\frac{\cos^2\alpha_r}{\sin\ \alpha_r} \tag{4.45}$$

$$C_\mathrm{d} = C_{\mathrm{d\ max}}\ \sin^2\alpha_r + K_\mathrm{D}\ \cos\ \alpha_r \ , \tag{4.46}$$

where

$$K_\mathrm{L} = (C_{\mathrm{l\,s}} - C_{\mathrm{d\ max}}\ \sin\alpha_\mathrm{s}\ \cos\alpha_\mathrm{s}))\frac{\sin\alpha_\mathrm{s}}{\cos^2\alpha_\mathrm{s}} \ , \tag{4.47}$$

and

$$K_\mathrm{D} = \frac{(C_{\mathrm{d\,s}} - C_{\mathrm{d\ max}}\ \sin^2\alpha_\mathrm{s}}{\cos^2\alpha_\mathrm{s}} \ , \tag{4.48}$$

wherein the value for $C_{\mathrm{d\ max}}$ is determined according to the aspect ratio of the blade, A_R, thus:

$$C_{\mathrm{d\ max}} = \begin{cases} 1.11 + 0.18A_\mathrm{R} & \text{if } A_\mathrm{R} \leq 50 \\ 2.01 & \text{if } A_\mathrm{R} > 50 \end{cases}$$

The aspect ratio of the blade was determined from the length and planar area of the blade

$$A_\mathrm{R} = \frac{l_\mathrm{B}^2}{A_\mathrm{B}} \ . \tag{4.49}$$

4.2.5 Prototype scale base case blade BEMT prediction

As discussed in Sections 2.2 and 4.4, aerofoil performance can be affected by many conditions in the flow and on the aerofoil, notably Re and free-stream turbulence.

Appropriate aerofoil data was necessary to take the BEMT code through a verification exercise with the tow tank data described in Section 4.3.3. As detailed in Table 3.7, the chord Re of the tests were in the range $4.3 \times 10^4 - 1.7 \times 10^5$. Aerofoil data for the NREL S814 has recently been experimentally obtained in a flume at Swansea University. This data was very kindly offered pre-publication by Togneri et al., for the purpose of verifying the BEMT code and establishing a base case performance BEMT prediction.

The maximum Re at which the aerofoil data was obtained was 5.1665×10^4 [118]. The free stream turbulence intensity in the flume was in the region of $5\ \% - 6\ \%$. This is rather higher than the turbulence intensity which would occur in measurements made of aerofoil performance in most wind tunnels. This is also most likely (though it was not measured) higher than any free-stream turbulence present in the relatively still water of the tow tank tests.

Although the Re at which the $0.5\ \mathrm{m\,s^{-1}}$ tests were taken most closely matched the Re of this 2D data, it was found that the BEMT prediction using this data gave a much better match for the test data at $0.8\ \mathrm{m\,s^{-1}}$.

Though Re is highly influential on aerofoil performance, other aspects of fluid flow also have an effect, as discussed in Section 2.2. These influences have an impact on both aerofoil sections and turbines, impacting the the performance of each. As discussed in Section 2.2, these effects are complicated and work is on-going to increase understanding of fluid flow on turbines. In terms of BEMT and other design tools it is most accurate to say that the aerofoil data used should have been obtained in a flow environment with physical characteristics most appropriate for those experienced by the turbine for which the prediction is undertaken. The effect of an alteration to one flow characteristic can be to augment or suppress other flow behaviours, meaning that representing the flow environment in terms of one characteristic alone – Re, for example – may not be sufficient.

In demonstration of this point, Sicot et al. found that increased freestream turbulence intensity delayed stall on a rotating blade, just as it had done on a non-rotating blade [119]. However, the authors noted that within the region of separated flow, the pressure difference between upper and lower surface was greater in the rotating case, suggesting (somewhat tentatively) "a qualitative indication of an aerofoil lift augmentation"; at the very least, it was shown that rotational effects on aerofoils working in a fairly turbulent environment produce altered pressure values on the blades, compared to non-rotating blades – and 2D-derived aerofoil data. This suggests that there may be a cross-influential impact made by rotational motion and turbulence intensity on the applicability of aerofoil data for use in predicting turbine performance.

Focussing on the rotational effects, Du and Selig developed a model solving the 3D integral boundary layer equations to investigate the effects of rotational motion on the boundary layer. It was found that the forces induced by rotational motion, the Coriolis and centrifugal effects, acting to delay separation of the boundary layer to later points along the chord, were greatest at the slower-moving in-board blade sections

and were suppressed by the reduced viscous dominance in higher Re [44]. This has the implications that aerofoil data may be less applicable to turbines in low Re situations such as the turbine tested here. The authors also drew the important conclusion that rotational effects will therefore be of greater importance in smaller turbines.

Considering now the turbulence intensity, Liebeck and Blackwelder found, in a set of controlled experiments, that increases in free-stream turbulence from 1 % to 9 % suppressed the laminar separation and reattachment behaviour of low Re flows, resulting in thinner boundary layers before and after transition, earlier transition within the bubble and reduced drag force [34]. This is of particular note in this case because laminar separation and reattachment was found by Milne to have occurred on the NREL S814 in a wind tunnel in a Re range similar to those of the tow tank tests [35]. The difference in turbulence intensities between the flume in which the aerofoil data was obtained and the tow tank in which the turbine was tested will very probably have caused a difference in the actual performance of the tested blade sections and aerofoil. As Figs. 3.17 and 3.18 show, significant performance degradation was seen in the turbine tests run at 0.5 $\mathrm{m\,s^{-1}}$. It is probable that there were laminar separation bubbles present in these tests, significantly affecting blade efficiency.

Considering these effects, the scale of the turbine, and the effects of turbulence on laminar separation, and generally on turbine performance, it is proposed that a difference in the levels of turbulence in the free stream between the Swansea flume and the Strathclyde tow tank, may have been the cause of the mismatch between the BEMT prediction and the turbine performance at the tow speed, 0.5 $\mathrm{m\,s^{-1}}$ which would seem to have been most appropriate in terms of Re.

In order to obtain a more appropriate match in the effect of the flow on the aerofoil section between the tow tank tests and the data used for the BEMT prediction, the formulation of the BEMT code described above was used to predict the performance of the base case turbine at 0.8 $\mathrm{m\,s^{-1}}$ rather than at 0.5 $\mathrm{m\,s^{-1}}$. The results of this are shown in Fig. 4.4. In the lower TSR range in these tests, the turbine showed lower power performance than predicted by the code. Generally, however, a fair match between the predicted and tested performance was found. The sensitivity if the aerofoil to Re at these low values was clearly seen in the test results, and a closer performance match was achieved at some λ values when compared to the 0.9 $\mathrm{m\,s^{-1}}$ tests, as shown in [75].

All final-stage designs should be run in a design code capable of more detailed analysis, such as a tool based on CFD. However inescapable the Re, rotational and turbulence intensity effects are at small scale, the purpose of BEMT tools is to perform the earlier design stage predictions for turbine blades, and comparisons with empirical data are most possible – financially and practically – with small scale rotors. Early stage design is most usefully undertaken with a computationally efficient design code; this is the greatest strength of BEMT tools. Many, many different design iterations can be run in the space of minutes, compared to the hours, days and even weeks associated with more advanced tools. Considering these factors, the formulation of the BEMT

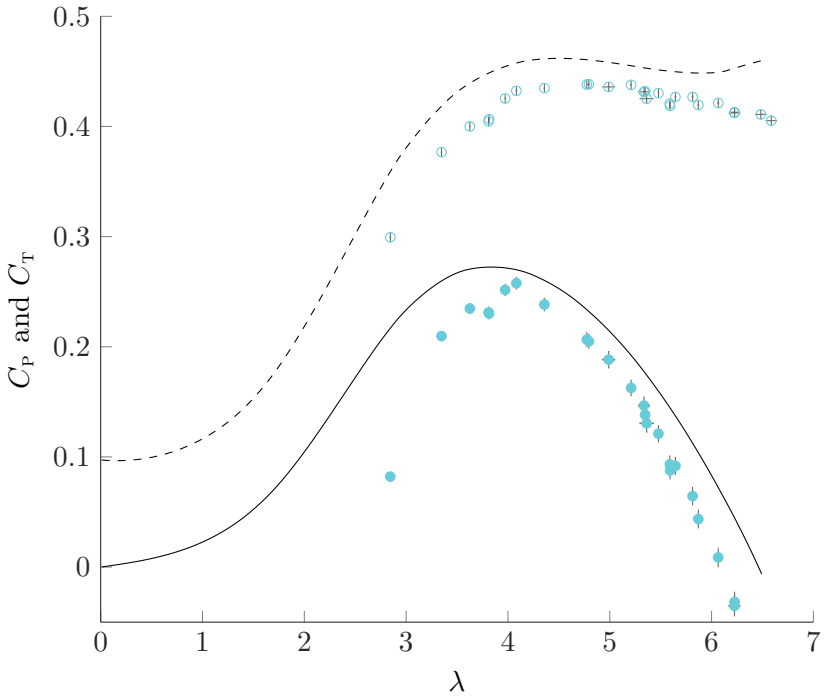

Figure 4.4: Tow tank and BEMT prediction of base case blade performance at 0.8 $\mathrm{m\,s^{-1}}$.

code presented was determined to be valid and of great utility for its purpose as the hydrodynamic performance model in this blade design methodology.

4.2.6 Use in the design methodology

The first blade assessed in the application of this design methodology will always be a base case. In the case presented here, this was a full-scale blade, the scale being defined by the design platform. The suitability for use in OSPR of each subsequent blade is then assessed in comparison to the performance of this base case blade. The manner in which the OSPR performance is assessed is given in Section 4.6.1.

4.3 Design platform

Focussing now on the design platform, this aspect of the design methodology provided the boundary conditions for all simulations of rotor performance. Fig. 4.5 illustrates the concept and identifies the variables which were set within the design platform. This section outlines the parameters and operational conditions considered in the design platform.

4.3.1 Purpose of the design platform

The parameters contained in the design platform were required in order that the operation of the base case blade and each blade design permutation could be numerically

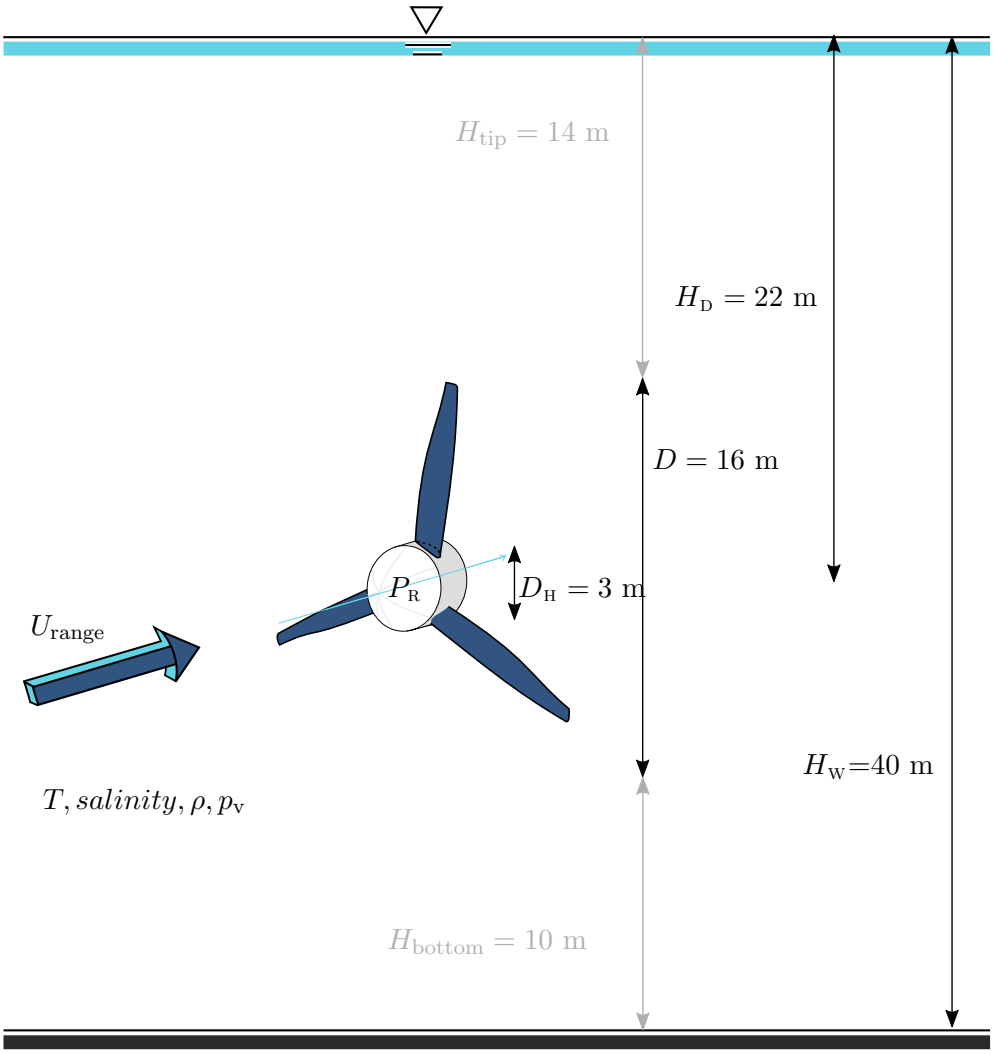

Figure 4.5: Scale diagram of design platform.

analysed in terms of the performance in overspeed – and in order that the impact made thereon by design changes could be assessed.

While assessment of the performance curves of blade permutations gives some information as to the impact of the blade design change(s) implemented, without further information it would not be possible to assess the maximum rotational velocity required for the system to regulate power successfully. This would make any quantitative cavitation inception analysis impossible, and implications with regards to thrust forces and voltage levels would be difficult to assess. Creation of the design platform therefore facilitated a numerical analysis of performance in which each blade permutation was assessed within boundary conditions representative of a real-world tidal site scenario.

4.3.2 Assumptions

Simplifications were made to the complex reality of tidal sites by assuming a turbulence and wave-free environment. Furthermore, it was assumed that the turbine would be

Table 4.1: Geometry of base case blade design

$r/L_b(-)$	$c_r/L_b(-)$	$\theta_r(°)$
0	0.22	0
0.1	0.21	-4.9
0.2	0.21	-10.6
0.3	0.19	-14.2
0.4	0.18	-16.7
0.5	0.17	-18.3
0.6	0.16	-19.2
0.7	0.14	-19.9
0.8	0.13	-20.4
0.9	0.12	-20.8
1	0.09	-21.1
	$\beta°$	26.9

aligned with the flow at all times. The likely impact of these simplifications, and suggestions with regards to the incorporation of greater complexity, will be discussed in Section 7.3.

4.3.3 Base case blade geometry

The base case blade design was required to be defined at the appropriate size for the full-scale scenario in which the turbine performance was to be analysed. The geometry of the base case blade tested in the tow tank was non-dimensionalised by dividing the radial and chord length values by the blade length, L_b, giving a scalable blade design, independent of hub size. In order to give the greatest meaning to the comparison between each blade design permutation and the base case, the blade pitch setting was optimised for the base case. This geometry is detailed in Table 4.1.

Illustrations of the base case blade design are included in Fig. 5.1a) and b); Fig. 5.1 c) and d) include the base case twist and chord distribution.

As discussed, the existing blade section of NREL S814 aerofoil shape was used consistently throughout all development and application of this design methodology. The NREL S814 was designed to have a high maximum lift, has the structural advantage of being relatively thick, and its insensitivity to surface roughness lends it to use in the biologically diverse and potentially sediment-carrying marine environment [120].

Further discussion of the aerofoil data used, which was dependent on the chord Reynolds number and therefore the operating conditions, will be given later in Section 4.4.

Table 4.2: Design platform parameters

Parameter	Symbol	Value
Rotor diameter	D	16 m
Hub diameter	D_{H}	3 m
Rated power	P_{R}	750 kW
Flow velocity range	U_{range}	0 – 3.11 $\text{m}\,\text{s}^{-1}$
Seawater temperature	T	12 °
Seawater density	ρ	1027 $\text{kg}\,\text{m}^{-3}$
Vaporisation pressure	p_{v}	1374.1 MPa
Site water depth	H_{W}	40 m
Deployment depth (measured to shaft)	H_{D}	22 m

4.3.4 Design platform parameters

The boundary conditions or set parameters required for a specific design scenario are the inputs to the design platform; the parameter values of the design platform can accordingly be altered in consideration of the specific design purpose. This gives a design methodology which results in blade designs malleable to the design conditions. Fig. 4.5 gives a pictorial representation the design platform.

Set parameter values

While neither the design platform nor the Methodology at large make any assumptions with regards to the values to which the design platform parameters *should*, nor constrains the values to which they *could* be set, some numbers had to be assigned to these variables in order to progress and create a platform from which to work. In the development of this blade design methodology, the set parameters forming the design platform were accordingly given the values shown in Table 4.2.

The values of $U_{\infty\text{max}}$ and R were based on those used in a design scenario based on the Portland Bill tidal site, presented by Batten et al. in 2007 [98]. The value set for P_{R} was influenced by the data presented in this paper. On plotting the energy yield against the rated power for each turbine design investigated (with optimum λ values of 4 and 5), it could be seen, as Fig. 4.6 shows, that the gradient of the energy yield reduced around 750 kW. This was, therefore, the value to which rated power of the turbine in the design platform was set. R_{h} was set as 1.5 m because initial developments of the methodology at the prototype scale indicated that large blade root chords would be required to meet the design requirements and there had to therefore be room on the hub for large blade root sections. This 5.3:1 hub-turbine radius ratio was not significantly different from the 6:1 ratio used by Tachmindji and Milam in their work on including the hub in the Goldstein factor [16], indicating that the physics should be relevant

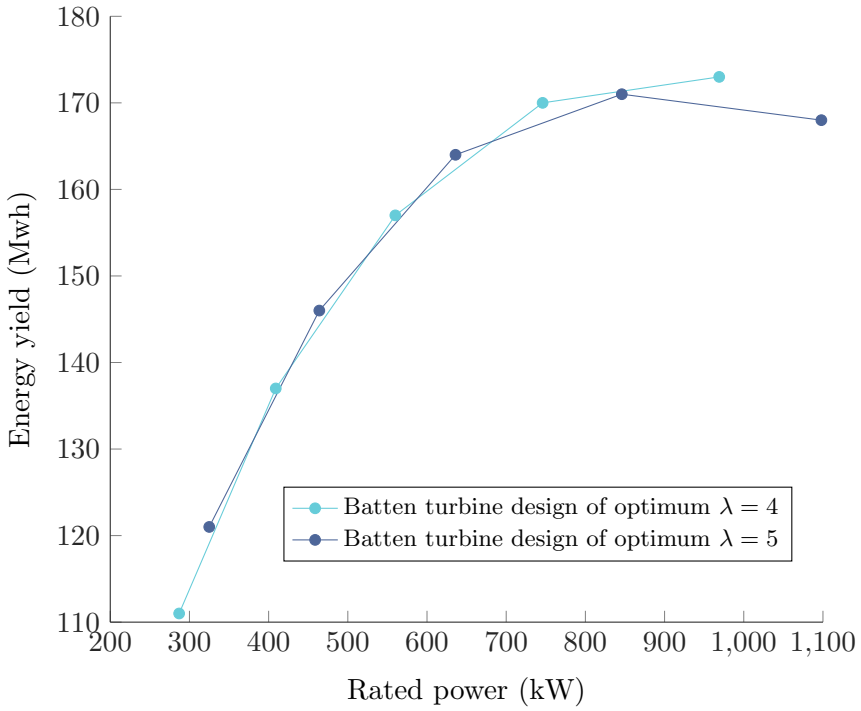

Figure 4.6: Plot of calculated energy yield against rated power for two turbines of different optimum tip speed ratio, all data as presented in [98]

and the assumption of hub size not detrimental to the turbine performance. The blade length was simply based on R and R_{h}. The blade root pitch setting was optimised for C_{P} for these conditions, giving the best case scenario for the base case blade.

The density of the modelled fluid is influential on the inception of cavitation; greater density reduces the possibility of cavitation. To assess the worse-case situations, North Sea (a likely deployment site) seawater at a Summer mean temperature of 12 °[121], and standard salinity was assumed, and the density of such seawater was calculated from tabulated data [122]. This gave $\rho = 1027\ \mathrm{kg\,m^{-3}}$. The value for p_{v}, similarly obtained, was 1374.1 MPa.

Black & Veatch reported, in [123], that: "Of the total Technically Extractable Resource, about 63% is at sites with depths greater than 40 m... Approximately 50% of the UK resource is in deep (> 40 m) sites with relatively high velocities.". Considering this, the depth of the design platform site was set to 40 m. The turbine deployment depth was set such that the shaft immersion was just over half the site depth, leaving 14 m from the free surface and 10 m from the seabed. This was the chosen immersion depth as giving a good balance between the constraints: 14 m clearance was considered to leave sufficient room for ship passage with a 4 m swell; and the 10 m between the blade tip and sea bed would remove the turbine from much of the seabed turbulence (as graphically shown, for example, with empirical data from separate sites in [124, 37]).

4.3.5 Definition of operation range and optimum and overspeed points

The design platform also defined the operating methodology – MPPT and OSPR – and, based on the required C_P at every value of flow velocity, allowed the rotor performance to de determined.

Operational regions

The BEMT tool was set to predict performance at 80 individual λ values spanning the C_P-λ curve from the extreme LHS to the runaway point. Densely populated data allowed accurate interpolation of intermediate points with a linear method. The arrays defining flow regimes and performance variables in the design platform were similarly dense.

Of the five regions in Fig. 2.10, Regions I and III were incorporated into the design platform, in which the power capture and flow conditions of each were defined according to the required operation. This allowed the flow regime to be defined, for each increment of U_∞. The aerofoil data appropriate for use in the full-scale BEMT code were determined according to the flow regime defined in the design platform. This is discussed in Section 4.4.

Region I

Region I was defined by the flow conditions $U_{\infty\text{cut-in}} \leq U_\infty \leq U_{\infty\text{R}}$ and $\lambda = \lambda_\text{O}$. In Region I MPPT is used to maintain optimum rotor efficiency; the C_P was therefore set to $C_{P\text{O}}$. The array location of the optimum operating λ was found by identifying the index of maximum C_P. In this operational region, the power captured, defined by

$$P_{\text{region I}} = \frac{1}{2}\rho A U_\infty^3 C_{P\text{O}} \ , \tag{4.50}$$

increased to the cube of U_∞. The value of $C_{T\text{O}}$ was found using the array index of the optimum operating point. The thrust at each increment of flow velocity in this range was then calculated according to $C_{T\text{O}}$:

$$Th_{\text{region I}} = \frac{1}{2}\rho A U_\infty^2 C_{T\text{O}} \ , \tag{4.51}$$

and the rotational velocity at each increment was calculated from

$$\Omega_{\text{region I}} = \frac{\lambda_\text{O} U_\infty}{R} \ . \tag{4.52}$$

With the elemental values of a_r and a'_r at the optimum operating point, the arrays of axial and tangential flow at each blade element – and subsequently, the corresponding relative flow array, $W_{\text{region I}}$ – were defined for each increment of U_∞ in Region I from Eq. (4.25). The corresponding elemental values of α_r and elemental contribution to torque and thrust, dQ_r and dF_r, were also found.

The overspeed point

The extreme operating point in Region III, reached when $U_\infty = U_{\infty\text{cut-out}}$, was the maximum operating point considered, and was determined according to the C_P to which rotor efficiency must be reduced to limit the power to P_R at this flow speed. This maximum operating point was termed the overspeed point; C_Povs was found from

$$C_\text{Povs} = \frac{P_\text{R}}{\frac{1}{2}\rho\pi R^2 U^3_{\infty\text{max}}} \ . \tag{4.53}$$

As the λ at which this C_P value occurred was not necessarily exactly equal to one of the 160 λ values defined in the BEMT, it was neccesery to interpolate for the values of λ_ovs, C_Tovs, α_ovs, dQ_ovs and dF_ovs.

The thrust at this point was then defined as

$$T_\text{ovs} = \frac{1}{2}\rho\pi R^2 U^2_{\infty\text{max}} C_\text{Tovs} \ . \tag{4.54}$$

The rotational velocity which the turbine is required to reach at the overspeed point depends on the relationship between C_P and λ, and can be defined in a rearrangement of Eq. (2.5):

$$\Omega_\text{ovs} = \frac{\lambda_\text{ovs} R}{U_{\infty\text{max}}} \ . \tag{4.55}$$

As Ω_ovs is the maximum rotational velocity at which an OSPR turbine will spin, it in this flow state that the turbine will be most at risk of cavitation inception. The rotational velocity of the turbine at this point depends on the relationship between C_P and λ, dependent in turn on the blade design.

Region III

Region III was defined by operation in the flow range $U_{\infty\text{R}} < U_\infty \leq U_{\infty\text{cut-out}}$. Technically, the region bounds in terms of λ should be defined $\lambda_\text{O} < \lambda \leq \lambda\text{ovs}$; however, the practical constraints of numerical tools meant that – as mentioned – even with the highly dense population of the performance curves, it was unlikely that the exact value λOVS would exist in the λ array output from BEMT. The definition of the flow regime of Region III was therefore completed as existing within the range $\lambda_\text{O} < \lambda \leq \lambda_{\text{ovs}+1}$, where $\lambda_{\text{ovs}+1}$ was the λ array entry corresponding to the first array entry of C_P satisfying both the conditions: $C_\text{P} < C_{\text{PO}}$ and $C_\text{P} \leq C_\text{Povs}$. All analyses concerning the overspeed point were, however, made with the values described above, determined by interpolation; the final values of each variable in Region III were replaced with the corresponding interpolated values.

The required C_P for each increment of U_∞ within this range was calculated according to:

$$C_{\text{Pregion III}} = \frac{P_\text{R}}{\frac{1}{2}\rho A U^3_\infty} \ . \tag{4.56}$$

From the BEMT prediction of the C_P-λ curve for the blade in question, the values of $C_{P\text{region III}}$ were used to find the required values of λ, $\lambda_{\text{region III}}$. This was undertaken by interpolating in the BEMT output arrays for the values of λ corresponding to the required values of C_P using the MATLAB function *interp1*. The resulting $\lambda_{\text{region III}}$ values, along with the attending values of U_∞, were then used to calculate the values of Ω in the regulation range, from

$$\Omega_{\text{region III}} = \frac{\lambda_{\text{region II}} U_\infty}{R} \ . \tag{4.57}$$

The values of C_T at each point in this operating range were also calculated by interpolation; in this case, *interp1* was used to find the values of C_T which corresponded with the λ values in $\lambda_{\text{region III}}$. Similar calculations were made to find the elemental values of a_r, a'_r, α_r, dQ_r and dF_r in Region III. As for Region I, the relative flow array, $W_{\text{region III}}$, was also calculated.

Full operational range

The full operational range was defined by concatenation of the arrays of Region I and Region III.

4.4 Aerofoil data

By defining the flow regime and turbine configuration, creation of the design platform allowed calculation of the chord Reynolds numbers occurring in the operational range; defining *Re* allowed relevant aerofoil data to be obtained from Eq. (2.11), repeated below:

$$Re = \frac{\rho W c_r}{\mu} \ . \tag{4.58}$$

The *Re* appropriate for the full scale rotor analyses undertaken were thus found to be in the range of $1\text{x}10^7$. In the absence of physical test data at these *Re*, the design code XFOIL, developed to give computationally efficient and reasonable predictions of aerofoil performance, was used to obtain NREL S814 data at the appropriate *Re*. As reported by Drela in [125], XFOIL uses several empirically-based corrections to predict aerofoil performance which, as the developers note in [125], are reasonable data until just after stall. As discussed in Section 4.2, the BEMT code used in this project includes a Viterna-Corrigan correction for more accurate modelling of post-stall behaviour.

Previous examples of the use of XFOIL for the prediction of aerofoil data for tidal turbine applications exist extensively in, for example, the projects reported in [126, 46, 47, 127].

The choice of the critical N_{crit} value for the e^N method, used by XFOIL to predict transition, was based on the recognition that tidal turbine rotors operate in a highly turbulent environment. As discussed in [128], to represent this large free-stream

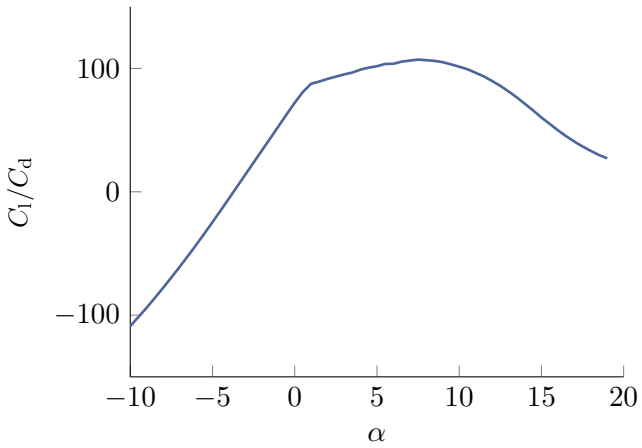

Figure 4.7: Plot of C_l/C_d with α at $Re = 1 \cdot 10^7$

disturbance in XFOIL, lower values of N can be set. According to the XFOIL User Primer, [129], setting N_{crit} to a value of 1 or less tells the programme to bypass transition. The sensitivity of the C_l and C_d predictions to N_{crit} in the range between $N_{crit} = 1$ and $N_{crit} = 2$ was found to be very low; an N_{crit} value of 2 was therefore selected as a best-fit value, setting transition to occur quickly due to large values of free-stream disturbances

As discussed in Section 2.2,Re has a reduced effect as it increases; though not fully-independent of its effects, the aerofoil data at this level did not change significantly, and one set of data were therefore used for all the full-scale BEMT predictions.

Fig. 4.7 shows the aerofoil data input to the BEMT tool. As the figure shows, the optimum α for this aerofoil at this Re is 7.5°; blade sections operating at this α will develop the greatest lift to drag force ratio.

As well as C_l and C_d data, XFOIL was set to produce the data for the coefficient of pressure, C_{pres}, for use in the cavitation analyses. This will be discussed further, in Section 4.6.2.

4.5 Blade design parameters

4.5.1 Blade Design Parameter Alterations

The major aspects of blade design which were set as variable parameters in the development of this methodology were the blade pitch, β, the twist distribution, θ_r and the chord distribution, c_r. The definitions of these parameters are indicated in Fig. 4.2. Each parameter was altered with functions, giving series of blade designs, each with discrete alterations made over a certain range. Initial assessments of the influence of each parameter informed the alteration range which was reasonable for each parameter - these decisions were based primarily upon reasonable levels of C_P and C_T, but also on the basic practicality of the blade design - e.g., designs with overlapping root chords were deemed impracticable.

The functions used to alter the blade design parameters each had a function variable, generically denoted γ, which was varied over a set range to produce a series of altered blade design permutations. The functions were applied to the blade design parameters, generically denoted Θ, in the manner of Eq. (4.59):

$$\Theta_{\text{permutation}} = \Theta_{\text{base case}} + f(\gamma) \ . \tag{4.59}$$

4.6 Blade design parameter impact analysis

The design requirements must inform the blade design methodology. A key factor in the development of the blade design methodology therefore, was to identify favourable turbine performance for OSPR, and define performance metrics which could measure how well each blade design permutation performed. By comparing this with the base case performance, it would then be possible to infer what impact was made by each blade design alteration, on each aspect of performance in OSPR.

This section describes the design requirements considered and the manner in which these were incorporated into the blade design methodology.

Design requirements

Previous sections have discussed the requirement that a turbine rotor designed for overspeed power regulation should be designed to limit the maximum rotational velocity. This would entail a design which limits the increase between the rotational velocity at the optimum and overspeed operating points, Ω_{O} and Ω_{ovs}; a design which results in a greater gradient in the relationship between C_{P} and λ on the overspeed side (i.e. the right-hand side) of the C_{P}-λ curve. As well as this, the more general design requirements pertaining to desired efficiency and constraints on thrust load need to be considered.

4.6.1 Overspeed Power Regulation Performance Metrics

Fig. 4.8 shows the BEMT prediction of the C_{P} and C_{T} performance of the base case rotor. This was used to identify the characteristics of rotor performance which were advantageous for operation in OSPR, and those which were detrimental. Important features of this figure are:

- The optimum operating point at λ_{O} where the maximum efficiency, C_{PO}, occurs. At this operating point $C_{\text{T}} = C_{\text{TO}}$.
- The runaway point, where efficiency drops to zero and C_{Prw}, C_{Trw} and λ_{rw} occur.
- And, between these two, some position where C_{Povs} and therefore C_{Tovs}, λ_{ovs} and Ω_{ovs} occur.

As Eq. (4.53) indicates, the value of C_{Povs}, and thus of λ_{ovs}, C_{Tovs} and Ω_{ovs}, depend on the site and turbine configuration.

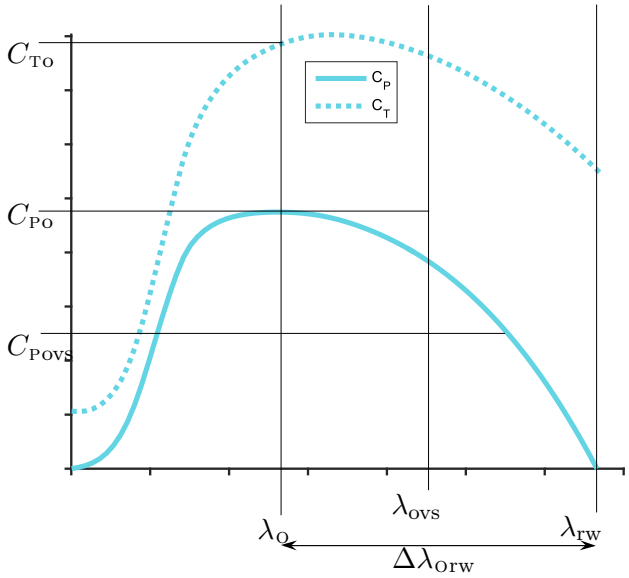

Figure 4.8: BEMT prediction of performance curves of base case, full-scale rotor, showing position of significant operating points and metrics of performance for overspeed power regulation

As discussed, a steeply negative gradient on the RHS of the C_P-λ, to give the required drop in C_P with a reduced increase in λ, was the key design requirement for OSPR. Improvements in this characteristic would result in rotor performance curves of an increasingly appropriate shape for OSPR, avoiding high rotational velocities. The metric used to measure this - and therefore the primary metric - was $\Delta\lambda_{o\ rw}$. A second metric was the rotor's angular velocity at the overspeed point, Ω_{ovs}, directly quantifying Ω at the crucial operation state. Both these metrics were required as the former gave insufficient information to ascertain whether cavitation would occur, but the latter gave no clear indication of the effect of a blade parameter change on the *shape* of the performance curve. As the value of C_{Po} is so influential on the annual energy output from a turbine, it was of benefit in this blade design process to gain an appreciation of blade design alterations which cause changes in the maximum efficiency the rotor could achieve. C_{Po} was therefore set as the third metric, improvements in which were measured as positive changes from the base case. C_{To} was set as the fourth metric, providing information on the effect of blade design changes on the thrust characteristics. This is a useful metric as C_T may be a limiting criterion; increases from the base case value in this metric were therefore defined as negative effects.

This reasoning gave a set of four performance metrics to be used in this design methodology:

- $\Delta\lambda_{o\ rw}$
- Ω_{ovs}
- C_{Po}
- C_{To}.

A general formula was used to calculate change in each metric, M, between the base case blade design value, M_{bc}, and that of each discrete design iteration, M_j. This formula took the form

$$M = \frac{M_{\text{bc}} - M_j}{M_{\text{bc}}} \tag{4.60}$$

for all cases except for C_{Po}, for which it had the form

$$M = \frac{M_j - M_{\text{bc}}}{M_{\text{bc}}} \ . \tag{4.61}$$

These fractional values were then expressed as percentages. The impact of blade design alterations could then be measured as the percentage change in the defined metrics. Setting the equations so as to define a positive change as an improvement, and negative change as indicating detrimental effects facilitated the sensitivity analysis impact assessment described in Section 4.6.3.

4.6.2 Cavitation Analysis

The subject of cavitation inception was introduced in 2.2. It has been discussed that cavitation is not a favourable flow behaviour; as such, explicit consideration of the inception of cavitation was required in the OSPRblade design methodology.

Though it is a simplification to state that cavitation occurs when the local fluid pressure, p_{L}, on a blade reaches the vapour pressure of the fluid, p_{v}, comparison between these two values is seen to be a fair measure of the likelihood of cavitation inception, should the flow environment continue in this state. This method of cavitation inception analysis has been previously used in, for example, the projects reported in [99] and [47], in each of which verification by comparison to experiments presented in the former has shown the method to be appropriate. This was therefore the method adopted in the present research.

As in [16], the local pressure distribution across a 2D aerofoil can be expressed with the coefficient of local pressure, defined as

$$C_{\text{pres}} = \frac{p_{\text{L}} - p_{or}}{\frac{1}{2}\rho W_r^2} \tag{4.62}$$

of which the minimum negative value - that is, the coefficient of the maximum suction pressure - is termed $C_{\text{pres, min}}$. The value of $C_{\text{pres, min}}$ on a 2D aerofoil changes with α, and can occur at the aerofoil nose, back or front faces.

A dimensionless cavitation number for a blade section at radius r can be defined, again as in [16], [99] and [47], as:

$$\sigma_r = \frac{p_{or} - p_{\text{v}}}{\frac{1}{2}\rho W_r^2} \tag{4.63}$$

where $\frac{1}{2}\rho W_r^2$ is the dynamic pressure, and the absolute hydrostatic pressure, p_{or}, is

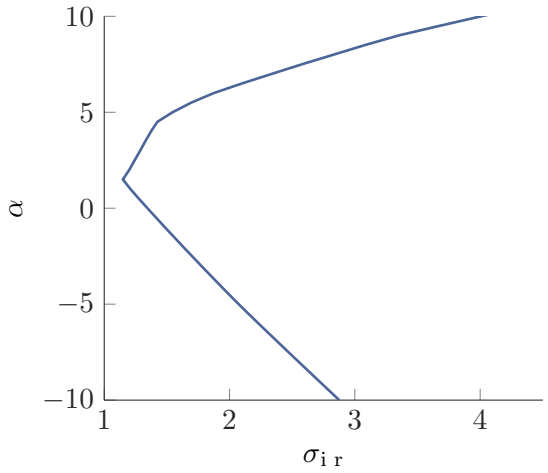

Figure 4.9: Cavitation envelope of the NREL S814 aerofoil in at $Re = 1 \times 10^7$.

defined as

$$p_{or} = p_{\text{atm}} + \rho g h_r \tag{4.64}$$

The hydrostatic pressure will be at its smallest value when a blade is in the top dead-centre position, meaning that if cavitation occurs on a rotor, it will occur first on a blade at this position.

As Eqs. (4.62) and (4.63) show, if the minimum negative $p_{\text{L}r}$ on a blade section is equal to p_{v}, then σ_r will be equal to the minimum negative value of $C_{\text{pres}r}$. Therefore, an inception cavitation number can be defined as

$$\sigma_{\text{i}r} = -C_{\text{pres min}r} \tag{4.65}$$

Assessment of cavitation inception on the blade designs therefore required comparison of σ_r and $\sigma_{\text{i}r}$, for each blade element, at each operation point. The $C_{\text{pres, min}}$ data required for this analysis was output from the aforementioned XFOIL analyses, as a function of α. Fig. 4.9 gives the cavitation envelope for the NREL S814 aerofoil, and marks the cavitation-free and cavitation inception zones. The likely location on the aerofoil of each cavitation instance on the envelope indicated.

4.6.3 Visual and Numerical Performance Analysis Tools

Several component tools were developed in the design of this methodology, which provide visual feedback based on numerical outputs from the analysis of each blade design alteration.

Design Space Analysis

Though the alterations to the blade design were initiated simultaneously with the alteration functions, each blade design alteration entailed a discrete change from the base case, allowing a sensitivity analysis to be undertaken with the One-at-a-Time

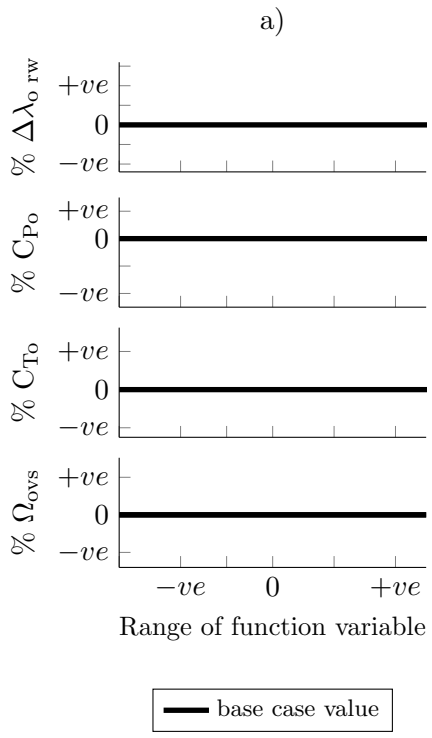

Figure 4.10: Black design space, illustrating the concept and showing how the base case performance provides the zero change value, against which the alteration to performance of any blade permutation can be measured with the OSPR metrics

(OAAT) method [130]. A design space analysis method was developed to provide numerical-visual feedback of the impact on each performance metric had by each design alteration.

As shown in the blank Design Space in Fig. 4.10, the basic concept of the Design Space approach was that the impact made on the suitability of a rotor design for OSPR, according to each OSPR metric, could be measured on a series of stacked y-axes, with positive impact above the base case, or zero, line, and detrimental impact below. Because the OAAT blade design changes were implemented with alteration functions, the range of the function variable could then measured on an x-axis, common to each metric's sub-plot.

Fig. 4.11 shows a Design Space with some example blade permutation results. For each blade design permutation, the results of the Design Space sensitivity analysis were displayed with circular markers. The commonly-used stem-type plot was eschewed in favour of the simpler dot marker to reduce complexity of the plots and increase the visual impact. Though none of the metrics explicitly measure cavitation inception, it was possible to include a level of cavitation analysis in the Design Space by including a conditional statement in the code, altering the marker-fill according to whether cavitation inception was predicted or not in each instance.

Fig. 4.11 illustrates the advantages of this approach:

- Plotting the impact of OAAT changes along x-axes allowed the impact of both

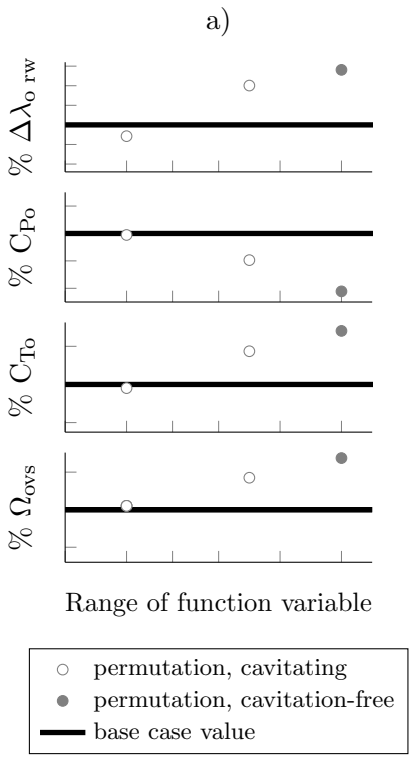

Figure 4.11: Populated design space showing how the effect of example blade permutations can be measured and compared, how trends and associations can be identified

individual parameter alterations to be studied

- At the same time, intra-parameter trends and gradients over the alteration range were immediately obvious
- It was further possible to immediately grasp inter-metric trends, i.e. whether positive impact on one metric was attended by positive or by detrimental impacts in other metrics
- While no information was give as to how close, or otherwise, a blade permutation was to the inception of cavitation, it was immediately obvious whether cavitation inception was predicted or not
- Furthermore, it was clear whether mitigation of cavitation inception was rapidly or slowly achieved with the implemented blade design alterations.

A Design Space was required for each blade design parameter altered. Three Design Spaces were created for the first stage blade design analyses - one for each parameter changed. These three spaces were stacked horizontally on a set of common y-axes, giving an overall Design Space, allowing further comparisons to be drawn on an inter-parameter level.

Cavitation Analysis

As discussed in Section 4.6.2, cavitation inception is deemed to occur when C_{press} (i.e. σ_{ir}) and σ_r are equal. For each flow condition investigated in the design platform, the values of σ_{ir} and σ_r for each blade element were calculated and compared numerically for each blade design. As their definitions in Eqs. (4.63) and (4.65) indicate, these values were a function of λ; as λ increased, for each blade element, σ_r decreases towards the value of σ_{ir}. Plotting these two cavitation-related numbers against λ, for elements all along the blade, gave a more detailed visual tool to assess the how close a blade was to the occurrence of cavitation, and the location(s) and extent of inception on the blade, across the entire operating range.

Fig. 4.12 shows the cavitation inception analysis plot for the base case blade, as assessed within the design platform. As the figure shows, σ_{ir} was plotted for every element, giving a dense band of cavitation envelopes, beneath each strand of which cavitation would occur on the relevant blade section. The σ_r curves for the tip and root elements were plotted, along with those for the elements at increments of 10% of the blade length. Fig. 4.12 illustrates that extensive cavitation would occur were the base case blade to be used in OSPR at the depth and flow speeds of the design platform.

Through comparisons between this method and experiments it was found, in [46], that the use of XFoil to generate the C_{pres} data was a reliable method for preliminary design stages. It is important to note, though, that it was also found that this over-predicted cavitation on the upper surface of the aerofoil; this method is therefore known to give a slightly conservative analysis of cavitation inception.

No assumptions were made in the development of this methodology as to whether predicted cavitation inception as determined by the employed method would be acceptable in a given design scenario. It may be possible that cavitation inception thus predicted could be acceptable over a certain percent of the blade. Therefore, as the blades comprised 140 elements, a written warning feedback was also set up in order to highlight the occurrence of cavitation should cavitation occur at any of the elements between those for which σ_r was displayed. This would inform the engineer of a greater extent of cavitation than displayed in the plot, should this be the case, and prompt alteration of the elements for which the cavitation number was displayed in the plot.

For each blade iteration, comparison of these plots indicated whether the design alterations induced more or less cavitation along the blade.

Diagnostics plots: α_r and dQ_r against r

The distribution of torque, Q, developed along the blade, and the elemental α are heavily influenced by the twist and chord distributions. It was possible to undertake a deeper inspection of blade performance by considering the local α_r and the torque developed by each blade section, dQ_r. This was achieved using plots of the distribution of α_r and dQ_r across the blade, at the optimum and overspeed operating points. A similar technique

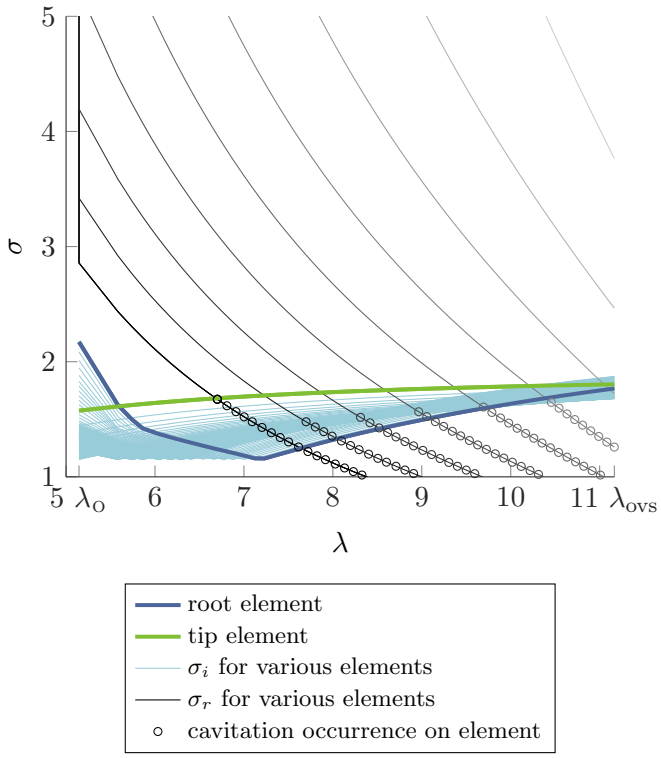

Figure 4.12: Cavitation plot for base case blade. The figure shows elemental cavitation numbers decreasing, as λ increases, towards the elemental cavitation envelopes, beneath the meeting of which predicted instances of cavitation inception are shown. Tip and root cavitation inception envelopes highlighted. Extensive cavitation inception predicted from ca $\frac{1}{3}$ of the way between λ_o and λ_{ovs}.

was used by Biskup et al. in [87], as discussed in Section 2.6. Analysis of these plots facilitated diagnosis of blade performance by allowing important or influential sections of a blade design, and possible improvements to be identified. Along with the other visual tools, these plots were set to appear in the analysis of each blade design. The diagnostic plots of for the base case are shown in Fig. 4.13.

The usefulness of these plots increases in the later stages of design; as an example though, it can be seen from Fig. 4.13 a) that the α_{tip} at λ_o was -1.63 ° and this coincided, according to Fig. 4.12, with a σ_r of 2.86. Taking these numbers, then, to Fig. 4.9, it can be seen that the prediction of *no cavitation* was because this α_{tip}-σ_r combination gave a point well inside the cavitation-free envelope. This kind of analysis will be further discussed in Chapter 5.

Plots of power and thrust in the design platform

The final stages of the methodology make greater use of the Cavitation and Diagnostics Plots, utilising the two-way information flow path shown in Fig. 4.1 between the manual process analysing design parameter effects and the data output from the design analysis. A further set of plots within the set of Visual-Numerical Tools are those of the actual power captured, and the thrust force, over the operation range defined in the design platform; Fig. 6.4 shows these for the base case blade design. Having worked towards a

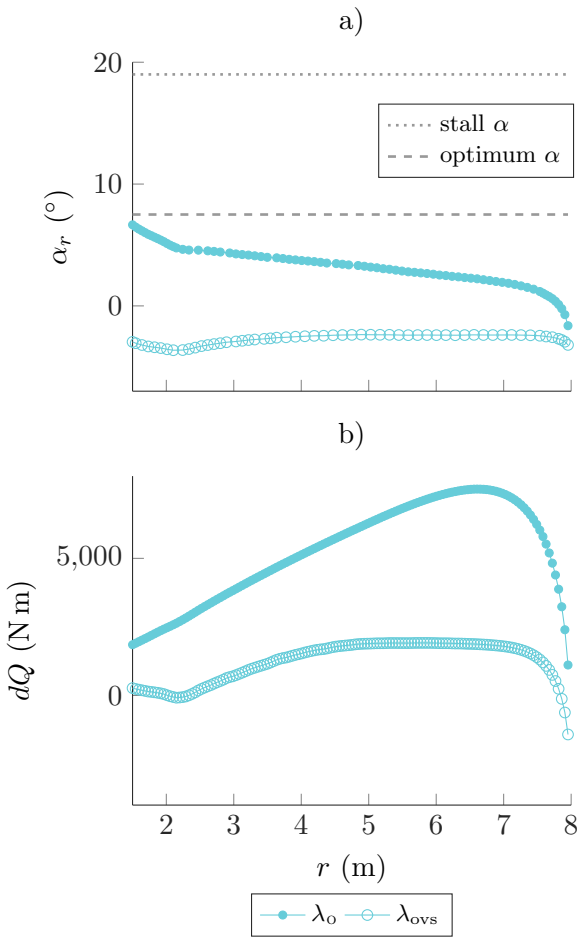

Figure 4.13: Diagnostic plots for base case blade, showing plots of local angle of attack, α_r, and elemental contribution to torque, dQ.

blade kind which operates with better success in the OSPR design platform, these plots should give information with regards to whether the design requirements would be met with (any of) the blade(s) in question.

4.7 Base case blade performance in ospr

A plot of the base case rotor design power and thrust (multiplied by 5 for visual clarity) output operated in the flow regime defined in the design platform plots of are shown in Fig. 6.4. Alongside, a plot of the available power and power at the Betz limit are shown for comparison. From the power plot, is clear that the objective of regulated power would be achieved, and the absence of discontinuities illustrated that no numerical errors occurred. However, the thrust plot showed that should the base case blade design be operated in OSPR, the thrust force would immediately increase as the turbine transitioned to OSPR.

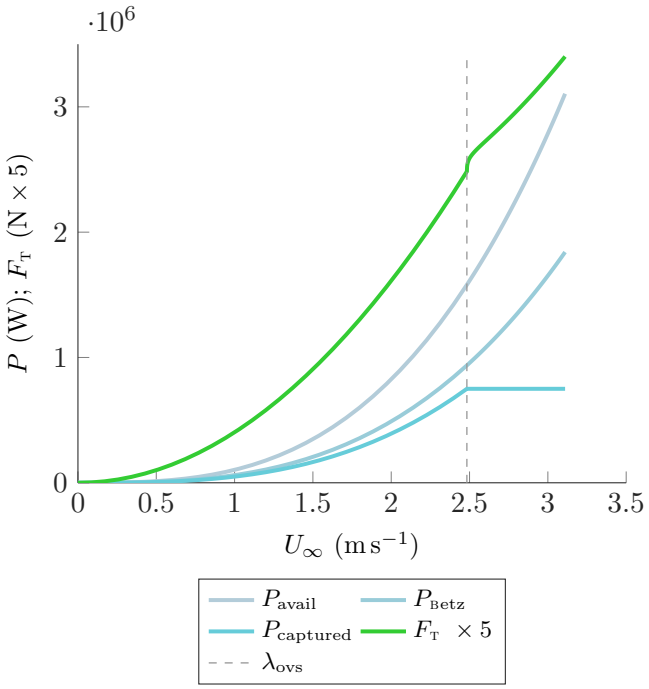

Figure 4.14: Power and thrust for base case blade operating in specified design platform. The captured power, $P_{captured}$ is shown alongside the power available at the Betz limit and in the flow. Thrust force is multiplied by 5 for visual clarity, showing the immediate increase in axial loading as turbine transitions to overspeed power regulation.

4.8 Further analysis - structural feasibility

A further stage of analysis developed but not included in the main design methodology was a structural feasibility study. The theory and method of implementation developed for this are presented in Appendix B.

4.9 Proposed application process

4.9.1 Reduced effort, increased learning

The design methodology was formed such that its component parts would facilitate a design process more rapid and thorough than one purely based on iteration/insight, and produce more experiential knowledge than an optimisation-algorithm blade design process. However, the proposed application procedure for the methodology remains iterative in that for each series of function-based alterations made, the engineer must use the tools developed to gain an understanding and then apply this knowledge in the proceeding set of alterations.

4.9.2 Early stage design alterations

The applied function-based alterations allow many versions of a type of blade design parameter change to be trialled, and, for each alteration made, insight to be gained and

shareable, experiential knowledge to be created. The initial function variables should have a wide range, while the First Stage results should feed forwards to allow more specific or more targeted alterations to be determined. These function variables may therefore be fewer and of smaller range than the preceding set, resulting in an iteration loop which spirals towards a focal point – though, in coupling alterations made on more than one design parameter is would be wise to maintain a wide range on the function variable of at least one parameter.

4.9.3 Fine-tuning hand-alterations

In the final stages, basing the alterations on functions to quickly capture a greater range of alterations should no longer be necessary, as the remaining kind of alteration(s) required to fulfil the Design Requirement should be by then determined, informed by the fore-going Design Space analyses and continued use of the Visual-Numerical tools. It is the recommendation that blade design alterations at this stage should be undertaken by hand, with the visual aid of plots of the chord and twist distribution alongside the defined Visual-Numerical tools. Areas of the blade which could be better exploited or which are in danger of cavitation can thereby be identified, and – drawing on the knowledge gained in use of the design methodology tools – measures taken to alter the influential design parameter.

In this stage, the specific design requirements are of increasing importance and use of the plots of power and thrust such as in Fig. 6.4, alongside the other Visual-Numerical Tools, should strongly inform the subsequent alterations made. Because it is not the recommendation to continue using alteration functions at this stage, automatic creation of the Design Space tends to be by-passed; however, either direct quantification of the maximum C_{P}, C_{T} or use of the Design Space analysis with hand-input data should continue as part of the methodology.

4.10 Conclusion

This chapter presented the composition of a blade design methodology for Overspeed Power Regulated tidal turbines. It detailed the theoretical bases and implementation of each component aspect of the Methodology.

It has been shown that should the base case blade design be operated in OSPR within the specified design platform, the rotor would experience extensive cavitation inception in $\frac{2}{3}$ of the overspeed region (between λ_{O} and λ_{ovs}), initiating at the tip at $\frac{\lambda_{\mathrm{ovs}}-\lambda_{\mathrm{O}}}{3}$. It should be noted, as mentioned above, deterministic cavitation inception analyses such as this method do not take into consideration the time required for nuclei to develop into cavities, possibly increasing the conservatism; on the other hand, neither does it account for molecular inclusions in the water, and therefore the cavitation-encouraging molecules present in the turbulent seas, including air and salt molecules, may counter-act the

conservative nature of the predictions to some degree. In any case, this method should be viewed as a design tool for early stages, and it would be appropriate to generate more specific cavitation data before the final design stages of a blade set.

With this blade design, the thrust force in the overspeed region would increase significantly, by 37 %. This performance is not favourable and would most likely result in extensive cavitation damage and performance alteration to the blades, while the high structural loads must result in highly expensive station-keeping systems.

The following chapter will present the application of the methodology to a specific set of design requirements designed to test the potential of the design methodology and the operation technique of OSPR itself. A blade design will be worked towards which meets the specified design requirements. This will be followed by details of the manufacture and empirical testing of the blade developed, at prototype-scale, in the tow tank at Strathclyde University.

Chapter 5

Application and empirical verification

This chapter presents an application of the OSPR blade design methodology to a particular design scenario - a set of design requirementse applied within the design platform as laid out in the foregoing chapter. A series of alteration functions were applied to the base case blade design in three main stages. In Stage One, a function was applied to each of the blade design parameters set as variables in the Deign Platform, each with the function variable set to a wide range. In Stage Two, additional alteration functions were applied to the chord distribution, a selection of which were then then coupled with the Stage One alteration to the twist distribution. Stage Three comprised hand alterations informed by the effects on cavitation and blade performance as determined using the Visual-Numerical tools of the design methodology. The end result was a new OSPR blade design which conformed to the set design requirementse.

This blade design was then produced at prototype scale, and tested in the Tow Tank facility at Strathclyde University, producing prototype-scale empirical performance data. Comparison between this data and the BEMT prediction confirmed that the power performance of the new blades was well predicted, verifying that the OSPR blades regulate power as designed. The thrust performance, however, was not as well predicted. Each of these results will be discussed in this chapter.

Although the new OSPR blade was designed to perform well at full-scale, comparison between the two sets of empirical data - for the base case and new OSPR blade designs - showed that the increase in λ and Ω between the optimum and runaway points was reduced by the new OSPR blade design even at the prototype scale.

5.1 Design requirements

The set parameters of the design platform were as detailed in Section 4.3. A set of design requirementse were defined:

- In order to push the capabilities of the design methodology, the foreseen challenge

of increased likelihood of cavitation inception associated with the OSPR technique was considered first, and the Design Requirement of *no cavitation inception* was set.

- The possibility of increased thrust loads, also associated with increased turbine rotational velocity, was considered and therefore a Design Requirement that C_{To} *at* λ_{O} *should not exceed that of the base case* was set.
- The third Design Requirement, reflecting the primary purpose of turbine blades, was that *the maximum value of* C_{Po} *obtainable under the first two design requirementse should be achieved.*

5.2 Stage One parameter alterations

5.2.1 Alteration functions

The first set of alterations were implemented as below, where the range applied to the function variables were as stated in Stage One of Table 5.1.

- Simple changes to the value of β; function variable: $\delta\beta$

$$\beta_{\text{permutation}} = \beta_{\text{base case}} + \delta\beta \ . \tag{5.1}$$

- Proportionally linear alterations to θ_r - from zero at the root to a value ζ at the tip; function variable: ζ

$$\theta_{r\ \text{permutation}} = \theta_{r\ \text{base case}} + \frac{\zeta}{L_{\mathrm{b}}}\ r \ . \tag{5.2}$$

- A scaling factor, τ, applied equally to c_r at each blade section; function variable6: τ

$$c_{r\ \text{permutation}} = \tau\ c_{r\ \text{base case}} \tag{5.3}$$

5.2.2 Illustrative plots

Fig. 5.1 c) and d) illustrate the Stage One design changes made in plots of chord and twist distribution along the blade radius. Fig. 5.1 a) and b) respectively illustrate a twist alteration to 13 ° at the tip and an alteration to the chord of scaling by a factor of 1.6. These particular alterations are also highlighted in Fig. 5.1 c) and d). In each subfigure, the base case blade geometry is highlighted with a thicker black line.

5.2.3 Design Space analysis

The design space results from the first stage of blade design parameter alterations are presented in Fig. 5.2. For reference, Fig. 5.1 illustrates examples of the kind of design

Table 5.1: The blade design parameters, manner and range of alterations made in the Stage One design changes

Parameter	**Alteration**	
	Description of function	Range of function variable
β	Setting angle altered	$-7° \leq \delta\beta \leq 13°$
θ_r	Proportionally linear alterations applied from zero at root to ζ at tip	$-17° \leq \zeta \leq 17°$
c_r	Multiplied by scaling factor τ	$0.1 \leq \tau \leq 3$
	Stage Two Alterations	
c_r	Proportionally linear addition to chord length, from zero at root to $T \cdot c_{\text{tip}}$ at tip	$0.3 \leq T \leq 1.3$
c_r	Parabolic addition to chord length, from zero at root to $\psi \cdot c_{\text{root}}$ at tip to zero at tip, with $T = 0.5$	$0.2 \leq \psi \leq 1.8$
	Stage Three Alterations	
θ_r	Proportionally linear alterations applied from zero at root to ζ at tip	$-1° \leq \zeta \leq 17°$

alterations made to produce these results. These plots showed that there were only seven blade permutations which eradicated cavitation, four resulting from alterations to β, and three from alterations to θ_r. Each of these blade designs had significantly reduced efficiency.

The sensitivity analysis showed that the primary metric, $\Delta\lambda_{\text{o rw}}$, was least sensitive to the applied c_r alterations. For the same degree of alteration, the sensitivity of $\Delta\lambda_{\text{o rw}}$ was greater to the alterations applied to β than to those applied to θ_r, having a greater rate of change in the former. As Fig. 2.12 shows, positive additions or alterations, respectively, to the twist or pitch reduced the angle between the tidal flow and the chord line at more blade stations, pointing the leading edge of the aerofoil section towards the incoming flow; in both cases this gave a positive impact on $\Delta\lambda_{\text{o rw}}$. The finding that blade designs with alterations of positive ζ and $\delta\beta$ values resulted in a more rapid feathering of the blades as U_∞ increased was therefore to be expected. However, it was possibleto achieve slightly greater impact on this performance metric by large alterations to θ_r than by the largest alterations applied to β. Alterations of more than 13° to β resulted in a blade with such poor efficiency that no power regulation was required at all; giving a limit to the possible positive alterations to β.

These two parameter alterations were also seen to have the greatest impact upon the second metric, Ω_{ovs}. Predicted cavitation inception was accordingly eradicated by alterations of $\delta\beta$ before alterations of ζ by the same degree. Reflecting on the resulting α_r for each blade section from these alterations, this is not surprising. The improvements

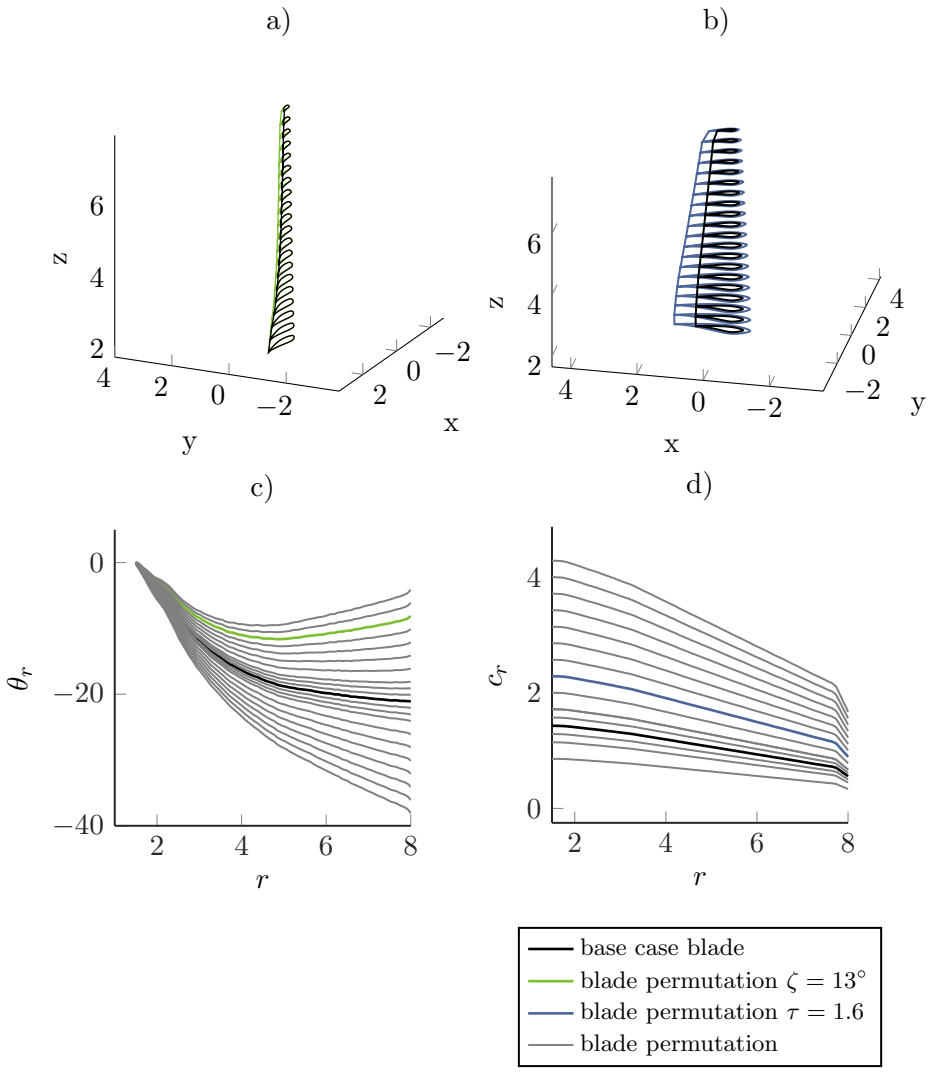

Figure 5.1: Graphical representation of comparison to base case blade of: a) and c) blade design iterations with proportionally linear twist alterations, including to $\zeta = 13°$ at the tip; b) and d) blade design iterations with scaled chord alterations, including by $\tau = 1.6$.

in the first two metrics made by alterations to β and θ came at the great expense of reductions in C_{Po}. The impact of altering β was greatest, with the consequence that the first cavitation-free blade permutations - with $\beta = 8$ ° and $\zeta = 13$ ° - had a similar C_{Po}, changed by -29.3 % and -32.6 % respectively from the base case. The plots of α with r, shown in Fig. 5.4 indicated that this decrease in C_{Po} occurred due to the resulting α for each blade station moving away from the optimum value at which lift force per drag force is maximised.

A significant, but reduced impact was made in this metric by scaling alterations made to the chord length. This impact was due to the increase in the lifting surface associated with an increase in chord length, and, as the plots of α and dQ showed, an increase in the values of α occurring over the blade, each of which increased the torque produced.

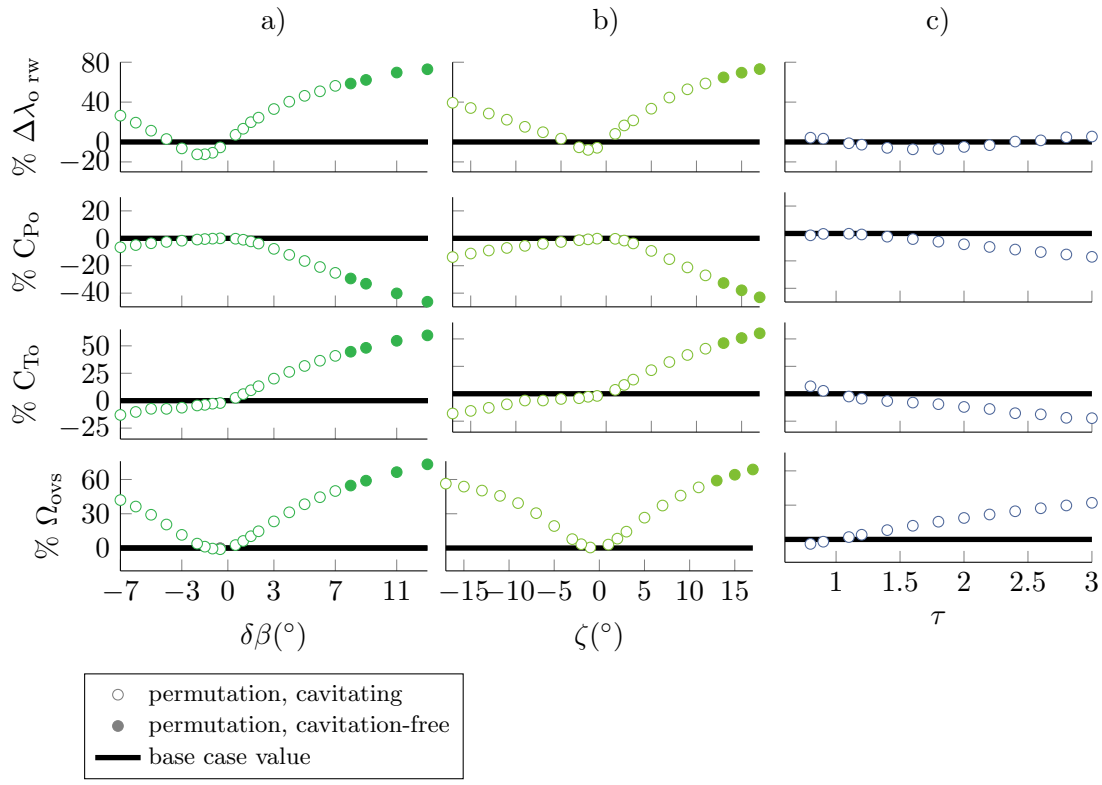

Figure 5.2: Design Space analysis, showing the results of the sensitivity analysis of OSPR performance metrics to first stage blade design parameter alterations to: a) the pitch setting, where +ve $\delta\beta$ changes indicate a root pitch which sets the root leading edge closer to the tidal flow vector; b) the twist distribution, where +ve ζ values indicate a blade with less twist along the span; and c) the chord distribution, where τ values greater than 1 indicate a blade with larger chord and cross-sectional area values.

The performance metric C_{To} was most sensitive to changes in β, its sensitivity having, again, a steeper gradient in response to $\delta\beta$ alterations than either ζ or scaled-c_r alterations. Alterations to β made in the positive sense reduced C_{To}, whereas those made in the negative sense had a detrimental effect on this metric. This was due to increases in α_r along the blade, resulting in an overall greater contribution to force in the axial direction (along the x axis). That the metric C_{To} was sensitive, though to a lesser degree, to the scaling alterations in c_r was, as for the impact on C_{Po}, due to the increase in the lifting surface producing greater lift and drag forces, resulting in a greater or lesser contribution to force in the axial direction for vales of τ smaller or greater than 1, respectively.

In general,the scaling alterations made to the chord length were less effective than either of the other alterations, and extremely large root chord lengths would result from the alterations which had greatest effect; this could cause difficulties in manufacturing and assembling a turbine, and would greatly add to the material mass and cost.

5.2.4 Cavitation Results

Cavitation was a consistent flow behaviour on most of the rotors in the Stage One blade design permutations; however, as the design space indicated, seven blade designs were successful in mitigating cavitation inception: those with parameter changes of $\delta\beta \geq 8°$ and $\zeta \geq 13°$.

In Fig. 4.12, the cavitation analysis plot for the full-scale base case design was shown. Fig. 5.3 shows cavitation analyses for a sequence of blades designs with alterations made to β (Fig. 5.3 a) - d)) and θ (Fig. 5.3 e)-h)). In each case, the first plot shows the cavitation analysis for the smallest change made in the series; the subsequent plots give the cavitation analysis as the relevant Function Variable increased, the last of each being the first blade permutation in that series for which cavitation inception was not predicted.

Referring back to the base case cavitation inception analysis, the vertical decrease in σ_r in the region $0 \leq U_\infty \leq U_{\infty\max}$ could be seen in this figure, occurring at $\lambda_o \approx 5$; no cavitation was predicted in this operation range. The same was true for each of the plots in Fig. 5.3; cavitation was not a flow behaviour predicted at the optimum operating point for any blade permutation.

Cavitation was, however, predicted to begin occurring at the tip of the blade at $\lambda = 6.70$ for the base case blade, and $\lambda = 6.68$ and $\lambda = 6.69$ for the blade designs $\delta\beta = 0.5°$ and $\delta\zeta = 1°$. Fig. 5.3 clearly shows that as the blade permutations were increasingly altered, cavitation inception occurred at an increasingly later operating point. With $\delta\beta = 8°$ and $\delta\zeta = 13°$, as Fig. 5.3 d) and h) show, no cavitation inception was predicted at all. In Fig. 5.3 h), the cavitation number of the tip element was perceptibly distanced from the tip element cavitation inception envelope, showing that cavitation was avoided by more than a just hair's breadth.

Although the fulfilment of the cavitation-free operation Design requirement was accompanied by significant improvements in terms of C_{To}, as indicated in the design space these alterations also resulted in a significant drop in C_{Po} which meant that the blade designs avoiding cavitation did not meet the remaining Design Requirement.

5.2.5 Diagnostic Plots

To investigate the cause of the performance degradation, the Diagnostic Plots were produced for the fist cavitation-free blade permutations, and plotted alongside the performance of the base case blade. Fig. 5.4 shows these plots.

The plots of α_r in Fig. 5.4 a) showed that, at λ_{o}, the mid sections of the altered blade designs were operating closer to the optimum α of 7.5, giving rise to the increase in dQ seen for the mid-sections of these blades in Fig. 5.4 b). However, Fig. 5.4 b) also showed that the upper regions of the altered blade designs produced less torque at λ_{o} than those of the base case blade; a drop-off in torque contribution in this region was particularly notable for the $\delta\zeta = 13°$ blade design. Considering the reduction in Ω over

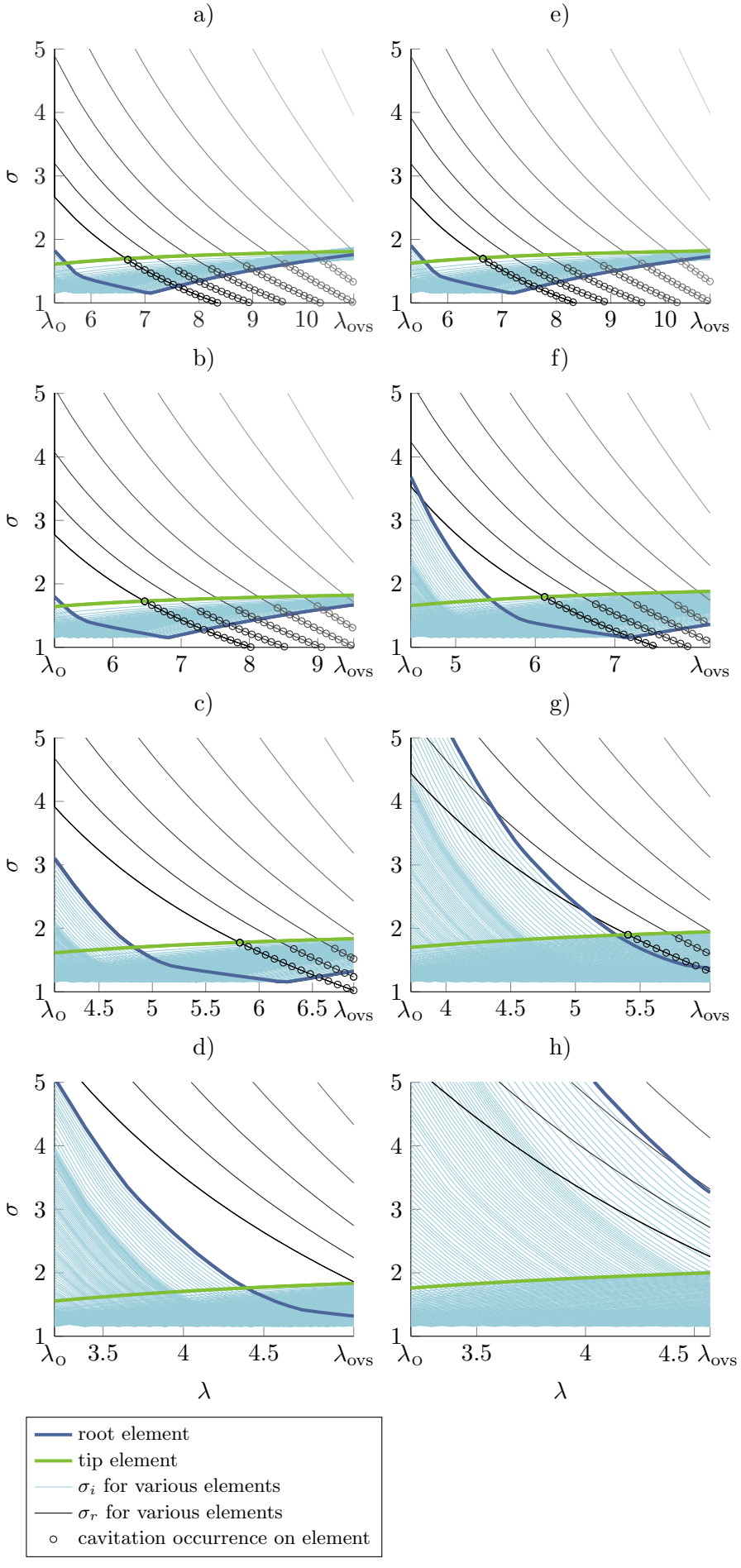

Figure 5.3: Cavitation diagrams illustrating progressive elimination of cavitation inception on blades with: pitch setting alterations of a) 0.5°, b) 2°, c) 5° and d) 8°; and linear twist distribution alterations of e) 1°, f) 5°, g) 9° and h) 13°.

the operating region of the altered blade designs compared to the base case, a matching increase in Q would be required to maintain the P_{mech} levels achieved by the base case blade design.

A further interesting results was that the base case blade design operated at λ_{ovs} with low values of dQ across the blade and had a small region of negative torque at the blade tip. The lower speed of the $\delta\beta = 8$ blade design meant that the dQ values were higher than those of the base case blade at this operating point. In contrast to either of these though, the $\delta\zeta = 13°$ blade design displayed a further increase in dQ in the lower two thirds of the blade, but a significant region of negative torque for around the upper meter of blade. These performance characteristics were reflected in the α_r plots which showed a generally flatter curve at each operating point for the base case blade, and an increasing gradient of the curve with the $\delta\beta = 8$ and $\delta\zeta = 13$ permutations. Reflection on the local pitch, ψ values in each blade gives the explanation required, illustrating that taking the blade twist further away from the "ideal" distribution for maximising C_{Po} in VS operation – discussed in, for example, [11, ch. 3] – blade designs which reach their peak performance and then reduce their efficiency more quickly may be achieved, due to more rapid alteration in the local flow angle occurring with the altered local twist. As this suggests, and as will be seen in Fig. 6.3, this does also result in a smaller range of λ for which performance is optimum; this is often referred to as a "peakier" power curve.

A performance feature also identified using Fig. 5.4 a) were the highly negative angles of attack occurring at the tip of the $\delta\zeta = 13°$ blade design at λ_{ovs}. As comparison with Fig. 4.9 showed, such values of α_r are within the region of concern in the NREL S814 cavitation envelope and can cause front face cavitation. Although, as previously noted, this blade did not exhibit cavitation behaviour, the extreme α_r values shown were of interest as they were thought to be most likely ensuing from the severe alteration to θ_r towards the tip illustrated in Fig. 5.1 c).

The plots also showed that, due to the slower Ω at the optimum operating point, the root to mid sections of the altered blades were operating at much higher values of α, yet had not exceeded the stall angle, which (in the steady flow assumed) would ensure an equally stable working flow environment on these altered blade designs as on the base case blade.

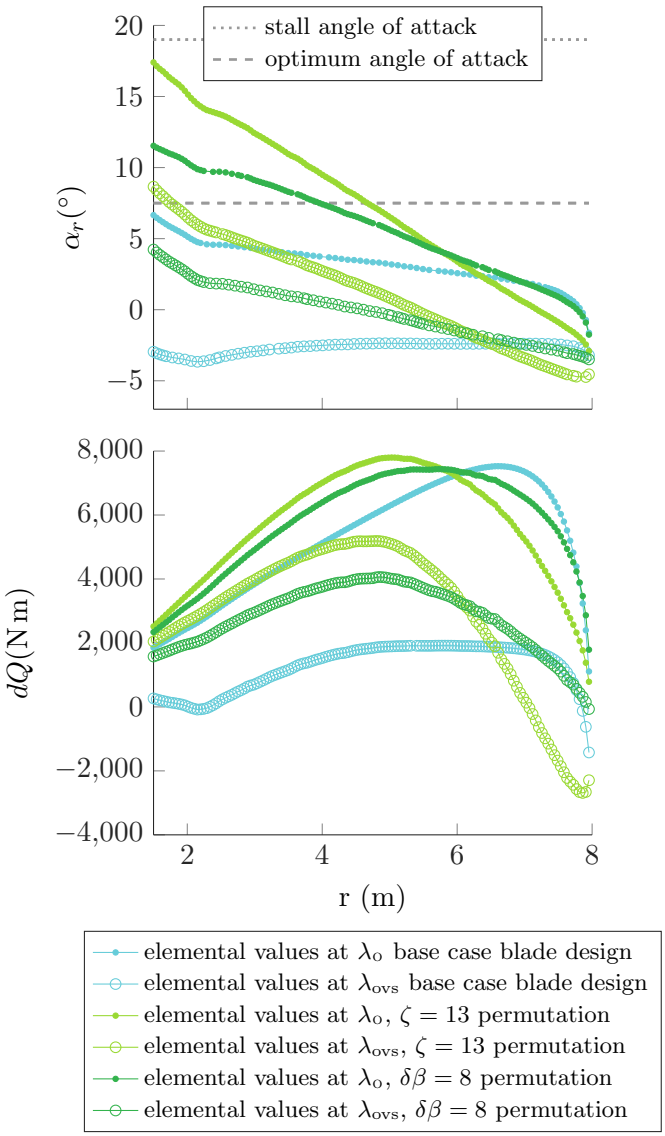

Figure 5.4: Diagnostic plots of the base case blade with the $\delta\beta = 8°$ and $\zeta = 13°$ blade permutations.

5.3 Stage Two Design Alterations

5.3.1 Distribution alterations to chord length

Analysis of the results from the Stage One design alterations showed that a Stage Two design process, using the same methodology, would be required to make alterations with which the requirement for improvements in C_{Po} could be worked towards. In Fig. 5.2 c), the design space analysis showed that increased chord length had a positive effect in the metric Ω_{scrovs}. Though none of these alterations increased C_{Po} of the base case blade, it was considered possible that the optimised pitch setting had contributed to this, and that increasing the lifting surface of a non-optimised rotor design may result in an improved C_{Po}. This, combined with the noted improvements in Ω_{scrovs}, suggested the possibility that alterations to the chord length coupled with alterations to θ or β

may allow cavitation-free operation at reduced values of ζ or $\delta\beta$, respectively. This, if successful, could result in cavitation-free blade permutations with a reduced impact on C_{PO}.

Alteration functions

Analysis of the Stage One design alteration process indicated that the applied Stage One alterations to c_r, which had the effect of scaling up the size of all the aerofoils by the same factor, had a similar scaling-type effect on the α, dQ over the blade. Considering the effect on the *distribution* of these parameters had by *distribution* alterations to the twist, rather than simple scaling alterations, a set of targeted function-based Stage Two alterations – detailed in the relevant rows of Fig. 5.1 – were made to the distribution of c_r.

- Proportionally linear increases were made to the chord length, increasing the chord to T, a proportion of the original chord tip length; function variable: T

$$c_{r\ \text{permutation}} = c_{\ \text{base case}} + \frac{T c_{\text{tip}}}{L_{\text{b}}}\ r\ . \tag{5.4}$$

- To make use of the α_r values close to optimum on the blade mid-sections and augment the effects of the foregoing chord distribution alterations, these alterations were combined with the previous set, with T set to 0.5. The base case c_r distribution was altered with a parabolic added-chord function which peaked at values of $c_{\text{root}}\psi$, a proportion of the original root chord length, which was then added to the base case and T-altered chord distribution. A term x_{parab}, the same length as the radius array, was created between -1 and 1 using MATLAB function *linspace*. The square of this term created the base parabolic shape used to create the desired alteration functions; function variable: ψ (always of $-ve$ value, giving a "hogged" parabola)

$$c_{r\ \text{permutation}} = c_{r\ \text{base case}} + \frac{0.5 c_{\text{tip}}}{L_{\text{b}}}\ r\ + \left(\psi c_{root} x_{\text{parab}}^2 - \psi c_{root}\right) \tag{5.5}$$

  where

```
xparab = linspace(-1,1,length(c))
```

It was possible in this way to have greater control over c_r across the blade, and thus to effect an altered distribution of dQ. This resulted in a similar impact in the metrics with - as integration of the c_r distribution terms showed - a similar overall increase in the blade area but, significantly, a reduced increase in the blade root chord length, leaving more room between blade roots.

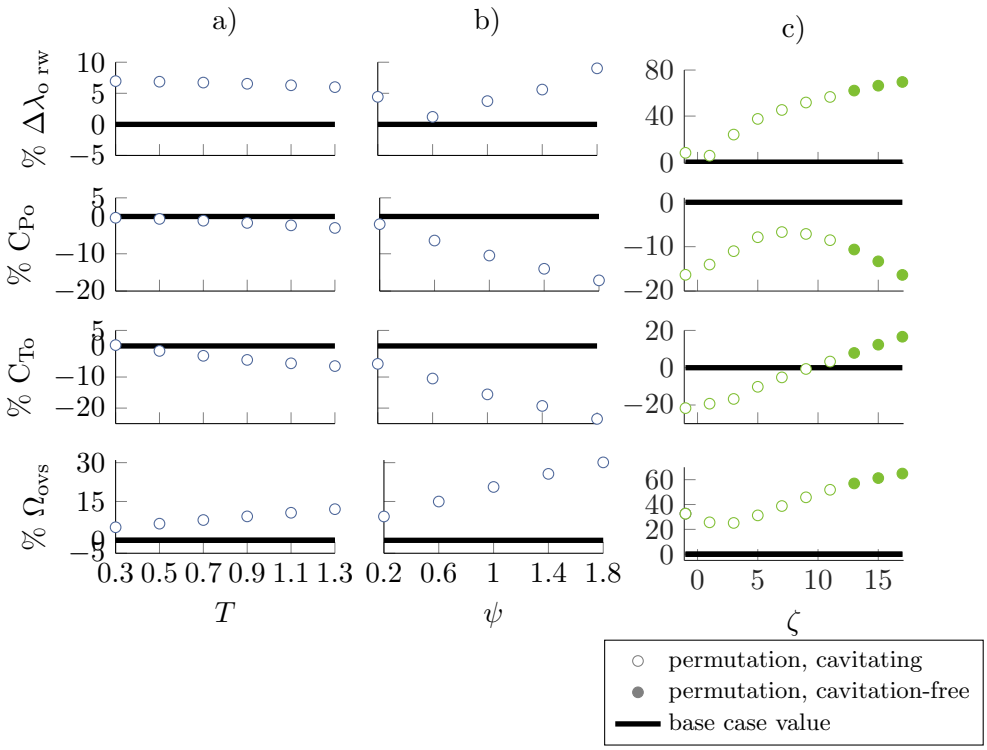

Figure 5.5: Design Space analyses of: a) and b) targeted alterations to c_r; c) combined alterations to c_r and θ_r.

Design space analysis

The design space result of this are presented in Fig. 5.5 a) and b). Fig. 5.5 a) showed that the same improvement – around 5% – was made in $\Delta\lambda_{\text{O rw}}$ with a proportionally linear alteration to the chord of $T = 0.5$ as was achieved by scaling the entire blade's chord by a factor of 3, and that this was at the expense of only 0.5% detriment to C_{P}, rather than 16%. However, though the gradient of the C_{P}-λ curve was thereby improved, the value of Ω was only improved by 6%, as opposed to the 29% achieved by the scaling factor alteration. Fig. 5.5 b) showed, though, that coupling this $T = 0.5$ alteration with a further parabolic alteration of $\psi = 1.4$ achieved at 26% improvement in the Ω_{ovs} metric to the detriment of 14% in C_{Po}; similar effects to the Stage One $\tau = 3$ alteration but, as **??** shows, a much reduced increase in overall blade volume and root chord length.

5.3.2 Coupled chord and twist distribution alterations

These effects introduced the possibility of transferring some of the improvements seen in Stage One, with β and θ alterations, to alterations on the chord distribution – i.e. the probability of useful outcomes in coupling such chord alterations with another of the Stage One alterations to β or θ. Therefore, in a second series of Stage Two alterations, blades with the chord distribution altered with T = 0.5 and $\psi = 1.4$ were coupled with alterations to θ_r of a range of ζ values.

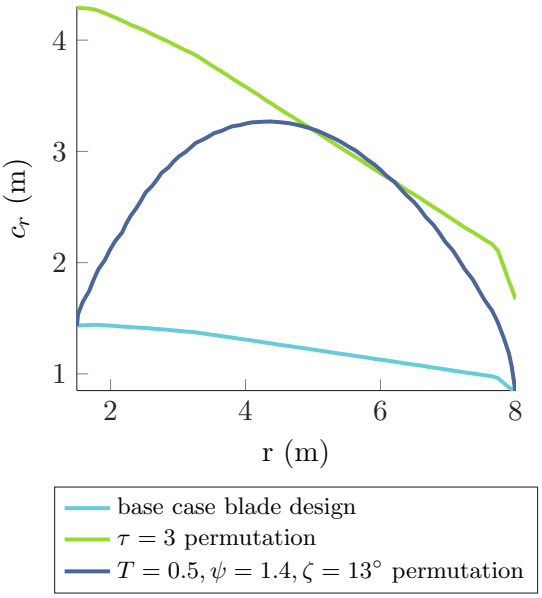

Figure 5.6: Select alterations to the chord made in Stage One and Stage Two of the application of the design methodology.

Design Space analysis

As Fig. 5.5 c) shows, predicted cavitation inception ceased when ζ reached 13 ° as before, but the detrimental impact on C_{Po} was reduced to -10.6%, rather than the -32.6% of the Stage One blade. This was a significant improvement. The C_{To} metric indicated that the thrust performance was also as desired by the design requirementse, improvements in this metric having been made by many of the design alterations, including the first cavitation-free permutation of the series. However, the C_{Po} was not as high as would be optimal. It was therefore desirable to alter this performance.

Diagnostic Plot analysis

The Diagnostic Plots for the base case, '$\zeta = 13$' and '$T = 0.5, \psi = 1.4, \zeta = 13$' design permutations are shown together in Fig. 5.7. Inspection of this showed that the desired increase in Q required to maintain high levels of P_{mech} with reduced operating Ω was achieved with the latter permutation. However, at the optimum operating point there was a slight fluctuation in the gradient of the dQ distribution around 3-4 m radius, which corresponded with a change in gradient in the α_r plot. The peak of the dQ curve was also somewhat sharper and dropped off at an earlier radius than the base case design, indicating that some improvement could be made there.

The α_r distribution showed that the lower sections of the blade were operating in stalled flow at λ_{O}. Furthermore it was noticed that the very negative values of α_r persisted at the tip of the blade, and were equal to those of the $\zeta = 13$ blade permutation; the cavitation plot showed that the tip of this blade design came very close to cavitation inception. The stalled flow at the blade root would result in separation, increased

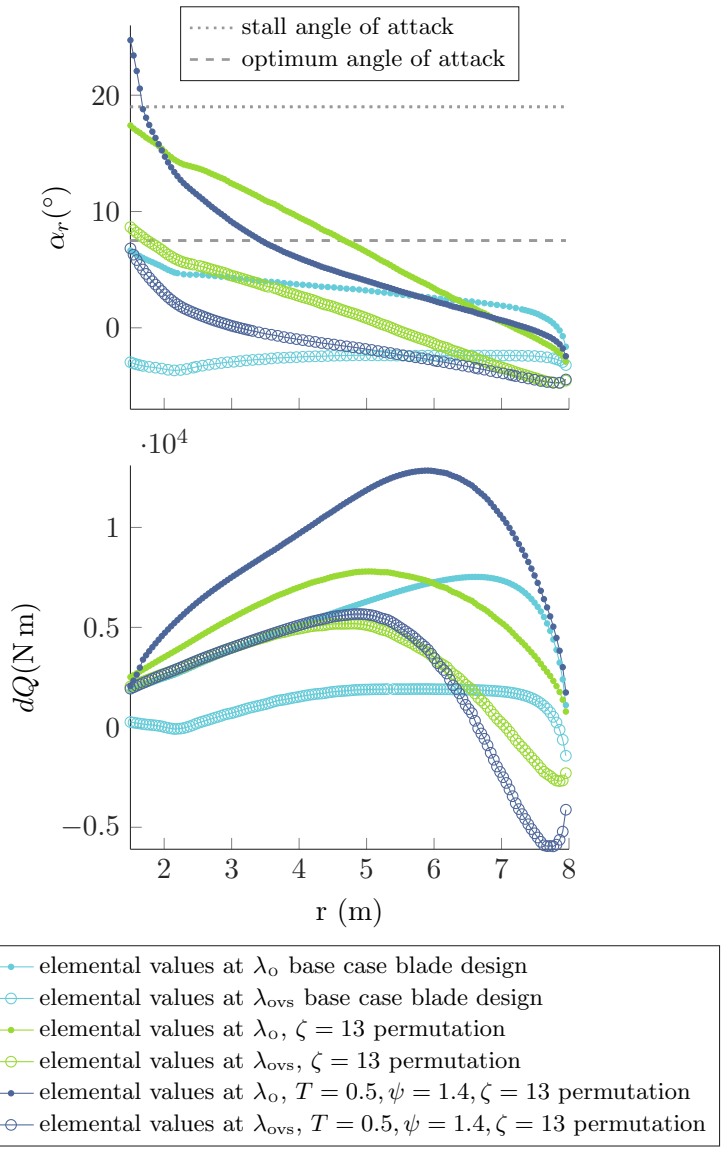

Figure 5.7: Diagnostic plots of the base case blade with the $\zeta = 13°$ and $T = 05, \psi = 1.4, \zeta = 13°$ blade permutations.

structural loads and possible fatigue loading due to cyclic stalling behaviour as the flow velocity varied; and while the negative α_{tip} values were not a concern for this particular blade under steady flow conditions, the finding of persistence in concerning α_r values was of importance to recall during further design alterations.

5.4 Stage Three alterations

5.4.1 Precise alterations to twist and chord distribution

The design process so far had indicated that alterations made to improve a blade design's suitability for operation in OSPR, as measured in one metric, were quite likely to have detrimental effects in another metric. A set of careful Stage Three alterations was

therefore required to finely-tune the blade design to obtain the required increase in C_{Po} without jeopardising the fulfilment of the other design requirementse. The most effective way to undertake this was to identify radial regions at which the blade performance was adversely affected by the current geometrical design and accordingly make alterations. The use of alteration functions was no longer appropriate; these alterations were made by hand.

Chord distribution alterations

As Fig. 5.8 b) shows, alterations to the chord distribution of the '$T = 0.5, \psi = 1.4, \zeta = 13$' permutation were made such as generally increased the chord length over the blade radius. The increases to the root chord, such as in the 'hand altered permutation' chord distribution shown, were not found to be favourable in increasing C_{Po}; subsequently the chord in the lower radial range was slightly reduced again. It was, however, found that continuing to increase c_r in the mid-blade sections was a useful design alteration; the final cord distribution of the new blade design – shown with the 'hand altered permutation ii' in Fig. 5.8 b) – illustrates.

Twist and pitch setting alterations

The foregoing discussion of Fig. 5.7 identified some improvements which could be made. The fluctuation in gradient of dQ and α_r distribution at λ_{O} was thought to have caused some performance degradation; as comparison of the twist distribution of the '$T = 0.5, \psi = 1.4, \zeta = 13$' design and that of the 'hand altered permutation i' shown in Fig. 5.8 a) shows, the twist between $r = 3$ and $r = 4$ m was accordingly increased. The sub-optimal shape of the dQ distribution noted at the upper regions of the blade at λ_{O} was improved by again locally reducing the θ_r in the region concerned. This brought the gradient of θ_r in the upper sections of the blade back to a similar shape to the base case blade, though at a lesser degree of twist. An alteration applied to the blade tip was a sharp, local increase in θ_r, implemented to take the tip of the blade out of the cavitation zone into which the foregoing alterations had brought it. The final alteration made to θ_r was implemented to take the root sections out of stall. This was achieved by isolating the bottom meter of blade and increasing the gradient of the twist in this section, bringing it into positive 3° twist at the root. In fact, the discretisation of terms referring to the angle between the blade and the plane of rotation is, mathematically speaking, simply convenience. Therefore, by removing 3° from each θ_r and increasing β by 3°, this blade geometry alteration was appropriately categorised in the terms herein used.

This alteration, however, did bring the tip of the blade back into the cavitation inception zone and gave a 2% negative impact on the metric C_{To}. One final series of design alterations was therefore required to ascertain whether the positive impact recently made on C_{Po} could be retained while regaining cavitation-free operation and

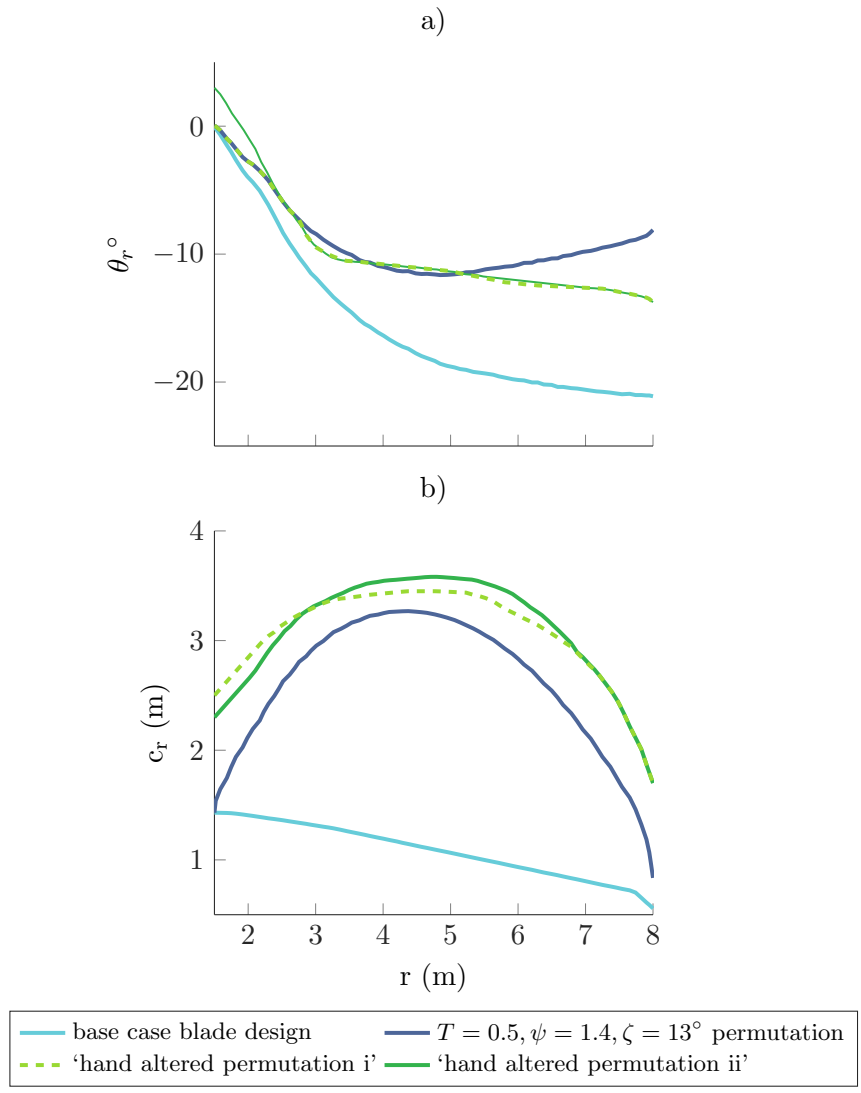

Figure 5.8: Stage Three alterations: progressive alterations made to $\theta_r$and c_r. The base case blade design and the most successful function-altered blade permutation are included for comparison and reference. Two hand-altered blade permutations are shown, the last of which shows the final θ_r and c_r distribution of the developed OSPR blade.

fulfilling the thrust force-based Design Requirement.

5.4.2 Optimisation of blade pitch setting

As identified in the Stage One design alterations (see Fig. 5.2), the most powerful design parameter was β. A set of $\delta\beta$ design permutations were therefore made to the new blade design, over the range $0 \leq \delta\beta \leq 3$. As the design space analysis shown in Fig. 5.9 indicated, it was found to be possible to thereby remove the blade tip from the cavitation zone and still retain some of the improvement in the C_{PO} metric. A change to β of 2° gave the required cavitation-free performance throughout the operation defined in the design platform, ensured the C_{TO} did not exceed that of the base case blade design, and reduced the improvement in C_{PO} from the hand-altered blade permutation (the impact

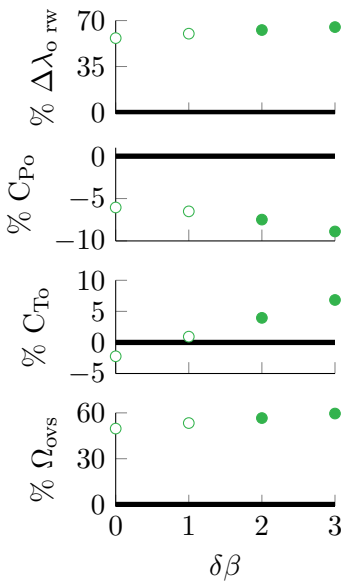

Figure 5.9: Design Space analysis of Stage Three pitch setting alteration; $\delta\beta$ alterations applied to regain cavitation-free operation while optimising power performance.

on the OSPR metrics of which is shown in Fig. 5.9, at $\delta\beta = 0$) by only 1.4%.

5.4.3 Additional design analysis

As previously mentioned, a structural feasibility analysis was also undertaken to ascertain whether the blade designs developed with the Methodology were physically practicable. Briefly, this analysis summed the bending moments around the bottom of each of the 140 blade elements for every operation condition considered in the design platform, and used Engineers' Bending Theory to ascertain the width of a square box-spar required, at each radial position, to withstand the structural forces; a safety factor of 2 was applied. The box spar sections were then graphically compared to the size of the enveloping hydrodynamic shape at each blade element; failure of the spar to fit comfortably inside the enveloping blade shape, at any point along the radius led to failure of the feasibility analysis. This was a basic version of a structural design method presented by NREL [131].

The new blade design passed this test. Full details of the analysis are given in Appendix B.

5.5 Proof of concept and verification of performance

In the case of an industrial development, further design considerations would be taken into account in the development of blades, such as generator design, further structural considerations, controller capabilities, and so on. This research has focussed on the hydrodynamic design only, taking into consideration the technical requirements detailed in the introduction to Chapter 4.

Be that as it may, performance predictions with a BEMT tool are generally used for design stage purposes, and further stages of design and/or verification of performance are generally undertaken prior to commissioning. For this reason, a second set of tank tests were undertaken, to verify that the performance of the new blade design was as expected.

The performance predicted for the new blades in the full-scale design platform would be less affected by the *Re* and turbulence issues discussed in Chapter 3; however, testing a full-scale turbine was not a possibility. Testing in the tow tank, however, is a very useful way to undertake the required verification, and would have the further advantage of facilitating comparison between the performance of the base case and new blade designs at prototype scale, as well as verification of the BEMT prediction of prototype-scale performance. This measure was therefore undertaken.

5.5.1 Aims

The aim of the second set of tow tank tests was to verify that the performance of the rotor had been altered in the desired manner. empirical test data was required to achieve this in two main ways:

- verify the BEMT prediction of the new blade performance at prototype scale
- compare the empirical performance data of the new blade design to that of the base case blade design and ascertain whether the requirements of an OSPR blade were better met with the new blade design.

5.5.2 Production of prototype-scale blades

The new blade geometry, defined in Table 6.1, was re-scaled to be of the same length as the tested prototype-scale base case blade, having a working length of 0.292 m. The tested blade geometry is given in Table 5.2.

This prototype-scale new blade design was then defined using a blade-plotting script in MATLAB, from which the definition of 21 aerofoil sections were passed to the AutoDesk CAD programme Inventor and used to create the blade shape from 20 elements.

MATLAB stage

The MATLAB script created the blade aerofoil sections by scaling the aerofoil section by the chord length at a node radially centred in each blade element. The aerofoil sections were positioned in the z-axis according to the node position. The angle of the chord line was determined according to the nodal value of θ_r; by twisting each aerofoil round the quarter-chord point by this value, the aerofoil sections were positioned in the x and y-axes. The quarter-chord point was chosen as the stationary aerofoil section location for three reasons. Firstly, as is industry standard, the base case blade was produced

Table 5.2: Geometry of new blade design, for use in an OSPR tidal turbine.

r(m)	c_r(m)	$\theta_r(^\circ)$
0.089	0.1033	0
0.1182	0.1242	-5.2882
0.1474	0.1457	-10.9
0.1766	0.1549	-13.515
0.2058	0.1595	-13.85
0.235	0.1609	-14.1875
0.2642	0.1592	-14.65
0.2934	0.1512	-15.075
0.3226	0.1361	-15.45
0.3518	0.1152	-15.7953
0.381	0.0764	-16.75
	β°	31.9

in this manner; it was desirable to match every variable in the second test set to the values of the first set to isolate, as far as possible, the altered blade geometry as the only change. Secondly, this reduced the sharpness of the blade tip; even with the rounded blade tip which was applied, twisting the sections round their nose would have therefore resulted in greater tip losses. And thirdly – perhaps in explanation of the first point and due, in part, to the second – an investigation into the effect of around which point the blade is twisted, undertaken by Osbourne in [132], concluded that the quarter-chord point was most appropriate; in the case therein studied it was found that moving the point of twist from the aerofoil nose to the quarter chord point increased C_{Po} by 9%.

Inventor stage

Each aerofoil section, defined with 66 points, was output to an excel sheet and subsequently imported to Inventor where the dots were joined with a spline vortex. The 21 aerofoil sections were defined sequentially and the lofting command was used to produce a single solid object, as shown in Fig. 5.10. To match the base case blades, thereby further reducing tip loss, a rounded blade tip of 0.1 meter was defined. This was done after the geometry of the main blade was completed, to avoid any alteration to the lofted shape made by the inclusion of the tip definition in the loft process.

A blade root connection was required to attach the blades to the turbine rig used. This rig was designed and made at Cardiff University, and was kindly made available for this series of tests. The root connection required, therefore, to fit into the existing connection on the turbine hub, and provide a mechanism to give an accurate blade root pitch setting. Fig. 5.11 shows the Cardiff turbine system used in the test rig; the nose cone visibility has been turned off and details of the hub can be seen, including the

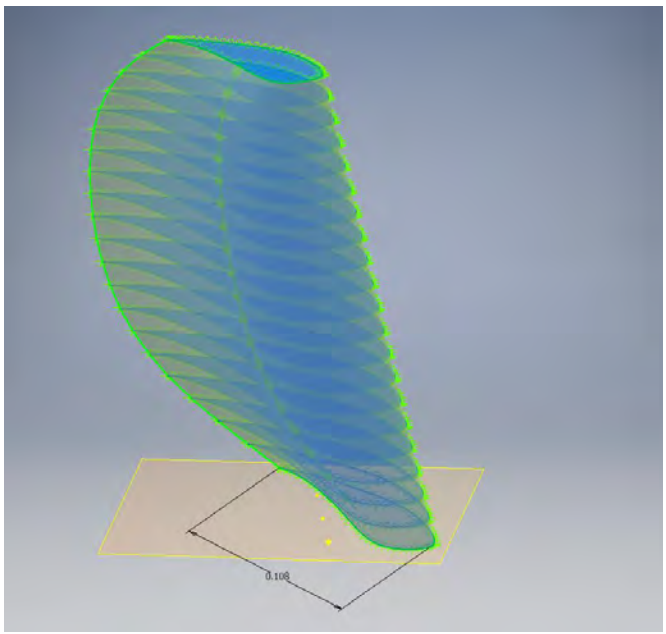

Figure 5.10: Loft of blade shape in Inventor: the 21 defining aerofoil sections are shown, as well as the lofting pattern, and the dimension of the bottom element's chord length is displayed.

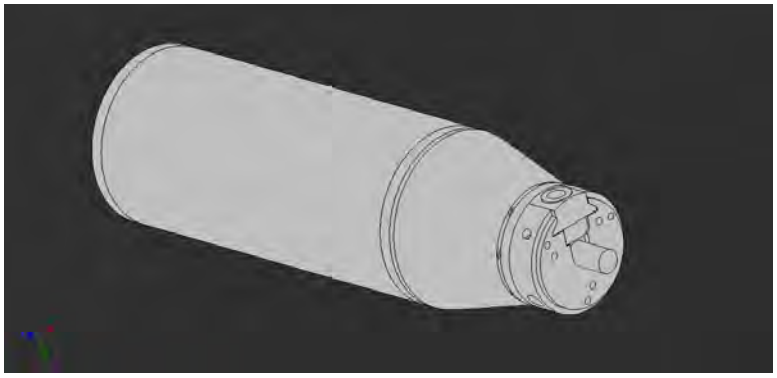

Figure 5.11: Turbine CAD showing hub connection and pin slot through hub.

pin-hole used by the developers to secure their blades to the hub. By creating a slot the same width as this pin hole in the blade root, as shown in Figs. 5.12 and 5.13, it was possible to accurately set the blade pitch. An indent was drilled into the back of the slot. This design would allow the blade to be secured in position with a sharpened bolt screwed through the hub, into the slot and tightly into the indent. This set the pitch angle and prevented the blades from being pulled out of the hub by the combined radial forces of gravity and rotational motion.

Physical blades

The blades were made of aluminium, milled on a 4-axis CNC machine Figs. 5.13 and 5.14 show photographs of the blades before the tests were run. In these photographs, the shape of the blade can be clearly seen, as well as the quality of the manufacturing.

Due to the increased chord lengths, the blades were of higher volume than a standard

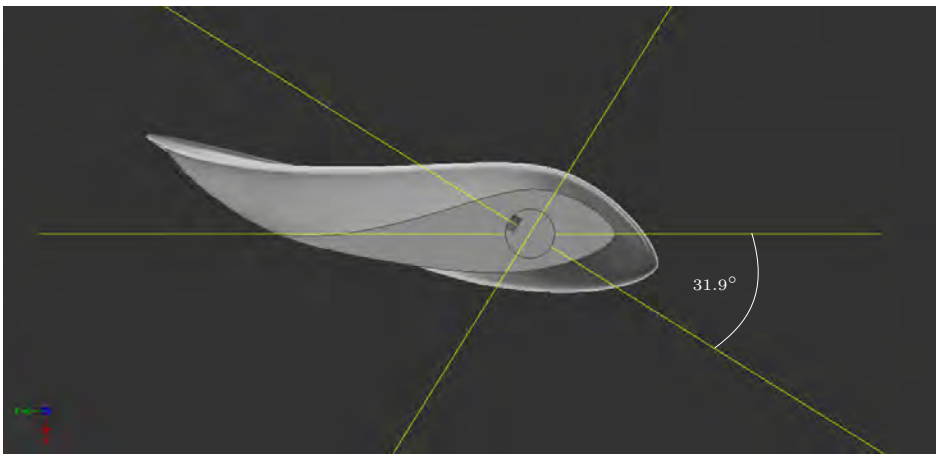

Figure 5.12: Bottom view of blade in Inventor software. Chord line and plane of rotation shown to indicate pitch setting angle, plane of inflow is also indicated. The pin slot can be seen, its alignment with the rotor's axis of rotation is clear; the measurement of the angle between the axis of rotation and the chord line of the bottom aerofoil is indicated.

Figure 5.13: Photograph of a blade before testing. Slot for pin can be seen on blade root shaft, as well as the twist distribution and the root aerofoil section.

tidal turbine blade; in the case of solid, milled aluminium blades, this increased the mass. The prototype blades each weighed 3.5 kg. Calculations were performed – the mathematical basis and method of which is as discussed in Appendix B – which confirmed that the blade root spar would withstand the force of such heavy blades. Should blades such as these be developed for industrial purpose, a composite or hollowed and structurally supported would require to be used to minimise material and mass costs.

5.5.3 Design of experiment

5.5.4 Isolation of experimental variables

Preventing any changes from the base case test programme in as many of the parameters of the tow tank tests as possible was an important factor in the design of experiment. It would thereby be possible to attribute any performance alterations observed in the tests to the varied test parameters – the altered β, θ_r and c_r of the new blade design.

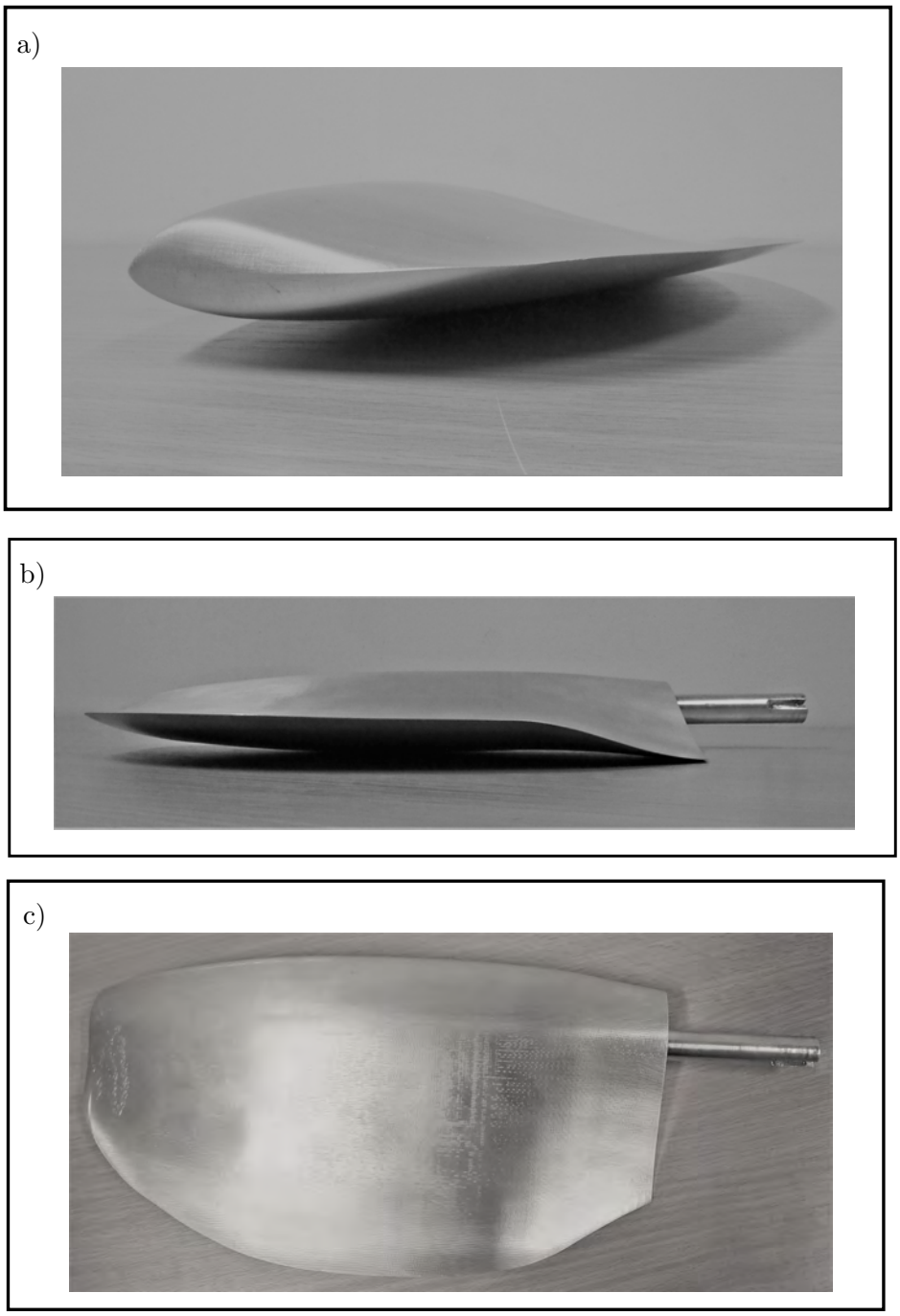

Figure 5.14: Photographs of the new blade design in milled aluminium, showing: a) the rounded tip prepared in CAD b) the twist distribution and c) the chord distribution.

To this end, the blade length was kept the same for the new tests.

The test turbine which was kindly made available for this set of tests had a physical hub radius of 0.05 m, 0.039 m smaller than that of the original turbine. The new blades were therefore designed to have a blade root connection which would protrude out from the physical hub by this 0.039 m, giving the desired hub radius. The aforementioned slots in the blade root spars were designed to have an upper edge – curved to match the circumference of the securing bolts – in the correct place to give the extra 0.039 m hub radius, and result in an overall turbine radius to match the 0.381 m of the base case turbine. Due to some in-test time constraints, it was not possible to put in place the constructed nose cone of increased radius to further match the conditions of the base case tests. This was a limitation in the match between the two test programmes.

The details of the rotor were therefore, broadly, the same as for the base case blade (see Table 3.6).

Test facility

The tests were undertaken at the Kelvin Hydrodynamics Laboratory's Tow Tank facility, as before. This facility was described in Section 3.2.2.

Carriage velocities

As previously discussed, the aerofoil data input to BEMT for the prototype scale predictions was obtained at one Re; this meant that the BEMT predictions were for a single set of flow conditions. The chord Reynolds number is dependent on the chord length (see Eq. (2.11)); as the new blade design had chord lengths substantially greater than the base case blade, the speed of the carriage during testing had to be altered to achieve the same Re as those in the base case tests and thereby test at appropriate flow conditions for the aerofoil data used in the BEMT model.

On the other hand, due to the sensitivity of the NREL S814 to the Re in this range, identified in Chapter 3 by the variation of performance with carriage velocity as well as by Milne et al. in [35, 109], it was appropriate to assume that the performance at a lower flow speed would not allow meaningful comparison of the two sets of tank data. A second set of tests were therefore planned which, instead of matching the Re of the first tests for verification of the BEMT code, matched the carriage speed for comparison with the 0.8 $\mathrm{m\,s^{-1}}$ base case blade tests.

Two test carriage speeds were therefore planned; 0.34 $\mathrm{m\,s^{-1}}$ to match the Re and 0.8 $\mathrm{m\,s^{-1}}$ to match the carriage speed of the base case tank tests. The value 0.34 $\mathrm{m\,s^{-1}}$ was found iteratively by comparing the Re predicted for the blade element at 7-% of the radius, operating at λ_{O}. Fig. 5.15 shows the range of Re predicted by BEMT in the 0.8 $\mathrm{m\,s^{-1}}$ base case tests and subsequent 0.34 $\mathrm{m\,s^{-1}}$ tests. It can be seen that the converged solution to the new test speed resulted in an appropriate range of Re; the 70% radius points were predicted to have very similar Re at the optimum operating point.

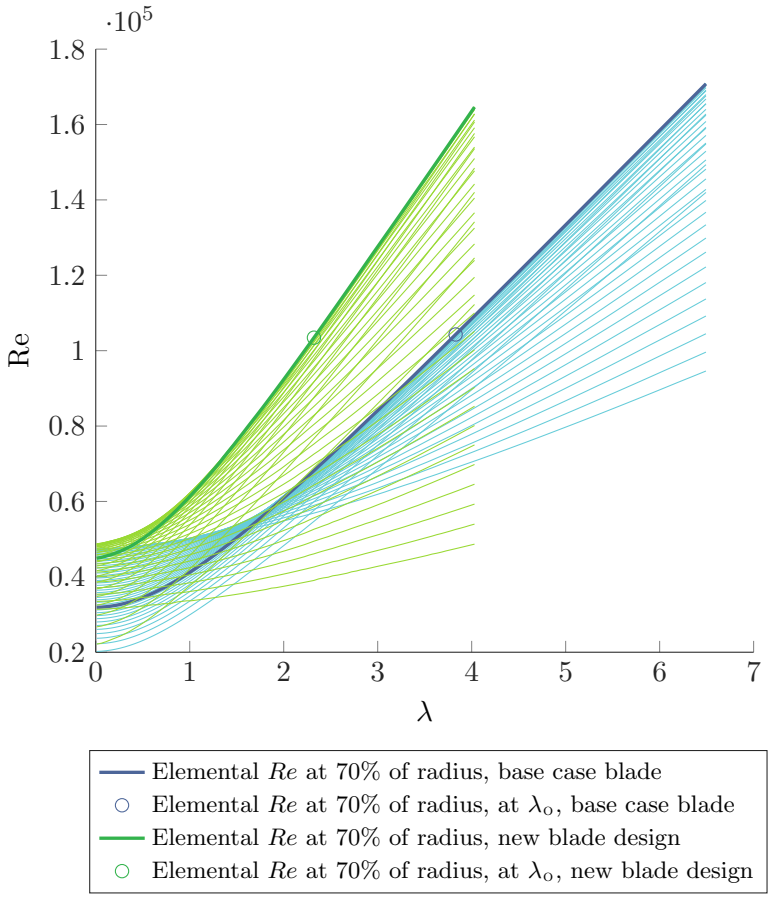

Figure 5.15: Reynold number range of base case and new blade designs in tow tank tests. The predicted range of Re for each element over the range of λ is shown, for base case tests at 0.8 $\mathrm{m\,s^{-1}}$ and new tests at 0.34 $\mathrm{m\,s^{-1}}$. The Re of the element at 70% radius is highlighted in each case. The predicted Re of these elements at the optimum operating point are indicated; the intended match is shown to be very close.

However, the root element data are also highlighted in the figure, and the position of these showed that the new tests were predicted to have a lower Re at this blade area than the base case tests, indicating the possibility of some performance discrepancy. However, the upper sections of the blade are generally more influential on rotor performance (as indicated by the discussed plots of α_r distribution), and it would not have been possible to exactly match the two Re ranges. This was therefore seen as a fair solution.

It was considered that a further set of tests, at a higher carriage velocity would be useful in allowing further comparisons between the two tests sets, confirming the rotor performance and investigating the extent of Re influence at this prototype scale on the new blade design. A third carriage speed of 1 $\mathrm{m\,s^{-1}}$ – dependent on the available time – was planned.

5.5.5 Instrumentation

Due to some technical difficulties, there were two experimental set-ups used over the test period. From the first tests, no axial force data was obtained; for the second set, though,

Table 5.3: Measured quantities and instrumentation

Final variable	Measurement	Instrumentation
C_P	Primary shaft torque, Q (N m)	Motor driver
	Shaft rotational velocity, Ω (rad s^{-1})	Motor encoder
λ	Carriage speed, U_∞ (m s^{-1})	Carriage speed
	Shaft rotational velocity, Ω (rad s^{-1})	Motor encoder
	Second set only	
C_T	Rotor thrust load, F_T (N)	Strain gauge on stanchion

a strain gauge was added to the system to capture this data. Broadly, the turbine rig used in the tests comprised:

- the turbine itself, with an integrated, in-line motor within the water-tight turbine casing and a hub set for either a 2 or 3-blade rotor configuration
- a motor drive configured for speed control of the turbine motor, to which the required test speed and from which information on the position of the encoder and the torque generating current (TGC) were sent
- a control and DAQ system based on a LabVIEW programme written by Matthew Allmark of Cardiff University, the hardware for which was: at the turbine side, an Arduino circuit board placed inside the water-tight turbine nose cone; and on the control side, National Instruments PXEe35, LabVIEW box and PXI hardware, and a Desktop computer with the required software installed. The sample frequency, f_s, was 137 Hz.
- a strain gauge measuring axial thrust force, positioned on the support stanchion attaching the turbine to the tow carriage.

Table 5.3 gives the data required to characterise the turbine performance, and the instrumentation used for each reading.

Fig. 5.16 shows photgraphs taken during the installation of the turbine in the tank. The turbine body, saddle connection to the stanchion, hub and nose cone are shown in Fig. 5.16 a). Fig. 5.16 b) shows the stanchion used to hang the rig from the carriage, the connecting brackets used to secure the stanchion to the tow carriage; a line was scribed at 0 ° on both the brackets and in the very centre of the stanchion and the connecting saddle, allowing accurate alignment of the turbine with the flow. The chain-block pulley system used to lower and raise the turbine is also shown in Fig. 5.16 b).Fig. 5.16 c) shows the new blades being attached to the turbine with the sharpened bolts and a

spanner. The curved upper edge of the slot in the blade root was aligned carefully with the pin hole in the turbine hub before the bolt was put in; the depth of the slot and drilled indent was greater than the sharpened section of the bolt, ensuring perfect alignment of the blade, both in the radial direction and in terms of the pitch setting.

The motor was an IndraDyn T PPM MST 130 E 35 model, with a rated torque of 22.5 N m and speed of 350 RPM. The shaft or mechanical torque, Q_{mech}, as in the previous set of tests, was the difference between the hydrodynamic and mechanical torques – the torque required from the motor to drive the turbine at the set speed through the flow velocity imparted by the towing of the turbine through the tank. This was therefore read from the TGC data stream from the motor.

5.5.6 Calibration and uncertainty

Torque

The TGC data obtained from the motor drive was calibrated according to the developers' directions, to obtain the Q_{mech} reading.

$$Q_{\text{mech}} = 6.66\,(0.31\ \text{TGC} - 1.2)) - Q_{\text{loss}}\ , \tag{5.6}$$

where the torque lost, Q_{loss}, to the turbine system inertia was defined:

$$Q_{\text{loss}} = -8 \times 10^{-6} \left(\frac{60\Omega}{2\pi}\right)^2 + 0.0056\frac{60\Omega}{2\pi} + 0.6811\ . \tag{5.7}$$

The resolution on this information – the certainty with which any measurement taken could be known – was 1 % of the rated torque, 0.225 N m.

Thrust

In the second set of these tests, as discussed, additional instrumentation was included to obtain thrust measurements. The strain gauge used was full-bridge, and was calibrated by axially loading the stanchion with a series of known masses in a similar process to that undertaken for the base case blade tests (see Section 3.2.4). Fig. 5.17 shows the calibration curve, including the uncertainty bounds. This calibration uncertainty analysis was undertaken in the same manner as for the base case tests, as described in Section 3.2.8.

The least squares regression analysis used to obtain the calibration equation gave a calibration factor of −30.7245. The uncertainty in calibration – the combined precision and bias uncertainties – for the thrust measured on the stanchion was 0.6825 N.

In order to quantify the thrust force imparted by the turbine hub and the wet section of the stanchion itself, a test was run at the flow speed of this second test set, 0.34 m s^{-1}, without the blades on the turbine. The thrust measured in this tests was subsequently removed from the measured thrust in each of the 0.34 m s^{-1} test runs.

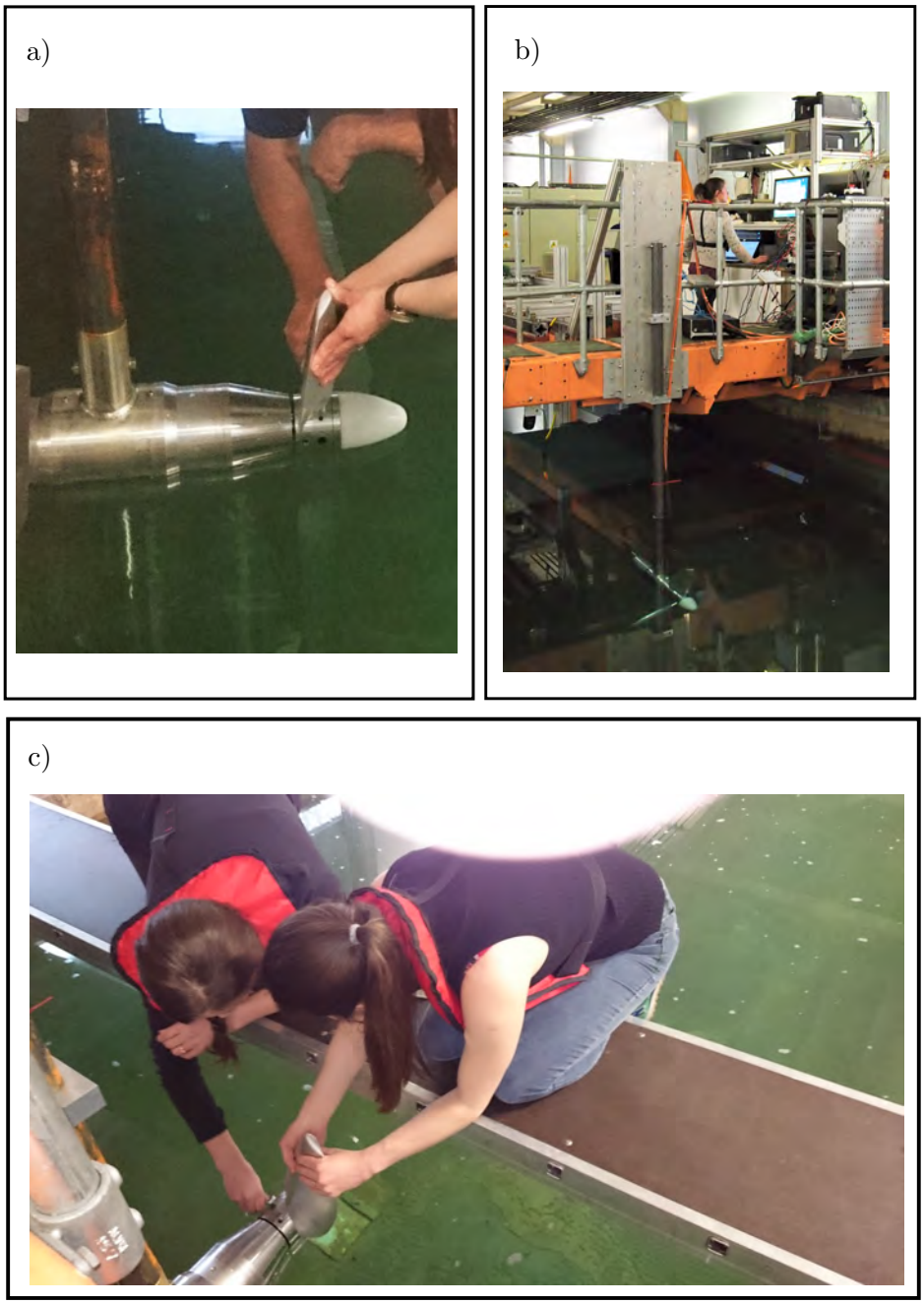

Figure 5.16: Photographs of turbine installation and testing: a) Turbine rig in position in the tank, showing the stanchion connection, nose cone, hub and blades being installed; b) Turbine on stanchion lowered into the water. Stanchion securing braces can be seen, as well as cable ties keeping cables in place; c) Bolts being screwed through hub of turbine and into slot on blade root shaft, securing blade to turbine.

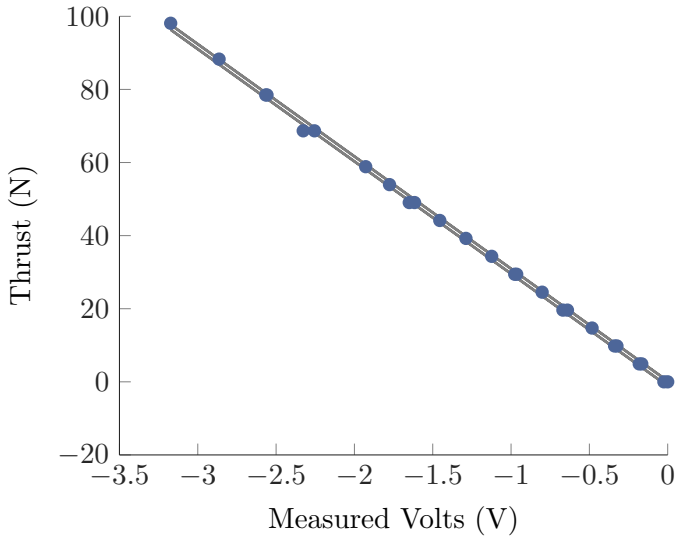

Figure 5.17: Calibration curve for the strain gauge used to measure thrust on the stanchion; data points and uncertainty bounds are shown.

Rotational velocity

The rotor velocity was output from the DAQ system in the first set of tests, and in the second set, which by-passed the LabVIEW code, was inferred from the encoder position data.

This encoder position data ran, at a constant gradient, from zero to a consistent peak value, before dropping instantaneously back to zero. It did, however, contain some noise. In the second set of tests, therefore, the encoder position data was first filtered using MATLAB's Savitzky-Golay filter function, *sgolayfilt*, with the window size set to $1.2\ \frac{f_s}{f_{rotor}}$ and the polynomial order to 4. This cleaned the data of noise sufficiently that the signal could then be binarised at the peak of each rotation, and thereby used to calculate a derived rotational velocity signal in the same manner as in the base case tests.

For each individual tests, the uncertainty in the rotational velocity reading was calculated as the standard deviation – of the output RPM signal in the first set and of the derived signal in the second set. These uncertainty values therefore varied from test to test.

Carriage velocity

As the tow tank facility was used in both test sets, the uncertainty in the carriage velocity was as for the base case tests.

5.5.7 Test procedure

The tests were conducted in much the same manner as the base case tests: a zero region to obtain the offset values was left at the start of each test run, the turbine was

ramped up to speed, followed by the carriage, which was then driven to the end of the tank and ramped down. A rough mean value for the torque data was obtained and pre-processed during the run back to the start of the tank, and during the rest-period, allowing informed decisions to be made as to which test run would best aid in describing the performance curve if run next.

A number of repeat runs were undertaken to ascertain the repeatability of the tests. The test order was generally randomised to limit any nuisance factor impact on the uncertainty, and movement upon the carriage was kept to a minimum during the tests.

5.5.8 Post-processing

Performance characteristics

The processing MATLAB script used for the base case tests was adapted for the new tests, allowing the data streams to be cut into the "zero" and "test" sections, as before. The cut-in time for the test period was always selected at a point after the torque signal had settled, as before, avoiding any transient effects from the ramp-up period affecting the data. Though this removed roughly 10 s of data, each "test" region, even those run at 1 $\mathrm{m\,s^{-1}}$, was at least 30 s in length; along with the sample frequency of 137 Hz, this ensured that ample data was collected to allow mean values to be obtained.

The calibration and data reduction equations were applied, obtaining the turbine performance characteristic at each flow state, as required and as listed in Table 5.3.

Uncertainty analysis

The uncertainty in the calibrated values of F_T, Q, Ω and U_∞ were given in Section 5.5.6. These values were used to calculate the uncertainty in each test case with the method described in Section 3.2.8. The uncertainties were propagated through the data reduction equations to yield equations of the form of Eq. (3.19), as the method outlined. Application of a Student's T coverage factor of 2 [133] to each of the final uncertainty values allowed the performance characterising terms – λ, C_P and C_T – to be expressed as existing within the uncertainty bounds, with 95% confidence.

5.6 Conclusion

A blade design methodology for overspeed power regulated tidal turbine rotors has been developed, which considers the operation site and power regulation methodology within the design requirement-based boundary conditions. Blade design parameter alterations have been made and assessed using three visual-numerical analysis tools: a design space analysis based on overspeed performance metrics; a full-blade cavitation analysis over the entire operation range expressed with plots of converging cavitation and pressure curves; and plots of local angle of attack and torque distribution across the blades.

It has been shown that, between the applied parameter alterations, changes to twist distribution and pitch setting are most effective at reducing the rotor's maximum angular velocity within the operating range and thus mitigating the inception of cavitation and reducing the maximum terminal voltages with which the system must be built to cope. These alterations, however, come at the expense of a reduction in optimum efficiency. While changes to the cross-sectional area of the blade via scaling and distributional alterations to the chord length have a lesser effect on the performance, these changes can be coupled with alterations to twist distribution to bring the optimum efficiency back towards acceptable levels without detrimental impact on the cavitation behaviour. Such coupled changes also affect the maximum coefficient of thrust and the effect this has on the turbine will need to be taken into account.

Cavitation analyses of the base case and altered blade designs have indicated that cavitation inception is an issue which should be considered, and which, depending on the aerofoil section and boundary conditions - site velocity profile and depth and turbine configuration - and may be a main driver for speed-limiting design alterations to blades for use in OSPR.

Analysis of the first stage of design alterations showed that several of the discrete parameter alterations may bring about improvements in the OSPR performance metrics. The results from the tools used also showed that localised parameter alterations coupled with initial discrete alterations can mitigate some of the detrimental effects from the initial alterations. For example, it was identified on inspection of $\alpha_r - r$ plots such as those in Figs. 5.4 and 5.7 that blade tips often had significantly lower α_r than the lower blade elements, resulting in the greater proximity, or cross-over of the σ_r and σ_{ir} curves for the tip elements, and leading to near or post-cavitation inception conditions. Localised θ_r alterations can be made to bring α_r to a less negative value at the blade tips, removing the predicted cavitation inception.

Chapter 6

Results and discussion

6.1 Performance improvement for operation in OSPR

6.1.1 OSPR blade shape

The final geometrical design of the FP blade herein developed for use in a turbine deployed in a site defined by the design platform, under the design requirements and controlled with MPPT and OSPR is defined by the chord and twist distributions and pitch setting given in Table 6.1. The geometry has been nondimensionalised by division of the chord lengths by the blade length, which was 6.5 m for the case defined in the design platform. The radial points at which the geometry is defined were expressed as fractions of the blade length. This gives a blade design which can be scaled according to the blade length, independent of the hub radius.

6.1.2 Comparison of performance to base case blade design

In Figs. 6.1 to 6.3 the performance of the new blade designs, suitable for use in OSPR under the stated design requirements and within the design platform, is compare to that of the base case blade design.

Fig. 6.1 shows the cavitation inception analyses for each of the blade designs, illustrating the effect the blade design parameter alterations had of increasing the values of σ_r, reducing the possibility of cavitation inception. The values of σ_i were also increased, particularly near the root, but to a much lesser degree, and the plots shows that the entire blade remained outside the cavitation zone throughout operation in Regions I and III, as required.

Fig. 6.2 shows that the final set of alterations produced the performance improvements identified from analysis of Fig. 5.7. It was confirmed that the blade root was no longer operating in stalled flow at λ_O. The reduction of θ_r in the upper regions of the blade had the desired effect on the dQ curve of rounding the shape in the region concerned. This produced the required increase in the contribution to Q at λ_O made by much of the blade from around the 5 m radial point. The α_r distribution plot showed

Table 6.1: Geometry of new blade design, for use in an OSPR tidal turbine.

$r/L_b(-)$	$c_r/L_b(-)$	$\theta_r(^\circ)$
0	0.354	0
0.1	0.426	-5.29
0.2	0.499	-10.90
0.3	0.531	-13.52
0.4	0.546	-13.85
0.5	0.551	-14.19
0.6	0.545	-14.65
0.7	0.518	-15.08
0.8	0.466	-15.45
0.9	0.395	-15.80
1	0.262	-16.75
	β°	31.9

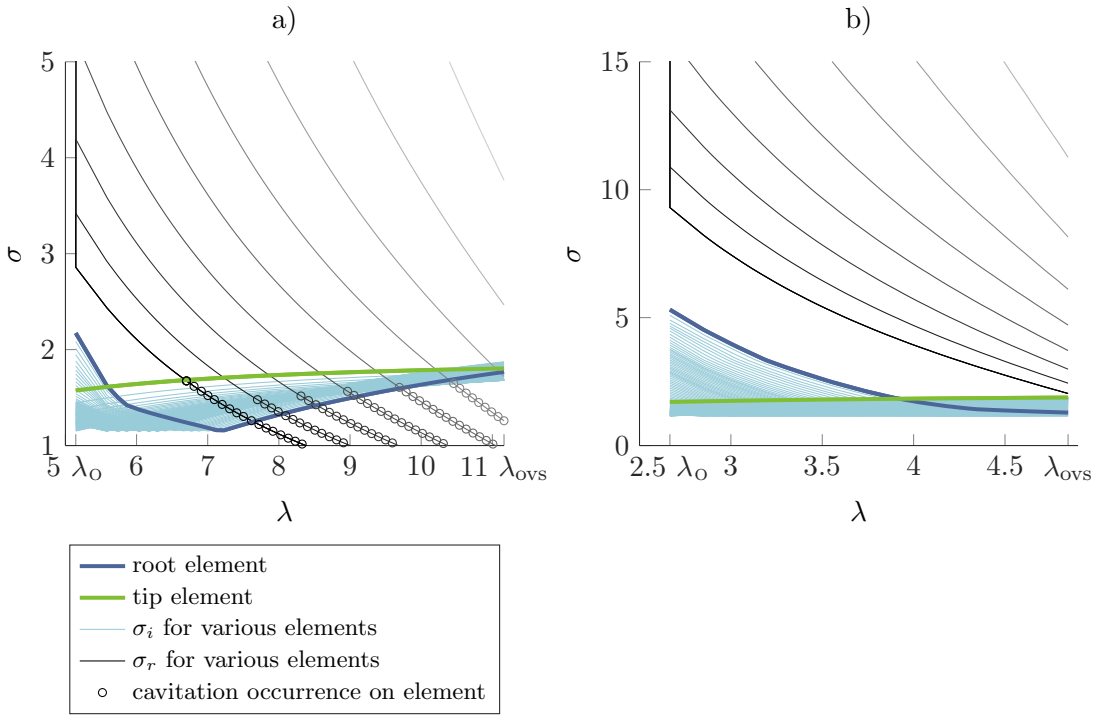

Figure 6.1: Cavitation plot for a) base case and b) new blade design. The removal of cavitation inception on the blade in the MPPT and OSPR operating regions, effected by the design changes between the base case and new blade design, is shown.

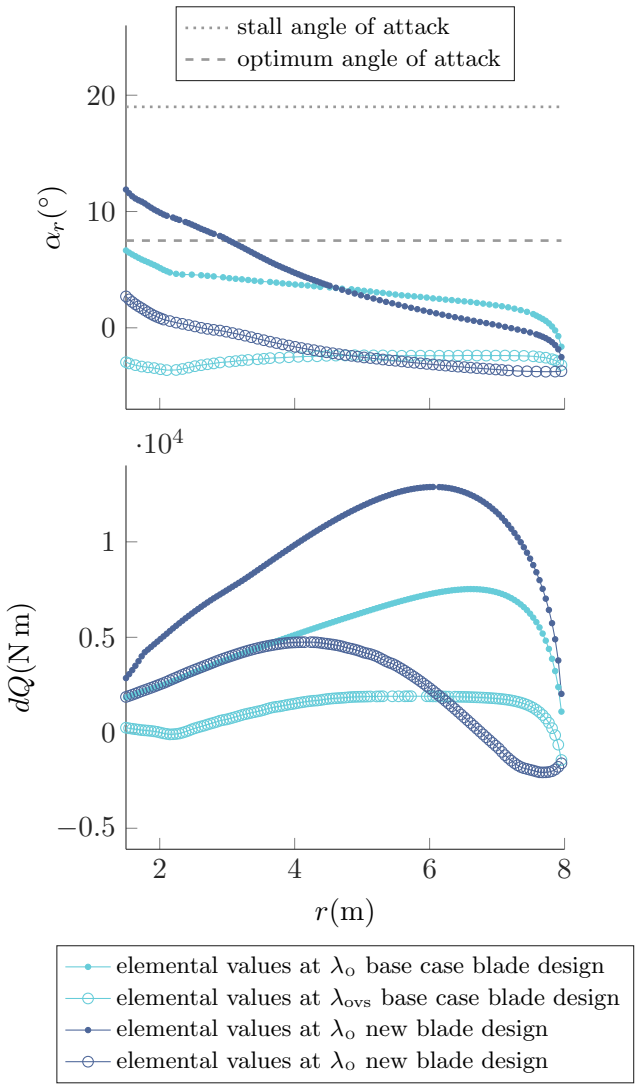

Figure 6.2: Diagnostic plots for the base case and new blade design.

that at λ_{ovs}, α_{tip} was no longer at such extremely negative values, and the effect on the dQ curve at λ_{ovs} was to reduce the steep dip into negative torque at higher radius values seen for other blade permutations (particularly the '$T = 0.5, \psi = 1.4, \zeta = 13$' permutation).

The performance curves, both of C_P and C_T-λ are shown for the base case and new blade designs in Fig. 6.3. The figure shows the significant improvements made with regards to suitability for operation in OSPR. The operation of the rotor was been shifted towards lower λ values, with a much more rapid drop-off in C_P on the RHS. The shape of the C_{To} was also affected, in a similar manner to C_{Po}. The following figure, Fig. 6.4 shows the effect had on the thrust by this change. As set by the design requirements, the thrust at λ_o – that is, the thrust in Region I, during MPPT – did not exceed that of the base case blade. However, the alterations applied to control cavitation behaviour and maximise the power performance had the knock-on effect of such a significant reduction in C_T on the overspeed side of the performance curve that even with increasing U_∞ in

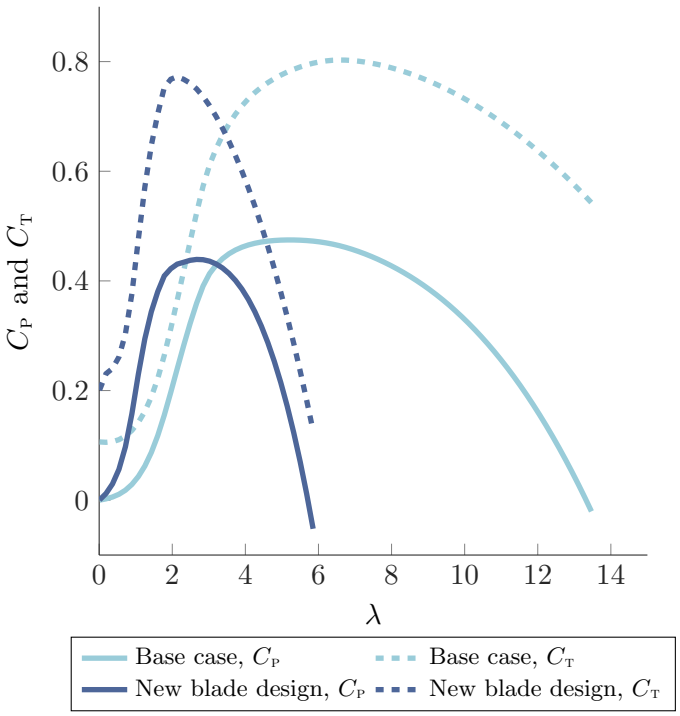

Figure 6.3: Characteristic performance curves of base case and new blade designs. Increased gradient on the right-hand-side of C_P-λ curve, and generally lower rotational velocities indicate a more appropriate performance for application in OSPR tidal turbines.

Region III, the thrust force decreased from the value at U_R.

As indicated in the Design Space analysis in Fig. 5.9 and the performance curves in Fig. 6.3, the new blade C_{Po} was slightly lower – 3.55% lower – than that of the base case. The effect of this difference can be seen in Fig. 6.4, both in the slight offset of the power curves and in the different value of U_R. Assuming the same availability from the base case blade operated in, for example, speed-assisted stall (FP VS operation), this would result in an overall reduction of captured annual energy from the new blade operated in OSPR. This will be discussed in Chapter 7.

Table 6.2 compares the increase in λ and Ω from the optimum operating point to the overspeed operation point and, for λ, to runaway. Presented in this way, the improvement in the required increase in operational Ω is apparent. Though the proportional increase was not improved, the actual increase was significantly improved. This has beneficial implications, as has been seen and as Fig. 6.1 illustrates, in terms of cavitation. Furthermore, the relationship between Ω the voltage previously discussed means that were blades of the new design used in an OSPR turbine, significantly lower voltage levels would occur than if the base case blades were used (disregarding the cavitation damage the latter would incur).

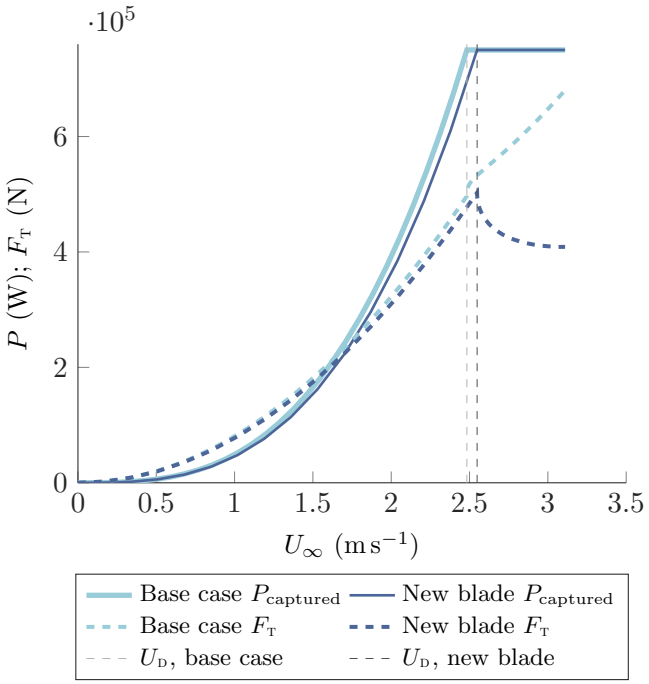

Figure 6.4: Power and thrust for the base case and new blade design, operating in the flow regime specified in the design platform; the captured power, $P_{captured}$, and thrust force, F_T, are shown for each blade design. The rated flow velocity, U_R, for each blade design – resulting from the specified rated rotor power $P_R = 75$ kW – are also shown.

Table 6.2: Comparison of the increase in λ and Ω from optimum operating point to runaway for the BEMT simulations of full-scale base case and new blade design performance.

BLADE DESIGN	λ_O	λ_R	$\Delta\lambda_{OR}$	λ_{ovs}	$\Delta\lambda_{O\text{-}ovs}$	$\Omega_{O_{U_R}}$ (RPM)	Ω_{ovs} (RPM)	$\Delta\Omega_{O\text{-}ovs}$ (RPM)
Base case	5.15	13.32	8.18	11.16	6.02	15.25	41.45	37.11
New blade	2.67	5.71	3.04	4.85	2.18	8.11	17.99	9.88

6.2 Results of the tow tank tests

The results of this second set of tow tank tests are given in tabulated form, in Table A.2, Appendix A.

6.2.1 Tank test results with uncertainty bounds

Power performance

Figs. 6.5 and 6.6 show the full set of results characterising the turbine performance in terms of C_P and C_T respectively, including the uncertainty bounds of each. Fig. 6.5 shows that the peak C_P obtained at each flow speed was: 0.2977 for the 0.34 m s^{-1}, occurring at a $\lambda = 1.98$; 0.2981 in the 0.8 m s^{-1} tests, occurring at $\lambda = 2.243$; and 0.3016 at 1 m s^{-1}, which occurred at $\lambda = 2.18$.

The closest data point to the runaway point for the 0.34 m s^{-1} tests was located

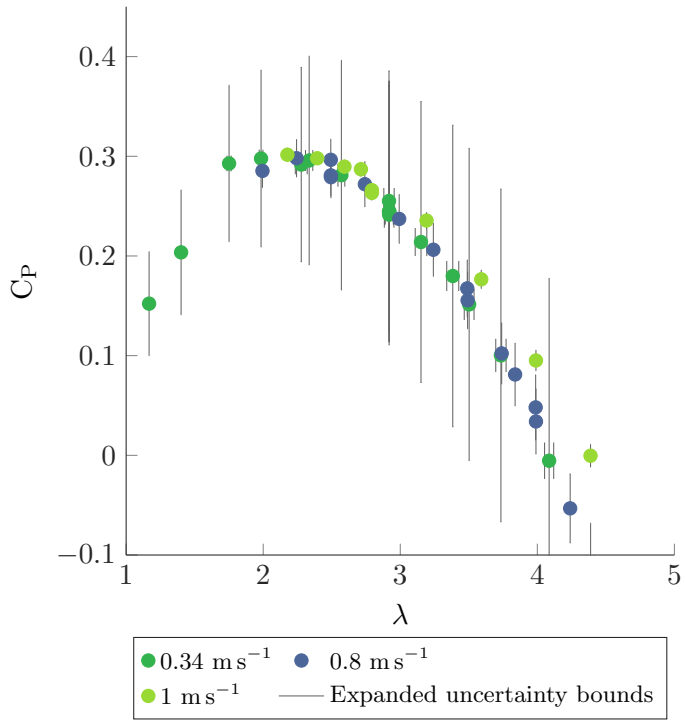

Figure 6.5: Empirical C_P-λ curve of the prototype-scale new blade design. The data obtained at each of the three carriage speeds are shown, along with the uncertainty bounds in both axes for each data point.

at $\lambda = 4.086$, where $C_P = -0.0054$. Linear interpolation between data points with C_P values of 0.03397 and -0.005399 gave a runaway point for the 0.8 m s^{-1} tests at $\lambda_{rw} = 4.087$. Finally, the closest data point to runaway for the 1 m s^{-1} tests, where $C_P = -0.0004$ was located at $\lambda = 4.389$.

The uncertainty bounds showed that the uncertainty in λ was very small, largely concealed by the mean result markers. The uncertainty in C_P was much larger for the tests run at 0.34 m s^{-1} than the other two test sets; the maximum uncertainty in C_P for the former was 0.1669 and – an order of magnitude smaller – 0.0326 and 0.0208, respectively, for the 0.8 m s^{-1} and 1 m s^{-1}. Investigation of the uncertainty analysis showed that the driving factor for the significantly larger uncertainty in the slower flow speed tests was the increased ratio of the calibration bias in the torque to the smaller measured torque values; inspection of Eq. (3.19) clarifies.

The uncertainty in the C_P values were higher in general than for the first set of tests, due to the aforementioned calibration bias, which was based on the rated tolerance of the motor. The range of torques measured, even at the fastest carriage speed, were an order of magnitude lower than the rated torque of the motor; the motor torque tolerance therefore gave a comparatively high uncertainty in the measurements. While this resulted in higher uncertainty, the five repeated tests, performed at the lowest flow speed 0.34 m s^{-1}, showed a much higher repeatability. The repeated tests had a range in λ of 0.002 (0.08%) and a range in C_P of 0.0138, which was 5.56% of the mean of the maximum and minimum values in the repeated group. This indicated high repeatability

Table 6.3: Summary of test results

U_∞ ($\mathrm{m\,s^{-1}}$)	C_{Po}	Mean U_{C_P}	λ_O	λ_rw	Mean U_λ
0.34	0.2977	0.1221	1.98	4.086	0.0289
0.8	0.2981	0.026	2.243	4.087	0.0245
1	0.3016	0.0163	2.18	4.389	0.0211

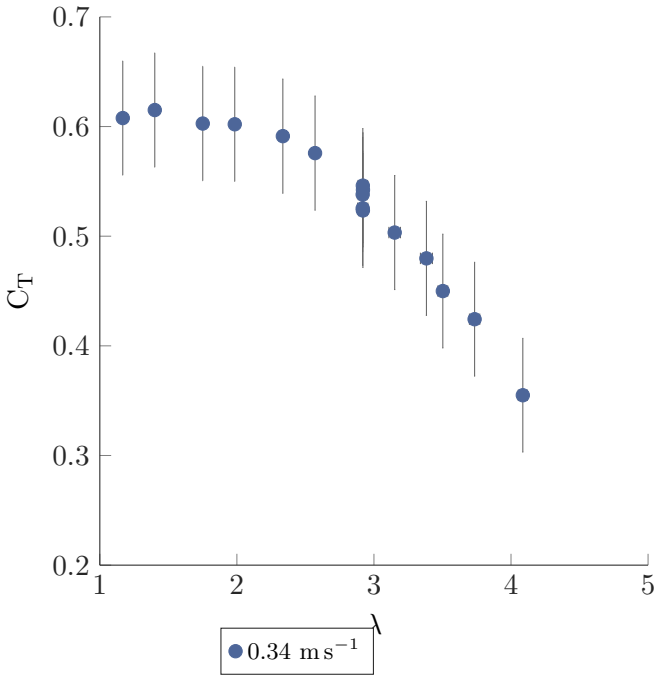

Figure 6.6: Empirical C_T-λ curve of the prototype-scale new blade design. The data for this was obtained at a carriage speed of 0.34 $\mathrm{m\,s^{-1}}$. The uncertainty bounds in both axes are shown for each data point.

in the system and gave increased reliability to the results.

The data displayed greater closeness between the C_P results in the 0.34 $\mathrm{m\,s^{-1}}$ and the 0.8 $\mathrm{m\,s^{-1}}$ tests than between either of these and the 1 $\mathrm{m\,s^{-1}}$ tests. This indicated that the turbine performance was influenced by some factor between the two lower and the highest carriage speeds. It is probable that this factor of influence was the Reynolds number.

Thrust performance

Fig. 6.6 shows the thrust results for the 0.34 $\mathrm{m\,s^{-1}}$ tests. The general trend showed a slow reduction in C_T in the lower λ range, which changed to a sharper decline at a point coinciding roughly with the maximum C_P. The C_T at this point was 0.6021; the maximum value, at $\lambda = 1.17$ was 0.6077, and the minimum value, occurring near the runaway point, $\lambda = 4.086$ was 0.354.

The uncertainty in the thrust measurements was also large, and was also due to the ratio of uncertainty to small measured values.

Table 6.4: Test velocity and Reynolds number ranges

$U_\infty(\mathrm{m\,s^{-1}})$	Ω RANGE (RPM)	RE RANGE (-)
0.34	10 - 45	69,000-170,000
0.8	40 - 85	220,000-410,000
1	55 - 110	290,000-530,000
BASE CASE TESTS		
0.8	57 - 121	66,000-140,000

6.2.2 Match between prototype-scale BEMT and tank data

Using the formulation of the BEMT code previously defined, BEMT predictions were made of the performance of the new blade in the tow tank. A comparison between this and the empirical data, obtained at 0.34 $\mathrm{m\,s^{-1}}$ in the tow tank, is shown in Fig. 6.7.

The BEMT prediction of the power performance was a very good match to the empirical data, verifying this aspect of the methodology. The BEMT predicted a slightly later peak to the curve than the data showed; however, the runaway point was well predicted. The trend in the empirical data, the peak value and the shape of the curve were very well matched by the BEMT code.

While, as discussed, the uncertainty in the 0.34 $\mathrm{m\,s^{-1}}$ tests was high, the data obtained at 0.8 $\mathrm{m\,s^{-1}}$ and 1 $\mathrm{m\,s^{-1}}$ had much lower uncertainty; the shared trend and range of values between the tests at three tow velocities helped to verify the 0.34 $\mathrm{m\,s^{-1}}$ results, illustrating that the performance was repeatable even between different carriage velocities. This level of match between the prediction of power performance and the experimental data gives a strong validation of the BEMT tool and, importantly, of the design methodology.

The thrust performance was not as well predicted by the BEMT code. There may be several reasons for this.Table 6.4 gives the carriage velocities at which the tests were run, the range of rotational velocities for each, and the corresponding chord Re at 70% of the radius, considering data points collected up to just before or just beyond the runaway point, according to availability. The table shows that the upper range of Reynolds numbers in the new tests at 0.34 $\mathrm{m\,s^{-1}}$ were higher than in the base case tests at 0.8 $\mathrm{m\,s^{-1}}$. As previously discussed, the aerofoil data available for prediction of performance at these test conditions, which were accordingly used in the BEMT code, were for one Re. It may be that the drag measurements in this data became less appropriate for the flow conditions as the Re increased with λ.

The poor match between the BEMT prediction and the collected data in the low λ region was possibly caused by laminar separation and reattachment, a phenomenon observed on this aerofoil at similar Reynolds numbers by Milne [35], as discussed in Sections 2.2.3 and 3.2.10. In Design and experimental results for the S814 airfoil [134],

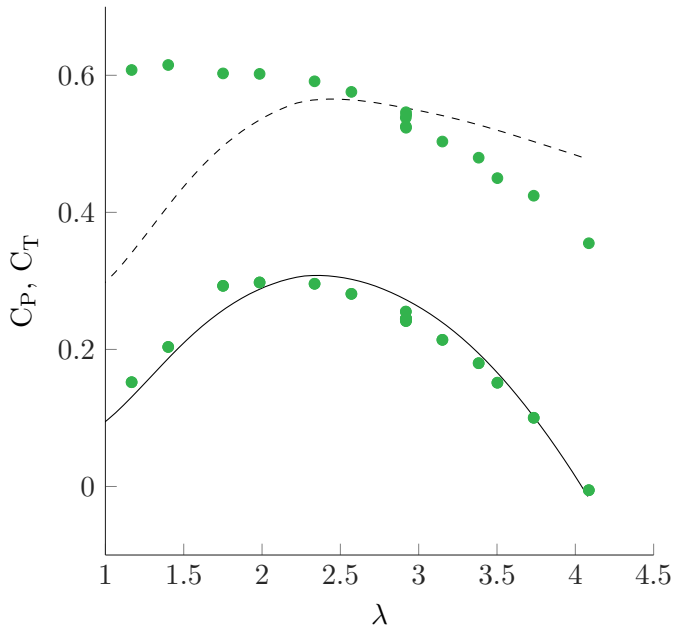

Figure 6.7: Comparison between the C_P and C_T-λ curves of the empirical data and BEMT prediction, each at 0.34 m s^{-1}.

it is noted that at the lowest *Re* of the aerofoil design tests, 0.7×10^6, the occurrence of significant laminar bubbles effects was eliminated in the the design of the NREL S814. The likelihood that laminar separation and reattachment occurred in the discussed tank tests, wherein the *Re* values were up to one order of magnitude lower than this, is therefore quite high, particularly in the lower *Re* tests. Further research by Milne, reported in his PhD thesis [35], evidenced the presence of these laminar separation bubbles and found that these were responsible for a significant increase in drag occurring on the aerofoils. As Fig. 4.3 shows, at low λ, at which α will be large, additional drag force will augment the normal force, N, increasing F_T. This may be the effect causing the increase in C_T over the predicted value seen at low λ. The lesser increase seen between the measured C_P and its predicted value at low λ could also be accounted for by laminar bubbles; bubbles on the back of an aerofoil, as discussed in Section 2.2.6, effectively increase the camber of the aerofoil, and this increases lift. An increase in lift, particularly near stall, increases the tangential force, giving higher power than a model would predict.

Noting, again, the fact that the BEMT prediction was based on one lift curve and one drag curve, obtained at one *Re* and one value of turbulence intensity, it may be that some differences between the predicted and experimentally-captured rotor behaviour were due to the much greater range of flow conditions experienced during the tests. It would be of great use to perform tests at higher carriage velocities to determining whether these flow phenomena had an effect on the results. The literature, and the results obtained in the base case tow tank tests performed at 0.5 m s^{-1}, would suggest that higher *Re* may help to suppress any laminar separation bubbles. The higher test Ω

which would result would also augment rotational effects and perhaps bring the actual flow conditions more in-line with those modelled in the BEMT, which employed 3D flow corrections; as was found in [44], rotational motion can suppress stall delay, but this effect is suppressed by higher Re.

A strong possibility exists that the thrust measurements themselves were a significant contributing factor to the discrepancy between the tests results and the BEMT prediction. The instrumentation used had a greater range than required by the thrust force imparted by the relatively slow-turning rotor. This greater measurement range was required to capture the thrust values predicted for a separate set of blades tested during the set of experiments. However, this meant that the maximum thrust forces measured in the 0.34 $\mathrm{m\,s^{-1}}$ tests were only one third of the measurement range of the strain gauges. This meant that the resolution available in measuring the smaller thrust values occurring on the new OSPR blade design at low tow velocities was lower, which increases the potential error in the measurement. A second aspect of this was that the thrust in the zero regions, removed from the measured thrust values, was of the same order of magnitude as the final values of thrust, further reducing the relative measurement resolution available within the range of actual measurements made.

As discussed, the measured thrust values were small compared to the calibration uncertainty, resulting in a high uncertainty in the measured values – the C_T values had a mean uncertainty of 10 %, which is higher than would be ideal, and higher than the low uncertainty obtained in the base case tow tank tests. This was due to the low measured values in this case.

While reliable torque data was obtained in the tests run at 0.8 $\mathrm{m\,s^{-1}}$ and 1 $\mathrm{m\,s^{-1}}$ and was available to give verification to the C_P results of the 0.34 $\mathrm{m\,s^{-1}}$ tests, the thrust sensors used in these higher U_∞ tests were malfunctioning, and so no thrust measurements were available to do the same for the C_T results of the 0.34 $\mathrm{m\,s^{-1}}$ tests.

Considering the strong coupling between the thrust and power performance of blade section, it would be surprising for a rotor to perform as expected in terms of power capture, yet act very differently than expected in terms of thrust. As discussed, the predicted power performance has been well verified with results from three different flow velocities corresponding to one-another and to the predicted performance, and displaying recognisable performance characteristics such as a clear Reynolds number influence. It is therefore deemed to be most likely that the measured values of thrust were erroneous, due to one or a combination of the factors discussed regarding the instrumentation.

An investigation into this would consist of further tow tank experiments run at higher flow velocities and with instrumentation designed specifically to capture the range of thrust values expected on this rotor design. This is discussed in Future Work, in Section 7.3.

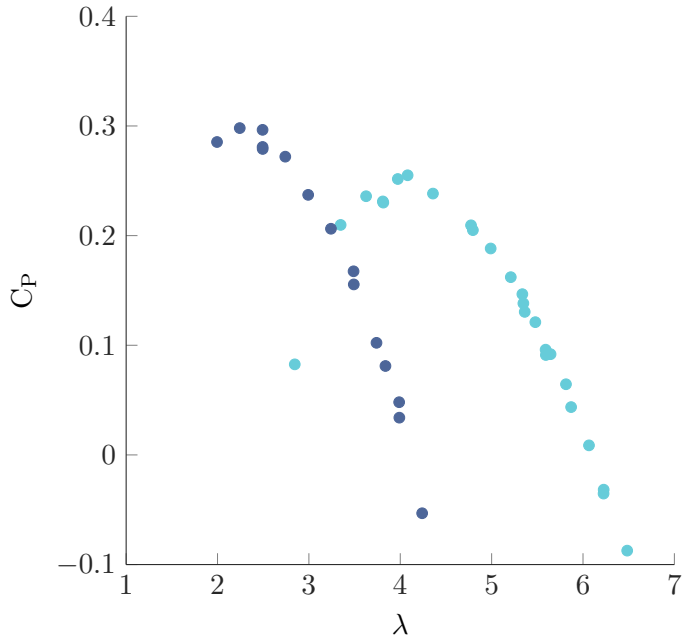

Figure 6.8: Comparison of the C_P-λ curves of the empirical data obtained at 0.8 m s^{-1} for the prototype-scale base case and new blade designs.

Table 6.5: Comparision of the increase in λ and Ω from optimum operating point to runaway for the 0.8 m s^{-1} tests run on the base case and new blade designs.

Test set	λ_O	λ_R	$\Delta\lambda_{OR}$	Ω_O (RPM)	Ω_R (RPM)	$\Delta\Omega_{OR}$ (RPM)
Base case	4.1	6.1	2	81.9	122.3	40.4
New blade	2.24	4.09	1.84	44.98	81.95	36.97

6.2.3 Comparison between base case and new blade empirical performance

Fig. 6.8 shows the empirically derived performance curves for the base case and the new blade designs, both taken at a carriage velocity of 0.8 m s^{-1}. Comparison of the twos data sets showed the increased gradient on the overspeed side of the C_P-λ curve from the base case to the new blade. Table 6.5 details the pertinent aspects of the data for the analysis of the impact made by the blade design alterations for suitability in an OSPR turbine, showing that the required increase from the optimum to runaway point in both λ and Ω was reduced.

Another notable aspect of this plot was the increase in optimum efficiency. This was, however, due not to a generally increased effectiveness of blade but to the more optimised β used on the new rotor design, and the increase in Re between the two test sets, as Table 6.4 details.

6.3 Conclusions

6.3.1 Blade design methodology

The different component parts of the methodology have been shown to be of great use in the development of a site-specific blade design which considers the intended operating method. The amount of information readily made available through the use of alteration functions, and the power of this method, in combination with the design space analysis, to expedite both the design process and the gain of increased knowledge of the operation of HATSTs in OSPR has been evidenced. The in-depth understanding gained through use of the cavitation and diagnostic plots, particularly as employed within the built-in feedback loop in the design methodology, has been shown to directly inform the engineer and positively influence subsequent stages – whether based on alteration functions or implemented on local blade radii.

The full-scale simulations showed that the new blade design regulated power as required, without any cavitation inception being predicted at any operating point. The design requirement that the thrust on the base case blade at optimum operating point was not exceeded by that of the new blade was also met. The increase in rotational velocity required to cap the power at the rated value in flow speeds up to the set cut-out ($3.11\ \mathrm{m\,s^{-1}}$) was reduced with the new blade design. This was due to the combination of an increase in the gradient of the overspeed side and an overall leftwards shift of the C_P-λ curve, effected by the blade design alterations.

Tow tank test verification

In order to empirically assess the performance of the designed blade – and thereby of the blade design methodology – tow tank tests were undertaken at various carriage velocities. Comparison of performance data, obtained at appropriate Reynolds numbers, to BEMT predictions of the new blade at prototype scale showed that the power performance was well predicted, verifying this aspect of the methodology and design. Verification of the thrust performance was not possible with the data collected in the test series, and further investigations would be required for this to be achieved.

Comparison of the performance of the base case and new blade designs at the same flow speed showed that, as in the full-scale simulations, the increase in λ and Ω from the optimum to runaway points were reduced, as required.

These observations led to the conclusion that the blade design methodology verifiably performed as required in terms of power performance, producing a blade design which met the design requirements within the platform in which it was assessed. The thrust performance, while not yet empirically verified, was as required in BEMT simulations of a full-scale turbine.

Chapter 7

Conclusions and future work

7.1 Conclusions

The research aims of this PhD were to investigate the overspeed power regulation method, increase understanding of the associated benefits and constraints, and develop a methodology for the design of blades suitable for use in overspeed power regulation.

The proposed method of achieving these aims gave rise to a set of research goals. These were to identify:

- potential issues with, and therefore design requirements for, the proposed operating method
- whether these requirements could be met with changes to the rotor design
- how the impact of any rotor design changes could measured in terms of these requirements
- what information could be gathered about the changes and impacts made by these blade design changes
- whether this information could be used to develop a blade which meets the requirements
- how this works in practice.

This thesis has addressed each of these goals.

Experiments in the wind tunnel showed that operation in OSPR with standard blade designs means higher rotational velocities; this leads, as shown in Chapter 3, to higher voltage levels. Higher thrust forces may be caused, depending on the thrust characteristics of the blades. An increased chance of cavitation inception on the blades also results.

Tow tank experiments on a base case blade defined the performance of a prototype-scale blade designed for use in a horizontal axis tidal stream turbine. These experiments showed that the increase in tip speed ratio between the optimum operating point and

runaway was large, indicating, again, that the risk of cavitation would increase should such blades be used in overspeed rather than in alternative regulation techniques. The thrust characteristics of the prototype tidal turbine rotor also indicated that higher thrust loads would be experienced in overspeed.

The collected tow tank data were matched with BEMT predictions to a degree which verified the tool for use in the design process.

It was determined that, as the fluid-structure interface of a turbine, as the design component which determines how the turbine interacts with the fluid in terms of power capture, thrust force and rotational velocities, the blade design was the component to which design alterations may be made with the goal of controlling performance in overspeed. Alterations to the blade design, it was hypothesised, could work to mitigate the challenges identified with operation in overspeed.

An investigation into the effects of various alterations to the geometrical blade design was established as a useful means of researching how the challenges of overspeed may be met. The blade root pitch setting, the twist distribution and the chord distribution were set as variable parameters. The aerofoil section, hub size and blade length were fixed.

Consideration of the parameters involved in a cavitation analysis and any calculation of actual power and thrust values, rather than simply the coefficients, indicated that a deployment scenario with numerical values assigned to many of the variables would be required. Furthermore, it was ascertained that the extent to which a rotor will be required to overspeed is dependent on the rated power of the device and the maximum flow speed in which it is expected to operate. The need to set boundary conditions thus led to the establishment of a design platform – which can be altered according to prospective deployment sites and turbine configurations – and the definition of a set of design requirements. This gave a full-scale scenario in which to make BEMT predictions of the performance of the tested base case tidal turbine blade.

The performance of the base case blade within the design platform was assessed in terms of the requirements of a blade working in overspeed, considering the desirable shape of the C_P-λ curve, the maximum required operating Ω, the optimum rotor efficiency, and the coefficient of thrust at the optimum operating point. This lead to the definition of a set of OSPR performance metrics, the first three expressed as the change made from the base case performance, and the last expressed as an absolute value:

- $\Delta\lambda_{\mathrm{Orw}}$, measuring the increase or reduction in gradient of the slope of the overspeed side of the C_P-λ curve
- ΔC_{Po}, expressing the impact made on the maximum efficiency of the rotor
- ΔC_{To}, measuring the difference made to the coefficient of thrust at the optimum operating point
- Ω_{ovs}, quantifying the maximum rotational velocity at which the rotor will be required to turn in order to regulate power at the rated value within the flow

velocities up to the cut-out.

A design space analysis was formed, based on making one change to one blade design parameter at a time and measuring the impact made upon the suitability of the blade for use in an OSPR turbine by use of the OSPR metrics. A series of stacked y-axes were used to measure the effected change in each metric of each design alteration. The blade design parameter changes were implemented over a range with the use of alteration functions. This allowed the effects had by a range of related blade permutations to be plotted along an x-axis. This approach expedited the process of selecting and applying blade design alterations, facilitated the identification of trends in the x-axis, and associated or coupled effects in the y-axes.

The OSPR metrics were seen to be most sensitive to the applied alterations to blade root pitch setting, closely followed by those made to the twist distribution. The blade root pitch setting, however, was a fairly crude design change and had consequentially little subtlety; the diversity of alterations and effect possible with the twist distribution made this a more useful design parameter in tuning blade performance. Alterations to the chord distribution had a comparatively small effect; however, the effect on the maximum rotational velocity was appreciable. It was found that by defining the distribution as a somewhat parabolic shape achieved similar effects as scaling alterations, but without resulting in over-large blade root sections.

Design space results of combining this chord distribution with the more useful range of twist alterations showed that the chord alterations had a significantly more useful impact on these non-optimised blade design permutations, effecting significant increases in the torque contributions of the blade elements and thereby increasing the maximum efficiency.

Hand-alterations were found to be required in the fine-tuning of the blade. Increasing the gradient of the twist in the lower blade – which effectively induced a localised root pitch setting change – and maintaining a fairly constant low gradient until the upper blade, improved the performance of the blade. The desired cavitation-free operation was re-gained by increasing the twist gradient near the tip and optimising the blade root pitch setting. This increased the angle of attack at the extreme operating condition, taking the cavitation number out of the face surface-bubble cavitation zone, while maximising the optimum efficiency within the constraint that the thrust coefficient at the optimum operating point did not exceed that of the base case blade.

The finalised blade design met the design requirements, running cavitation-free throughout operation in MPPT and in OSPR, not exceeding the thrust of the base case blade at the optimum operating point and achieving a maximum power coefficient comparable, though slightly lower, than the base case blade.

The maximum operational Ω of the new blade – developed under the design platform and set of design requirements detailed in Sections 4.3 and 5.1 – was a great improvement on that of the base case blade. It also compared favourably, in terms of cavitation and

voltage, to the performance of the blade developed for OSPR in [88], which would require to rotate at 23 RPM at the maximum flow speed set herein, 3.11 $\mathrm{m\,s^{-1}}$. However, the torque required to achieve comparable power capture would be consequentially higher for the blade developed in this thesis. High rotor torque levels can cause increased structural stress in drive-train components, and requires a generator designed to reciprocate with corresponding electromagnetic torque. This may a drawback of the particular combination of design platform parameters and design requirements; however, alterations to the boundary conditions may mitigate this. Deeper deployment, a slower site, a higher rated power, different requirements in terms of thrust force or rotor efficiency and, perhaps of most interest for the future development of this research, an aerofoil with more benign cavitation characteristics – particularly in negative angles of attack – and the inclusion of maximum torque limit as an additional OSPR performance metric would alter the process of design, the resulting blade shape and thus the rotor performance.

Tow tank tests of a prototype-scale blade of the new design verified the performance in terms of power. Thrust performance remains to be verified. Comparison of the performance of the base case and new blade designs at the same flow speed showed that, as in the full-scale simulations, the increase in λ and Ω from the optimum to runaway points were reduced.

The observations made in these tow tank experiments led to the conclusion that the blade design methodology verifiably performed as required in terms of power performance, producing a blade design which met the design requirements within the platform in which it was assessed. The thrust performance, while not yet empirically verified, was as required in BEMT simulations of a full-scale turbine.

7.1.1 Conclusive remarks on the design methodology

The different component parts of the methodology have been shown to be each of great use in the development of a site-specific blade design which considers the intended operating method. The methods have a sound theoretical basis and have the further advantage of giving to the user an increased understanding of how rotors work, of what happens when changes are made, both at the scale of power and thrust performance and at the scale of elemental forces, angles of attack and fluid flow behaviours. This information is output in a form which can be easily shared with others for an easy appreciation of complex matters.

7.2 Contributions made

The major contributions to the field of tidal energy made in this research and supported in this thesis are: an increase in the knowledge held on the operation of HATSTs in overspeed, as pertaining to the use of overspeed for power regulation; an increase in the knowledge of the impact of blade design alterations; and a blade design methodology

for overspeed power regulation of horizontal axis tidal turbines.

The methodology developed sets the geometrical parameters of blade root pitch setting, twist distribution and chord length distribution as variables. In the first stages of alterations made, the changes are defined by function-based alterations, and in the latter stages by hand-picked fine-tuning changes, informed by the foregoing findings. A design platform is used to give a scenario in which the blade design changes can be assessed for performance in maximum power point tracking and overspeed power regulation as the flow increases from cut-in to cut-out. The methodology uses a set of metrics – developed to ascertain how the blade design changes affected the suitability of blade designs for use in overspeed power – and a design space sensitivity analysis approach, alongside a whole-blade cavitation analysis and diagnostic plots of the torque distribution and angle of attack. The combination of these methods and tools gives an efficient yet open-box procedure, which allows information to be gathered and used in an iterative spiral in which blade permutations are made increasingly suitable for overspeed power regulated tidal turbines.

The concept of using OSPR performance metrics in a design space analysis has been developed in the research, the purpose of which is to enable the rotor design to be moulded to a set of explicitly defined performance requirements. This allows any design changes to be made in the design process, and the impact on the suitability of each rotor design permutation to be qualitatively – beneficial or detrimental, positive or negative – and quantitatively – whether in "change from base case" or numerical terms – determined.

The expedited application of blade design alterations via the use of function-based alterations has, to the knowledge of the author – not been previously presented as a method within an "open-box" design procedure. In combination with batch-run BEMT-predictions and the design space sensitivity analysis, this allows many blade design alterations to be analysed efficiently while retaining a pattern in the alterations made. The advantage of this is that the effects of making a *type* of change can be investigated and – with the visual-numerical approach herein presented – appreciated, both in terms of each individual change made and in terms of the *range* over the change was made.

Shareable experiential knowledge has been generated in this research. The twist and blade root pitch setting alterations were found to be most powerful in altering the shape of the C_P-λ curve. It was seen that, on the otherwise optimised (for maximum power capture) base case blade, alterations which increased the gradient of the overspeed side of the C_P-λ curve had a detrimental effect on the maximum rotor efficiency. However, it was found that useful twist and chord alterations could be coupled to maintain the useful effects on the overspeed gradient while regaining much of the lost maximum efficiency. Once function-based alterations have been used to make the main design changes, hand alterations to the blade design have been found to be required to fine-tune the lade shape and, thereby, its performance. Any future use of the design methodology will continue to produce experiential knowledge which can be used to inform and help in

the understanding of blade design and rotor performance analysis.

Two sets of prototype-scale turbine tests have been produced. The first set, along with the extensive uncertainty analysis performed on the measurements, have been published in a peer-reviewed journal; these data now exist for use as a set of empirical data with which rotor performance prediction tools can be taken through a verification process.

It has been shown that the blade design methodology can be used to overcome challenges associated with overspeed and produce blades which give a significant performance improvement in terms of applicability in overspeed power regulation.

7.3 Future work

7.3.1 Development to the design methodology

Structural analysis

The methodology does not yet contain a full structural integrity analysis, though a simple structural feasibility analysis has been undertaken to ascertain that the blade shapes defined hydrodynamically were actually practicable. This is presented in Appendix B. Further development of the methodology would take further account of the structural aspects of blade design, most likely with quasi-static structural integrity analyses. Amongst the other aspects of structural performance, this would consider strain relief due to blade rotational velocity.

Torque limits

Depending on the generator configuration and the scale of any turbine for which the proposed power regulation method is overspeed, the maximum torque may be a further design constraint. At present, this has not been considered in the blade design methodology. Incorporation of an OSPR metric which considers the maximum torque allowable would enable this design consideration to become part of the design process.

Cavitation resistant aerofoils

Consideration of aerofoils with greater cavitation resistance may allow the C_P-λ curve to move rightwards, and for the rotor velocities to be increased and the torques borne by the system to be thereby decreased. This research would add strength to the acceptability of overspeed as a power regulation method.

Unsteady flow

Inclusion of free-stream disturbance in the design platform would allow deeper analysis of the potential of this method of power regulation. Peak forces, fatigue loading, the effects of turbulence, yawed flow and the wave-induced effect of depth-altered cavitation inception

potential are all aspects of the dynamic marine environment from the consideration of which this methodology would benefit.

7.3.2 Further verification of the design methodology

The thrust values measured in the tow tank tests of the new blade design did not compare well with the BEMT predictions, while the power performance did compare well. As discussed, the sensativity of the measurement range of the instrumentation may not have been appropriate for the magnitude of thrust measured during these tests and, while it was worthwhile making the measurements, the results were not found to be reliable. The large "zero" – or offset – thrust values were most probably been due to the relatively large mass of the blades tested compared to the smaller blades tested during this set of tests. An improvement on this would be to calibrate strain gauges using the thrust range expected, with a mass equivalent to that of the rotor putting an equivalent pre-strain on the stanchion, and to amplify the voltage signal to increase the resolution of the measurements at the level appropriate for these tests.

Further research would also run tests at higher flow velocities and obtain thrust measurements with higher Re, thereby providing verification of the measurements, and further insight into the behaviour of the blades in terms of thrust. Higher Re may help to suppress any laminar separation and reattachment occurring on the blades at the lower carriage velocity.

7.3.3 Additional aerofoil data

In any future application of this blade design methodology, it would be of interest and benefit to use additional sets of aerofoil data – if modelling is within a flow range in which aerofoil performance may be affected by flow phenomena – obtained in an appropriate range of flow conditions. Appropriate variations in the Reynolds number, and the turbulence intensity between the sets of aerofoil data would be of consequence, particularly in a case in which the design methodology – and thus the BEMT code – will be followed up with physical tests, either of prototype scale or a full-scale but small turbine, in which, it has been noted, such flow phenomena have a significant influence on the performance of aerofoils.

Appendix A

Appendix A tabulated tow tank results

A.1 Base case tow tank tests

Table A.1: Results of the tow tank tests with the base case blade design, with an NREL S814 aerofoil

U_∞	RPM	λ	Q	F_T	M_y	M_x	C_P	C_P	$C_{\mathrm{M}y}$	$C_{\mathrm{M}x}$	U_λ	U_{C_P}	U_{C_T}	$U_{C_{\mathrm{M}y}}$	$U_{C_{\mathrm{M}x}}$
0.50	37.82	3.02	0.45	16.30	0.93	-0.07	0.0633	0.2874	0.0431	-0.0035	0.009802	0.011199	0.020057	0.001422	-0.001485
0.50	50.35	4.03	0.40	17.48	1.19	-0.04	0.0749	0.3089	0.0554	-0.0019	0.015856	0.014960	0.020119	0.001445	-0.001494
0.50	63.11	5.05	0.32	22.27	1.37	-0.02	0.0747	0.3931	0.0636	-0.0009	0.020913	0.018700	0.020153	0.001458	-0.001490
0.50	69.68	5.57	0.16	21.65	1.99	0.02	0.0406	0.3820	0.0923	0.0010	0.015594	0.020634	0.020142	0.001526	0.001493
0.50	75.71	6.05	-0.16	24.61	1.97	0.14	-0.0453	0.4341	0.0912	0.0065	0.031361	-0.022404	0.020178	0.001522	0.001487
0.80	56.92	2.84	1.60	43.47	2.45	-0.30	0.0821	0.2993	0.0442	-0.0055	0.003386	0.004076	0.004355	0.000604	-0.000581
0.80	67.00	3.35	3.47	54.70	3.72	-0.81	0.2097	0.3767	0.0673	-0.0146	0.002200	0.004643	0.004146	0.000676	-0.000586
0.80	72.58	3.63	3.58	58.13	4.45	-0.71	0.2347	0.4000	0.0804	-0.0129	0.001859	0.005011	0.004068	0.000725	-0.000585
0.80	76.26	3.81	3.36	58.79	4.52	-0.65	0.2312	0.4046	0.0816	-0.0118	0.002208	0.005294	0.004053	0.000729	-0.000584
0.80	76.37	3.81	3.34	59.10	4.51	-0.65	0.2301	0.4066	0.0813	-0.0118	0.001979	0.005301	0.004044	0.000728	-0.000584
0.80	79.53	3.97	3.51	61.81	4.57	-0.73	0.2516	0.4254	0.0825	-0.0132	0.002119	0.005501	0.003980	0.000733	-0.000585
0.80	81.73	4.08	3.49	62.83	4.70	-0.71	0.2577	0.4324	0.0849	-0.0128	0.002605	0.005656	0.003954	0.000743	-0.000585
0.80	87.24	4.36	3.03	63.19	4.76	-0.59	0.2383	0.4348	0.0860	-0.0107	0.002565	0.006099	0.003945	0.000747	-0.000583
0.80	95.57	4.77	2.39	63.64	4.89	-0.40	0.2065	0.4381	0.0884	-0.0072	0.002709	0.006765	0.003935	0.000757	-0.000581
0.80	95.98	4.79	2.37	63.68	4.90	-0.39	0.2050	0.4383	0.0886	-0.0070	0.003077	0.006796	0.003933	0.000758	-0.000581
0.80	99.86	4.99	2.09	63.32	7.38	-0.31	0.1883	0.4359	0.1334	-0.0056	0.058623	0.007438	0.003943	0.000963	-0.000581
0.80	104.25	5.21	1.73	63.57	5.00	-0.20	0.1626	0.4378	0.0904	-0.0036	0.003915	0.007452	0.003938	0.000766	-0.000580
0.80	106.70	5.34	1.52	62.55	5.06	-0.15	0.1466	0.4315	0.0916	-0.0027	0.052624	0.007798	0.003971	0.000771	-0.000581
0.80	107.04	5.35	1.43	62.75	4.99	-0.12	0.1382	0.4319	0.0901	-0.0021	0.004027	0.007669	0.003957	0.000764	-0.000580
0.80	107.26	5.36	1.34	61.70	4.96	-0.11	0.1305	0.4252	0.0897	-0.0020	0.064434	0.007864	0.003989	0.000763	-0.000581
0.80	109.65	5.48	1.22	62.50	5.02	-0.05	0.1211	0.4302	0.0907	-0.0010	0.002508	0.007871	0.003963	0.000767	-0.000581
0.80	111.89	5.59	0.92	61.11	4.99	0.03	0.0932	0.4206	0.0901	0.0005	0.003997	0.008047	0.003998	0.000764	0.000579
0.80	111.98	5.59	0.87	60.87	4.95	0.04	0.0877	0.4186	0.0894	0.0007	0.003613	0.008047	0.004000	0.000761	0.000579
0.80	112.99	5.65	0.90	62.00	5.04	0.03	0.0919	0.4268	0.0910	0.0005	0.004455	0.008129	0.003976	0.000768	0.000580
0.80	116.37	5.81	0.61	62.01	5.10	0.13	0.0645	0.4268	0.0921	0.0023	0.004366	0.008383	0.003976	0.000772	0.000580

Continued on next page

Table A.1 (continued from previous page)

U_∞	RPM	λ	Q	F_T	M_y	M_x	C_P	C_P	$C_{\mathrm{M}y}$	$C_{\mathrm{M}x}$	U_λ	U_{C_P}	U_{C_T}	$U_{C_{\mathrm{M}y}}$	$U_{C_{\mathrm{M}x}}$
0.80	117.50	5.87	0.41	60.94	5.06	0.22	0.0436	0.4194	0.0914	0.0040	0.004177	0.008470	0.004002	0.000769	0.000580
0.80	121.41	6.07	0.08	61.21	5.11	0.32	0.0087	0.4213	0.0923	0.0058	0.004869	0.008755	0.003995	0.000774	0.000581
0.80	124.48	6.23	-0.31	59.77	5.03	0.37	-0.0353	0.4123	0.0911	0.0066	0.053541	-0.009008	0.004038	0.000769	0.000582
0.90	68.71	3.06	3.08	59.56	3.47	-0.67	0.1346	0.3249	0.0496	-0.0096	0.012665	0.003439	0.003220	0.000520	-0.000463
0.90	79.81	3.55	5.32	75.59	5.59	-1.23	0.2707	0.4126	0.0801	-0.0176	0.002457	0.003699	0.002877	0.000637	-0.000471
0.90	81.36	3.62	5.12	77.54	14.83	-1.16	0.2645	0.4223	0.2120	-0.0165	0.003029	0.003791	0.002821	0.001313	-0.000469
0.90	83.59	3.71	5.15	79.30	5.77	-1.11	0.2736	0.4318	0.0825	-0.0159	0.002857	0.003888	0.002772	0.000646	-0.000468
0.90	87.66	3.90	4.93	81.29	5.93	-1.04	0.2744	0.4426	0.0847	-0.0149	0.003360	0.004110	0.002716	0.000656	-0.000467
0.90	92.11	4.10	4.55	80.29	6.03	-0.91	0.2668	0.4381	0.0864	-0.0130	0.019869	0.004568	0.002750	0.000664	-0.000466
0.90	93.87	4.17	4.40	81.97	6.07	-0.89	0.2625	0.4463	0.0867	-0.0127	0.003445	0.004476	0.002696	0.000665	-0.000465
0.90	99.24	4.41	4.02	82.97	6.23	-0.77	0.2536	0.4518	0.0891	-0.0110	0.003875	0.004786	0.002667	0.000676	-0.000463
0.90	104.43	4.64	3.57	82.60	6.32	-0.63	0.2366	0.4498	0.0904	-0.0090	0.003811	0.005093	0.002678	0.000681	-0.000462
0.90	107.41	4.77	3.23	80.91	8.72	-0.56	0.2208	0.4409	0.1247	-0.0081	0.024808	0.005402	0.002729	0.000847	-0.000461
0.90	110.74	4.92	2.96	82.43	6.38	-0.46	0.2086	0.4490	0.0913	-0.0066	0.004697	0.005474	0.002684	0.000686	-0.000461
0.90	116.93	5.20	2.36	81.97	6.42	-0.29	0.1753	0.4463	0.0918	-0.0042	0.004982	0.005833	0.002696	0.000688	-0.000459
0.90	121.00	5.38	1.98	81.30	15.57	-0.19	0.1519	0.4425	0.2225	-0.0027	0.005250	0.006066	0.002715	0.001371	-0.000459
0.90	125.13	5.56	1.52	81.43	6.46	-0.06	0.1206	0.4437	0.0924	-0.0009	0.004134	0.006312	0.002714	0.000691	-0.000459
0.90	130.36	5.79	0.94	79.18	6.48	0.11	0.0775	0.4312	0.0926	0.0016	0.005575	0.006600	0.002776	0.000692	0.000459
0.90	135.57	6.03	0.34	76.99	6.44	0.22	0.0296	0.4199	0.0921	0.0032	0.048590	0.006898	0.002839	0.000690	0.000460
0.90	139.76	6.21	-0.04	77.32	6.55	0.40	-0.0038	0.4214	0.0937	0.0057	0.006385	-0.007115	0.002828	0.000697	0.000460
1.00	67.17	2.68	2.69	67.76	3.72	-0.55	0.0832	0.2976	0.0429	-0.0064	0.005557	0.002423	0.002480	0.000426	-0.000372
1.00	72.93	2.91	3.45	72.67	4.11	-0.74	0.1156	0.3190	0.0474	-0.0086	0.005776	0.002595	0.002393	0.000441	-0.000373
1.00	81.52	3.25	6.26	89.10	5.63	-1.52	0.2352	0.3917	0.0650	-0.0176	0.005054	0.002660	0.002030	0.000511	-0.000384
1.00	85.09	3.40	6.93	94.98	6.58	-1.61	0.2711	0.4170	0.0758	-0.0185	0.003457	0.002667	0.001858	0.000558	-0.000385
1.00	88.42	3.53	7.00	97.34	7.00	-1.58	0.2854	0.4280	0.0808	-0.0182	0.003552	0.002765	0.001784	0.000581	-0.000385

Continued on next page

Table A.1 (continued from previous page)

U_∞	RPM	λ	Q	F_T	M_y	M_x	C_P	C_P	$C_{\mathrm{M}y}$	$C_{\mathrm{M}x}$	U_λ	U_{C_P}	U_{C_T}	$U_{C_{\mathrm{M}y}}$	$U_{C_{\mathrm{M}x}}$
1.00	95.63	3.82	6.49	100.44	7.37	-1.43	0.2852	0.4410	0.0850	-0.0165	0.003924	0.003066	0.001674	0.000600	-0.000382
1.00	102.55	4.09	5.87	101.57	7.60	-1.25	0.2768	0.4461	0.0876	-0.0144	0.004269	0.003382	0.001633	0.000613	-0.000379
1.00	104.71	4.18	5.73	101.69	7.68	-1.18	0.2760	0.4467	0.0886	-0.0137	0.004142	0.003473	0.001628	0.000618	-0.000378
1.00	107.40	4.29	5.54	102.59	7.80	-1.14	0.2737	0.4505	0.0899	-0.0132	0.004075	0.003586	0.001593	0.000624	-0.000378
1.00	110.70	4.42	5.18	102.74	7.84	-1.02	0.2635	0.4512	0.0904	-0.0117	0.004455	0.003747	0.001587	0.000626	-0.000376
1.00	110.71	4.42	5.23	103.23	7.87	-1.03	0.2669	0.4539	0.0908	-0.0118	0.004627	0.003748	0.001569	0.000629	-0.000377
1.00	110.73	4.42	5.21	103.06	7.87	-1.01	0.2657	0.4527	0.0908	-0.0116	0.004742	0.003745	0.001575	0.000628	-0.000376
1.00	110.74	4.42	5.24	102.91	7.87	-1.01	0.2667	0.4519	0.0907	-0.0117	0.004789	0.003741	0.001580	0.000628	-0.000376
1.00	110.76	4.42	5.21	102.28	7.86	-1.02	0.2656	0.4492	0.0907	-0.0117	0.004696	0.003746	0.001605	0.000628	-0.000376
1.00	111.49	4.45	5.14	102.73	7.87	-1.00	0.2637	0.4516	0.0908	-0.0115	0.004786	0.003786	0.001589	0.000628	-0.000376
1.00	117.68	4.70	4.45	101.33	7.97	-0.80	0.2409	0.4450	0.0918	-0.0093	0.004599	0.004075	0.001641	0.000633	-0.000374
1.00	123.29	4.92	3.89	101.14	8.05	-0.63	0.2206	0.4442	0.0928	-0.0073	0.004676	0.004334	0.001649	0.000638	-0.000372
1.00	127.44	5.09	3.54	101.01	8.14	-0.52	0.2078	0.4437	0.0938	-0.0060	0.007015	0.004521	0.001654	0.000643	-0.000372
1.00	128.85	5.14	3.29	100.60	8.07	-0.46	0.1948	0.4417	0.0930	-0.0053	0.005649	0.004589	0.001668	0.000639	-0.000371
1.00	129.11	5.15	3.31	100.57	8.09	-0.46	0.1969	0.4420	0.0933	-0.0053	0.005931	0.004602	0.001670	0.000641	-0.000371
1.00	129.88	5.19	3.19	99.92	8.08	-0.42	0.1908	0.4393	0.0932	-0.0049	0.005900	0.004643	0.001695	0.000640	-0.000371
1.00	130.19	5.20	3.24	101.13	8.14	-0.45	0.1938	0.4442	0.0938	-0.0051	0.005343	0.004642	0.001649	0.000643	-0.000371
1.00	131.53	5.25	3.04	100.04	8.10	-0.39	0.1836	0.4392	0.0934	-0.0045	0.006094	0.004706	0.001688	0.000641	-0.000371
1.00	133.77	5.34	2.80	99.69	8.12	-0.32	0.1724	0.4375	0.0935	-0.0037	0.005709	0.004803	0.001701	0.000641	-0.000370
1.00	136.81	5.46	2.49	98.86	8.12	-0.23	0.1566	0.4344	0.0936	-0.0026	0.005815	0.004945	0.001731	0.000642	-0.000371
1.00	137.26	5.48	2.53	99.48	8.18	-0.23	0.1595	0.4371	0.0943	-0.0026	0.005481	0.004956	0.001709	0.000645	-0.000370
1.00	140.35	5.60	2.16	98.53	8.15	-0.14	0.1392	0.4327	0.0940	-0.0016	0.006291	0.005091	0.001742	0.000644	-0.000370
1.00	142.65	5.69	1.96	97.67	8.17	-0.06	0.1282	0.4285	0.0940	-0.0007	0.006110	0.005180	0.001770	0.000644	-0.000370
1.00	145.62	5.81	1.54	96.03	8.12	0.06	0.1034	0.4218	0.0937	0.0007	0.006653	0.005319	0.001825	0.000642	0.000370
1.00	148.08	5.91	1.36	95.55	8.15	0.10	0.0926	0.4195	0.0939	0.0012	0.006740	0.005412	0.001840	0.000643	0.000370
1.00	150.60	6.01	1.18	95.38	8.21	0.15	0.0816	0.4186	0.0945	0.0017	0.007356	0.005509	0.001845	0.000646	0.000370

Continued on next page

Table A.1 (continued from previous page)

U_∞	RPM	λ	Q	F_T	M_y	M_x	C_P	C_P	$C_{\mathrm{M}y}$	$C_{\mathrm{M}x}$	U_λ	U_{C_P}	U_{C_T}	$U_{C_{\mathrm{M}y}}$	$U_{C_{\mathrm{M}x}}$
1.00	158.85	6.34	0.39	92.35	8.17	0.32	0.0287	0.4056	0.0942	0.0037	0.007993	0.005836	0.001937	0.000645	0.000370
1.00	160.22	6.39	0.18	91.47	8.13	0.38	0.0130	0.4017	0.0937	0.0044	0.007561	0.005894	0.001962	0.000642	0.000371
1.00	161.26	6.44	0.07	91.42	8.12	0.44	0.0051	0.4019	0.0937	0.0051	0.007694	0.005942	0.001965	0.000642	0.000371
1.00	162.14	6.47	-0.06	90.53	8.07	0.46	-0.0047	0.3976	0.0930	0.0053	0.006777	-0.005978	0.001989	0.000639	0.000371
1.00	163.12	6.51	-0.06	89.95	8.07	0.45	-0.0045	0.3954	0.0932	0.0051	0.008962	-0.006010	0.002006	0.000640	0.000371

A.2 Tow tank tests on the new blade

Table A.2: Results of the tow tank tests with the new OSPR blade design, with an NREL S814 aerofoil

U_∞	RPM	λ	U_λ	U_λ %	Q	U_Q	C_P	U_{C_P}	U_{C_P} %	F_{Tzero}	F_T	U_{F_T}	C_T	U_{C_T}	U_{C_T} %
0.342	10.002	1.167	0.011	0.914	-1.313	0.450	0.152	0.052	34.333	14.588	16.064	1.365	0.608	0.052	8.577
0.342	14.999	1.751	0.015	0.867	-1.683	0.450	0.293	0.078	26.799	14.121	15.925	1.365	0.603	0.052	8.651
0.342	19.998	2.335	0.026	1.132	-1.274	0.450	0.296	0.105	35.373	13.867	15.612	1.365	0.591	0.052	8.821
0.342	25.007	2.919	0.032	1.104	-0.844	0.450	0.245	0.131	53.356	13.680	13.830	1.365	0.523	0.052	9.939
0.342	30.009	3.503	0.036	1.018	-0.435	0.450	0.151	0.157	103.370	13.475	11.893	1.365	0.450	0.052	11.537
0.342	12.001	1.401	0.011	0.809	-1.463	0.450	0.204	0.063	30.806	13.226	16.253	1.365	0.615	0.052	8.480
0.342	16.999	1.984	0.013	0.677	-1.510	0.450	0.298	0.089	29.848	13.291	15.908	1.365	0.602	0.052	8.660
0.342	22.002	2.570	0.025	0.973	-1.099	0.450	0.281	0.115	40.983	13.174	15.191	1.365	0.576	0.052	9.061
0.342	27.000	3.151	0.042	1.341	-0.684	0.450	0.214	0.141	65.839	13.270	13.304	1.365	0.503	0.052	10.327
0.342	25.000	2.918	0.038	1.292	-0.881	0.450	0.255	0.130	51.144	13.114	13.889	1.365	0.525	0.052	9.897
0.342	28.985	3.383	0.044	1.296	-0.536	0.450	0.180	0.151	84.051	12.923	12.682	1.365	0.480	0.052	10.827
0.342	25.001	2.919	0.035	1.198	-0.833	0.450	0.241	0.131	54.090	12.831	14.427	1.365	0.546	0.052	9.533
0.342	34.999	4.086	0.033	0.814	0.013	0.450	-0.005	-0.183	3383.954	12.867	9.376	1.365	0.355	0.052	14.605
0.342	25.001	2.918	0.033	1.114	-0.844	0.450	0.244	0.130	53.349	12.933	14.225	1.365	0.538	0.052	9.667
0.342	31.997	3.734	0.038	1.009	-0.270	0.450	0.100	0.167	166.460	12.910	11.216	1.365	0.424	0.052	12.227
0.342	24.999	2.920	0.030	1.030	-0.842	0.450	0.245	0.131	53.448	12.847	14.312	1.365	0.542	0.052	9.609
0.800	44.982	2.243	0.025	1.124	-7.328	0.450	0.298	0.019	6.283						
0.800	76.953	3.838	0.029	0.752	-1.166	0.450	0.081	0.031	38.621						
0.800	54.973	2.742	0.024	0.889	-5.472	0.450	0.272	0.023	8.302						
0.800	69.955	3.489	0.024	0.690	-2.647	0.450	0.167	0.029	17.027						
0.800	49.989	2.493	0.023	0.923	-6.559	0.450	0.296	0.021	6.959						
0.800	79.960	3.988	0.027	0.668	-0.665	0.450	0.048	0.033	67.678						
0.800	49.994	2.493	0.021	0.859	-6.213	0.450	0.281	0.021	7.328						
0.800	59.995	2.992	0.019	0.624	-4.372	0.450	0.237	0.025	10.336						
0.800	64.996	3.242	0.027	0.821	-3.509	0.450	0.206	0.027	12.868						

Continued on next page

Table A.2 (continued from previous page)

U_∞	RPM	λ	U_λ	U_λ %	Q	U_Q	C_P	U_{C_P}	U_{C_P} %	F_Tzero	F_T	U_{F_T}	C_T	U_{C_T}	U_{C_T} %
0.800	74.989	3.740	0.028	0.757	-1.508	0.450	0.102	0.031	29.865						
0.800	39.993	1.995	0.020	1.027	-7.891	0.450	0.285	0.017	5.837						
0.800	70.003	3.491	0.021	0.612	-2.457	0.450	0.155	0.029	18.343						
0.800	80.004	3.990	0.027	0.664	-0.470	0.450	0.034	0.033	95.834						
0.800	50.013	2.494	0.021	0.860	-6.170	0.450	0.279	0.021	7.378						
0.800	94.940	4.735	0.031	0.648	-7.714	0.450	0.662	0.039	5.912						
0.800	104.939	5.234	0.028	0.528	-6.467	0.450	0.614	0.043	7.014						
0.800	94.965	4.736	0.029	0.607	-7.545	0.450	0.648	0.039	6.036						
0.800	85.009	4.240	0.031	0.729	-0.413	0.450	0.032	0.035	108.973						
0.800	89.997	4.488	0.030	0.659	-5.786	0.450	0.471	0.037	7.837						
0.800	87.998	4.389	0.028	0.643	-3.530	0.450	0.281	0.036	12.782						
1.000	54.550	2.176	0.046	2.116	-1.491	0.450	0.038	0.011	30.251						
1.000	60.009	2.394	0.018	0.745	-0.339	0.450	0.009	0.013	132.904						
1.000	109.985	4.388	0.023	0.520	-0.069	0.450	0.004	0.023	654.677						
1.000	69.996	2.793	0.018	0.640	-8.124	0.450	0.263	0.015	5.605						
1.000	79.994	3.192	0.017	0.529	-6.360	0.450	0.236	0.017	7.118						
1.000	90.002	3.591	0.018	0.496	-4.238	0.450	0.177	0.019	10.645						
1.000	100.004	3.990	0.017	0.436	-2.055	0.450	0.095	0.021	21.907						
1.000	64.985	2.593	0.017	0.643	0.705	0.450	-0.021	-0.014	63.827						
1.000	69.998	2.793	0.018	0.641	-8.209	0.450	0.266	0.015	5.548						
1.000	67.998	2.713	0.019	0.712	-3.144	0.450	0.099	0.014	14.342						

Appendix B

Appendix B - Structural feasibility

B.1 Structural feasibility

The structural feasibility of blade designs is an important consideration. While it was not the focus of this work to undertake a full structural analysis, or to look at appropriate materials, a very preliminary structural feasibility analysis of the designs was included in the methodology. As blades can be constructed in various different manners, and of various different materials, the simplest approach to this problem was to simplify the possibilities and assume a structural spar, of square cross-section, would take the load on the blade, and that a non-load-bearing sleeve would give the blade its outer shape.

This was undertaken by the simple expedient of considering whether the structural forces predicted by the BEMT and design methodology codes would be supportable by a structural element which would fit inside the blade's outer hydrodynamic shape, based on the Engineers Beam Theory. The failure criterion set was the tensile yield strength multiplied by a safety factor or 2; this dictated the size of the structural spar. The pass criteria for this simple, preliminary check of structural feasibility was that, for a blade design operating within the set design platform, *the cross-section of each element of the required structural spar should comfortably fit inside the enveloping aerofoil cross-section.*

A more detailed (yet still computationally efficient) analysis of blade design structural integrity was reported by NREL, in [131]; incorporation of this analysis would bring more rigour to this design methodology. However, this method also does not account for fatigue in the blade, and so the method would remain preliminary.

Method overview

In this feasibility analysis, by manipulating the elemental force results output by the BEMT tool, the axial and radial load taken by each blade element was calculated for each analysed blade design iteration. As in the BEMT code, the loads were assumed to be concentrated at nodes positioned at the middle of the elements. The bending

moments resulting from these loads on the bottom of each spar element were calculated considering, for element el, the load applied to each element from el to the tip, with each corresponding moment arm. Each element was taken as a separate beam, around the bottom of which a moment was applied, and the required depths of a series of square spar elements were calculated. Assessment was then made to ascertain whether, at each element, the required structural spar would fit comfortably inside the enveloping aerofoil shape of the corresponding blade section.

Assumptions

The radial loads were seen to be much smaller than the axial loads, and were therefore not considered within this preliminary analysis; furthermore, it was assumed that the loads would be transferred directly to the corresponding spar element. At this stage, no torsional loading from the aerofoil onto the spar was considered.

Mathematical model

A mathematical model was constructed which enabled the require depth of a tapered, square cross-section spar to be calculated based on the maximum axial forces applied during the blade's operation.

The axial moment around the bottom of element i on a blade with el elements, each of which has length l_{el}, can be found from:

$$M_{y,i} = F_i \frac{l_{el}}{2} + F_{i+1} 3 \frac{l_{el}}{2} + F_{i+2} 5 \frac{l_{el}}{2} \cdots + F_{i+n}(2n+1)\frac{l_{el}}{2} \tag{B.1}$$

or, generally,

$$M_{y,i} = \sum_{n=0}^{el-i} F_{i+n}(2n+1)\frac{l_{el}}{2} \ . \tag{B.2}$$

Assuming any deformations are small and within the elastic region, the bending moment at a cross section of a structural component can be related to the stress in the component and the induced deflection using the Euler-Bernoulli beam theory, or "engineers' theory of bending". Applied to the case of the spar this is given, simply, by

$$\frac{M_{y,i}}{I_{y,i}} = \frac{\sigma}{y_i} = \frac{E}{R_i} \ , \tag{B.3}$$

where, for element i, $M_{y,i}$ is the bending moment around the neutral axis, $I_{y,i}$ is the second moment of area around this axis, σ is the stress in the structural fibres at which the stress is to be calculated, y_i is the distance between the neutral axis and these fibres, E is the Young's Modulus of the material and R_i is the radius of curvature induced in the bending. The second moment of area of a square cross-section is defined

$$I_{y,i} = \frac{1}{12} b_i^3 \ . \tag{B.4}$$

Taking into account the maximum bending moment applied during the operational range of the turbine, considering extreme fibres of the cross-section of the spar elements and by setting the σ value to the maximum allowable stress, it was possible to substitute Eq. (B.4) into Eq. (B.3) and rearrange to find b for each element, the depth of a square beam which would withstand the maximum bending moment applied at that element:

$$b_i = \sqrt[3]{\frac{6M_{y,i}}{\sigma}} \ . \tag{B.5}$$

Setting the value of σ to half of the yield strength (YS) of the spar material includes a safety factor of 2 in the spar design.

B.2 Application of the mathematical model

B.2.1 Maximum elemental bending moments

Having established the mathematical basis, the structural analysis was then implemented in MATLAB. As in the BEMT model, the number of blade elements was denoted el and the number of λ values at which the momentum calculations were made was denoted p. The annuli axial force matrix, $\boldsymbol{F}_{y,\mathrm{an}}$, a matrix of size el by p, was directly extracted from the BEMT model results, and divided by B, the number of blades, to give $\boldsymbol{F}_{y,\mathrm{el}}$, an el by p matrix of the elemental axial forces on one blade for each λ value. $\boldsymbol{F}_{y,\mathrm{el}}$ was therefore given by

$$\boldsymbol{F}_{y,\mathrm{el}} = \frac{1}{B}\begin{pmatrix} F_{y,1},\lambda_1 & F_{y,1},\lambda_2 & \cdots & F_{y,1},\lambda_p \\ F_{y,2},\lambda_1 & F_{y,2},\lambda_2 & \cdots & F_{y,2},\lambda_p \\ \vdots & \vdots & \ddots & \vdots \\ F_{y,el},\lambda_1 & F_{y,el},\lambda_2 & \cdots & F_{y,el},\lambda_p \end{pmatrix} \tag{B.6}$$

An el by el matrix, $\boldsymbol{K}_{\mathrm{el}}$, was required to give the $2n+1$ term in Eq. (B.2). This upper-diagonal matrix was defined as:

$$\boldsymbol{K}_{\mathrm{el}} = \begin{pmatrix} 1 & 3 & 5 & \cdots & 2(el-1)+1 \\ & 1 & 3 & \cdots & 2(el-2)+1 \\ & & 1 & \cdots & 2(el-3)+1 \\ & & & \ddots & \vdots \\ \mathbf{0} & & & & 2(el-el)+1 \end{pmatrix} \tag{B.7}$$

The final matrix, $\boldsymbol{N}_{\mathrm{el}}$, by which to multiply the force matrix, was given by

$$\boldsymbol{N}_{\mathrm{el}} = \frac{l_{\mathrm{el}}}{2}\boldsymbol{K}_{\mathrm{el}} \ , \tag{B.8}$$

and an el by p matrix of the elemental moments was then obtained by multiplying $\boldsymbol{F}_{y,\mathrm{el}}$

by $\boldsymbol{K}_{\mathrm{el}}$:

$$\boldsymbol{M}_{y,\mathrm{el}} = \boldsymbol{N}_{\mathrm{el}}\boldsymbol{F}_{y,\mathrm{el}} \ . \tag{B.9}$$

As the BEMT model was configured to produce non-dimensionalised coefficients, it was set up with one flow speed input. The analysis of moments over the example operational range therefore required the elemental axial moments to be non-dimensionalised as coefficients of axial moment, and then multiplied by the relevant free stream flow velocity, U_∞, for each tip speed ratio, λ. The full operational range - optimum-point tracking and power-regulation operation - of an OSPR turbine can be defined with the U_∞ and λ ranges:

$$0 \leq U_\infty \leq U_{\infty\mathrm{D}} \quad \text{wherein } \lambda = \lambda_{\mathrm{o}} \tag{B.10}$$

and

$$U_{\infty\mathrm{D}} \leq U_\infty \leq U_{\infty\mathrm{MAX}} \quad \text{wherein } \lambda_{\mathrm{O}} \leq \lambda \leq \lambda_{\mathrm{OVS}} \ . \tag{B.11}$$

This gave p^{OPRAN} points, where $p^{\mathrm{OPRAN}} < p$. Considering this, a free stream flow velocity matrix, $\boldsymbol{U}_\infty^{\mathrm{OPRAN}}$, of size el by p was created from the two ranges of U_∞ to give p columns, and vertically repeated to give el rows. The $\boldsymbol{M}_{\mathrm{y,\,el}}$ matrix was also curtailed at the overspeed point, p^{OPRAN}.

With the operational range defined in each of the variables, the calculation of the elemental moments during the full operational range, $\boldsymbol{M}_{\mathrm{y,\,el}}^{\mathrm{OPRAN}}$, was possible according to:

$$\boldsymbol{M}_{y,\mathrm{el}}^{\mathrm{OPRAN}} = \left(\frac{\boldsymbol{M}_{y,\mathrm{el}}}{(U_{\infty\mathrm{BEMT}})^2}\right)(\boldsymbol{U}_\infty^{\mathrm{OPRAN}})^2 \ . \tag{B.12}$$

To assess the extreme of the structural requirements, the maximum bending moment experienced by each element throughout the operational range was determined. This gave a vector, $\boldsymbol{m}_{y,el}^{\mathrm{MAX}}$, of length el. The corresponding values of λ and U_∞ were also determined to enable graphical visualisation of the results.

B.2.2 Creation of the spar

A common structural steel, ASTM-A36, was selected as a reasonable and inexpensive material from which to set the material properties at this stage. This gave a yield strength, YS of 250 MPa. The calculation of the geometry of a tapered spar strong enough to withstand the maximum bending moment at each element was then achieved by setting the maximum allowable stress $\sigma_{\max}$ to half the YS value, and inputting this, and $\boldsymbol{m}_{y,el}^{\mathrm{MAX}}$, into Eq. (B.5):

$$\boldsymbol{b}_{\mathrm{el}} = \sqrt[3]{\frac{6\ \boldsymbol{m}_{y,\mathrm{el}}^{\mathrm{MAX}}}{\sigma_{\max}}} \ . \tag{B.13}$$

A safety factor of 2 was included in the design by setting $\sigma_{\max}$ to half the YS.

B.3 Results

B.3.1 Elemental bending moments

Shown in Fig. B.1, a plot of elemental bending moment over the flow range was produced to confirm that the maximum bending moment for each element had been correctly found. This was included to make certain that the bending moment value for each element was the maximum possible within the model test site. Fig. B.1 shows that the maximum moments were predicted to occur at slightly different flow speeds along the blade; this indicated that the analysis performed was slightly conservative as the moments in $\boldsymbol{m}_{y,el}^{\mathrm{MAX}}$ did not all occur at the same flow velocity.

B.3.2 Structural integrity

The aerofoil shape used in this case was an NREL S814, which has maximum thickenss of 14% of the chord. A comparison of this thickness and the required spar depth at each section, as shown graphically in Fig. B.2, showed that the required spar sections were consistently less thick than their corresponding blade sections. The 3-dimensional plot in Fig. B.3 confirmed visually that the entire calculated spar sections - including the corners of the squares - fit well within the enveloping aerofoil sections.

It was therefore possible to conclude that, according to this simple structural analysis,

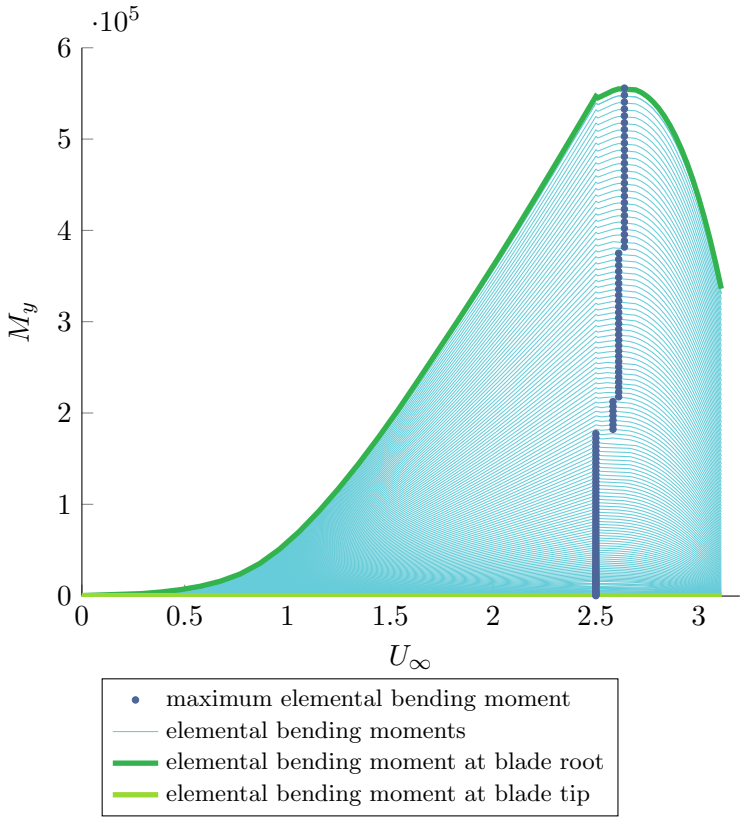

Figure B.1: Elemental bending moments varying with U_∞

it is possible to make this blade design structurally sound.

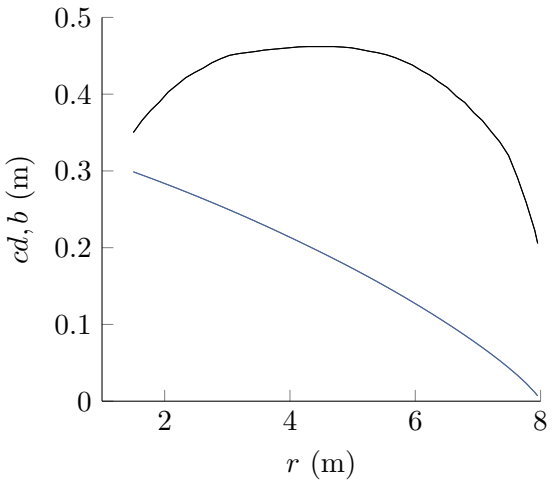

Figure B.2: Required spar size and maximum aerofoil thickness along blade radius at operating point of highest F_{T}, 2D comparison.

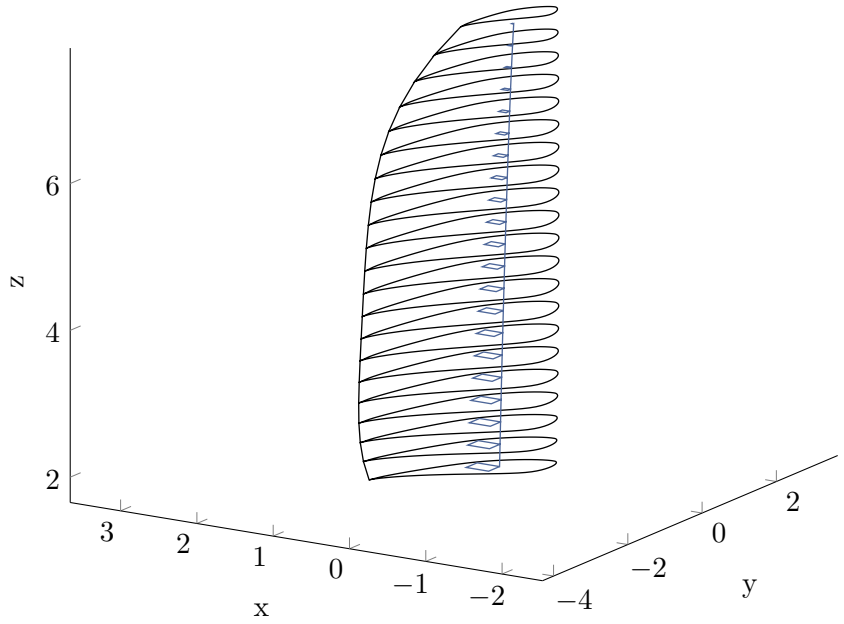

Figure B.3: Required spar size and maximum aerofoil thickness along blade radius at operating point of highest F_{T}. One view of a 3D comparison.

Bibliography

[1] I G Bryden, S J Couch, A Owen, and G Melville. Tidal current resource assessment. *Proceedings of the Institution of Mechanical Engineers, Part A: Journal of Power and Energy*, 221(2):125–135, 2007. ISSN 0957-6509. doi: 10.1243/09576509JPE238. URL http://pia.sagepub.com/lookup/doi/10.1243/09576509JPE238.

[2] ABPmer, The Met Office, and Proudman Oceanographic Laboratory. Atlas of UK Marine Renewable Energy Resources : Technical Report. (May):181, 2008.

[3] NOVELTIS. IRENA: Global Atlas, Tide Prediction Service from high resolution mapping. URL http://tips.noveltis.com/.

[4] Jack Hardisty. The Analysis of Tidal Stream Power, 2009. URL http://books.google.com/books?hl=en{&}lr={&}id=SFUztwHVyHgC{&}pgis=1.

[5] Jian Zhang, Luc Moreau, Mohamed Machmoum, and Pierre-Emmanuel Guillerm. State of the art in tidal current energy extracting technologies. In *2014 International Conference on Green Energy*, pages 1–7, 2014. ISBN 978-1-4799-3602-1. doi: 10.1109/ICGE.2014.6835388.

[6] International Energy Agency and Nuclear Energy Agency. Projected cost of generating electricity - Executive summary. Technical report, 2015. URL https://www.iea.org/Textbase/npsum/ElecCost2015SUM.pdf.

[7] International Energy Agency and Nuclear Energy Agency. Projected Costs of Generating Electricity 2010. Technical report, 2010. URL https://www.iea.org/publications/freepublications/publication/projected{_}costs.pdf.

[8] International Energy Agency. Technology Roadmap. pages 1–58, 2013. doi: 10.1007/SpringerReference_7300.

[9] E. Echavarria, B. Hahn, G. J. W. van Bussel, and T. Tomiyama. Reliability of Wind Turbine Technology Through Time. *Journal of Solar Energy Engineering*, 130(3):031005, 2008. ISSN 01996231. doi: 10.1115/1.2936235.

[10] T M Nevalainen. *The effect of unsteady sea conditions on tidal strea mturbine loads and durability*. Phd thesis, University of Strathclyde, 2016.

[11] MOL Hansen. *Aerodynamics of wind turbines*. 2008. ISBN 9781844074389. URL http://books.google.com/books?hl=en{&}lr={&}id=GVD{_}HDPix6YC{&}oi=fnd{&}pg=PR6{&}dq=Aerodynamics+of+Wind+Turbines{&}ots=1OLSUWv3zO{&}sig=dfRdy1GoKMd0qKgwxvy7a5HwfmU.

[12] T Burton, D Sharpe, N Jenkins, and E Bossanyi. *Wind energy handbook*. John Wiley & Sons Ltd., Chichester, 2001. ISBN 0471489972. URL http://books.google.com/books?hl=en{&}lr={&}id=dip2LwCRCscC{&}oi=fnd{&}pg=PT14{&}dq=Wind+Energy+Hand+Book{&}ots=IbCMSqEsHb{&}sig={_}{_}fGWH60ILZ-30hDixeqjp7bVmU.

[13] J. F. Manwell, J. G. McGowna, and A. L. Rogers. *Wind Energy Explained*. John Wiley & Sons Ltd., Chichester, 2009. ISBN 9780470015001.

[14] Ira H Abbot and Albert E von Doenhoff. *Theory of Wing Sections*. Dover Publications, Inc., New York, 1949.

[15] a. Mason-Jones, D. M. O'Doherty, C. E. Morris, T. O'Doherty, C. B. Byrne, P. W. Prickett, R. I. Grosvenor, I. Owen, S. Tedds, and R. J. Poole. Non-dimensional scaling of tidal stream turbines. *Energy*, 44(1):820–829, 2012. ISSN 03605442. doi: 10.1016/j.energy.2012.05.010. URL http://dx.doi.org/10.1016/j.energy.2012.05.010.

[16] John S. Carlton. *Marine propellers and propulsion*. Elsevier Ltd., Oxford, second edi edition, 2007. ISBN 9780750681506.

[17] Wen Zhong Shen, Robert Mikkelsen, Jens N??rkaer S??rensen, and Christian Bak. Tip loss corrections for wind turbine computations. *Wind Energy*, 8(4):457–475, 2005. ISSN 10954244. doi: 10.1002/we.153.

[18] Marshall L Buhl. A new empirical relationship between thrust coefficient and induction factor for the turbulent windmill state. *Technical Report NREL/TP-500-36834*, (August), 2005.

[19] L. A. Viterna and R. D. Corrigan. Fixed pitch rotor performance of large horizontal axis wind turbines. In *Proc. Workshop on Large Horizontal Axis Wind Turbines, NASA CP-2230, DOE Publication CONF-810752*, pages 69–85, Cleveland, 1981. NASA Lewis Research Center. ISBN 9788578110796. doi: 10.1017/CBO9781107415324.004.

[20] T. J. Mueller, L. J. Pohlen, P. E. Conigliaro, and B. J. Jansen. The influence of free-stream disturbances on low Reynolds number airfoil experiments. *Experiments in Fluids*, 1(1):3–14, 1983. ISSN 0723-4864. doi: 10.1007/BF00282261. URL http://link.springer.com/10.1007/BF00282261.

[21] C.P. Butterfield, D.A. Simms, W.P. Musial, and G.N. Scott. Spanwise aerodynamic loads on a rotating wind turbine blade. Technical Report SERI TP-257-3983, 1990.

[22] D A Simms, M M Hand, L J Fingersh, and D W Jager. Unsteady aerodynamics experiment phases II – IV Test configurations and available data campaigns. Technical Report July, 1999.

[23] James L Tangler. The Nebulous Art of Using Wind-Tunnel Airfoil Data for Predicting Rotor Performance. In *ASME Wind Energy Conference*, number January, Reno, 2002. National Renewable Energy Laboratory.

[24] J. Gordon Leishman. Challenges in modelling the unsteady aerodynamics of wind turbines. *Wind Energy*, 5(2-3):85–132, apr 2002. ISSN 1095-4244. doi: 10.1002/we.62. URL http://doi.wiley.com/10.1002/we.62.

[25] R.H. Barnard and D.R. Philpott. *Aircraft Flight*. Pearson Education Limited, Harlow, third edition, 2004. ISBN 0-13-120043-7.

[26] John D. Jr Anderson. *Fundamentals of Aerodynamics*. McGraw-Hill, Singapore, third edition, 2001. ISBN 0-07-118146-6.

[27] National Wind Technology Centre. Index of airfoils Coefficients. URL http://wind.nrel.gov/airfoils/Coefficients/.

[28] Mark Drela. XFoil. URL http://web.mit.edu/drela/Public/web/xfoil/.

[29] Michael Togneri, Ian Masters, Matthew Allmark, and Faris Elasha. Unsteady BEMT for fault diagnosis and prognosis in tidal stream turbines. *The 11th European Wave and Tidal Energy Conference*, (August):1–7, 2015. doi: 10.13140/RG.2.1.3570.8248.

[30] Hannah Buackland. *Combined current, wave and turbulent flows and their effects on tidal energy devices*. Doctoral, Swansea University, 2014.

[31] Thomas Mikael Nevalainen, Cameron M Johnstone, and Andrew Grant. An Unsteady Blade Element Momentum Theory for Tidal Stream Turbines with Morris Method Sensitivity Analysis. *Proceedings of the 11th European Wave and Tidal Energy Conference*, pages 1–10, 2015.

[32] P B S Lissaman. Low-Reynolds-Number Airfoils. *Annual Review of Fluid Mechanics*, 15(1):223–239, jan 1983. ISSN 0066-4189. doi: 10.1146/annurev.fl.15.010183.001255. URL http://www.annualreviews.org/doi/abs/10.1146/annurev.fl.15.010183.001255.

[33] Michaels Selig, James J Guglielmo, Andy P Broeren, and Philippe Giguere. *Summary of low-speed airfoil data*, volume 1. SoarTech Publications, Virginia Beach, 1995. ISBN 0964674718.

[34] Robert Liebeck and Ron Blackwelder. Low Reynolds - Number Separation Bubble. Technical report, Defense Technical Information Centre, 1984.

[35] I A Milne. *An Experimental Investigation of Turbulence and Unsteady Loading on Tidal Turbines*. PhD thesis, 2014.

[36] Tom Blackmore, Luke E. Myers, and AbuBakr S. Bahaj. Effects of turbulence on tidal turbines: Implications to performance, blade loads, and condition monitoring. *International Journal of Marine Energy*, 14:1–26, 2016. ISSN 22141669. doi: 10.1016/j.ijome.2016.04.017. URL http://www.sciencedirect.com/science/article/pii/S2214166916300297.

[37] Thomas H. E. Clark. Turbulence in Marine Environments (TiME): A framework for understanding turbulence and its effects on tidal devices. In *Proceedings of the 11th European Wave and Tidal Energy Conference*, pages 1–10, 2015.

[38] K Black, J Ibrahim, R Helsby, J McKay, T Clark, N Pearson, R Moore, and J Hernon. Turbulence: Best practices for measurement of turbulent flows. A guide for the tidal power industry. Technical report, 2015.

[39] W. J. McCroskey. The Phenomenon of Dynamic Stall. Technical report, NASA, 1981.

[40] C.P. Butterfield, A.C. Hansen, D. Simms, and G. Scott. Dynamic stall on wind turbine blades. In *Windopower 91' Conference*, Palm Springs, 1991.

[41] J.W. Larsen, S.R.K. Nielsen, and S. Krenk. Dynamic stall model for wind turbine airfoils. *Journal of Fluids and Structures*, 23(7):959–982, 2007. ISSN 08899746. doi: 10.1016/j.jfluidstructs.2007.02.005. URL http://linkinghub.elsevier.com/retrieve/pii/S0889974607000291.

[42] T.S.R. Reddy and K.R.V. Kaza. Analysis of an unswept propfan blade with semiempirical dynamic stall model. Technical report, National Aeronautics and Space Administration, 1989.

[43] Danmei Hu, Ouyang Hua, and Zhaohui Du. A study on stall-delay for horizontal axis wind turbine. *Renewable Energy*, 31(6):821–836, 2006. ISSN 09601481. doi: 10.1016/j.renene.2005.05.002.

[44] Zhaohui Du and MS Selig. The effect of rotation on the boundary layer of a wind turbine blade. *Renewable Energy*, 20:167–181, 2000. ISSN 09601481. doi: 10.1016/S0960-1481(99)00109-3. URL http://www.sciencedirect.com/science/article/pii/S0960148199001093.

[45] International Electrotechnical Commission. IEC 61400-12-1. Wind turbines – Part 12-1: Power performance measurements of electricity producing wind turbines, 2005. URL www.iec.ch.

[46] a F Molland, a S Bahaj, J R Chaplin, and W M J Batten. Measurements and predictions of forces, pressures and cavitation on 2-D sections suitable for marine current turbines. *Proceedings of the Institution of Mechanical Engineers, Part M: Journal of Engineering for the Maritime Environment*, 218(2):127–138, jan 2004. ISSN 1475-0902. doi: 10.1243/1475090041651412. URL http://pim.sagepub.com/lookup/doi/10.1243/1475090041651412.

[47] H. C. Buckland, I. Masters, J. a. Orme, and T. Baker. Cavitation inception and simulation in blade element momentum theory for modelling tidal stream turbines. *Proceedings of the Institution of Mechanical Engineers, Part A: Journal of Power and Energy*, 227(4):479–485, 2013. ISSN 0957-6509. doi: 10.1177/0957650913477093. URL http://pia.sagepub.com/lookup/doi/10.1177/0957650913477093.

[48] Bin Wu, Yongqiang Lang, Navid Zargari, and Samir Kouro. *Power conversion and control of wind energy systems*. 2011. ISBN 9781118029008 1118029003 9781118028995 1118028996. doi: 10.1002/9781118029008.

[49] Fernando D. Bianchi, Hernán De Battista, and Ricardo J. Mantz. *Wind turbine control systems. Principles, modelling and gain scheduling design.*, volume 26. Springer-Verlag London Limited, 2007. ISBN 1846284929. URL http://dx.doi.org/10.1007/1-84628-493-7{_}2.

[50] S. Benelghali, M.E.H. Benbouzid, and J.F. Charpentier. Generator systems for marine current turbine applications: A comparative study. *IEEE Journal of Oceanic Engineering*, 37(3):554–563, 2012. ISSN 0364-9059. doi: 10.1109/JOE.2012.2196346. URL http://ieeexplore.ieee.org/xpls/abs{_}all.jsp?arnumber=6211451.

[51] B. Hahn, M. Durstewitz, and K. Rohrig. Reliability of wind turbines - Experience of 15 years with 1500WTs. *Wind Energy*, (January 2006):329–332, 2006.

[52] Shawn Sheng, Mark McDade, and Robert Errichello. Wind Turbine Gearbox Failure Modes – A Brief (Presentation), 2011. URL http://www.nrel.gov/docs/fy12osti/53084.pdf.

[53] Katharina Fischer. Reliability and maintenance of wind turbines. *Wind Energy*, 2013. URL http://www.gaccmidwest.org/fileadmin/ahk{_}chicago/2013{_}EVENTS/2013{_}GRP{_}Windenergie/PPTs{_}Wind{_}Conference/02{_}Fischer.pdf.

[54] Yuanye Xia, Khaled H Ahmed, and Barry W Williams. Different torque ripple reduction methods for wind energy conversion systems using diode rectifier and boost converter. In *IEEE International electric machines & drives conference (IEMDC)*, pages 729–734, 2011. ISBN 9781457700613. doi: 10.1109/IEMDC.2011.5994902.

[55] P L Fraenkel. Marine current turbines: pioneering the development of marine kinetic energy converters. *Proceedings of the Institution of Mechanical Engineers, Part A: Journal of Power and Energy*, 221(2):159–169, jan 2007. ISSN 0957-6509. doi: 10.1243/09576509JPE307. URL http://pia.sagepub.com/lookup/doi/10.1243/09576509JPE307.

[56] J.W. Park, K.W. Lee, and H.J. Lee. Wide speed operation of a doubly-fed induction generator for tidal current energy. In *The 30th Annual Conference of the IEEE Industrial Electronics Society*, pages 1333–1338, Busan, 2004.

[57] S E Ben Elghali, M E H Benbouzid, and J F Charpentier. Marine Tidal Current Electric Power Generation Technology : State of the Art and Current Status. In *IEEE Electric machines & drives conference*, pages 1407–1412, Antalya, 2007. ISBN 1424407435. doi: 10.1109/IEMDC.2007.383635.

[58] Ralf Starzmann, Nils Hirsch, Martin Baldus, and Stefan Scholl. A stepwise approach towards the development and full-scale testing of a marine hydrokinetic turbine. pages 1–6, 2013.

[59] Ozan Keysan, Alasdair S. McDonald, and Markus Mueller. A direct drive permanent magnet generator design for a tidal current turbine(SeaGen). *2011 IEEE International Electric Machines & Drives Conference (IEMDC)*, pages 224–229, may 2011. doi: 10.1109/IEMDC.2011.5994850. URL http://ieeexplore.ieee.org/lpdocs/epic03/wrapper.htm?arnumber=5994850.

[60] Zhibin Zhou, Franck Scuiller, Jean Frederic Charpentier, Mohamed Benbouzid, and Tianhao Tang. An up-to-date review of large marine tidal current turbine technologies. In *International power electronics and application conference and exposition*, pages 480–484, 2014. ISBN 978-1-4799-6768-1. doi: 10.1109/PEAC.2014.7037903. URL http://ieeexplore.ieee.org/lpdocs/epic03/wrapper.htm?arnumber=7037903.

[61] J. Clarke, G. Connor, A. Grant, C. Johnstone, and S. Ordonez-Sanchez. Contra-rotating Marine Current Turbines: Performance in Field Trials and Power Train Developments. In *Proceedings of the 10th World Renewable Energy Congress*, 2008.

[62] Luis R N Rivas, Amable L Piñeiro, José a S Sánchez, and Eva M N Rojas. The GESMEY Project . Design and Development of a Second Generation TEC. *EWTEC 2011 Proceedings*, 2011.

[63] L. Drouen, Jean Frédéric Charpentier, E. Semail, and S. Clenet. Study of an innovative electrical machine fitted to marine current turbines. In *OCEANS 2007 - Europe*, pages 1–6, Aberdeen, 2007. ISBN 978-1-4244-0635-7. doi: 10.1109/OCEANSE.2007.4302284.

[64] Ozan Keysan, Markus Mueller, R. Doherty, M. Hamilton, and A.S. McDonald. C-GEN, a lightweight direct drive generator for marine energy converters. *5th IET International Conference on Power Electronics, Machines and Drives (PEMD 2010)*, pages 244–244, 2010. doi: 10.1049/cp.2010.0021. URL http://digital-library.theiet.org/content/conferences/10.1049/cp.2010.0021.

[65] Sanjida Moury and M Tariq Iqbal. A permanent magnet generator with PCB stator for low speed marine current applications. *2009 1st International Conference on the Developements in Renewable Energy Technology (ICDRET)*, pages 1–4, 2009. doi: 10.1109/ICDRET.2009.5454205. URL http://ieeexplore.ieee.org/lpdocs/epic03/wrapper.htm?arnumber=5454205.

[66] Thomas Ackermann and Lennart Söder. An overview of wind energy-status 2002. *Renewable and Sustainable Energy Reviews*, 6(1-2):67–128, 2002. ISSN 13640321. doi: 10.1016/S1364-0321(02)00008-4.

[67] John K. Kaldellis and Ali Sayigh, editors. *Comprehensive renewable energy. Volume 2: Wind energy*. Elsevier Ltd. ISBN 978-0-08-087873-7. URL http://www.sciencedirect.com/science/referenceworks/9780080878737{#}ancv2.

[68] David Goodfellow. *Variable speed operation of wind turbines*. Phd thesis, Univeristy of Leicester, 1986. URL http://hdl.handle.net/2381/7822.

[69] T. Thiringer and J. Linders. Control by variable rotor speed of a fixed-pitch wind turbine operating in a wide speed range. *IEEE Transactions on Energy Conversion*, 8(3):520–526, 1992. ISSN 08858969. doi: 10.1109/60.257068. URL http://ieeexplore.ieee.org/lpdocs/epic03/wrapper.htm?arnumber=257068.

[70] E Muljadi, K Pierce, P Migliore, National Wind, and National Renewable. Control strategy for varaible-speed Stall-Regulated Wind Turbines. *American Control Conference, 1998*, (April):1710–1714, 1998.

[71] E Muljadi, K Pierce, and P Migliore. Soft-stall control for variable-speed stall-regulated wind turbines. *Journal of Wind Engineering and Industrial Aerodynamics*, 85(3):277–291, 2000. ISSN 01676105. doi: 10.1016/S0167-6105(99)00130-0. URL http://linkinghub.elsevier.com/retrieve/pii/S0167610599001300.

[72] R. Pena, J.C. Clare, and G.M. Asher. Doubly fed induction generator uising back-to-back PWM converters and its application to variable- speed wind-energy generation. *Electrical Power Applications, IEE Proceedings*, 143(3):231–241, 1996.

[73] R. Cárdenas, G.M. Asher, W.F. Ray, and R. Pena. Power limitation in variable speed wind turbines with fixed pitch angle. In *Opportunities and Advances in International Power Generation*, number 419, pages 44–48. IEE, 1996.

[74] Rachel F Nicholls-Lee, Stephen R Turnock, and Stephen W Boyd. Simulation Based Optimisation of Marine Current Turbine Blades. *International Conference on Computer and IT Applications in the Maritime Industries*, pages 314–328, 2008. URL http://eprints.soton.ac.uk/id/eprint/51108.

[75] Robynne E. Murray, Thomas Nevalainen, Katie Gracie-Orr, Darrel A. Doman, Michael J. Pegg, and Cameron M. Johnstone. Passively adaptive tidal turbine blades: Design tool development and initial verification. *International Journal of Marine Energy*, 14:101–124, 2016. ISSN 22141669. doi: 10.1016/j.ijome.2016.02.001. URL http://dx.doi.org/10.1016/j.ijome.2016.02.001.

[76] Ramona B Barber and Michael R Motley. A Numerical Study of the Effect of Passive Control on Cavitation for Marine Hydrokinetic Turbines. In *European Wave and Tidal Energy Conference 2015*, pages 1–8, Nantes, 2015.

[77] Ben Whitby and Carlos E. Ugalde-Loo. Performance of pitch and stall regulated tidal stream turbines. *IEEE Transactions on Sustainable Energy*, 5(1):64–72, 2014. ISSN 19493029. doi: 10.1109/TSTE.2013.2272653.

[78] Matthias Arnold, Frank Biskup, and Po Wen Cheng. Load reduction potential of variable speed control approaches for fixed pitch tidal current turbines. pages 1–10, 2015.

[79] Penny Jeffcoate, Ralf Starzmann, Bjoern Elsaesser, Stefan Scholl, and Sarah Bischoff. Field measurements of a full scale tidal turbine. *International Journal of Marine Energy*, 12:3–20, 2015. ISSN 22141669. doi: 10.1016/j.ijome.2015.04.002. URL http://dx.doi.org/10.1016/j.ijome.2015.04.002.

[80] R Starzmann, M Baldus, E Groh, N Hirsch, N A Lange, and S Scholl. Full-scale testing of a tidal energy converter using a tug boat. 2008.

[81] Black rock tidal power. URL http://www.blackrocktidalpower.com/home/.

[82] Tidal Energy Limited. Ramsey Sound, 2015. URL http://www.tidalenergyltd.com/?page{_}id=650.

[83] Tidal Energy Limited. Welcome to Tidal Energy Ltd. (In Administration). URL http://www.tidalenergyltd.com/.

[84] MCT. Marine Current Turbines - An Atlantis Company. URL http://www.marineturbines.com/.

[85] The Scottish Government. Wave Energy Scotland - Fact Sheet. Technical report, Scottish Government. URL http://www.gov.scot/Resource/0046/00464410.pdf.

[86] C. Freeman, J. Amaral Teixeira, F. Trarieux, and R. Ayre. Design of a gravity stabilised fixed pitch tidal turbine of 400kW. *8th European Wave and Tidal Energy Conference, Uppsala, Sweden, 2009*, pages 376–383, 2009.

[87] Frank Biskup, Matthias Arnold, Philipp Daus, Raphael Arlitt, and Martin Hohberg. Effects of Rotor Blade Tip Modifications on a Tidal In-Stream Energy Converter – Voith HyTide ®. In *EWTEC*, Aalborg, 2013.

[88] Alexei Winter. Speed Regulated Operation for Tidal Turbines with Fixed Pitch Rotors. In *OCEANS 2011*, pages 1–8, Waikoloa, 2011.

[89] Alexei Winter and Theo Tryfonas. A constrained optimisation process for the design of tidal turbine blades with experimental validation. (3), 2011.

[90] Zhibin Zhou, Franck Scuiller, Jean Frédéric Charpentier, Mohamed El, Hachemi Benbouzid, Senior Member, Tianhao Tang, and Senior Member. Power control of a nonpitchable PMSG-based marine current turbine at overrated current speed with flux-weakening strategy. *IEEE Journal of oceanic engineering*, 40(3):536–545, 2015.

[91] Michael J. Lawson, Ye Li, and Danny C. Sale. Development and verification of a computational fluid dynamics model of a horizontal-axis tidal current turbine. *Proceedings of the ASME 2011 30th International Conference on Ocean, Offshore and Arctic Engineering*, (October), 2011.

[92] G. S. Bir, M. J. Lawson, and Y. Li. Structural design of a horizontal-axis tidal current turbine composite blade. *ASME 30th International Conference on Ocean, Offshore, and Arctic Engineering*, (October):14, 2011. doi: 10.1115/OMAE2011-50063.

[93] R.F. Nicholls-Lee, S.R. Turnock, and S.W. Boyd. Application of bend-twist coupled blades for horizontal axis tidal turbines. *Renewable Energy*, 50:541–550, feb 2013. ISSN 09601481. doi: 10.1016/j.renene.2012.06.043. URL http://linkinghub.elsevier.com/retrieve/pii/S0960148112003941.

[94] Rachel F. Nichols-Lee. *Adaptive composite blades for horizontal axis tidal turbines*. Phd, University of Southampton, 2011. URL https://core.ac.uk/download/files/34/2734423.pdf.

[95] R E Murray, C Gracie, D A Doman, M J Pegg, and C M Johnstone. Design of a Passively Adaptive Rotor Blade for Optimized Performance of a Horizontal-Axis Tidal Turbine. In *EWTEC*, Aalborg, 2013.

[96] Robynne E. Murray. *Passively adaptive tidal turbine blades: design methodology and experimental testing*. Phd, Dalhousie University, 2017.

[97] C. E. Morris, D. M. O'Doherty, T. O'Doherty, and A. Mason-Jones. Kinetic energy extraction of a tidal stream turbine and its sensitivity to structural stiffness attenuation. *Renewable Energy*, 88:30–39, 2016. ISSN 18790682. doi: 10.1016/j.renene.2015.10.037. URL http://dx.doi.org/10.1016/j.renene.2015.10.037.

[98] W.M.J. Batten, A.S. Bahaj, A.F. Molland, and J.R. Chaplin. Experimentally validated numerical method for the hydrodynamic design of horizontal axis tidal turbines. *Ocean Engineering*, 34(7):1013–1020, may 2007. ISSN 00298018. doi: 10.1016/j.oceaneng.2006.04.008. URL http://linkinghub.elsevier.com/retrieve/pii/S0029801806001843.

[99] a.S. Bahaj, a.F. Molland, J.R. Chaplin, and W.M.J. Batten. Power and thrust measurements of marine current turbines under various hydrodynamic flow conditions in a cavitation tunnel and a towing tank. *Renewable Energy*, 32(3):407–426, mar 2007. ISSN 09601481. doi: 10.1016/j.renene.2006.01.012. URL http://linkinghub.elsevier.com/retrieve/pii/S0960148106000516.

[100] Personal communications with D. Sharman of Ampair., 2013.

[101] TSI Instruments Ltd. Airflow Type 4 Test Set. Operating Instructions.

[102] RRWX. METAR, North England, Scotland and Ireland. URL http://wx.rrwx.com/metar-uk-no.htm.

[103] Rapid Electronics Ltd. Data sheet - Multitype Thermometer and datalogger re, 2007.

[104] Optick Technology Inc. Product Bulletin OPB703W, 2006.

[105] National Instruments. Data Sheet for 24-Bit Universal Analog Input NI 9219, 2010.

[106] GI Comyn, DS Nobes, and BA Fleck. Performance Evaluation and Wake Study of a Mirco Wind Turbine. *Transactions of the Canadian Society for Mechanical Engineering*, 35(1):101–117, 2011. URL http://www.tcsme.org/Papers/Vol35/Vol35No1Paper7.pdf.

[107] P. C. Sen. *Principles of Electric Machines and Power Electronics*. John Wiley & Sons, Inc., 1989. ISBN 0-471-85084-5.

[108] T. McCombes, C. Johnstone, B. Holmes, L. E. Myres, A. S. Bahaj, and J. P. Kofoed. EquiMar Deliverable D3.4 Best practice for tank testing of small marine energy devices. Technical report.

[109] I.a. Milne, a.H. Day, R.N. Sharma, and R.G.J. Flay. Blade loads on tidal turbines in planar oscillatory flow. *Ocean Engineering*, 60:163–174, mar 2013. ISSN 00298018. doi: 10.1016/j.oceaneng.2012.12.027. URL http://linkinghub.elsevier.com/retrieve/pii/S0029801812004465.

[110] Specialist Committee on Uncertainty Analysis of 25th ITTC. ITTC – Recommended Procedures and Guidelines 7.5-01-03-01: Uncertainty Analysis Instrument Calibration. Technical report, 2008.

[111] National Institute of Standards and Technology and SEMATECH. *Engineering Statistics Handbook*. 2012 updat edition, 2012. URL http://www.itl.nist.gov/div898/handbook/index.htm.

[112] Benoît Gaurier, Peter Davies, Albert Deuff, and Grégory Germain. Flume tank characterization of marine current turbine blade behaviour under current and wave loading. *Renewable Energy*, 59:1–12, 2013. ISSN 09601481. doi: 10.1016/j.renene.2013.02.026. URL http://dx.doi.org/10.1016/j.renene.2013.02.026.

[113] W.M.J. Batten, a.S. Bahaj, a.F. Molland, and J.R. Chaplin. Hydrodynamics of marine current turbines. *Renewable Energy*, 31(2):249–256, feb 2006. ISSN 09601481. doi: 10.1016/j.renene.2005.08.020. URL http://linkinghub.elsevier.com/retrieve/pii/S0960148105002314.

[114] D. Taylor. Wind Energy. In G. Boyle, editor, *Renewable Energy: Power for a Sustainable Future*. Oxford University Press, Oxford, 2004.

[115] D A Doman, Robynne E Murray, M J Pegg, Katie Gracie, C M Johnstone, and Thomas Nevalainen. Dynamic testing of a 1/20th scale tidal turbine. In *AWTEC*, Tokyo, 2014.

[116] I. Masters, J.C. Chapman, M.R. Willis, and J.A.C. Orme. A robust blade element momentum theory model for tidal stream turbines including tip and hub loss corrections. *Journal of Marine Engineering & Technology*, 10(1):25–35, 2011. doi: 10.1080/20464177.2011.11020241. URL http://dx.doi.org/10.1080/20464177.2011.11020241.

[117] Mathworks, 'Optimisation Toolbox – fmincon'.

[118] M. Togneri, I. Masters, R. Malki, and A. Rio. Flume measurements of lift and drag for selected tidal turbine blade sections.

[119] C. Sicot, P. Devinant, S. Loyer, and J. Hureau. Rotational and turbulence effects on a wind turbine blade. Investigation of the stall mechanisms. *Journal of Wind Engineering and Industrial Aerodynamics*, 96(8-9):1320–1331, 2008. ISSN 01676105. doi: 10.1016/j.jweia.2008.01.013.

[120] D M Somers. The S814 and S815 Airfoils October 1991 — July 1992 The S814 and S815 Airfoils. (December), 2004.

[121] Lewis M. Alexander. North Sea; Hydrology. URL http://www.britannica.com/EBchecked/topic/419398/North-Sea/33268/Hydrology.

[122] International Towing Tank Conference. ITTC - Recommended Procedures 7.5-02-01-03. Fresh water and seawater properties. Technical report, 26th ITTC Specialist Committee on Uncertainty Analysis, 2011. URL http://ittc.sname.org/CD2011/pdfProcedures2011/7.5-02-01-03.pdf.

[123] Black & Veatch. Tidal stream resource and technology summary report. Technical Report 0, Carbon Trust, Isleworth, 2005.

[124] Justine M Mcmillan, Alex E Hay, Rolf G Lueck, and Fabian Wolk. An assessment of the dissipation rates at a tidal energy site using a VMP and an ADCP. In *Proceedings of 11th European Wave and Tidal Energy Conference, Nantes, France*, 2015.

[125] M Drela. XFOIL: An analysis and design system for low Reynolds number airfoils, 1989. URL http://link.springer.com/chapter/10.1007/978-3-642-84010-4{_}1.

[126] Dimitri V Val and Leon Chernin. Reliability-Based Design of Rotor Blades in Tidal Stream Turbines. In *European Wave and Tidal Energy Conference*, Southampton, 2011.

[127] R. Evans, R. McAdam, M. Royle, and L Mcewen. Optimum geometry for axial flow free stream tidal turbine blades. *10th European Wave and Tidal Energy Conference (EWTEC 2013), Aalborg, DK, 02. - 05. Sep 2013.*

[128] J L Van Ingen. The eN method for transition prediction. Historical review of work at TU Delft. In *Fluid Dynamics Conference and Exhibit*, number June, pages 1–49, Seattle, 2008.

[129] Mark Drela and Harold Youngren. XFOIL 6.9 User Primer, 2001.

[130] D M Hamby. A review of techniques for parameter sensitivity analysis of environmental models. *Environmental monitoring and assessment*, 32(2):135–54, sep 1994. ISSN 0167-6369. doi: 10.1007/BF00547132. URL http://www.ncbi.nlm.nih.gov/pubmed/24214086.

[131] G Bir and P Migliore. Preliminary structural design of composite blades for two- and three-blade rotors. NREL Technical report 500-31486. Technical Report September, National Renewable Energy Laboratory, 2004.

[132] Nicholas A.G. Osbourne. *3D modelling of a tidal turbine - a numerical investigation of wake phenomena*. Master of applied science, Dalhousie University, 2015.

[133] T. McCombes, C. Johnstone, B. Holmes, L. E. Myres, A. S. Bahaj, VJ. P. Kofoed Heller, J. Finn, and C. Bittencourt. EquiMar Deliverable D3.3 - Assessment of current practice for tank testing of small marine energy devices. Technical report, 2010.

[134] Dan M Somers. Design and Experimental Results for the S814 Airfoil. Technical Report January, National Renewable Energy Laboratory, 1997.